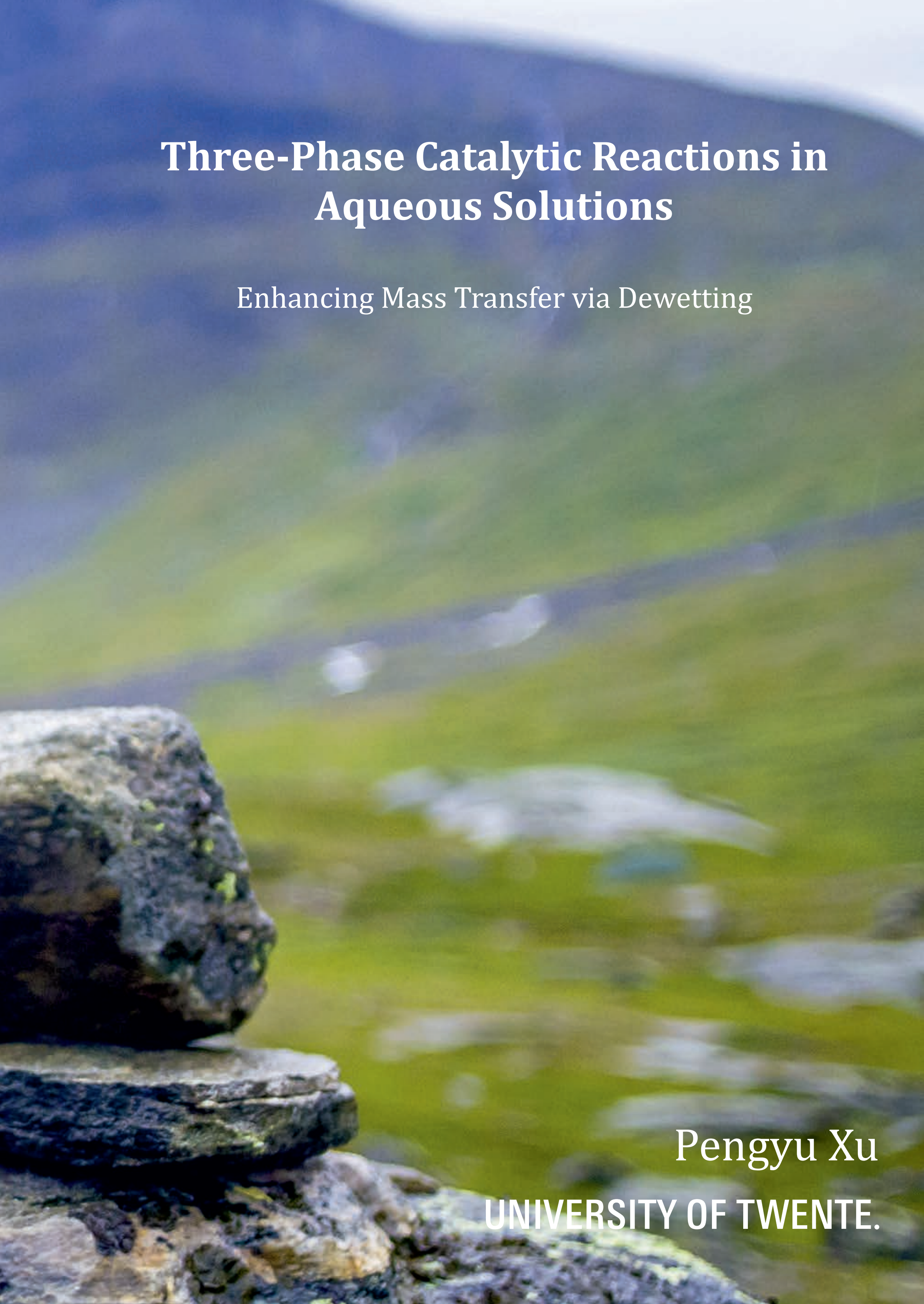

Three-Phase Catalytic Reactions in Aqueous Solutions

Enhancing Mass Transfer via Dewetting

Pengyu Xu

UNIVERSITY OF TWENTE.

THREE-PHASE CATALYTIC REACTIONS IN AQUEOUS SOLUTIONS

ENHANCING MASS TRANSFER VIA DEWETTING

Pengyu Xu

Graduation Committee

Chairman: Prof. dr. J. L. Herek	University of Twente, NL
Promoter: Prof. dr. ir. L. Lefferts	University of Twente, NL
Committee Members:	
Prof. dr. ir. R. G. H. Lammertink	University of Twente, NL
Prof. dr. J. G. E. Gardeniers	University of Twente, NL
Prof. dr. F. Kapteijn	Delft University of Technology, NL
Prof. dr. ir. J. van der Schaaf	Eindhoven University of Technology, NL
Prof. dr. ing. M. Wessling	RWTH Aachen University, DE
Prof. dr. P. Granger	Université de Lille, FR

The research described in this thesis was carried out at the *Catalytic Processes and Materials* (CPM) group of the University of Twente, The Netherlands. I acknowledge the financial support for my PhD study from *China Scholarship Council* (CSC).

Cover design: Pengyu Xu

Printed by: Gildeprint, Enschede, The Nethelands.

ISBN: 978-90-365-5047-5

DOI: 10.3990/1.9789036550475

THREE-PHASE CATALYTIC REACTIONS IN AQUEOUS SOLUTIONS

ENHANCING MASS TRANSFER VIA DEWETTING

DISSERTATION

to obtain
the degree of doctor at the University of Twente,
on the authority of the rector magnificus,
prof. dr. T.T.M. Palstra,
on account of the decision of the Doctorate Board,
to be publicly defended
on the Friday 2nd October 2020 at 14:45 hrs

by

Pengyu Xu

born on the 09th June 1990
in Xiangyang, Hubei, China

This dissertation has been approved by the promoter:

Prof. dr. ir. L. Lefferts

献给我的家人

Dedicated to my family

天道酬勤

Contents

Summary

A catalytic chemical reaction is always coupled with mass transfer since the reactants have to travel to the location where the conversion takes place while the products have to travel away. It is crucial to understand the influence of mass transfer on both activity and selectivity. The consequence of internal mass transfer limitation is that reactant gradients will develop, so that active site are exposed to different concentrations of reactants and products, influencing activity and selectivity.

In order to gain better understanding of the mechanism of nitrite hydrogenation over Pd/γ-Al_2O_3 catalyst, the intrinsic kinetics was determined in a wide window of nitrite and hydrogen concentrations. The results (**Chapter 2**) shows that the reaction orders for hydrogen and nitrite vary significantly with varying concentrations of nitrite and hydrogen. For the first time, reaction order 2 in hydrogen and negative order -0.9 in nitrite are observed, in case of low hydrogen concentration and high nitrite concentration. At high hydrogen concentration, the order in hydrogen decreases significantly from 2 to around 0.3. When hydrogen concentration is high, the order in nitrite varies between 0.5 at low nitrite concentration (below 1 mM) and 0 at higher nitrite concentration. The fact that the reaction order in hydrogen is 2 at low hydrogen concentration implies that adsorbed H (H_{ads}) is not only involved directly in the rate-determining-step (RDS), but is also involved in three pre-equilibria elementary steps, determining the influence of the hydrogen pressure on the concentration of species in the RDS. According to this principle, possible rate determining steps are discussed. It is concluded that formation of NH_{ads} via dissociative hydrogenation of $HNOH_{ads}$ is the rate determining step for formation of ammonia, whereas molecular N_2 forms via reaction of NH_{ads} with either NO_{ads}, NOH_{ads} or $HNOH_{ads}$. N-N bond formation via dimerization of adsorbed NO or adsorbed N can be excluded.

In order to overcome mass transfer limitations in the large catalyst particles, partially hydrophilic catalyst Pd/γ-Al_2O_3 has been successfully synthesized and tested (**Chapter 3**). The partially hydrophilic catalyst is synthesized by physical mixing of hydrophilic domains (below 38 μm) with hydrophobic domains (below 38 μm), followed by making a tablet by cold pressurizing, breaking and sieving to obtain ideal particle size. The hydrophobic domains are modified with FOTS (Trichloro(1H,1H,2H,2H-perfluorooctyl)silane) and do not contain any Pd as active phase, whereas hydrophilic domains contain Pd metal. The ratio of the amount of hydrophobic domains and hydrophilic domains in the partially hydrophilic catalysts is well controlled and independent of the particle size. The partially hydrophilic catalyst shows increased activity and selectivity to ammonium, compared to hydrophilic catalyst at the same hydrogen pressure and nitrite concentration. We prove that partially hydrophilic catalyst achieves the same rate per gram Pd at much lower hydrogen pressure compared to hydrophilic catalyst, forming less ammonia at the same time.

In **Chapter 4**, we present the influence of trace amounts of oxygen on formic acid decomposition reaction. The kinetics of formic acid decomposition over Pd/γ-Al_2O_3 is strongly influenced by deactivation. Trace amounts of oxygen can boost the reaction and prolong the catalyst lifetime by suppressing catalyst deactivation. However, oxygen reacts not only with CO, but also with H_2 simultaneously. Operation at low oxygen concentration (below 0.1 vol%) enhances the production of hydrogen. Furthermore, increasing oxygen concentration from 0.1 vol% to 2 vol% cause significant increasing in the rate of conversion of formic acid while decreasing the H_2 production due to formic acid oxidation, dominating the reaction.

Formic acid has been studied in **Chapter 5** as an alternative reductant for nitrite, instead of hydrogen. The results show that formic acid successfully reduces nitrite in the pH range between 4.5 and 8, forming negligible amounts of ammonium. By investigating the effect of oxygen and initial formic acid concentration, order 1.4 in formic acid was observed and it is found that the nitrite conversion rate and the formic acid decomposition rate are controlled by competitive adsorption on Pd of nitrite, forming NO, and formic acid, forming adsorbed hydrogen and CO_2. When the pH of the solution is below 4.5, homogeneous disproportionation reaction of nitrous-acid forming NO and nitric-acid takes place (Equation 1) resulting in NO poisoning. The catalyst shows no activity at pH above 8 due to the fact that formate ions are not reactive under our conditions.

$$3HNO_2 \rightarrow 2NO + HNO_3 + H_2O \quad eq1$$

Chapter 6 lists the most important findings and conclusions. Based on the conclusions, the recommendations are made.

Samenvatting

Een katalytische chemische reactie is altijd gekoppeld aan massa trasport sinds de reactanten naar de locatie moeten bewegen waar de conversie plaats vindt terwijl de producten zich hiervan weg bewegen. Het is cruciaal om de invloed van massa transport op de activiteit en selectiviteit te begrijpen. De consequentie van interne massa trasport limitatie is dat reactant gradiënten zich ontwikkelen. Een gevolg hiervan is dat de actieve sites aan verschillende reactant en product concentraties worden blootgesteld wat de activiteit en selectiviteit zal beïnvloeden.

Om het mechanisme van nitriet hydrogenering over Pd/γ-Al_2O_3 katalysator beter te begrijpen is de intrinsieke kinetiek bepaald van een uitgebreide reeks van waterstof en nitriet concentraties. De resultaten in **Hoofdstuk 2** wijzen uit dat de reactie orde voor waterstof en nitriet significant variëren bij verschillende waterstof en nitriet concentraties. Voor de eerste keer is een reactie orde van 2 voor waterstof en een negatieve orde van -0.9 voor nitriet geobserveerd in het geval van een lage waterstof concentratie en een hoge nitriet concentratie. De waterstof reactie orde neemt significant af van 2 naar 0.3 bij een hoge waterstof concentratie. Wanneer de waterstof concentratie hoog is varieert de reactie orde van nitriet tussen de 0.5 bij lage nitriet concentraties (onder 1 mM) tot 0 bij hoge nitriet concentraties. Het feit dat de reactie orde voor waterstof 2 is bij een lage nitriet concentratie betekend dat de geadsorbeerde H (H_{ads}) niet alleen direct betrokken is in de snelheidsbepalende stap maar ook betrokken is in drie pre-evenwicht elementaire stappen. Deze elementaire stappen bepalen de invloed van waterstofdruk op de concentratie van moleculen in de snelheidsbepalende stap. Volgens dit principe worden mogelijke snelheidsbepalende stappen besproken. Er wordt in dit hoofdstuk geconcludeerd dat de formatie van NHads via dissociatieve hydrogenering van $HNOH_{ads}$ de snelheidsbepalende stap is voor de formatie van ammoniak. Hiernaast wordt moleculaire N_2 gevormd via reacties met NH_{ads} en NO_{ads}, NOH_{ads} of $HNOH_{ads}$. De formatie van N-N bindingen via dimerisatie van geadsorbeerd NO of N kan worden uitgesloten

Om massa transport limitaties in grote katalysatordeeltjes te overkomen is een partieel hydrofiele Pd/γ-Al_2O_3 katalysator succesvol gesynthetiseerd en getest (**Hoofdstuk 3**). De partieel hydrofiele katalysator is gesynthetiseerd door fysiek mengen van hydrofiele domeinen (onder 38 μm) met hydrofobe domeinen (onder 38 μm). Hierop volgend wordt er een tablet geformeerd door middel van koud persen. Vervolgens is dit tablet gebroken en gezeefd om de ideale deeltjesgrootte te verwerven. De hydrofobe domeinen worden gemodificeerd met FOTS (Trichloor(1H,1H,2H,2H-perfluorooctyl)silaan en bevatten geen Pd als actieve fase. Hiertegenover bevatten de hydrofiele domeinen wel Pd metaal. Bij vergelijkbare waterstofdruk en nitriet concentratie toont de partieel hydrofiele katalysator verhoogde activiteit en selectiviteit naar ammonium vergeleken met de hydrofiele katalysator. Wij bewijzen dat de partieel hydrofiele katalysator een vergelijkbare reactiesnelheid per gram Pd bereikt op lagere waterstofdruk vergeleken met hydrofiele katalysator. Hiernaast wordt minder ammoniak gevormd bij het gebruik van de partieel hydrofiele katalysator.

In **Hoofdstuk 4** wordt de invloed van kleine hoeveelheden zuurstof op de decompositie reactie van mierenzuur gepresenteerd. De kinetiek van mierenzuur decompositie over Pd/γ-Al_2O_3 katalysator wordt sterk beïnvloed door deactivering. Sporen van zuurstof kan de reactie stimuleren en de levensduur van de katalysator verlengen door deactivering tegen te gaan. Echter reageert het zuurstof niet alleen met het gevormde CO maar tegelijkertijd met H_2. Bij lage zuurstofconcentraties (onder 0.1 vol%) wordt de waterstof productie verhoogd. Het verder verhogen van de zuurstofconcentratie van 0.1 vol% naar 2 vol% veroorzaakt een verhoging in het conversiepercentage, echter zal de waterstof productie afnemen doordat de oxidatie van het mierenzuur de reactie zal domineren.

In **Hoofstuk 5** wordt mierenzuur bestuurd als een alternatieve reductor voor nitriet in plaats van waterstof. De resultaten laten zien dat tussen een pH 4.5 en 8 nitriet succesvol is gereduceerd met behulp van mierenzuur. Bij deze reductie worden verwaarloosbare hoeveelheden ammonium gevormd. Ten gevolge van onderzoek naar het effect van zuurstof en initiële mierenzuur concentratie is een reactie orde van 1.4 in mierenzuur geobserveerd. Hiernaast is gevonden dat de nitriet conversiesnelheid en de mierenzuur deactivatie snelheid op Pd worden gedomineerd door de competitieve adsorptie van nitriet wat NO vormt en mierenzuur wat waterstof en CO_2 vormt. Wanneer de pH van de oplossing onder de 4.5 is zal de homogene disproportioneringsreactie van salpeterigzuur plaatsvinden (vergelijking 1). Hierbij zal NO en salpeterzuur worden gevormd wat resulteert in NO vergiftiging van de katalysator. De katalysator vertoont geen activiteit bij een pH boven de 8 doordat de formiaat ionen niet reactief zijn onder onze condities.

$$3HNO_2 \rightarrow 2NO + HNO_3 + H_2O \quad vgl.1$$

Hoofdstuk 6 Beschrijft de belangrijkste bevindingen en conclusies. Gebaseerd op deze conclusies zijn aanbevelingen voor vervolgonderzoeken geformuleerd.

Chapter 1

Introduction

1. Kinetic study

Chemical kinetics, also known as reaction kinetics, is the study on rates of chemical processes and the effect of variables such as the reactant concentrations, reaction temperature and the presence of a catalyst [1]. Kinetic studies provides information on the rate of a reaction under specific reaction condition, obtaining reaction orders and rate constants, including apparent activation barriers. The resulting reaction rate equation is valuable for engineers to design and operate reactors in chemical plants, maximizing yields and selectivity to the desired product. Another important reason to study kinetics is that it provides information on the mechanism of chemical reactions. Besides being of intrinsic scientific interest, knowledge of reaction mechanisms is of practical use for optimizing processes, e.g. by optimizing the formulation of the catalyst. Intrinsic kinetics is obtained when influence of heat and mass transfer is absent, both within as well as outside porous catalyst particles. Reliable intrinsic kinetic information is important for both reactor design/optimization as well as mechanistic studies, identifying reaction intermediates on the catalyst surface, elementary steps and rate determining steps.

2. Mass transfer

The rate of a heterogeneous catalyzed reaction can be determined by both intrinsic kinetics as well as mass transfer rate. In case of a porous catalyst, both external and internal mass transfer can influence the overall reaction rate.

In this thesis, nitrite hydrogenation is used as a model reaction, reducing nitrite to N_2 and ammonium with hydrogen gas as the reductant (Equation 1 and equation 2).

$$2NO_2^- + 3H_2 + 2H^+ \xrightarrow{Catalyst} N_2 + 4H_2O \qquad eq1$$

$$NO_2^- + 3H_2 + 2H^+ \xrightarrow{Catalyst} NH_4^+ + 2H_2O \qquad eq2$$

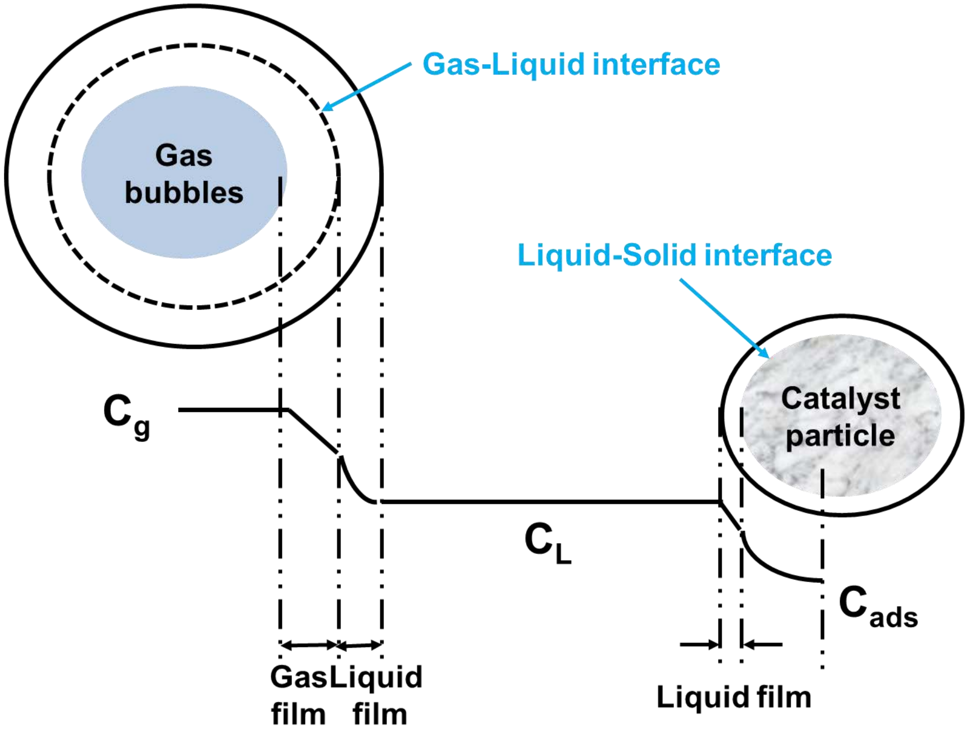

Figure 1. Typical mass transfer process in the three phase reaction.

Transport of hydrogen to the catalyst in a slurry reactor is schematically shown in Figure 1. Hydrogen gas first dissolves in water at the gas-liquid interface and diffuses through the stagnant liquid film at the gas-liquid interface. The bulk of the water is well mixed and dissolved hydrogen gas diffuses through the stagnant liquid film at the outside of the catalyst support particles, followed by diffusion into the pores of the catalyst support, before reaching the active site. The catalyst is completely wetted with water and the pores are completely filled with water. In contrast, transport of nitrite and protons proceeds via diffusion from the bulk of the liquid, via the stagnant liquid film at the external catalyst surface, to the active sites inside the pores. In case mass transfer rate is slower than the intrinsic kinetic rate, the observed reaction rate will be determined by mass transfer rather than kinetics. The consequence of mass transfer limitation is that the active sites are not fully used and are exposed to different reactant concentrations, e.g. locally lowered reactant concentrations. Therefore, the activity will decrease and selectivity of the reaction can also change [2].

2.1. Internal mass transfer

The Weisz-Prater criterion (C_{wp}, equation 3 for a first order reaction) is normally used as a criterion to estimate whether pore diffusion resistance can significantly influence the reaction rate [3].

$$C_{wp} = \frac{R_{obv} \times L^2 \times \rho_{Cat}}{C_s \times D_{eff}} \qquad eq3$$

Where R_{obv} is the reaction rate per mass of catalyst (mol*s^{-1}*kg^{-1}), L is the characteristic length of spherical catalyst particle (m), ρ_{Cat} is the density of the catalyst particles (kg*m^{-3}), C_s is the reactant concentration at the particle surface (mol*m^{-3}), and D_{eff} is the effective diffusivity (m^2*s^{-1}).

$$L = \frac{d_p}{3} \qquad eq4$$

$$D_{eff} = \frac{D_{AB} \times \phi}{\tau} \qquad eq5$$

In which d_p is radius of the catalyst particles, D_{AB} is the bulk diffusion coefficient of species [4], ϕ is the particle porosity, normally a value between 0.2 and 0.7, and τ is the tortuosity, normally varying between 1 and 10. When the value of C_{wp} is much small than 1, the effect of internal mass transfer limitation can be ignored. On the contrary, internal mass transfer affects the apparent catalyst activity if C_{wp} is larger than 1.

2.2. External mass transfer

For the gas-liquid mass transfer, we can examine under different amount of the catalyst. If the activity remains constant, it can be concluded that gas-liquid transfer is not limiting.

The liquid-solid mass transfer limitation can be validated by comparing between reaction rate and liquid-solid mass transfer rate. No liquid-solid mass transfer limitation are expected if liquid-solid mass transfer rate is much larger than the observed reaction rate [5]:

$$R_{l-s} \gg R_{obv} \qquad eq6$$

Where R_{l-s} is the estimated liquid-solid mass transfer rate, and R_{obv} is observed reaction rate. The mass transfer is first order. So the maximum mass transfer rate at concentration C_s in the bulk of the liquid, can be calculated by the following equation:

$$rate_{l-s} = k_{ls} * a_s * C_s \qquad eq7$$

Where k_{ls} is liquid-solid mass transfer coefficient, a_s geometric surface area of the catalyst per volume of solution.

The liquid-solid mass transfer coefficient is calculated according to the following expression:

$$k_{ls} = \frac{D_{AB}*Sh}{d_h} \qquad eq8$$

in which D_{AB} is the reactant diffusion coefficient in pure water (m^2*s^{-1}), d_h is the hydrodynamic size of the catalysts (m). In a typical slurry tank reactor, as the small particles essentially move with the liquid, with limited shear at the surface of the particles, this indicated the value of Sh is rather similar to the value for a particle in stagnant liquid (Sh = 2).

The geometric surface area of the catalyst per volume of solution is:

$$a_s = \frac{A_p*m}{\rho_c* V_p* V_R} \qquad eq9$$

Where A_p is the geometric surface area of one catalyst particle (m^2), m is the mass of the catalyst in the experiments (kg), V_p is the volume of one catalyst particle (m^3), and V_R is the volume of reaction solution (m^3).

If calculated R_{l-s} is significantly larger than the observed reaction rate. Therefore, liquid-solid mass transfer is not limiting.

Mears criterion allows us to estimate significance of external mass transfer limitations at both the gas-liquid and liquid-solid interfaces [6].

$$\frac{-r_{obs}\rho_b d_p n}{K_c C_s} < 0.15 \qquad eq10$$

Where $-r_{obs}$ is the observed rate per unit mass of catalyst (mol*kg^{-1}*s^{-1}), n is the reaction order, d_p is the catalyst particle radius (m), ρ_b is bulk density of the catalyst (kg*m^{-3}), C_s is bulk concentration (mol*m^{-3}), and K_c is the mass transfer coefficient (m/s). External mass transfer limitations can be ignored if Mears criterion value is smaller than 0.15.

3. Structured catalyst

In a chemical reaction, the catalyst is designed to maximize the mass transfer and the number of active sites. Therefore, support materials with high surface area are preferred in order to maximize the number of active sites by maximizing both metal loading as well as metal dispersion. However, according to equation 3, increasing the catalyst size could increase internal mass transfer resistance, resulting in lower activity. This can be counteracted by using small catalyst support particles [2,7,8] or egg-shell catalyst [9] in a slurry phase reactor. Furthermore, based on equation 5, it is also shown that tortuosity of the catalyst influences the internal mass transfer. The regularly channel support materials such as SBA [10], entangled carbon nanofibers [11] and MOF [12,13] can be used to minimize the tortuosity of the catalyst support. However it is not practical to use small catalyst particles in a fixed bed reactor or trickle bed reactor due to the high pressure drop in the operation. Trickle bed reactors are frequently used in practice [14], despite the fact that internal diffusion limitations often occur because of the larger support particle size, implying longer diffusion lengths.

In order to prevent long diffusion lengths in large catalyst support particles, considering the pressure drop, structured catalyst supports such as monoliths [15–17] and foam support [18–20] can be used. However, both monoliths and open foam supports exhibit a very high porosity but very low specific surface area. The specific surface area is usually increased by wash coating with a material with a high specific surface area. For Ni open foam support, carbon nanofibers (CNF) grown on the foam is used to increase the surface area and Ni foam supported CNF catalysts have been studied in our group [4,11,20–22], demonstrating significant improvement of the rate of internal mass transfer.

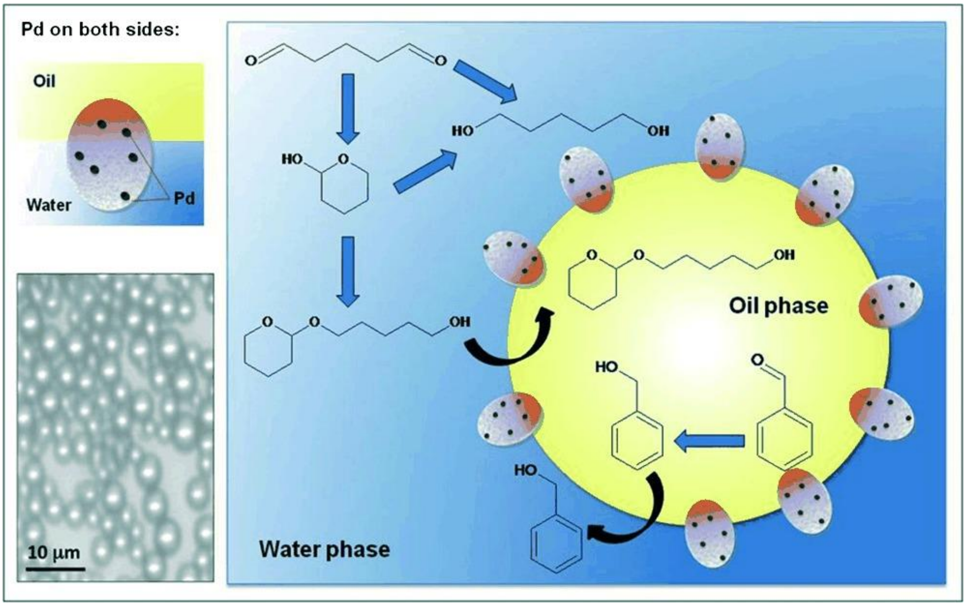

Figure 2. Microscopy image of the oil-in-water emulsion produced with the Janus particles together with a schematic illustration of the hydrogenation reactions taking place at the water/oil interface catalyzed by Pd clusters supported on both sides of the Janus nanoparticles. At the beginning of the reaction, glutaraldehyde is present in the aqueous phase and benzaldehyde in the oil phase [28].

Partially hydrophobic catalysts have been explored for improving the mass transfer [23–27]. "Janus" type of catalyst particles have been developed to increase the external mass transfer in liquid-liquid phase system e.g. hydrogenation of benzaldehyde and glutaraldehyde [28]. As shown in Figure 2, the surface of the support of a Pd catalyst was modified as half hydrophilic and half hydrophobic. The hydrophilic and hydrophobic property enables that the catalyst to conduct the reaction at the interface of oil and water. However, only the external surface is modified in such Janus particles which means the external mass transfer is enhanced, but not the internal mass transfer.

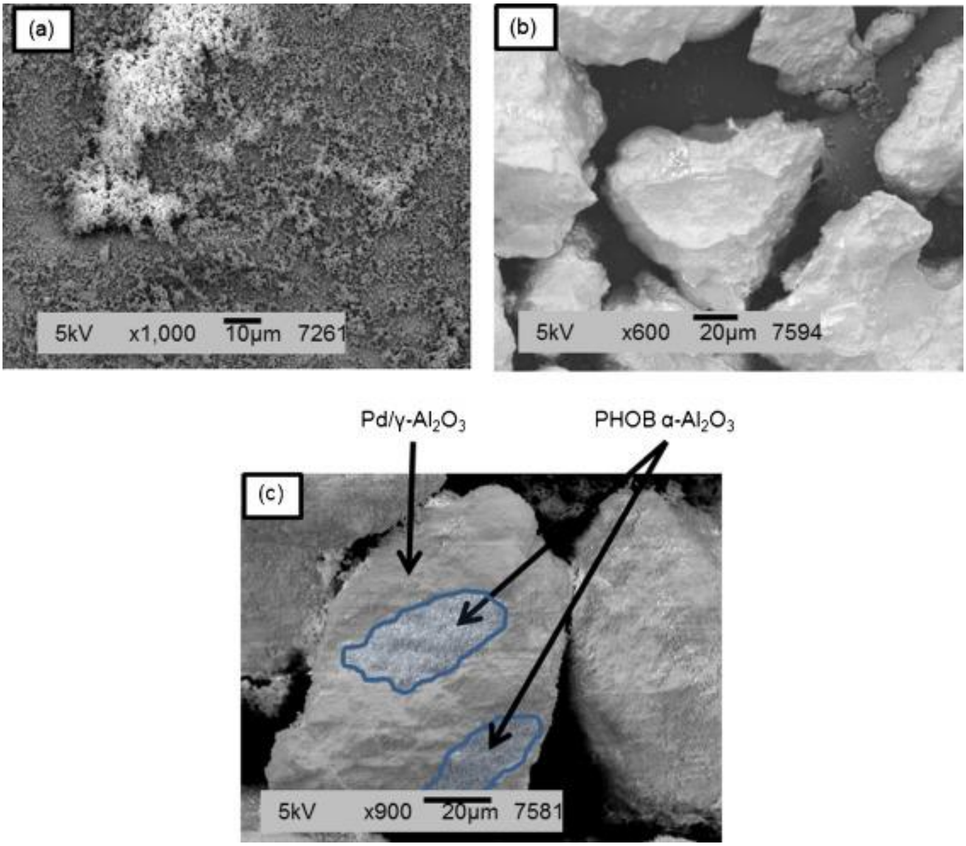

Figure 3. SEM picture of: (a) α-alumina; (b) γ-alumina; (c) physical mixture of hydrophobic α-alumina and hydrophilic γ-alumina [2].

In our previous work, we reported on the influence of partial hydrophobization of Pd/γ-Al_2O_3 on the catalytic activity and selectivity of nitrite hydrogenation in a slurry reactor [2]. Be noted, the partially hydrophilic catalyst is obtained via physical mixing hydrophilic domains (γ-Al_2O_3) and hydrophobic domains (α-Al_2O_3), followed by pelletization, breaking and sieving. This is first attempt so far to change both internal and external wettability (Figure 3). It turned out that the ammonium selectivity increased significantly whereas the activity slightly increased as a result of partial hydrophobization of the catalyst. The increasing ammonium selectivity is ascribed enhancement of hydrogen mass transfer, increasing the hydrogen concentration at the active sites and in turn increasing the selectivity to undesired ammonium. Nevertheless, this result proved that mass transfer can be manipulated via the catalyst wettability.

4. Nitrite hydrogenation

Nitrate and nitrite in drinking water is becoming a severe worldwide problem caused by intensive agricultural and industrial activities [29]. Nitrate and nitrite in drinking water can threaten human health, including blue baby syndrome, high blood pressure, diabetes and liver damage, [30–33]. According to the World Health Organization (WHO) regulations, the maximum allowable levels of nitrate and nitrite concentration in drinking water are 50 mg/L and 3 mg/L as nitrate and nitrite ion respectively [34].

Various processes have been developed to remove nitrate and nitrite from water, including ion exchange, reverse osmosis, electro dialysis, photocatalytic reduction, catalytic reduction, and biological methods [30,32,35–40]. Catalytic reduction is the more promising technique for purification of drinking water. Using biological method to convert nitrite and nitrate in drinking water is not practical since it lacks nutrients for microorganisms. Ion exchange as another process has been used for water treatment. While effective, ion exchange does not convert nitrite ions. Rather, a nitrite contaminated brine solution is produced, requiring either post-treatment or has to be discarded otherwise while emissions are increasingly being banned [30,32,35,39,41–45].

Since the first paper published by Vorlop and Tacke et al. reporting on catalytic reduction of nitrate in the early 90s [31], nitrate and nitrite hydrogenation has been studied by many researchers. It is well known that hydrogenation of nitrate proceeds in two steps. First, nitrate is reduced to nitrite, requiring a non-noble promotor such as e.g. Cu, which is generally rate determining. Further conversion of nitrite is much faster and determines the selectivity according to the following reaction equations:

$$NO_3^- + H_2 \xrightarrow{Catalyst} NO_2^- + H_2O \qquad eq11$$

$$2NO_2^- + 3H_2 + 2H^+ \xrightarrow{Catalyst} N_2 + 4H_2O \qquad eq1$$

$$NO_2^- + 3H_2 + 2H^+ \xrightarrow{Catalyst} NH_4^+ + 2H_2O \qquad eq2$$

The very fast nitrite hydrogenation reaction is ideal for studying mass transfer. In addition, it is known that the product distribution is very sensitive to subtle changes in the local concentrations at the active sites, influencing the surface coverages of N-species and H- species on Pd surface [2,4]. Therefore, the selectivity is strongly influenced by mass transfer of both hydrogen and nitrite.

5. Formic acid

Hydrogen may play an important role in power generation in the future as a green energy carrier. Due to the low density, extreme low critical point (−239.95 °C, 12.8 atm) and its high flammability, hydrogen storage is difficult and potentially dangerous [59–62]. Liquid hydrogen carriers have been proposed recently, including formic acid [63–66], ammonia [67], methanol [68], methane [59] as well as higher hydrocarbons [62]. Formic acid is also an important byproduct in many biomass processes. It is a chemical with low-toxicity that can be easily stored, transferred and handled [63,66,69,70], suitable as a liquid hydrogen carrier. More importantly, formic acid can be recyclable by the "formic acid-carbon dioxide cycle", which does not produce any exhaust [71].

Formic acid decomposition reactions can proceed via two pathways:

$$HCOOH \xrightarrow{Catalyst} CO_2 + H_2 \qquad eq12$$

$$HCOOH \xrightarrow{Catalyst} CO + H_2O \qquad eq13$$

Formic acid needs to decompose via the dehydrogenation pathway (Equation 12) to retrieve H_2 out, instead of dehydration (Equation 13). Formic acid decomposition has been studied with homogeneous [61,66,70] and heterogeneous catalyst [65,71–73].

Homogeneous catalyst achieved higher activity than heterogeneous catalysts but it faces difficulties in catalyst separation and catalyst stability, which causes more complexity in the design of equipment for practical applications. On the contrary, heterogeneous catalysts have the advantage of easier separation and regeneration.

Extensive efforts have been made to improve the catalyst performance with different combinations of active metal [13,74–78] and different support materials [79–84]. However, the side product CO can cause catalyst deactivation which would be an obstacle for using formic acid in the energy applications. In the gas phase reaction, due to the elevated temperature, CO desorbs much easier from active sites, preventing CO poisoning [85]. Additionally, both product groups can be interconnected via the water–gas shift reaction at elevated reaction temperatures [66]. In contrast, liquid phase formic acid decomposition at low temperatures is easier poisoned by CO [72,86–88]. However, also other hypothesis on the deactivation mechanism have been proposed, including poisoning by H atoms [89] and formate [73], requiring further investigations.

6. Scope and outline of the thesis

In this thesis, we explore a new method to enhance mass transfer via modification of the catalyst wettability. The method is aiming at manipulating both external and internal mass transfer at the same time. Nitrite hydrogenation and formic acid are chosen as the model reactions to study the mass transfer. Nitrite hydrogenation is a three phase reaction with H_2 gas used as the reductant considering H_2 gas transferring to the inside of the catalyst, whereas formic acid decomposition forms significant amount of gas products considering the gas products transferring to the outside of the catalyst. We are trying to understand how the structure of the hydrophilic/hydrophobic catalyst determines the mass transfer outside and inside the catalyst particles. The concept is explained in Figure 3, bottom of the figure, showing that gas bubbles will not only interact with the hydrophobic parts of the external surface, but will also fill the pores in the hydrophobic domains with gas. As a result, a gas-liquid interface exists inside the catalyst particles, resulting in extremely short diffusion pathways in wetted pores (**Chapter 3**).

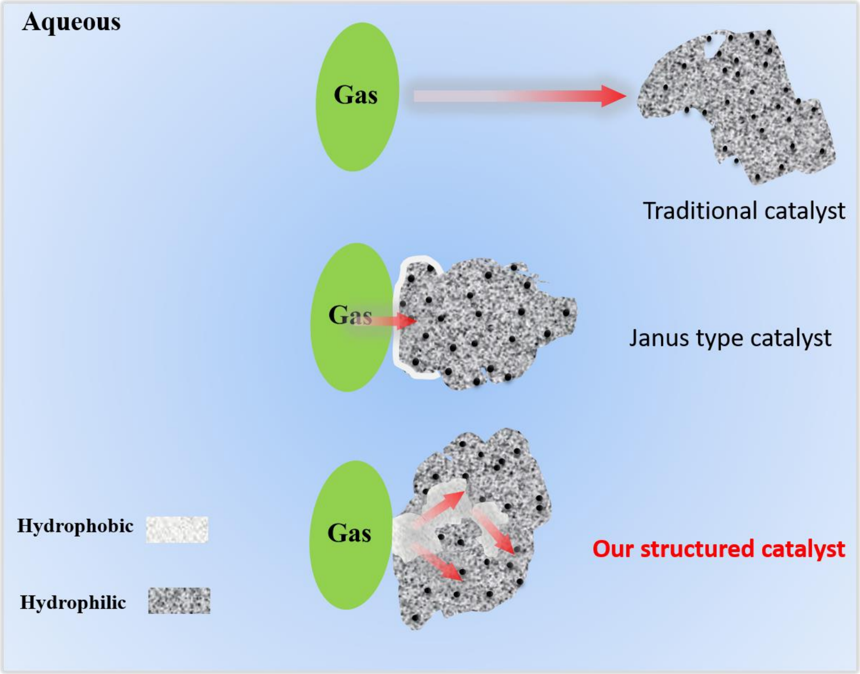

Figure 3. Schematic representation of the concept of the interaction of catalyst containing hydrophobic domains with gas bubbles in water (bottom), compared to a traditional hydrophilic catalyst (top) and a Janus particle with hydrophobicity exclusively at the external surface (middle) (**Chapter 3**).

In **Chapter 2**, we performed a rigorous intrinsic kinetic study for nitrite hydrogenation to obtain the reaction orders in nitrite and hydrogen in a wide operation window. Significant high order in hydrogen was observed at low hydrogen pressures and a negative order in nitrite was reported, for the first time. Based on these reaction order, various reaction mechanism schemes have been discussed and some of them can be rejected.

In **Chapter 3**, partially hydrophilic catalyst was successfully synthesized, as shown in Figure 3, for improving the mass transfer of hydrogen, using nitrite hydrogenation as a case study to prove the principle. We test the hypothesis that a partially hydrophilic catalyst can operate at lower hydrogen pressure with the same activity and at the same time lower selectivity to ammonia, compared to a classical hydrophilic catalyst. In addition, the influences of the support particle size as well as the ratio between hydrophilic and hydrophobic domains have been discussed.

In order to eliminate the H_2 mass transfer influence, formic acid is chosen as the reductant since formic acid can decompose to H_2 and CO_2. Therefore, H_2 can be locally used for nitrite reduction directly. However before we study the catalyst performance of nitrite reduction with formic acid, formic acid decomposition needs to be well investigated first. As we know, the supported Pd catalyst suffers severe deactivation for formic acid decomposition. In **Chapter 4**, we studied the influence of oxygen on the reaction rate, product distribution and deactivation in formic acid decomposition over Pd catalysts. The influence of the pH of the solution and the formic acid concentration are also discussed.

After investigating the formic acid decomposition reaction over Pd catalyst (**Chapter 4**), in **Chapter 5** we further studied the use of formic acid as reductant to reduce nitrite. The performance of Pd catalysts is tested under well controlled conditions, including pH and the presence of oxygen. The influence of pH and oxygen and formic acid concentration have been studied. ATR-IR technique is also applied to study the adsorbed species on Pd surface to help to understand the reaction mechanism.

Chapter 6 summarizes the main findings of the thesis and concludes with recommendations for further work.

Reference

[1] P. Pfeifer, *Chemical Kinetics*, InTech, **2012**.

[2] C. Franch, R. G. H. Lammertink, L. Lefferts, *Appl. Catal. B Environ.* **2014**, *156–157*, 166–172.

[3] D. Shuai, J. K. Choe, J. R. Shapley, C. J. Werth, *Environ. Sci. Technol.* **2012**, *46*, 2847–2855.

[4] R. Brunet Espinosa, D. Rafieian, R. G. H. Lammertink, L. Lefferts, *Catal. Today* **2016**, *273*, 50–61.

[5] A. J. Frierdich, J. R. Shapley, T. J. Strathmann, *Environ. Sci. Technol.* **2008**, *42*, 262–269.

[6] D. E. Mears, *Ind. Eng. Chem. Process Des. Dev.* **1971**, *10*, 541–547.

[7] Y. Zhao, L. Jia, J. A. Medrano, J. R. H. Ross, L. Lefferts, *ACS Catal.* **2013**, *3*, 2341–2352.

[8] Y. Zhao, J. A. Baeza, N. Koteswara Rao, L. Calvo, M. A. Gilarranz, Y. D. Li, L. Lefferts, *J. Catal.* **2014**, *318*, 162–169.

[9] R. Brunet Espinosa, D. Rafieian, R. S. Postma, R. G. H. Lammertink, L. Lefferts, *Appl. Catal. B Environ.* **2018**, *224*, 276–282.

[10] M. H. Jin, D. Oh, J. H. Park, C. B. Lee, S. W. Lee, J. S. Park, K. Y. Lee, D. W. Lee, *Sci. Rep.* **2016**, *6*, 33502.

[11] J. K. Chinthaginjala, J. H. Bitter, L. Lefferts, *Appl. Catal. A Gen.* **2010**, *383*, 24–32.

[12] H. Alamgholiloo, S. Zhang, A. Ahadi, S. Rostamnia, R. Banaei, Z. Li, X. Liu, M. Shokouhimehr, *Mol. Catal.* **2019**, *467*, 30–37.

[13] M. Wen, K. Mori, Y. Futamura, Y. Kuwahara, M. Navlani-García, T. An, H. Yamashita, *Sci. Rep.* **2019**, *9*, 1–10.

[14] A. M. Bergquist, M. Bertoch, G. Gildert, T. J. Strathmann, C. J. Werth, *J. Am. Water Works Assoc.* **2017**, *109*, E129–E143.

[15] J. Wärn, I. Turunen, T. Salmi, T. Maunula, *Chem. Eng. Sci.* **1994**, *49*, 5763–5773.

[16] A. Devard, M. A. Ulla, F. A. Marchesini, *Catal. Commun.* **2013**, *34*, 26–29.

[17] G. Bercˇicˇ, A. Pintar, *Chem. Eng. Sci.* **1997**, *52*, 3709–3719.

[18] R. Tschentscher, R. J. P. Spijkers, T. A. Nijhuis, J. Van Der Schaaf, J. C. Schouten, in *Ind. Eng. Chem. Res.*, **2010**, pp. 10758–10766.

[19] P. W. a. M. Wenmakers, J. van der Schaaf, B. F. M. Kuster, J. C. Schouten, *J. Mater. Chem.* **2008**, *18*, 2426–2436.

[20] J. K. Chinthaginjala, D. B. Thakur, K. Seshan, L. Lefferts, *Carbon N. Y.* **2008**, *46*, 1638–1647.

[21] R. Brunet Espinosa, L. Lefferts, *ACS Catal.* **2016**, *6*, 5432–5440.

[22] J. K. Chinthaginjala, A. Villa, D. S. Su, B. L. Mojet, L. Lefferts, *Catal. Today* **2012**, *183*, 119–123.

[23] V. Hessel, P. Angeli, A. Gavriilidis, H. Löwe, *Ind. Eng. Chem. Res.* **2005**, *44*, 9750–9769.

[24] M. J. Geerken, T. S. van Zanten, R. G. H. Lammertink, Z. Borneman, W. Nijdam, C. J. M. van Rijn, M. Wessling, *Adv. Eng. Mater.* **2004**, *6*, 749–754.

[25] A. Quintanilla, J. J. W. W. Bakker, M. T. Kreutzer, J. A. Moulijn, F. Kapteijn, *J. Catal.* **2008**, *257*, 55–63.

[26] C. Grote, M. Rosu, A. Schumpe, *Can. J. Chem. Eng.* **2010**, *88*, 633–637.

[27] H. Yang, X. Jiao, S. Li, *Chem. Commun.* **2012**, *48*, 11217–11219.

[28] J. Faria, M. P. Ruiz, D. E. Resasco, *Adv. Synth. Catal.* **2010**, *352*, 2359–2364.

[29] G. Gulis, M. Czompolyova, J. R. Cerhan, *Environ. Res.* **2002**, *88*, 182–187.

[30] C. S. Bruning-Fann, J. B. Kaneene, *Vet. Hum. Toxicol.* **1993**, *35*, 521–538.

[31] S. Hörold, K.-D. Vorlop, T. Tacke, M. Sell, *Catal. Today* **1993**, *17*, 21–30.

[32] V. Matějů, S. Čižinská, J. Krejčí, T. Janoch, *Enzyme Microb. Technol.* **1992**, *14*, 170–183.

[33] J. Schullehner, B. Hansen, M. Thygesen, C. B. Pedersen, T. Sigsgaard, *Int. J. Cancer* **2018**, *143*, 73–79.

[34] W. H. Organization, “Guidelines for Drinking-water Quality FOURTH EDITION,” **n.d.**

[35] H. C. Aran, J. K. Chinthaginjala, R. Groote, T. Roelofs, L. Lefferts, M. Wessling, R. G. H. H. Lammertink, *Chem. Eng. J.* **2011**, *169*, 239–246.

[36] J. J. F. Scholten, in *Stud. Surf. Sci. Catal.*, **1979**, pp. 685–714.

[37] A. Bothner-By, L. Friedman, *J. Chem. Phys.* **1952**, *20*, 459–462.

[38] M. Boudart, *Chem. Rev.* **1995**, *95*, 661–666.

[39] K. T. Ranjit, B. Viswanathan, *J. Photochem. Photobiol. A Chem.* **1997**, *108*, 73–78.

[40] A. Pintar, G. Berčič, J. Levec, *AIChE J.* **1998**, *44*, 2280–2292.

[41] A. Obuchi, S. Naito, T. Onishi, K. Tamaru, *Surf. Sci.* **1982**, *122*, 235–255.

[42] V. Höller, I. Yuranov, L. Kiwi-Minsker, A. Renken, *Catal. Today* **2001**, *69*, 175–181.

[43] S. D. Ebbesen, B. L. Mojet, L. Lefferts, *Langmuir* **2008**, *24*, 869–879.

[44] A. J. Lecloux, *Catal. Today* **1999**, *53*, 23–34.

[45] M. Hu, Y. Liu, Z. Yao, L. Ma, X. Wang, *Front. Environ. Sci. Eng.* **2018**, *12*, 1–18.

[46] G. Strukul, R. Gavagnin, F. Pinna, E. Modaferri, S. Perathoner, G. Centi, M. Marella, M. Tomaselli, *Catal. Today* **2000**, *55*, 139–149.

[47] O. M. Ilinitch, L. V. Nosova, V. V. Gorodetskii, V. P. Ivanov, S. N. Trukhan, E. N. Gribov, S. V. Bogdanov, F. P. Cuperus, *J. Mol. Catal. A Chem.* **2000**, *158*, 237–249.

[48] F. Ruiz-Beviá, M. J. Fernández-Torres, *J. Clean. Prod.* **2019**, *217*, 398–408.

[49] G. Mendow, N. S. Veizaga, C. A. Querini, B. S. Sánchez, *J. Environ. Chem. Eng.* **2019**, *7*, 102808.

[50] K. N. Heck, S. Garcia-Segura, P. Westerhoff, M. S. Wong, *Acc. Chem. Res.* **2019**, *52*, 906–915.

[51] Y. Sakamoto, K. Nakamura, R. Kushibiki, Y. Kamiya, T. Okuhara, *Chem. Lett.* **2005**, *34*, 1510–1511.

[52] D. Gašparovičová, M. Králik, M. Hronec, Z. Vallušová, H. Vinek, B. Corain, *J. Mol. Catal. A Chem.* **2007**, *264*, 93–102.

[53] U. Prüsse, M. Hähnlein, J. Daum, K. D. Vorlop, *Catal. Today* **2000**, *55*, 79–90.

[54] A. Kapoor, T. Viraraghavan, *J. Environ. Eng.* **1997**, *123*, 371–380.

[55] A. Pintar, J. Batista, J. Levec, T. Kajiuchi, *Appl. Catal. B Environ.* **1996**, *11*, 81–98.

[56] J. Sá, J. Montero, E. Duncan, J. A. Anderson, *Appl. Catal. B Environ.* **2007**, *73*, 98–105.

[57] H. O. N. Tugaoen, S. Garcia-Segura, K. Hristovski, P. Westerhoff, *Sci. Total Environ.* **2017**, *599–600*, 1524–1551.

[58] S. Tyagi, D. Rawtani, N. Khatri, M. Tharmavaram, *J. Water Process Eng.* **2018**, *21*, 84–95.

[59] E. Rivard, M. Trudeau, K. Zaghib, *Materials (Basel).* **2019**, *12*, DOI 10.3390/ma12121973.

[60] F. Sánchez, D. Motta, N. Dimitratos, *Appl. Petrochemical Res.* **2016**, *6*, 269–277.

[61] M. Yadav, Q. Xu, *Energy Environ. Sci.* **2012**, *5*, 9698–9725.

[62] U. Bossel, B. Eliasson, *Eur. Fuel Cell Forum, Lucerne* **2002**, 36.

[63] K. Grubel, H. Jeong, C. W. Yoon, T. Autrey, *J. Energy Chem.* **2020**, *41*, 216–224.

[64] M. Navlani-García, K. Mori, D. Salinas-Torres, Y. Kuwahara, H. Yamashita, *Front. Mater.* **2019**, *6*, 1–18.

[65] H. Zhong, M. Iguchi, M. Chatterjee, Y. Himeda, Q. Xu, H. Kawanami, *Adv. Sustain. Syst.* **2018**, 1700161.

[66] M. Grasemann, G. Laurenczy, *Energy Environ. Sci.* **2012**, *5*, 8171–8181.

[67] W. Wang, J. M. Herreros, A. Tsolakis, A. P. E. York, *Int. J. Hydrogen Energy* **2013**, *38*, 9907–9917.

[68] M. Bertau, H. Offermanns, L. Plass, F. Schmidt, H. J. Wernicke, *Methanol: The Basic Chemical and Energy Feedstock of the Future: Asinger's Vision Today*, **2014**.

[69] A. K. Singh, S. Singh, A. Kumar, *Catal. Sci. Technol.* **2015**, *6*, 12–40.

[70] R. van Putten, T. Wissink, T. Swinkels, E. A. Pidko, *Int. J. Hydrogen Energy* **2019**, DOI 10.1016/j.ijhydene.2019.01.153.

[71] L. Zhang, W. Wu, Z. Jiang, T. Fang, *Chem. Pap.* **2018**, *72*, 2121–2135.

[72] M. Navlani-García, D. Salinas-Torres, D. Cazorla-Amorós, *Energies* **2019**, *12*, DOI

10.3390/en12214027.

[73] M. Caiti, D. Padovan, C. Hammond, *ACS Catal.* **2019**, *9*, 9188–9198.

[74] T. Feng, J. M. Wang, S. T. Gao, C. Feng, N. Z. Shang, C. Wang, X. L. Li, *Appl. Surf. Sci.* **2019**, *469*, 431–436.

[75] Z. Dong, F. Li, Q. He, X. Xiao, M. Chen, C. Wang, X. Fan, L. Chen, *Int. J. Hydrogen Energy* **2019**, *44*, 11675–11683.

[76] Y. Kim, J. Kim, D. H. Kim, *RSC Adv.* **2018**, *8*, 2441–2448.

[77] Y. Huang, J. Xu, T. Long, Q. Shuai, Q. Li, *J. Nanosci. Nanotechnol.* **2017**, *17*, 3798–3802.

[78] S. Akbayrak, Y. Tonbul, S. Özkar, *Appl. Catal. B Environ.* **2017**, *206*, 384–392.

[79] M. Navlani-García, D. Salinas-Torres, K. Mori, A. F. Léonard, Y. Kuwahara, N. Job, H. Yamashita, *Catal. Today* **2019**, *324*, 90–96.

[80] Y. Shi, Z. Xiang, J. Deng, J. Nan, B. Zhang, *Mater. Lett.* **2019**, *237*, 61–64.

[81] M. H. Jin, J. H. Park, D. Oh, J. S. Park, K. Y. Lee, D. W. Lee, *Int. J. Hydrogen Energy* **2019**, *44*, 4737–4744.

[82] T. Y. Ding, Z. G. Zhao, M. F. Ran, Y. Y. Yang, *J. Colloid Interface Sci.* **2019**, *538*, 474–480.

[83] J. Sun, H. Qiu, W. Cao, H. Fu, H. Wan, Z. Xu, S. Zheng, *ACS Sustain. Chem. Eng.* **2019**, *7*, 1963–1972.

[84] Y. Wu, M. Wen, M. Navlani-García, Y. Kuwahara, K. Mori, H. Yamashita, *Chem. - An Asian J.* **2017**, *12*, 860–867.

[85] D. A. Bulushev, S. Beloshapkin, J. R. H. Ross, *Catal. Today* **2010**, *154*, 7–12.

[86] Y. Wang, Y. Qi, D. Zhang, C. Liu, *J. Phys. Chem. C* **2014**, *118*, 2067–2076.

[87] Q. Lv, Q. Meng, W. Liu, N. Sun, K. Jiang, L. Ma, Z. Peng, W. Cai, C. Liu, J. Ge, L. Liu, W. Xing, *J. Phys. Chem. C* **2018**, *122*, 2081–2088.

[88] M. Yurderi, A. Bulut, M. Zahmakiran, M. Kaya, *Appl. Catal. B Environ.* **2014**, *160–161*, 514–524.

[89] D. M. Ruthven, R. S. Upadhye, *J. Catal.* **1971**, *21*, 39–47.

Chapter 2

Mechanism of nitrite hydrogenation over Pd/γ-Al_2O_3 according a rigorous kinetic study

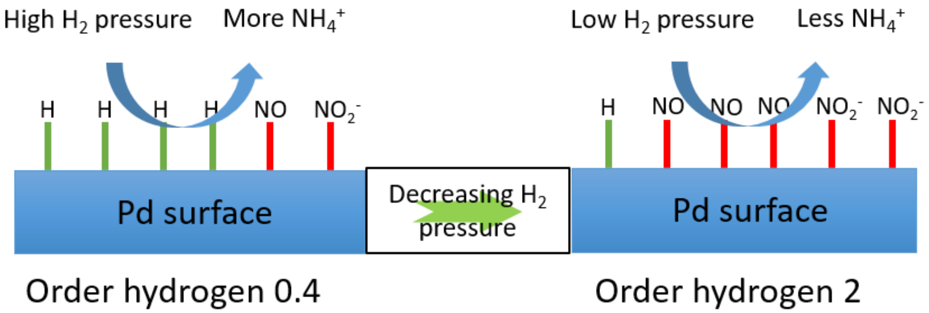

Published as: Mechanism of nitrite hydrogenation over Pd/γ-Al_2O_3 according a rigorous kinetic study, Journal of Catalysis, Volume 383, March 2020, Pages 124-134

Abstract:

The kinetics of nitrite hydrogenation over a Pd/γ-Al_2O_3 catalyst was studied in a semi-batch slurry reactor at atmospheric pressure, in absence of any mass transfer effects. The hydrogen concentration and pH were kept constant during an experiment by continuously flowing a gas mixture containing hydrogen and 10 % v/v CO_2. The kinetic experiments were performed in an unprecedented wide concentration window of nitrite and hydrogen, revealing extreme variation in the apparent orders in hydrogen and nitrite, including reaction orders in hydrogen between 2 and 0.3, whereas the order in nitrite varied between 0.4 and -0.9. The rate of reaction is almost exclusively determined by the rate of formation of N_2 as the selectivity to ammonia is very low. A Langmuir-Hinshelwood mechanism with competitive adsorption is in operation. Several mechanistic pathways, as well as possible rate determining steps in those pathways, are discussed based on these observations in combination with prior knowledge on the mechanism in literature, resulting in a revised mechanistic scheme. It is concluded that formation of NH via dissociative hydrogenation of HNOH is the rate determining step, whereas molecular N_2 forms via reaction of NH with either NO, NOH or HNOH. N-N bond formation via dimerization of adsorbed NO or adsorbed N can be excluded.

1. Introduction

Nitrate pollution in water is becoming a severe problem all over the world caused by emissions from agricultural and industrial activities [1], threatening human health, including blue baby syndrome, high blood pressure, diabetes, liver damage, and various cancers [2–5]. The World Health Organization (WHO) the maximum allowable levels of nitrate and nitrite concentration in drinking water are 50 mg/L as nitrate ion for nitrate, 3 mg/L as nitrite ion for nitrite, and 1.5 mg/L for ammonia, respectively [6]. Various processes have been developed to remove nitrate from water, including ion exchange, reverse osmosis, electro dialysis, photocatalytic reduction, catalytic reduction, and biological methods [2,4,7–12]. Among these techniques, catalytic reduction of nitrate with reducing agents is attractive because it converts nitrate to harmless nitrogen gas in the absence of any nutrients and without producing a highly concentrated brine [2,4,10,12–17].

Since the first successful demonstration of catalytic reduction of nitrate by Vorlop and Tacke [3], extensive research [18–30] has been performed, mostly using hydrogen gas as the reducing agent. It is well known that hydrogenation of nitrate proceeds in two steps. First, nitrate is reduced to nitrite, requiring a non-noble promotor such as e.g. Cu, which is generally rate determining. Further conversion of nitrite is much faster and determines the selectivity according to the following reaction equations:

$$2NO_2^- + 3H_2 + 2H^+ \xrightarrow{Catalyst} N_2 + 4H_2O \qquad eq1$$

$$NO_2^- + 3H_2 + 2H^+ \xrightarrow{Catalyst} NH_4^+ + 2H_2O \qquad eq2$$

Catalytic hydrogenation of nitrite in water has been studied using different noble metal catalysts and different support materials [3,10,31–38]. Among them, Hörold et al. [3] tested different active metal catalyst including Pd, Pt, Ir, Ru and Rh, reporting that Pd based catalyst have good activity and the lowest selectivity to NH_4^+, which has been confirmed in several other studies [12,39–46]. Maximizing the selectivity to N_2 is the key issue because NH_4^+ is at least equally undesired in drinking water with a maximal acceptable concentration of 1.5 mg/L [6].

Further suppressing of ammonia formation requires good knowledge of reaction kinetics and the catalytic mechanism. Few studies on kinetic and mechanism have been published. Wärn et al. [47] presented detailed kinetic data on nitrate hydrogenation over Pd-Cu/γ-Al_2O_3 in a monolith reactor and proposed a mechanistic reaction pathway. In this mechanism, adsorbed NO (NO_{ads}) is proposed as a key intermediate species in the conversion of nitrite to N_2 and NH_3. NO_{ads} is also proposed as the key intermediate species in nitrite hydrogenation [19,48–51]. Ebbesen et al. [49] were the first to actually observe NO_{ads} as the intermediate species during nitrite hydrogenation based on ATR-IR spectroscopy. On the other hand, NO_{ads} can also dissociate into N_{ads} and O_{ads} atom, as observed by Zhao et al. work [51]. To summarize, the pathway from NO_{ads} to N_2 and NH_4^+ is still unclear and under debate. Most hypotheses in literature rely on knowledge based on NO hydrogenation on Pd at relatively high temperature and ultra-high-vacuum conditions [13,19,48,52,53]. Clearly, these conditions are very different compared to operation in aqueous solution and the mechanism in operation might be quite different.

The first study on intrinsic kinetics of nitrite hydrogenation by Pintar et al. [11] reported an overall rate expression based on a Langmuir-Hinshelwood mechanism. Table 1 shows an overview of the results in later studies on the kinetics of nitrite hydrogenation. The concentration range used in these studies is relatively narrow; for nitrite between 0.1 and 1 mM and hydrogen pressure between 0.1 and 1 bar [11,12,48,54–56]. The apparent reaction order in hydrogen and nitrite varies in the range between 0 and 0.5 and 0 and 1, respectively.

We observed an apparent negative reaction order in hydrogen in previous work by Postma et al. [57] and Espinosa et al. [54] using membrane reactors, which was rationalized based on extreme low concentration ratio of the nitrite/hydrogen achieved in the membrane reactor. These results were qualitative though because of the complex concentration gradients in these studies. To confirm this quantitatively, intrinsic kinetic experiments in a broad window of nitrite and hydrogen concentrations are required.

Table 1. Kinetics of nitrite hydrogenation at room temperature reported in literature; papers labelled a report qualitative apparent data.

Catalyst	pH	reactor	Hydrogen pressure (bar)	Nitrite concentration (mM)	H_2 order	NO_2^- order
Pd/Al_2O_3 [11]	4.7	Slurry	0.11 - 1	0.11 – 0.65	0 – 0.5	0 - 1
Pd/ACC [55]	4.5 - 8	Slurry	1.8 – 6.4	1.63	0	1
Pd_Cu/AC [48]	5.4	Tubular	0.1 - 1	0.65 – 1.08	0.3	1
Pd/AC [56]	4.5 - 9	Fixed bed	0.3 – 0.7	0.27 – 0.45	0.4	0.7
Pd/Al_2O_3 [12]a	7	Membrane	0.01 - 1	0.24 – 2.4	0	N/A
Pd/CNF [54]a	7	Membrane	0.2 - 1	0.044 – 0.22	< 0	N/A

The goal of this work is to determine intrinsic kinetics in an extremely wide window of concentrations, in order to test the hypothesis that reaction orders can become negative. The kinetic data are obtained in an isothermal semi-batch slurry reactor. The consequence of this rigorous kinetic data for hypotheses on the reaction mechanism will be discussed as well.

2. Experimental section

2.1. Materials

Commercial γ-Al_2O_3 powder used as catalyst support in this study was obtained from BASF. Palladium precursor tetra-ammine-palladium (II) nitrate solution (10 wt% in H_2O, 99.99 %), sodium nitrite (99.99 %) and ammonium (50 % v/v water) were purchased from Sigma-Aldrich. All the aqueous solutions were prepared using ultra purified water obtained from a water purification system (Millipore, Synergy).

2.2. Catalyst preparation

The 1 wt% Pd/γ-Al_2O_3 catalyst was prepared by wet impregnation method. Typically 10 g of the sieved alumina support (particle smaller than 20 μm) was calcined at 600 °C for 4 hours to remove any organic contaminants. Then the calcined support was suspended in 100 mL millQ water. The pH of the solution was adjusted by adding 2 mL ammonia solution to maintain the pH around 9, in order to ensure electrostatic interaction of $Pd(NH_3)_4^{2+}$ with the negatively charged alumina surface. Subsequently, 3 g of the palladium precursor solution (10 wt%) was slowly added in the suspended solution. The final solution was stirred at room temperature for at least 1 h and then transferred to a rotary evaporator to remove water. Finally the catalyst was calcined in air (flow rate 30 mL/min) at 400 °C for 3 h (heating rate 5 °C /min), and subsequently reduced in 50 % H_2 diluted in N_2 (total flow rate 60 mL/min) at the same temperature for 3 h.

2.3. Catalyst characterization

The BET surface area of the prepared catalyst was determined with N_2 physisorption at 77 K (Micromeritics Tristar). For BET analysis, all the samples were degassed in vacuum at 300 °C for 24 h. Pd loading on the alumina support was determined with X-ray fluorescence spectroscopy (XRF, Philips PW 1480). Pd particle size was determined using TEM (FEI Tecnai F30), measuring at least 300 particles at ten different spots in the sample. CO chemisorption at room temperature was used to determine the accessible metal surface area in gas phase (Chemisorb 2750, Micromeritics). Typically, the sample was reduced at room temperature in hydrogen for 1 h and then flushed with He at the same temperature for 0.5 h. Then CO was introduced as pulses and the responses were recorded using a TCD detector. We assumed that the stoichiometric ratio of number of adsorbed CO molecules and number of accessible Pd surface atoms is one.

2.4. Catalytic tests

Activity and selectivity of the catalysts were measured in a 1 L batch reactor at 20 °C, atmospheric pressure and a pH value of 5.5 maintained by buffering continuously with CO_2 (0.1 bar). The glass reactor (DURAN® BAFFLED, WIDE MOUTH BOTTLE GLS 80®) with diameter of 10.1 cm and height 22.2 cm is used for the catalytic testing (Figure A1). The reactor has four connections on the reactor lid for gas-in, gas-out, sampling and stirring shaft equipped with 4 stirring blades.

Typically for a standard experiment, 0.05 g catalyst was suspended in 0.3 L millQ water and stirred at 625 rpm under 0.8 bar hydrogen (0.1 bar CO_2, 0.1 bar He) for at least 1 h, removing dissolved oxygen and reducing the catalyst. After that, the hydrogen pressure is changed to the value of choice. Reaction is started on introduction of 3 mL $NaNO_2$ solution (100 mmol/L) in the glass reactor. Hydrogen pressure was varied between 0.01 and 0.8 bar, and the nitrite concentration was varied between 0.3 and 10 mmol/L. Experiments with higher catalyst load were performed under the same reaction conditions to check the absence of mass transfer limitations.

During the catalytic test, samples were collected using a 2.5 mL syringe (BD Plastipak) and filtered using a syringe filter (PTFE, 0.2 μm, Whatman) to remove catalyst particles. Nitrite and ammonium concentrations were measured using ion-chromatography (DIONEX, ICS 3000) equipped with an UltiMate autosampler. Nitrite conversion and ammonium selectivity were calculated according to equation 3 and equation 4, respectively. Since it is well known that ammonia and nitrogen are the only products formed during hydrogenation of nitrite reaction [47–50,54] , nitrogen was calculated based on the mass balance.

$$NO_2^- \ conversion_{t1} = \frac{[NO_2^-]_{t0} - [NO_2^-]_{t1}}{[NO_2^-]_{t0}} * 100 \qquad eq3$$

$$NH_4^+ \ selectivity_{t1} = \frac{[NH_4^+]_{t1}}{[NO_2^-]_{t0} - [NO_2^-]_{t1}} * 100 \qquad eq4$$

Where $[NO_2^-]_{t0}$ is the initial nitrite concentration, $[NO_2^-]_{t1}$ is the concentration of nitrite at t1, $[NH_4^+]_{t1}$ is the concentration of ammonium at t1.

The initial activity is reported as a TOF in mole nitrite per mole surface Pd per minute.

3. Results

3.1. Characterization of the catalyst

Table 2 summarizes the characterization results of the prepared catalysts, showing that the metal loading is close to the targeted 1 wt%. The BET surface area of the support and Pd/γ-Al_2O_3 catalyst are equal, indicating the structure and porosity of the support remain unchanged after metal loading. The Pd dispersion is 58 % according CO chemisorption, equivalent to an averaged particle size of 2 nm, assuming Pd is hemisphere shape and the size of uniform. This is in good agreement with estimated Pd particle size based on TEM. Typical HRTEM images of the catalyst are shown in the supplementary information (Figure A2). The particle size distribution of the Pd particles is shown in Figure A3, showing that, although the majority of the particles is sized 2 nm, also some larger Pd particles are present.

Table 2. Characterization results of the Pd/γ-Al_2O_3 catalyst.

Catalyst particle size, μm	< 20
BET surface area, m^2/g	195
XRF metal loading, wt%	0.9
Pd dispersion, CO-chemisorption, %	58
Pd particle size, CO-chemisorption, nm	2
Mean Pd particle size based on TEM, nm	2.2

3.2. Nitrite hydrogenation reaction

Figure 1 shows a typical experimental result, showing the change in concentration of nitrite and ammonium with time during nitrite hydrogenation. The initial rate is calculated from the slope in the nitrite concentration profile, considering exclusively data at conversion lower than 10%, as shown in the inset of Figure 1a. Figure 1b shows that the ammonium concentration increases gradually with time, which is usually assigned to the decreasing nitrite/hydrogen ratio [3,51,56,58]. Similar experiments were performed in a wide window of reactant concentrations as presented in Table 3, including variation of the nitrite concentration between 0.3 and 10 mmol/L and H_2 pressure between 0.01 and 0.8 bar. Consequently, the H_2 concentration in water varied between 0.01 and 0.6 mmol/L, calculated based on the Henry coefficient (1282.05 L*atm/mol at 25 °C) [59]. It should be noted that determining kinetics based on batch experiments is possible only when assuming that both deactivation as well as dynamic changes in the catalyst structure during the experiment do not influence the performance. The catalyst is stable in continuous steady-state experiments for days (not shown) and any deactivation would not influence the results anyhow because we asses exclusively initial activity. This assumption that any dynamic changes during the initial stage of the batch experiment do not influence the results, cannot be tested with steady state experiments and is usually implicitly made in kinetic studies with batch experiments, which is generally accepted.

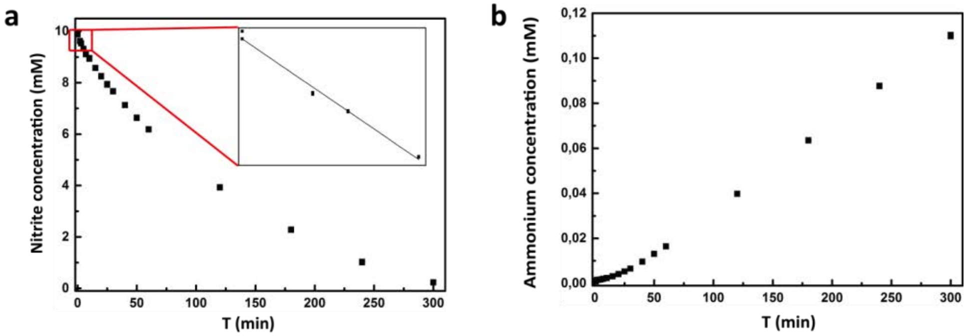

Figure 1. a) Nitrite concentration as a function of time obtained using slurry reactor with 10 mM initial nitrite concentration and 0.8 bar hydrogen pressure, with a zoomed-in initial points that are used to obtain initial rate, b) ammonium concentration as a function of time.

Table 3. Range of operating conditions of the nitrite hydrogenation in a slurry reactor.

Reaction temperature, ^oC	20
Reaction volume, L	0.3
pH of the solution	5.5
Stirring speed, rpm	625
Catalyst particles size, μm	< 20
Amount of catalyst, g	0.05
Total gas flow rate, mL/min	100
Total operating pressure, bar	1
Carbon dioxide partial pressure, bar	0.1
Hydrogen partial pressure, bar	0.01 - 0.8
Helium partial pressure (balance), bar	0.1 – 0.89
Initial nitrite concentration, mmol/L	0.3 - 10

3.3. The effect of the hydrogen pressure and initial nitrite concentration

Figure 2a shows that the initial activity varies with hydrogen pressure in a similar manner for both 1 mM and 10 mM nitrite concentrations, except that higher rates are observed with low nitrite concentration (1 mM) in combination with low hydrogen pressure. The selectivity to ammonium increases with decreasing nitrite/hydrogen ratio, in agreement with literature [3,51]. However, Figure 2b shows that the initial selectivity to ammonium remains constant with increasing hydrogen pressure for both 1 and 10 mM nitrite concentrations.

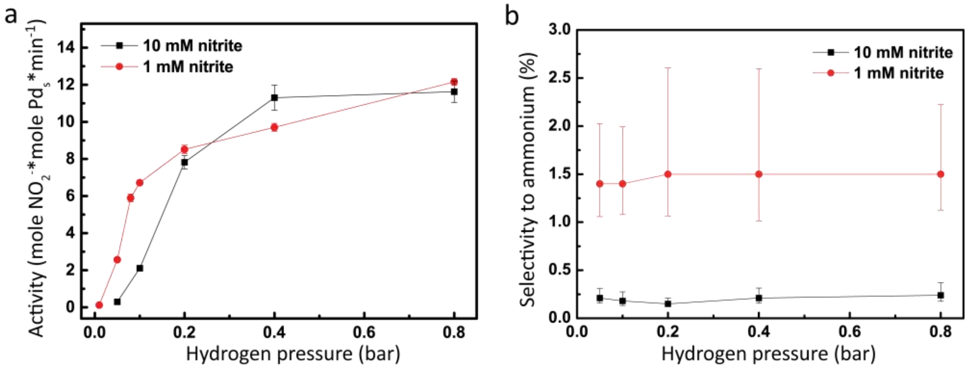

Figure 2. a) Initial activity and b) initial selectivity to ammonium as a function of hydrogen pressure for 10 (red curve) and 1 mM (black) nitrite concentration.

Figure 3a presents the effect of the initial nitrite concentration on the catalytic activity. Surprisingly, this effect is strongly influenced by the hydrogen pressure. At 0.8 bar hydrogen pressure, the activity first increases with nitrite concentration and then stabilizes. In contrast, at 0.05 bar hydrogen pressure, the activity decreases significantly with increasing nitrite concentration. Figure 3b presents the trend in the selectivity to ammonium varying the nitrite concentration, resulting in very similar trends at different hydrogen pressures. Selectivity to ammonium decreases with increasing nitrite concentration. Clearly, the selectivity to ammonium is much more strongly affected by the nitrite concentration (Figure 3b) than by hydrogen pressure (Figure 2b). Experimental data on ammonia selectivity have a significant error margin, especially in the case of low nitrite concentration. This is caused by the fact that the ammonia concentration in the initial part of the experiment are so low that ammonia analysis is possible only with significant experimental scatter.

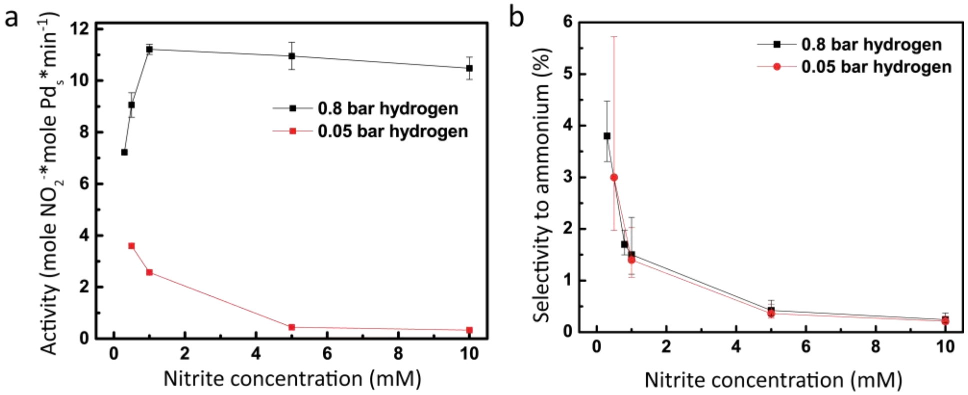

Figure 3. a) Initial activity and b) initial selectivity to ammonium as a function of initial nitrite concentration for 0.8 bar and 0.05 bar hydrogen pressure.

3.4. Mass transfer

In order to study intrinsic kinetics of nitrite hydrogenation, absence of any mass transfer limitation must be ensured. We performed several experiments to rule out both internal and external mass transfer limitations.

3.4.1. Internal mass transfer

The catalyst particle size has no effect on the initial rate when the particles are 45 µm or smaller, as shown in Table A1 in supplementary information (section 3.1), whereas larger catalyst particles clearly show evidence that internal mass transfer is limiting because the activity decreases with increasing particle size. Therefore, the data presented are not influenced by internal mass transport limitations, as all experiments were performed with catalyst with particles smaller than 20 µm. This is in good agreement with values of the Weisz-Prater criterion (C_{wp}) smaller than 1 (Table A2), for all nitrite and hydrogen concentrations applied. The calculation are presented in the Appendix, section 3.1.

3.4.2. External mass transfer

Increasing the amount of catalyst does not influence the activity per gram catalyst (Table A3, section 3.2), demonstrating experimentally that transport at the gas-liquid interface (G-L) is not limiting. In addition, the rate-constant for transport at the external surface of the catalyst (L-S) ($k_{ls} * a_s$) is estimated to be 3.3 $*10^{-3}$ s^{-1}, one order of magnitude larger than the maximum observed rate constant (k_{obs} $=1.92*10^{-4}$ s^{-1}, see Appendix for details in section 3.2). Also Mears criterion shows that external transport is not limiting. In short, we can exclude mass transfer limitation in and around the catalyst particles.

4. Discussion

The activity as well as the trends with concentrations of the reactants vary significantly in the broad window of hydrogen and nitrite concentrations, as can be seen in Figures 2a and 3a. The first part of the discussion will provide the resulting reaction orders. The influence of concentration on reaction orders will then be discussed qualitatively in terms of a Langmuir-Hinshelwood mechanism, as full modelling of the relatively complex micro-kinetic scheme is impossible with the information available. The reaction rate is strongly dominated by the rate of formation of N_2 as the selectivity to ammonia is typically a few percent. After discussion of reaction rates, the reaction schemes will be elaborated based on the selectivity data.

4.1. Apparent reaction orders

Figure 4 shows the reaction orders in nitrite and hydrogen as obtained from log-log plots of activity and reactant concentrations. The slopes in the plot indicate the reaction order in hydrogen (Figure 4a) and nitrite (Figure 4b). As shown in Figure 4a, the order in hydrogen is about 2 at low hydrogen pressure and almost independent of the nitrite concentration. Increasing the hydrogen pressure causes the order in hydrogen to decrease significantly to around 0.3 and 0.4 for nitrite concentration of 1 mM and 10 mM, respectively.

As can be seen in Figure 4b (black line), the order in nitrite is always negative at 0.05 bar hydrogen pressure, independent of the nitrite concentration. In contrast, at high hydrogen pressure (0.8 bar) the order in nitrite varies between 0.5 at low nitrite concentration (below 1 mM) and 0 at higher nitrite concentration (above 1 mM).

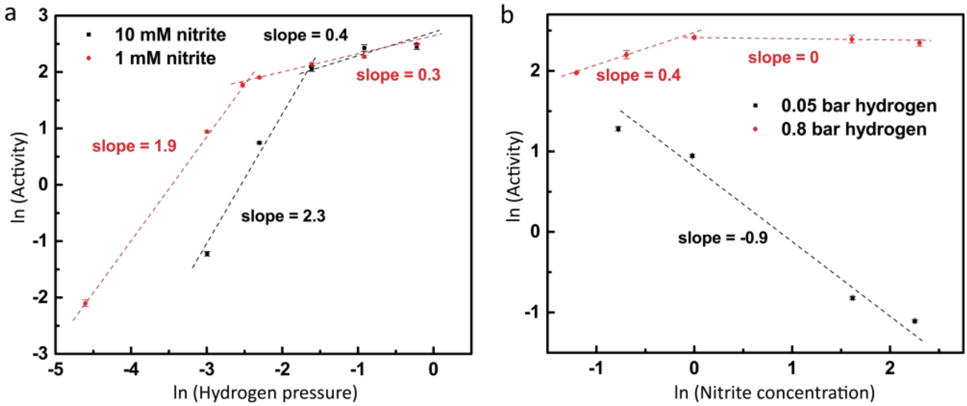

Figure 4. a) Effect of hydrogen pressure on reaction rate for 1 and 10 mM nitrite concentration, b) effect of nitrite concentration on reaction rate for 0.05 and 0.8 bar hydrogen pressure.

Table 4 summarizes the observed apparent reaction orders in nitrite and hydrogen. The results obtained at high hydrogen pressure and low nitrite concentration (0.3 order in H_2 and 0.4 in nitrite) are in good agreement with literature (Table 1). The high reaction order of 2 in hydrogen as well as the negative order in nitrite at low hydrogen pressures (0.05 bar) have never reported before to the best of our knowledge, which can be understood based on the fact that the window of concentrations in this study is much broader than in previous studies.

Table 4. Overview of the apparent reaction orders in nitrite and hydrogen information in all ranges of the nitrite and hydrogen concentrations.

	Low hydrogen pressure		High hydrogen pressure	
	H_2 order	Nitrite order	H_2 order	Nitrite order
Low nitrite concentration	1.9 ± 0.1	- 0.9 ± 0.1	0.3 ± 0.1	0.4 ± 0.1
High nitrite concentration	2.3 ± 0.1	- 0.9 ± 0.1	0.4 ± 0.15	0 ± 0.05

However, recent work from our group with membrane contact reactors [54,57] provided qualitative proof for negative reaction order in hydrogen, which was tentatively explained with zones in the contact membrane operating at extreme low nitrite concentration. Negative orders in hydrogen are not observed in this work (Table 4), which seems reasonable when considering that the nitrite concentration in the experiments with the membrane contact reactor could be decreased to much lower values (0.044 mM) compared to batch experiments (0.3 mM) without compromising accuracy of the experiment. The concentrations gradients in the membrane contactor discussed above induce even lower concentrations.

Summarizing, negative reaction orders in nitrite and hydrogen are observed, here and in previous work, only when the windows of concentrations are sufficiently broad, pointing to competitive adsorption in a Langmuir-Hinshelwood mechanism. We will discuss the mechanism further below.

4.2. Reaction mechanism

Several reaction mechanisms have been proposed for the reduction of nitrite in aqueous solutions using Pd based catalysts [50,51,60–64]. There is general consensus about three elementary steps, i.e. nitrite adsorption, dissociative adsorption of hydrogen and conversion of nitrite to adsorbed NO_{ads}. Furthermore, dissociation of NO_{ads} to N_{ads} is often assumed [47,48,65,66] , implying that NO_{ads} and N_{ads} are key intermediate species that are further converted to N_2 and NH_4^+, via pathways that are under debate.

To date three reaction pathways have been proposed for the conversion of adsorbed NO_{ads}.

I. NO_{ads} reduction to NH_{ads} species [19,47,67]
II. NO_{ads} reduction to NOH_{ads} species [62]
III. NO_{ads} coupling without H_{ads}, e.g. NO_{ads} dimerization (as also proposed in electrochemical studies [68–71]) or coupling of N_{ads} and NO_{ads} to N_2O_{ads} [48,49,65,66];

We will now discuss the fit of these models to the experimental observations, assuming in all three cases:

1) Fast and equilibrated adsorption of H_2 and NO_2^-;

2) Langmuir-Hinshelwood mechanism with one type of active site, implying competitive adsorption. This is obviously necessary to account for negative reaction orders. The fact that the orders change strongly in still a relatively narrow window of conditions is probably caused by competition of multiple species at the Pd surface;

3) All reactions after the rate determining step (RDS) are fast and the equilibrium is at the side of desorbed products, resulting in low surface coverages of the species involved on Pd.

Please note that we do not discuss separate pathways to N_2 and NH_4^+ at this stage because the reaction rate is almost exclusively determined by the formation of N_2, as explained above. The interpretation is qualitative because full micro-kinetic modelling for this complex reaction with the data available is simply not possible. Therefore, models I, II and III will be simplified to schemes with the same type of intermediates but limited to the proposed RDS and the accompanying pre-equilibria. The fact that the reaction order in hydrogen is 2 at low hydrogen pressure (Table 1) implies that H_{ads} is not only involved in the RDS, but must also be involved in three pre-equilibria elementary steps, determining the concentration of H_{ads} in the RDS. According to this principle, possible RDSs are selected.

4.2.1. Model I: NO_{ads} reduction to NH_{ads}

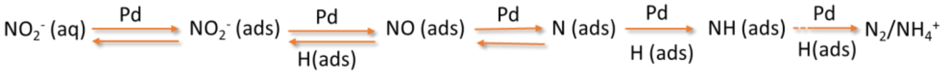

Scheme 1. NO_{ads} reduction to NH_{ads} species pathway.

This scheme, proposed by Wärn et al. [47] , suggests that NO_{ads} dissociates first to atomic N_{ads} before the N-H bond is formed. The proposition was rejected in several studies [48,49,65,66] based on the fact that NH_{ads} species has never been detected. Unfortunately, these arguments are based on NO_{ads} conversion on Pd at relatively high temperature and ultra-vacuum conditions. So we cannot exclude this scheme for reaction in aqueous phase.

The overall rate equation is derived based on the elementary steps as shown below. The reaction 6 is selected as the RDS according to the argument described above: four adsorbed hydrogen atoms need to be involved, respectively in three pre-equilibria and in the RDS. All steps after the RDS are not relevant because of assumption 3.

$H_2 + 2* \leftrightharpoons 2H^*$ (equilibrium reaction 1, K_1)

$NO_2^- + * \leftrightharpoons NO_2^{-*}$ (equilibrium reaction 2, K_2)

$NO_2^{-*} + H^* + H^+ \leftrightharpoons NO^* + H_2O + *$ (equilibrium reaction 3, K_3)

$NO^* + * \leftrightharpoons N^* + O^*$ (equilibrium reaction 4, K_4)

$O^* + 2H^* \leftrightharpoons 3* + H_2O$ (equilibrium reaction 5, K_5)

$\boldsymbol{N^* + H^* \rightarrow NH^* + *}$ **(reaction 6, $\boldsymbol{k_6}$) RDS**

Where * represents an empty site on the Pd surface and O* represents an oxygen atom adsorbed on the Pd surface, as an example for all surface species.

It should be noted that reaction 5 can also be replaced by stepwise hydrogenation of O_{ads} via OH_{ads} to H_2O, resulting in the same mathematical description as all these steps are in equilibrium. The details and derivation of the rate expression are shown in Appendix section 4.1, leading to the rate equation 5.

$$Rate = k_6\theta_H\theta_N = \frac{{K_1}^2K_2K_3K_4K_5k_6[H^+][NO_2^-][H_2]^2}{(1+{K_1}^{0.5}[H_2]^{0.5}+K_2[NO_2^-]+{K_1}^{0.5}K_2K_3[H^+][NO_2^-][H_2]^{0.5}+{K_1}^{1.5}K_2K_3K_4K_5[H^+][NO_2^-][H_2]^{1.5})^2} \quad eq5$$

In case the hydrogen pressure is low, the equation simplifies to equation 6:

$$Rate = \frac{{K_1}^2K_2K_3K_4K_5k_6[H^+][NO_2^-][H_2]^2}{(1+K_2[NO_2^-])^2} \qquad eq6$$

Clearly, the reaction order in hydrogen is 2 at low hydrogen pressure, whereas the reaction order in nitrite can vary between -1 and 1, agreeing well with the experimental results (Table 4). It should be noted that the RDS cannot be a reaction before reaction 6, as it would lead to a lower maximal order in hydrogen. Equilibrium step 4 enhances the concentration of N_{ads} via NO_{ads}, whereas equilibrium 5 prevents high coverage with O_{ads}. In case of high hydrogen pressure, the reaction orders in hydrogen can vary between -1 and 2, whereas the order in nitrite may vary between -1 and 1, which is also in agreement with experimental results (details in Appendix section 4.1). In conclusion, model I is one candidate for the reaction mechanism.

4.2.2. Model II: NO_{ads} reduction to NOH_{ads}

The second option is that NO_{ads} reacts with H_{ads} to form NOH_{ads}, without first dissociation to atomic N_{ads}. This type of mechanism was proposed based on DFT calculations by Shin et al. [62], we consider three possible pathways meeting the condition that three hydrogen atoms are involved in the pre-equilibria steps and one hydrogen atom is involved in the RDS. The essential difference in these schemes is the level of hydrogenation of the $NOH_{x,ads}$ undergoing cleavage of the N-O bond, i.e. NOH_{ads}, $HNOH_{ads}$ and H_2NOH_{ads}:

Model IIa

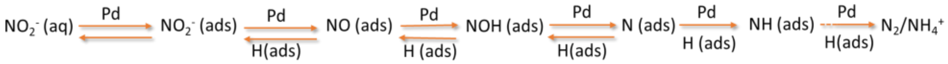

Scheme 2a. NO_{ads} reduction to NOH_{ads}, first pathway via dissociative hydrogenation of NOH_{ads} with N_{ads} hydrogenation as RDS.

Model IIb

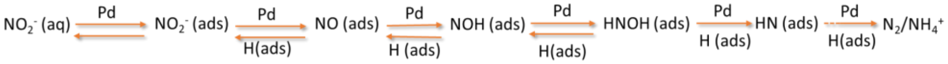

Scheme 2b. NO_{ads} reduction to NOH_{ads}, second pathway dissociative hydrogenation of $HNOH_{ads}$ as RDS.

Model IIc

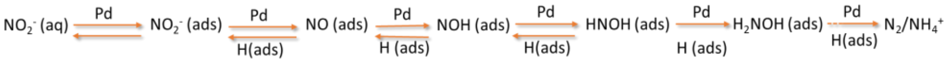

Scheme 2c. NO_{ads} reduction to NOH_{ads}, third pathway via associative hydrogenation of $HNOH_{ads}$.

Here we illustrate the evaluation of the kinetic scheme for the first pathway (Model IIa) as an example, whereas the same detailed description for Models IIb and IIc are shown in Appendix section 4.2.

For model IIa the elementary steps are:

$H_2 + * \leftrightharpoons 2H^*$ (equilibrium reaction 1, K_1)

$NO_2^- + * \leftrightharpoons NO_2^{-*}$ (equilibrium reaction 2, K_2)

$NO_2^{-*} + H^* + H^+ \leftrightharpoons NO^* + H_2O + *$ (equilibrium reaction 3, K_3)

$NO^* + H^* \leftrightharpoons NOH^* + *$ (equilibrium reaction 4, K_4)

$NOH^* + H^* \leftrightharpoons N^* + H_2O + *$ (equilibrium reaction 5, K_5)

$\boldsymbol{N^* + H^* \rightarrow NH^* + *}$ **(reaction 6, $\boldsymbol{k_6}$) *RDS***

As in the previous section, it is assumed that the formation of NH_{ads} is the RDS as otherwise second order in hydrogen cannot be obtained. The resulting kinetic equation is derived in the Appendix section 4.2:

$$Rate = k_6\theta_H\theta_N = \frac{{K_1}^2K_2K_3K_4K_5k_6[H^+][NO_2^-][H_2]^2}{(1+{K_1}^{0.5}[H_2]^{0.5}+K_2[NO_2^-]+{K_1}^{0.5}K_2K_3[H^+][NO_2^-][H_2]^{0.5}+K_1K_2K_3K_4[H^+][NO_2^-][H_2]+{K_1}^{1.5}K_2K_3K_4K_5[H^+][NO_2^-][H_2]^{1.5})^2} \quad eq7$$

At low hydrogen pressure, the equation simplifies to:

$$Rate = \frac{{K_1}^2K_2K_3K_4K_5k_6[H^+][NO_2^-][H_2]^2}{(1+K_2[NO_2^-])^2} \qquad eq8$$

This confirms that also in this case the reaction order in hydrogen is 2, whereas the reaction orders in nitrite may vary between -1 and 1, agreeing well with the experimental results at low hydrogen pressure (Table 4). The resulting reaction orders in hydrogen and in nitrite are also in good agreement with our experimental results at high hydrogen pressure (details in Appendix section 4.2).

Summarizing, Model I and the three variations on model II agree with the kinetic data and cannot be rejected based on that. The difference between these models in the pathway for NO dissociation. In model I NO_{ads} dissociates directly, whereas NO_{ads} dissociation is H-assisted via NOH_{ads}, $HNOH_{ads}$ or H_2NOH_{ads} in respectively model IIa, IIb and IIc. Therefore, the intermediate surface species available for N-N bond formation in Model I are NO_{ads} and N_{ads}. More intermediate species are involved in Model II; not only NO_{ads} and N_{ads}, but also HNO_{ads} or $HNOH_{ads}$, as all these species are involved in pre-equilibria before the RDS.

4.2.3. N-N bond formation

The mechanisms discussed so far do not consider formation of the N-N bond, implicitly assuming that NH_{ads} converts somehow to N_2, proceeding relatively fast after the RDS in the mechanistic schemes. The formation of the N-N bond is thus supposedly not the RDS. We will now show that any scheme assuming formation of the N-N bond to be rate determining, cannot comply with the observed kinetic data.

Let us first consider the following example, assuming that the N-N bond formation via NO_{ads} and N_{ads} to form N_2O_{ads}, is the RDS according the following scheme, as proposed in several studies [48,50,72]:

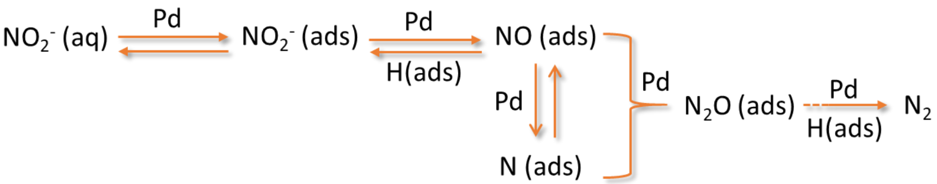

Scheme 3. NO_{ads} coupling with N_{ads} to N_2O_{ads} pathway.

The elementary steps for this case are:

$H_2 + 2* \leftrightharpoons 2H^*$ (equilibrium reaction 1, K_1)

$NO_2^- + * \leftrightharpoons NO_2^{-*}$ (equilibrium reaction 2, K_2)

$NO_2^{-*} + H^* + H^+ \leftrightharpoons NO^* + H_2O + *$ (equilibrium reaction 3, K_3)

$NO^* + * \leftrightharpoons N^* + O^*$ (equilibrium reaction 4, K_4)

$O^* + 2H^* \leftrightharpoons 3* + H_2O$ (equilibrium reaction 5, K_5)

$\boldsymbol{N^* + NO^* \rightarrow N_2O^* + *}$ **(reaction 6, $\boldsymbol{K_6}$) *RDS***

It should be noted that reaction 5 can again be replaced by stepwise hydrogenation of O_{ads} via OH_{ads} to H_2O, like in section 4.2.1.

Following rate equation is derived based on this mechanism.

$$Rate = k_6\theta_{NO}\theta_N = \frac{{K_1}^2K_2K_3K_4K_5k_6[NO_2^-]^2[H_2]^2[H^+]^2}{(1+{K_1}^{0.5}[H_2]^{0.5}+K_2[NO_2^-]+{K_1}^{0.5}K_2K_3[H^+][NO_2^-][H_2]^{0.5}+{K_1}^{1.5}K_2K_3K_4K_5[H^+][NO_2^-][H_2]^{1.5})^2} \quad eq9$$

When hydrogen pressure is low, the equation simplifies to:

$$Rate = k_6\theta_{NO}\theta_N = \frac{{K_1}^2K_2K_3K_4K_5k_6[NO_2^-]^2[H_2]^2[H^+]^2}{(1+K_2[NO_2^-])^2} \quad eq10$$

Thus, the reaction order in hydrogen is 2, but the reaction order in nitrite cannot turn negative, conflicting with our experimental data. Alternative schemes for N-N bond formation by coupling of combinations N_{ads}, NO_{ads}, NOH_{ads}, $NO_2{}^{-}{}_{,ads}$ and NH_{ads} as RDS are evaluated in the Appendix section 4.3. Some of these scenarios agree with the observed orders in hydrogen, but none of them can account for the observed negative reaction order in nitrite. Therefore, all options assuming the formation of the N-N bond as RDS are rejected, including the NO_{ads} dimerization pathway which is generally accepted for electrochemical reduction of nitrite [68–71]. Nevertheless, at least one of these pathways must be in operation to explain formation of N_2, but the N-N bond formation is apparently fast, proceeding after the RDS. Actually, two pathways need consideration, i.e. to N_2 and NH_4^+ respectively. Both pathways are slow compared to the formation on NH_{ads}, whereas the pathway to ammonia is even slower than the pathway to N_2, as the selectivity to N_2 is always high.

4.3. Selectivity to N_2 and NH_4^+

Previous work in our group by Zhao et al. [51] showed that at the very end of a nitrite hydrogenation batch experiment, the Pd surface is significantly covered with N atoms. Continued exposure to hydrogen causes formation of ammonia at an extremely low rate and this reaction is therefore clearly not kinetically relevant. Apparently, hydrogenation of N_{ads} is too slow to contribute to the formation of ammonia. Therefore, we reject model I as well as model IIa. This conclusion disagrees with most of the propositions in literature [19,48,50,62,67,72] although it should be considered that formation of N_2 via associative desorption of absorbed N-atoms is proposed as a logical option without real experimental evidence. Also Obuchi et al. [13] and Tanaka et al. [73] suggested N_2 forms via dimerization of N_{ads}; however, these studies were performed in the gas phase instead of in water. The result discussed above [51], i.e. very slow formation of ammonia during exposure of a N covered Pd surface, also implies that associative adsorption of adsorbed N is apparently even slower and therefore not relevant.

Thus, the models IIb and IIc are the remaining options. The essential difference between IIb and IIc is that in IIb HNOH hydrogenates and dissociates immediately according:

$$HNOH^* + H^* \rightarrow NH^* + H_2O + * \quad (reaction\ 1)$$

Whereas in IIc the dissociation is not immediate:

$$HNOH^* + H^* \rightarrow H_2NOH^* + * \, (reaction\ \ 2)$$

However, considering assumption 3 in section 4.2, all reactions after the RDS are fast and in model IIc this implies fast conversion according e.g.:

$$H_2NOH^* + H^* \rightarrow NH_2^* + H_2O + * \, (reaction\ 3)$$

ATR-IR experiments in aqueous phase by Ebbesen et al. [49] showed that $NH_{2,ads}$ converts to ammonium when exposed to H_2. In contrast, NO_{ads} on the same Pd surface reacts significantly faster with H_2, forming N_2. Therefore, model IIc can be ruled out because $NH_{2,\ ads}$ cannot be an intermediate in the formation of N_2. Thus model IIb is the only option left, in which N_2 forms via NH_{ads} as an intermediate, in agreement with the results of Wärna et al. [47] and Pintar et al. [27] based on kinetic studies.

Six different N-containing species, i.e. NH_{ads}, N_{ads}, NO_{ads}, $NO_2{}^-{}_{ads}$, NOH_{ads} and $HNOH_{ads}$ could be involved in the pathway to N_2 by reacting with NH_{ads}, according to model IIb. All possible reactions are listed below. The reactions suggested below are completely associative, i.e. only one species is formed in addition to an open site. This is not certain though and also not important for the argument. The essence is that a product forms with an N-N bond as part of the pathway to form molecular N_2.

$NH^* + NH^* \rightarrow N_2H_2{}^* + *\ \ (reaction\ 1)$

$NH^* + N^* \rightarrow N_2H^* + *\ \ (reaction\ 2)$

$NH^* + NO^* \rightarrow N_2OH^* + *\ \ (reaction\ 3)$

$NH^* + NO_2^{-*} \rightarrow N_2O_2H^{-*} + *\ \ (reaction\ 4)$

$NH^* + NOH^* \rightarrow N_2OH_2{}^* + *\ \ (reaction\ 5)$

$NH^* + HNOH^* \rightarrow HN_2OH_2{}^* + *\ \ (reaction\ 6)$

The result Zhao et al. [51], as discussed above, showed that N_{ads} converts extremely slowly into ammonium exclusively. As this pathway necessarily goes via NH_{ads}, both reactions 1 and 2 can be ruled out as part of the pathway to N_2. The ATR-IR study of Ebbesen et al. [49] showed formation of NO_{ads} and $NH_{2,ads}$ as a result of titrating adsorbed hydrogen on Pd with nitrite, causing exhaustion of hydrogen; however, no $NO_2{}^-{}_{ads}$ was observed, excluding reaction 4. So in conclusion, the remaining reactions 3, 5 and 6 are the possible pathways to form N_2.

Scheme 4 presents a revised mechanism for nitrite hydrogenation over Pd catalysts. The dotted lines to N_2 indicated that NH_{ads} reacts with NO_{ads}, NOH_{ads} or $HNOH_{ads}$, whereas the equilibrium between these three species is clearly on the side of NO_{ads} when hydrogen is exhausted, as NO_{ads} is detected with ATR-IR under such conditions. The reaction of NH_{ads} with NO_{ads}, NOH_{ads} or $HNOH_{ads}$ is fast compared to the overall RDS, but also fast compared to reaction of $NH_{2,ads}$ to NH_3. This explains why $NH_{2,ads}$ hydrogenation proceeds only after exhaustion of NO_{ads} in the ATR-IR titration experiment [49] and that the selectivity to N_2 is very high is steady-state operation. The route via N_{ads} is basically a dead-end as the reaction of N_{ads} to NH_{ads} extremely slow, whereas N_{ads} dimerization is apparently even slower.

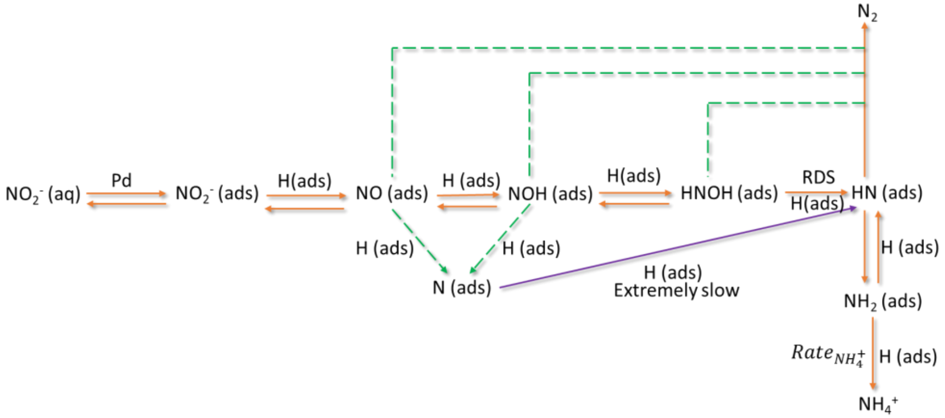

Scheme 4. Proposed mechanism of nitrite hydrogenation over Pd catalyst, dashed line indicate three possible reaction steps contributing to formation of N_2, as well as two possible steps to N_{ads}.

5. Conclusions

Intrinsic kinetic data in an extreme wide concentration window of nitrite and hydrogen reveals extreme variation in the orders in hydrogen and nitrite, varying between 2 and 0.3 for hydrogen and between 0.4 and -0.9 for nitrite. This clearly indicates that a Langmuir-Hinshelwood mechanism with competitive adsorption is in operation. The rate of conversion is determined by the rate of formation of N_2 as the selectivity to ammonia is always very low. Several mechanistic pathways as well as possible rate determining steps in those pathways are discussed based on these observations in combination with prior knowledge on the mechanism in literature, resulting in a revised mechanistic scheme. It is concluded that formation of NH_{ads} via dissociative hydrogenation of $HNOH_{ads}$ is the rate determining step, whereas molecular N_2 forms via reaction of NH_{ads} with either NO_{ads}, NOH_{ads} or $HNOH_{ads}$. N-N bond formation via dimerization of adsorbed NO or adsorbed N can be excluded. Formation of NH_4^+ proceeds via hydrogenation of NH_{ads}, which is significantly slower than reaction of NH_{ads} with NO_{ads}, NOH_{ads} or $HNOH_{ads}$. Atomic N on Pd is a spectator with extreme low reactivity.

Reference

[1] G. Gulis, M. Czompolyova, J. R. Cerhan, *Environ. Res.* **2002**, *88*, 182–187.

[2] C. S. Bruning-Fann, J. B. Kaneene, *Vet. Hum. Toxicol.* **1993**, *35*, 521–538.

[3] S. Hörold, K.-D. Vorlop, T. Tacke, M. Sell, *Catal. Today* **1993**, *17*, 21–30.

[4] V. Matějů, S. Čižinská, J. Krejčí, T. Janoch, *Enzyme Microb. Technol.* **1992**, *14*, 170–183.

[5] J. Schullehner, B. Hansen, M. Thygesen, C. B. Pedersen, T. Sigsgaard, *Int. J. Cancer* **2018**, *143*, 73–79.

[6] W. H. Organization, “Guidelines for Drinking-water Quality FOURTH EDITION,” **n.d.**

[7] J. J. F. Scholten, in *Stud. Surf. Sci. Catal.*, **1979**, pp. 685–714.

[8] A. Bothner-By, L. Friedman, *J. Chem. Phys.* **1952**, *20*, 459–462.

[9] M. Boudart, *Chem. Rev.* **1995**, *95*, 661–666.

[10] K. T. Ranjit, B. Viswanathan, *J. Photochem. Photobiol. A Chem.* **1997**, *108*, 73–78.

[11] A. Pintar, G. Berčič, J. Levec, *AIChE J.* **1998**, *44*, 2280–2292.

[12] H. C. Aran, J. K. Chinthaginjala, R. Groote, T. Roelofs, L. Lefferts, M. Wessling, R. G. H. H. Lammertink, *Chem. Eng. J.* **2011**, *169*, 239–246.

[13] A. Obuchi, S. Naito, T. Onishi, K. Tamaru, *Surf. Sci.* **1982**, *122*, 235–255.

[14] V. Höller, I. Yuranov, L. Kiwi-Minsker, A. Renken, *Catal. Today* **2001**, *69*, 175–181.

[15] S. D. Ebbesen, B. L. Mojet, L. Lefferts, *Langmuir* **2008**, *24*, 869–879.

[16] A. J. Lecloux, *Catal. Today* **1999**, *53*, 23–34.

[17] M. Hu, Y. Liu, Z. Yao, L. Ma, X. Wang, *Front. Environ. Sci. Eng.* **2018**, *12*, 1–18.

[18] G. Strukul, R. Gavagnin, F. Pinna, E. Modaferri, S. Perathoner, G. Centi, M. Marella, M. Tomaselli, *Catal. Today* **2000**, *55*, 139–149.

[19] O. M. Ilinitch, L. V. Nosova, V. V. Gorodetskii, V. P. Ivanov, S. N. Trukhan, E. N. Gribov, S. V. Bogdanov, F. P. Cuperus, *J. Mol. Catal. A Chem.* **2000**, *158*, 237–249.

[20] F. Ruiz-Beviá, M. J. Fernández-Torres, *J. Clean. Prod.* **2019**, *217*, 398–408.

[21] G. Mendow, N. S. Veizaga, C. A. Querini, B. S. Sánchez, *J. Environ. Chem. Eng.* **2019**, *7*, 102808.

[22] K. N. Heck, S. Garcia-Segura, P. Westerhoff, M. S. Wong, *Acc. Chem. Res.* **2019**, *52*, 906–915.

[23] Y. Sakamoto, K. Nakamura, R. Kushibiki, Y. Kamiya, T. Okuhara, *Chem. Lett.* **2005**, *34*, 1510–1511.

[24] D. Gašparovičová, M. Králik, M. Hronec, Z. Vallušová, H. Vinek, B. Corain, *J. Mol. Catal. A Chem.* **2007**, *264*, 93–102.

[25] U. Prüsse, M. Hähnlein, J. Daum, K. D. Vorlop, *Catal. Today* **2000**, *55*, 79–90.

[26] A. Kapoor, T. Viraraghavan, *J. Environ. Eng.* **1997**, *123*, 371–380.

[27] A. Pintar, J. Batista, J. Levec, T. Kajiuchi, *Appl. Catal. B Environ.* **1996**, *11*, 81–98.

[28] J. Sá, J. Montero, E. Duncan, J. A. Anderson, *Appl. Catal. B Environ.* **2007**, *73*, 98–105.

[29] H. O. N. Tugaoen, S. Garcia-Segura, K. Hristovski, P. Westerhoff, *Sci. Total Environ.* **2017**, *599–600*, 1524–1551.

[30] S. Tyagi, D. Rawtani, N. Khatri, M. Tharmavaram, *J. Water Process Eng.* **2018**, *21*, 84–95.

[31] F. Deganello, L. F. Liotta, A. Macaluso, A. M. Venezia, G. Deganello, *Appl. Catal. B Environ.* **2000**, *24*, 265–273.

[32] M. D'Arino, F. Pinna, G. Strukul, *Appl. Catal. B Environ.* **2004**, *53*, 161–168.

[33] A. Miyazaki, T. Asakawa, Y. Nakano, I. Balint, *Chem. Commun.* **2005**, 3730–3732.

[34] F. Liang, J. Fan, Y. Guo, M. Fan, J. Wang, H. Yang, *Ind. Eng. Chem. Res.* **2008**, *47*, 8550–8554.

[35] K. Wada, T. Hirata, S. Hosokawa, S. Iwamoto, M. Inoue, *Catal. Today* **2012**, *185*, 81–87.

[36] H. Qian, Z. Zhao, J. C. Velazquez, L. A. Pretzer, K. N. Heck, M. S. Wong, *Nanoscale* **2014**, *6*, 358–364.

[37] J. Lee, Y. G. Hur, M.-S. Kim, K.-Y. Lee, *J. Mol. Catal. A Chem.* **2015**, *399*, 48–52.

[38] R. Brunet Espinosa, L. Lefferts, *ACS Catal.* **2016**, *6*, 5432–5440.

[39] Y. Matatov-Meytal, V. Barelko, I. Yuranov, M. Sheintuch, *Appl. Catal. B Environ.* **2000**, *27*, 127–135.

[40] H. Hayashi, S. Sugiyama, Y. Nomura, T. Yamazaki, *J-Stage* **2004**, 1–7.

[41] J. K. Chinthaginjala, J. H. Bitter, L. Lefferts, *Appl. Catal. A Gen.* **2010**, *383*, 24–32.

[42] J. K. Chinthaginjala, A. Villa, D. S. Su, B. L. Mojet, L. Lefferts, *Catal. Today* **2012**, *183*, 119–123.

[43] D. Shuai, J. K. Choe, J. R. Shapley, C. J. Werth, *Environ. Sci. Technol.* **2012**, *46*, 2847–2855.

[44] A. H. Pizarro, I. Torija, V. M. Monsalvo, *J. Water Supply Res. Technol.* **2018**, 615–625.

[45] Z. Zhang, W. Shi, W. Wang, Y. Xu, X. Bao, R. Zhang, B. Zhang, Y. Guo, F. Cui, *Environ. Sci. Nano* **2018**, *5*, 338–349.

[46] Y. Zhao, W. Liang, Y. Li, L. Lefferts, *Catal. Today* **2017**, *297*, 308–315.

[47] J. Wärn, I. Turunen, T. Salmi, T. Maunula, *Chem. Eng. Sci.* **1994**, *49*, 5763–5773.

[48] I. Mikami, Y. Sakamoto, Y. Yoshinaga, T. Okuhara, *Appl. Catal. B Environ.* **2003**, *44*, 79–86.

[49] S. D. Ebbesen, B. L. Mojet, L. Lefferts, *J. Catal.* **2008**, *256*, 15–23.

[50] R. Zhang, D. Shuai, K. A. Guy, J. R. Shapley, T. J. Strathmann, C. J. Werth, *ChemCatChem* **2013**, *5*, 313–321.

[51] Y. Zhao, N. Koteswara Rao, L. Lefferts, *J. Catal.* **2016**, *337*, 102–110.

[52] C. A. De Wolf, B. E. Nieuwenhuys, *Surf. Sci.* **2000**, *469*, 196–203.

[53] K. ichi Tanaka, M. Ikai, *Top. Catal.* **2002**, *20*, 25–33.

[54] R. Brunet Espinosa, D. Rafieian, R. S. Postma, R. G. H. Lammertink, L. Lefferts, *Appl. Catal. B Environ.* **2018**, *224*, 276–282.

[55] Y. Matatov-Meytal, Y. Shindler, M. Sheintuch, *Appl. Catal. B Environ.* **2003**, *45*, 127–134.

[56] J. K. Chinthaginjala, L. Lefferts, *Appl. Catal. B Environ.* **2010**, *101*, 144–149.

[57] R. S. Postma, R. Brunet Espinosa, L. Lefferts, *ChemCatChem* **2018**, *10*, 3770–3776.

[58] C. Franch, R. G. H. Lammertink, L. Lefferts, *Appl. Catal. B Environ.* **2014**, *156–157*, 166–172.

[59] Molecular Hydrogen Institute, “http://www.molecularhydrogeninstitute.com/concentration-and-solubility-of-h2,” **n.d.**

[60] V. Höller, K. Rådevik, I. Yuranov, L. Kiwi-Minsker, A. Renken, *Appl. Catal. B Environ.* **2001**, *32*, 143–150.

[61] S. D. Ebbesen, B. L. Mojet, L. Lefferts, *J. Phys. Chem. C* **2009**, *113*, 2503–2511.

[62] H. Shin, S. Jung, S. Bae, W. Lee, H. Kim, *Environ. Sci. Technol.* **2014**, *48*, 12768–12774.

[63] C. P. Theologides, G. G. Olympiou, P. G. Savva, K. Kapnisis, A. Anayiotos, C. N. Costa, KonstantinosKapnisis, A. Anayiotos, C. N. Costa, *Appl. Catal. B Environ.* **2016**, *205*, 443–454.

[64] X. Huo, D. J. Van Hoomissen, J. Liu, S. Vyas, T. J. Strathmann, *Appl. Catal. B Environ.* **2017**, *211*, 188–198.

[65] R. Zhang, D. Shuai, K. A. Guy, J. R. Shapley, T. J. Strathmann, C. J. Werth, *ChemCatChem* **2013**, *5*, 313–321.

[66] X. Fan, C. Franch, E. Palomares, A. A. Lapkin, *Chem. Eng. J.* **2011**, *175*, 458–467.

[67] H. Liu, Y. Zhang, *Adv. Mater. Res.* **2011**, *322*, 195–200.

[68] M. Duca, B. Van Der Klugt, M. A. Hasnat, M. MacHida, M. T. M. Koper, *J. Catal.* **2010**, *275*, 61–69.

[69] M. Duca, B. Van Der Klugt, M. T. M. Koper, *Electrochim. Acta* **2012**, *68*, 32–43.

[70] M. T. De Groot, M. Merkx, M. T. M. Koper, *J. Am. Chem. Soc.* **2005**, *127*, 16224–16232.

[71] M. T. De Groot, M. T. M. Koper, *J. Electroanal. Chem.* **2004**, *562*, 81–94.

[72] J. Martínez, A. Ortiz, I. Ortiz, *Appl. Catal. B Environ.* **2017**, *207*, 42–59.

[73] Ken-ichi Tanaka, Taro Yamada, B. E. Nieuwenhuys, *Surf. Sci.* **1991**, *242*, 503–507.

Appendix:

1. Setup

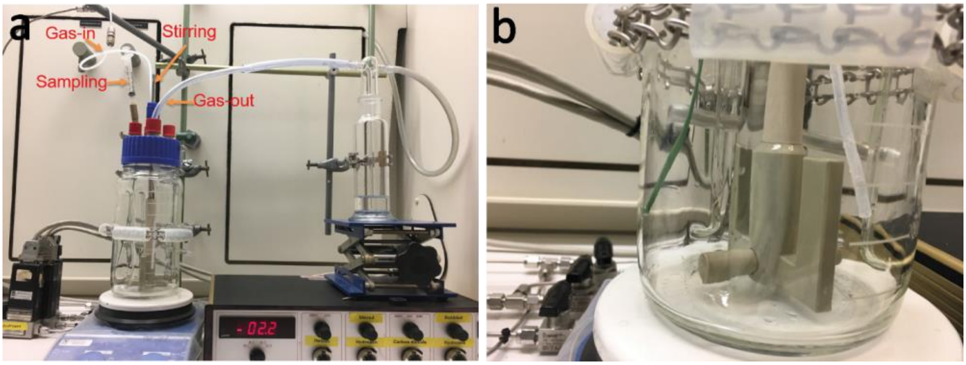

Figure A1. a) The figure of the set-up, b) the zoom-in of the stirring part.

2. Pd metal particles

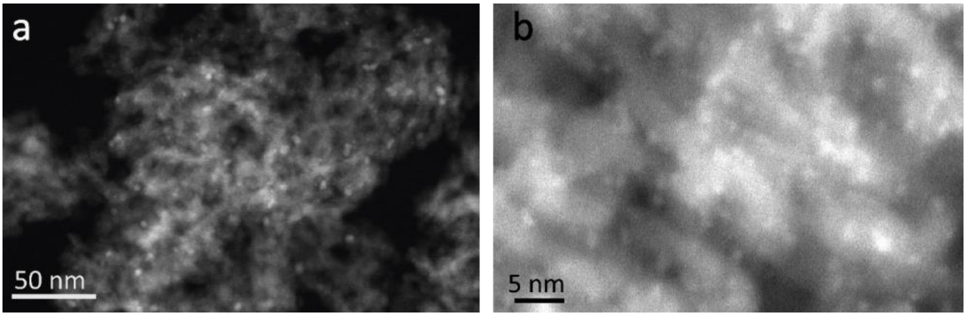

Figure A2. TEM image of the Pd/γ-Al_2O_3.

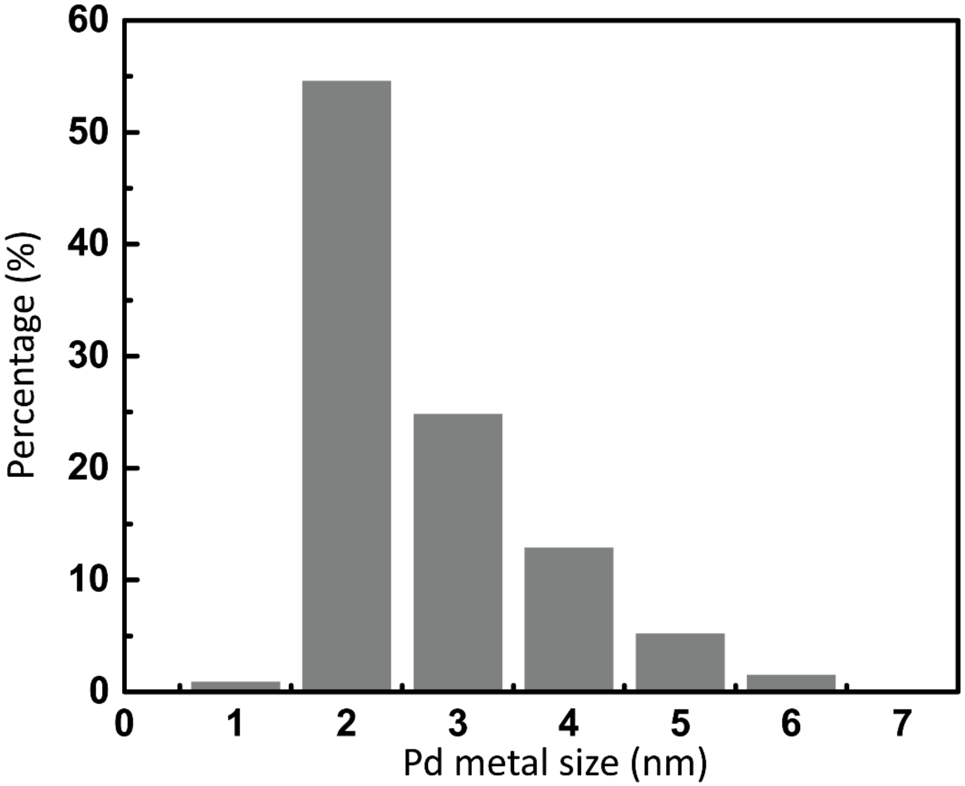

Figure A3. Pd metal size distribution.

3. Mass transfer

3.1. Internal mass transfer

3.1.1. Experiments with different particle size

Table A1. Nitrite hydrogenation using different catalyst particle size (0.3 mM nitrite, 0.8 bar hydrogen, 0.1 bar CO_2, 0.1 bar He).

Particle size (μm)	Initial rate (mM*min^{-1})
0 - 38	0.1
38 - 45	0.1
45 – 100	0.06
100 - 250	0.02
250 -300	0.01
300 - 425	0.008

The original small catalyst particles were pressurized at 4000 bar for 2 min in a cold isostatic press. The pressurized pellet was broken and sieved to obtain samples with particle sizes in the windows 0 - 38, 38 – 45, 45 – 100, 200 – 250, 250 – 300 and 300 – 425 μm.

3.1.2. Weisz-Prater criterion

Weisz-Prater criterion is normally used as the criteria to estimate whether pore diffusion resistance can significantly influence the reaction rate [1].

$$C_{wp} = \frac{R_{obv} \times L^2 \times \rho_{Cat}}{C_s \times D_{eff}} \qquad eq11$$

Where R_{obv} is the reaction rate per mass of catalyst (mol*s^{-1}*kg^{-1}), L is the characteristic length (m), ρ_{Cat} is the density of the catalyst particles (kg*m^{-3}), C_s is the reactant concentration at the particle surface (mol*m^{-3}), and D_{eff} is the effective diffusivity (m^2*s^{-1}).

$$L = \frac{d_p}{3} \qquad eq12$$

$$D_{eff} = \frac{D_{AB} \times \phi}{\tau} \qquad eq13$$

In which d_p is radius of the catalyst particles, D_{AB} is the bulk diffusion coefficient of species [2], ϕ is the particle porosity, normally between 0.2 and 0.7, based on the BET measurement, here we get 0.7, and τ is the tortuosity, normally varies between 1 and 10, here we choose 3.

If there is no obvious diffusion limitations: $C_{wp} < 1$

However, if there is severe diffusion limitations: $C_{wp} > 1$

In Table A2, shown nitrite concentration at 10 mM and 0.5 mM, hydrogen pressure varies between 0.05 and 0.8 bar, the calculation of the Weisz-Prater criterion.

Table A2. At different reaction conditions, calculate the nitrite and hydrogen Weisz-Prater criterion.

Nitrite concentration (mM)	Hydrogen pressure (bar)	Nitrite Weisz-Prater	Hydrogen Weisz-Prater
10	0.8	0.011	0.20
10	0.05	0.00028	0.08
0.5	0.8	0.16	0.13
0.5	0.05	0.062	0.82

As shown in Table A2, all the results is below 1, so internal mass transfer limitation has negligible influence on the reaction rate.

3.2. External mass transfer

3.2.1. Experimental check

Table A3. Catalyst activity per gram catalyst.

Amount of catalyst (g)	Activity (mM/min/g Cat)
0.05	1.7 ± 0.4
0.1	1.6 ± 0.3

Table A3 presents the catalyst activity per gram catalyst measured with different amount of catalyst. As the activity remains constant, it can be concluded that gas-liquid transfer: hydrogen is not limiting.

3.2.2. Liquid-Solid mass transfer

The liquid-solid (L-S) mass transfer rate constant for nitrite was calculated based on the literature [3]. Slip velocity of the catalyst particles is first calculated and used to conservatively estimate the mass transfer rate between aqueous solution and the solid. Stokes' law was assumed to apply and the particle's slip velocity was calculated by:

$$\mathcal{U}_t = \frac{g * d_h^2 * (\rho_p - \rho)}{18\mu} = \frac{9.81 * 1.5 * 1.5 * 10^{-10} * (1059 - 1000)}{18 * 1.002 * 10^{-3}} \; m * s^{-1}$$
$$= 7.2 * 10^{-6} \quad eq14$$

Where g is the standard gravity (9.81 m*s^{-2}), ρ_p is average density of the catalysts (1059 kg*m^{-3}), ρ is water density (1000 kg*m^{-3} at 20 °C), μ is absolute viscosity of water (1.002*10^{-3} kg*m^{-1}*s^{-1} at 20 °C), and d_h is the hydrodynamic size of the catalysts (1.5*10^{-5} m). Hence, the slip velocity is 7.2 * 10^{-6} m*s^{-1}. The corresponding Reynolds number was calculated by the following expression:

$$R_e = \frac{d_h * \mathcal{U}_t}{\upsilon} = \frac{1.5 * 10^{-5} * 7.2 * 10^{-6}}{1.003 * 10^{-6}} = 1.08 * 10^{-4} \qquad eq15$$

in which υ is kinematic viscosity of water (1.003 * 10^{-6} m^2*s^{-1} at 20 °C). The Reynolds number Re is 1.08 * 10^{-4} $<$ 1. This is indicative of laminar flow and Stokes law is applicable.

The Peclet number (Pe) and Sherwood number (Sh) were calculated based on the following equations:

$$Pe = \frac{d_h * \mathcal{U}_t}{D} = \frac{1.5 * 10^{-5} * 7.2 * 10^{-6}}{1.9 * 10^{-9}} = 5.68 * 10^{-2} \qquad eq16$$

$$Sh = \frac{4}{Pe} * ln\left(\frac{1}{1 - {Pe}/{2}}\right) = \frac{4}{0.0568} * \ln\left(\frac{1}{1 - {0.0568}/{2}}\right) = 2.03 \qquad eq17$$

in which D is the nitrite diffusion coefficient in pure water (1.9×10^{-9} m^2*s^{-1}). Note that the value of Sh is rather similar to the value for a particle in stagnant liquid (Sh = 2), which is typical for a slurry reactor as the small particles essentially move with the liquid, with limited shear at the surface of the particles. The L-S mass transfer coefficient for nitrite is calculated according to the following expression:

$$k_{ls} = \frac{D * Sh}{d_h} = \frac{1.9 * 10^{-9} * 2.03}{1.5 * 10^{-5}}\ m * s^{-1} = 2.57 * 10^{-4}\ m * s^{-1} \qquad eq18$$

The value of k_{ls} is 2.57*10^{-4} m*s^{-1}. The geometric surface area of the catalyst per volume of solution is:

$$a_s = \frac{A_p * m}{\rho_c * V_p * V_R} \qquad eq19$$

Where A_p is the geometric surface area of one catalyst particle (m^2), m is the mass of the catalyst in the experiments (kg), V_p is the volume of one catalyst particle (m^3), and V_R is the volume of reaction solution (m^3).

$$a_s = \frac{4\pi * (1.5 * 10^{-5}\ m)^2 * 5 * 10^{-5}\ kg}{1059\ kg * m^{-3} * \frac{4\pi}{3} * (1.5 * 10^{-5}\ m)^3 * 3 * 10^{-4}\ m^3} = 12.58\ m^{-1}$$

The mass transfer rate constant was then calculated by multiplying the mass transfer coefficient by the geometric surface area of the catalyst per volume of solution:

$k_{ls} * a_s = 2.57 * 10^{-4} * 12.58\ s^{-1} = 3.23 * 10^{-3}\ s^{-1}$

The mass transfer is first order. So the maximum mass transfer rate at concentration C_S in the bulk of the liquid, can be calculated by the following equation:

$Max\ mass\ transfer\ rate =\ k_{ls} * a_s * C_s$

For an example, at nitrite concentration is 1 mM, the mass transfer rate is 0.19 mM*min^{-1}, which is significantly larger than even the highest reaction rate (0.09 mM*min$_{-1}$) at same nitrite concentration. Therefore, L-S mass transfer is not limiting.

3.2.3. External mass transfer; combined G-L and L-S

Mears criterion allows to estimate any limitation at the G-L and/or L-S interface [4,5].
Mears criteria (G-S):

$$\frac{-\mathrm{r_{obs}}\rho_\mathrm{b} d_p \mathrm{n}}{\mathrm{K_c C_s}} < 0.15 \qquad \mathrm{eq20}$$

Where $-\mathrm{r_{obs}}$ is the observed rate per unit mass of catalyst (mol*kg^{-1}*s^{-1}), n is the reaction order, d_p is the catalyst particle radius (m), ρ_b is bulk density of the catalyst (kg*m^{-3}), $\mathrm{C_s}$ is hydrogen concentration in the bulk gas (mol*m^{-3}), and $\mathrm{K_c}$ is the mass transfer coefficient (m/s).
Since the gas stream is flow through the liquid, therefore the gas bubbles are moves along with the catalyst particles. According to the previous section 3.2.2. calculation, the Re number is $1.08 * 10^{-4}$ much smaller than 1, which indicates the mass transfer coefficient can be estimated based on following equation [4]:

$$Sh = \frac{K_c * 2 * d_p}{D_{AB}} = 2 \qquad eq21$$

Where Sh is the Sherwood number, d_p is the catalyst particle radius (m), D_{AB} is H_2 gas phase diffusivity (m^2*s^{-1}). We estimated the diffusivity D_{AB} for H_2 is 6.3*10^{-5} m^2*s^{-1} [4].

$$K_c = \frac{D_{AB}}{d_p} = \frac{6.3 * 10^{-5}\ m^2 * s^{-1}}{5 * 10^{-6}\ m} = 12.6\ m * s^{-1}$$

Table A4. Value of the different parameters and the results of Mears criteria.

-r_{obs}(H_2)	mol*s^{-1}*kg^{-1}	3.4*10^{-2}
ρ_b	kg*m^{-3}	1059
n	N/A	0.3
d_p	m	5.0*10^{-6}
C_s (H_2)	mol*m^{-3}	35.7
K_c (H_2)	m*s^{-1}	12.6
Mears criteria (H_2)	N/A	1.2*10^{-7}

Based on the calculation, it shows that the gas-liquid and liquid-solid mass transfer limitation can be ignored.

4. Derivation of overall rate expressions for nitrite hydrogenation

4.1. Derivation of rate expressions, NO reduction to NH

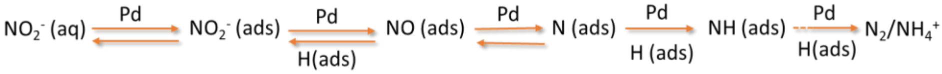

Scheme A1. NO_{ads} reduction to NH_{ads} specie pathway.

$H_2 + 2* \leftrightharpoons 2H^*$ (equilibrium reaction 1, K_1)

$NO_2^- + * \leftrightharpoons NO_2^{-*}$ (equilibrium reaction 2, K_2)

$NO_2^{-*} + H^* + H^+ \leftrightharpoons NO^* + H_2O + *$ (equilibrium reaction 3, K_3)

$NO^* + * \leftrightharpoons N^* + O^*$ (equilibrium reaction 4, K_4)

$O^* + 2H^* \leftrightharpoons 3* + H_2O$ (equilibrium reaction 5, K_5)

$\boldsymbol{N^* + H^* \rightarrow NH^* + * \quad (reaction\ 6,\ k_6)\ RDS}$

we assume reaction 6 is the RDS. So on the Pd site there will have H*, NO_2-*, NO*, N*, O*,

$\theta_H = K_1^{0.5}[H_2]^{0.5}\theta^*$

$\theta_{NO_2^-} = K_2[NO_2^-]\theta^*$

$$\theta_{NO} = {K_1}^{0.5}K_2K_3[H^+][NO_2^-][H_2]^{0.5}\theta^*$$

$$\theta_N = {K_1}^{1.5}K_2K_3K_4K_5[H^+][NO_2^-][H_2]^{1.5}\theta^*$$

$$\theta_O = \frac{1}{K_1K_5}\frac{\theta^*}{[H_2]}$$

$$1 = \theta_H + \theta_{NO_2^-} + \theta_{NO} + \theta_N + \theta_O + \theta^*$$

We assume that K_5 is very large so that θ_O is very low, rewriting the equation to:

$$1 = \theta_H + \theta_{NO_2^-} + \theta_{NO} + \theta_N + \theta^*$$

$$1 = {K_1}^{0.5}[H_2]^{0.5}\theta^* + K_2[NO_2^-]\theta^* + {K_1}^{0.5}K_2K_3[H^+][NO_2^-][H_2]^{0.5}\theta^* + {K_1}^{1.5}K_2K_3K_4K_5[H^+][NO_2^-][H_2]^{1.5}\theta^* + \theta^*$$

So

$$\theta^* = \frac{1}{1+{K_1}^{0.5}[H_2]^{0.5}+K_2[NO_2^-]+{K_1}^{0.5}K_2K_3[H^+][NO_2^-][H_2]^{0.5}+{K_1}^{1.5}K_2K_3K_4K_5[H^+][NO_2^-][H_2]^{1.5}} \qquad eq22$$

$$Rate = k_6\theta_H\theta_N = k_6{K_1}^{0.5}[H_2]^{0.5}\theta^*{K_1}^{1.5}K_2K_3K_4K_5[H^+][NO_2^-][H_2]^{1.5}\theta^* = {K_1}^2K_2K_3K_4K_5k_6[H^+][NO_2^-][H_2]^2{\theta^*}^2 = \frac{{K_1}^2K_2K_3K_4K_5k_6[H^+][NO_2^-][H_2]^2}{(1+{K_1}^{0.5}[H_2]^{0.5}+K_2[NO_2^-]+{K_1}^{0.5}K_2K_3[H^+][NO_2^-][H_2]^{0.5}+{K_1}^{1.5}K_2K_3K_4K_5[H^+][NO_2^-][H_2]^{1.5})^2} \qquad eq23$$

So at low hydrogen pressure, the ignore items which contains hydrogen.

So we can rewrite the equation:

$$Rate = \frac{{K_1}^2K_2K_3K_4K_5k_6[H^+][NO_2^-][H_2]^2}{(1+K_2[NO_2^-])^2} \qquad eq24$$

So the order in hydrogen is 2, the nitrite order is [-1, 1]

So if at high hydrogen pressure, we can ignore the $K_2[NO_2^-]$, so we can rewrite the equations.

$$Rate = \frac{{K_1}^2K_2K_3K_4K_5k_6[H^+][NO_2^-][H_2]^2}{(1+{K_1}^{0.5}[H_2]^{0.5}+{K_1}^{0.5}K_2K_3[H^+][NO_2^-][H_2]^{0.5}+{K_1}^{1.5}K_2K_3K_4K_5[H^+][NO_2^-][H_2]^{1.5})^2} \qquad eq25$$

If the hydrogen pressure is high enough, the hydrogen order can varies from [-1, 2], for nitrite can varies from [-1, 1]. Which will cover all the range of the order we observed in our experiment.

Table A5. Hydrogen and nitrite order in different concentration zone based on the rate equation.

Low H_2 & low nitrite	High H_2 & low nitrite
H_2 order : 2	H_2 order : [-1, 2]
Nitrite order : [-1, 1]	Nitrite order : [-1, 1]
Low H_2 & high nitrite	**High H_2 & high nitrite**
H_2 order : 2	H_2 order : [-1, 2]
Nitrite order : [-1, 1]	Nitrite order : [-1, 1]

4.2. Derivation of rate expressions, NO reduction to NOH

I.

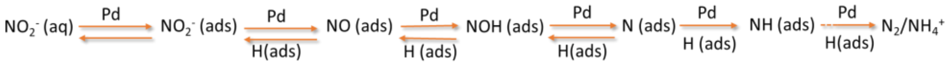

Scheme A2. NO_{ads} reduction to NOH_{ads}, first pathway NOH_{ads} dissociation.

$$H_2 + 2* \leftrightharpoons 2H^* \quad \text{(equilibrium reaction 1, } K_1\text{)}$$

$$NO_2^- + * \leftrightharpoons NO_2^{-*} \quad \text{(equilibrium reaction 2, } \quad K_2\text{)}$$

$$NO_2^{-*} + H^* + H^+ \leftrightharpoons NO^* + H_2O + * \quad \text{(equilibrium reaction 3, } K_3\text{)}$$

$$NO^* + H^* \leftrightharpoons NOH^* + * \quad \text{(equilibrium reaction 4, } K_4\text{)}$$

$$NOH^* + H^* \leftrightharpoons N^* + H_2O + * \quad \text{(equilibrium reaction 5, } K_5\text{)}$$

$$\boldsymbol{N^* + H^* \rightarrow NH^* + *} \quad \textbf{(reaction 6, } \boldsymbol{k_6}\textbf{)} \quad \boldsymbol{RDS}$$

We assume reaction 6 is the RDS. So on the Pd site there will have H*, NO_2^{-}*, NO*, NOH*, N*

$$\theta_H = {K_1}^{0.5}[H_2]^{0.5}\theta^*$$

$$\theta_{NO_2^-} = K_2[NO_2^-]\theta^*$$

$$\theta_{NO} = {K_1}^{0.5}K_2K_3[H^+][NO_2^-][H_2]^{0.5}\theta^*$$

$$\theta_{NOH} = K_1K_2K_3K_4[H^+][NO_2^-][H_2]\theta^*$$

$$\theta_N = {K_1}^{1.5}K_2K_3K_4K_5[H^+][NO_2^-][H_2]^{1.5}\theta^*$$

$$1 = \theta_H + \theta_{NO_2^-} + \theta_{NO} + \theta_{NOH} + \theta_N + \theta^*$$

$$\theta^* = \frac{1}{1+{K_1}^{0.5}[H_2]^{0.5}+K_2[NO_2^-]+{K_1}^{0.5}K_2K_3[H^+][NO_2^-][H_2]^{0.5}+K_1K_2K_3K_4[H^+][NO_2^-][H_2]+{K_1}^{1.5}K_2K_3K_4K_5[H^+][NO_2^-][H_2]^{1.5}}$$

$$Rate = k_6\theta_H\theta_N = k_6{K_1}^{0.5}[H_2]^{0.5}\theta^*{K_1}^{1.5}K_2K_3K_4K_5[H^+][NO_2^-][H_2]^{1.5}\theta^* = {K_1}^2K_2K_3K_4K_5k_6[H^+][NO_2^-][H_2]^2{\theta^*}^2 = \frac{{K_1}^2K_2K_3K_4K_5k_6[H^+][NO_2^-][H_2]^2}{(1+{K_1}^{0.5}[H_2]^{0.5}+K_2[NO_2^-]+{K_1}^{0.5}K_2K_3[H^+][NO_2^-][H_2]^{0.5}+K_1K_2K_3K_4[H^+][NO_2^-][H_2]+{K_1}^{1.5}K_2K_3K_4K_5[H^+][NO_2^-][H_2]^{1.5})^2} \quad eq26$$

When at low hydrogen pressure, we ignore the item which contains hydrogen in the denominator, then we rewrite the equation:

$$Rate = \frac{{K_1}^2K_2K_3K_4K_5k_6[H^+][NO_2^-][H_2]^2}{(1+K_2[NO_2^-])^2} \qquad eq27$$

So the order in hydrogen is 2, the nitrite order is [-1, 1]

So if at high hydrogen pressure, we can ignore the $K_2[NO_2^-]$, so we can rewrite the equations.

$$Rate = \frac{{K_1}^2K_2K_3K_4K_5k_6[H^+][NO_2^-][H_2]^2}{(1+{K_1}^{0.5}[H_2]^{0.5}+{K_1}^{0.5}K_2K_3[H^+][NO_2^-][H_2]^{0.5}+K_1K_2K_3K_4[H^+][NO_2^-][H_2]+{K_1}^{1.5}K_2K_3K_4K_5[H^+][NO_2^-][H_2]^{1.5})^2} \qquad eq28$$

If the hydrogen pressure is high enough, the hydrogen order can varies from [-1, 2], for nitrite can varies from [-1, 1]. Which will cover all the range of the order we observed in our experiments.

II.

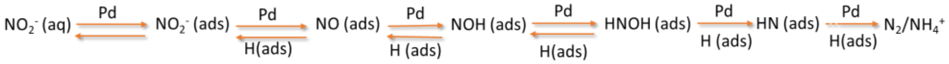

Scheme A3. NO_{ads} reduction to NOH_{ads}, second pathway $HNOH_{ads}$ dissociation.

$H_2 + 2* \leftrightharpoons 2H^*$ (equilibrium reaction 1, K_1)

$NO_2^- + * \leftrightharpoons NO_2^{-*}$ (equilibrium reaction 2, K_2)

$NO_2^{-*} + H^* + H^+ \leftrightharpoons NO^* + H_2O + *$ (equilibrium reaction 3, K_3)

$NO^* + H^* \leftrightharpoons NOH^* + *$ (equilibrium reaction 4, K_4)

$NOH^* + H^* \leftrightharpoons HNOH^* + *$ (equilibrium reaction 5, K_5)

$\boldsymbol{HNOH^* + H^* \rightarrow NH^* + H_2O + *}$ **(reaction 6, $\boldsymbol{k_6}$) *RDS***

we assume reaction 6 is the RDS. So on the Pd site there will have H*, NO_2-*, NO*, NOH*, HNOH*,

$$\theta_H = {K_1}^{0.5}[H_2]^{0.5}\theta^*$$

$$\theta_{NO_2^-} = K_2[NO_2^-]\theta^*$$

$$\theta_{NO} = {K_1}^{0.5}K_2K_3[H^+][NO_2^-][H_2]^{0.5}\theta^*$$

$$\theta_{NOH} = K_1K_2K_3K_4[H^+][NO_2^-][H_2]\theta^*$$

$$\theta_{HNOH} = {K_1}^{1.5}K_2K_3K_4K_5[H^+][NO_2^-][H_2]^{1.5}\theta^*$$

$$1 = \theta_H + \theta_{NO_2^-} + \theta_{NO} + \theta_{NOH} + \theta_{HNOH} + \theta^*$$

$$\theta^* = \frac{1}{1+{K_1}^{0.5}[H_2]^{0.5}+K_2[NO_2^-]+{K_1}^{0.5}K_2K_3[H^+][NO_2^-][H_2]^{0.5}+K_1K_2K_3K_4[H^+][NO_2^-][H_2]+{K_1}^{1.5}K_2K_3K_4K_5[H^+][NO_2^-][H_2]^{1.5}}$$

$$Rate = k_6\theta_H\theta_{HNOH} = k_6{K_1}^{0.5}[H_2]^{0.5}\theta^*{K_1}^{1.5}K_2K_3K_4K_5[H^+][NO_2^-][H_2]^{1.5}\theta^* =$$

$${K_1}^2K_2K_3K_4K_5k_6[H^+][NO_2^-][H_2]^2{\theta^*}^2 =$$

$$\frac{{K_1}^2K_2K_3K_4K_5k_6[H^+][NO_2^-][H_2]^2}{(1+{K_1}^{0.5}[H_2]^{0.5}+K_2[NO_2^-]+{K_1}^{0.5}K_2K_3[H^+][NO_2^-][H_2]^{0.5}+K_1K_2K_3K_4[H^+][NO_2^-][H_2]+{K_1}^{1.5}K_2K_3K_4K_5[H^+][NO_2^-][H_2]^{1.5})^2} \quad eq29$$

When at low hydrogen pressure, we ignore the item which contains hydrogen in the denominator, then we rewrite the equation:

$$Rate = \frac{{K_1}^2K_2K_3K_4K_5k_6[H^+][NO_2^-][H_2]^2}{(1+K_2[NO_2^-])^2} \quad eq30$$

So the order in hydrogen is 2, the nitrite order is [-1, 1]

So if at high hydrogen pressure, we can ignore the $K_2[NO_2^-]$, so we can rewrite the equations.

$$Rate =$$

$$\frac{{K_1}^2K_2K_3K_4K_5k_6[H^+][NO_2^-][H_2]^2}{(1+{K_1}^{0.5}[H_2]^{0.5}+{K_1}^{0.5}K_2K_3[H^+][NO_2^-][H_2]^{0.5}+K_1K_2K_3K_4[H^+][NO_2^-][H_2]+{K_1}^{1.5}K_2K_3K_4K_5[H^+][NO_2^-][H_2]^{1.5})^2} \quad eq31$$

If the hydrogen pressure is high enough, the hydrogen order can varies from [-1, 2], for nitrite can varies from [-1, 1]. Which will cover all the range of the order we observed in our experiments.

III.

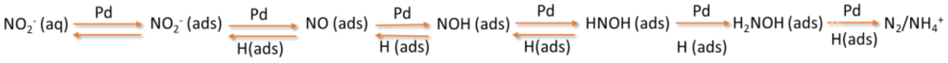

Scheme A4. NO_{ads} reduction to NOH_{ads}, thrid pathway $HNOH_{ads}$ hydrogenation.

$H_2 + 2* \leftrightharpoons 2H^*$ (equilibrium reaction 1, K_1)

$NO_2^- + * \leftrightharpoons NO_2^{-*}$ (equilibrium reaction 2, K_2)

$NO_2^{-*} + H^* + H^+ \leftrightharpoons NO^* + H_2O + *$ (equilibrium reaction 3, K_3)

$NO^{*} + H^{*} \leftrightharpoons NOH^{*} + *$ (equilibrium reaction 4, K_4)

$NOH^{*} + H^{*} \leftrightharpoons HNOH^{*} + *$ (equilibrium reaction 5, K_5)

$\boldsymbol{HNOH^{*} + H^{*} \rightarrow H_2NOH^{*} + *}$ (**reaction 6,** $\boldsymbol{k_6}$) $\boldsymbol{RDS}$

We assume reaction 6 is the RDS. So on the Pd site there will have H*, NO_2^-*, NO*,NOH*, HNOH*

$$\theta_H = {K_1}^{0.5}[H_2]^{0.5}\theta^{*}$$

$$\theta_{NO_2^-} = K_2[NO_2^-]\theta^{*}$$

$$\theta_{NO} = {K_1}^{0.5}K_2K_3[H^+][NO_2^-][H_2]^{0.5}\theta^{*}$$

$$\theta_{NOH} = K_1K_2K_3K_4[H^+][NO_2^-][H_2]\theta^{*}$$

$$\theta_{HNOH} = {K_1}^{1.5}K_2K_3K_4K_5[H^+][NO_2^-][H_2]^{1.5}\theta^{*}$$

$$1 = \theta_H + \theta_{NO_2^-} + \theta_{NO} + \theta_{NOH} + \theta_{HNOH} + \theta^{*}$$

$$\theta^{*} = \frac{1}{1+{K_1}^{0.5}[H_2]^{0.5}+K_2[NO_2^-]+{K_1}^{0.5}K_2K_3[H^+][NO_2^-][H_2]^{0.5}+K_1K_2K_3K_4[H^+][NO_2^-][H_2]+{K_1}^{1.5}K_2K_3K_4K_5[H^+][NO_2^-][H_2]^{1.5}}$$

$$Rate = k_6\theta_H\theta_{HNOH} = k_6{K_1}^{0.5}[H_2]^{0.5}\theta^{*}{K_1}^{1.5}K_2K_3K_4K_5[H^+][NO_2^-][H_2]^{1.5}\theta^{*} = {K_1}^{2}K_2K_3K_4K_5k_6[H^+][NO_2^-][H_2]^{2}\theta^{*2} = \frac{{K_1}^{2}K_2K_3K_4K_5k_6[H^+][NO_2^-][H_2]^{2}}{(1+{K_1}^{0.5}[H_2]^{0.5}+K_2[NO_2^-]+{K_1}^{0.5}K_2K_3[H^+][NO_2^-][H_2]^{0.5}+K_1K_2K_3K_4[H^+][NO_2^-][H_2]+{K_1}^{1.5}K_2K_3K_4K_5[H^+][NO_2^-][H_2]^{1.5})^2} \quad eq32$$

When at low hydrogen pressure, we ignore the item which contains hydrogen in the denominator, then we rewrite the equation:

$$Rate = \frac{{K_1}^{2}K_2K_3K_4K_5k_6[H^+][NO_2^-][H_2]^{2}}{(1+K_2[NO_2^-])^2} \quad eq33$$

So the order in hydrogen is 2, the nitrite order is [-1, 1]

So if at high hydrogen pressure, we can ignore the $K_2[NO_2^-]$, so we can rewrite the equations.

$$Rate = \frac{{K_1}^2 K_2 K_3 K_4 K_5 k_6 [H^+][NO_2^-][H_2]^2}{(1+{K_1}^{0.5}[H_2]^{0.5}+{K_1}^{0.5}K_2K_3[H^+][NO_2^-][H_2]^{0.5}+K_1K_2K_3K_4[H^+][NO_2^-][H_2]+{K_1}^{1.5}K_2K_3K_4K_5[H^+][NO_2^-][H_2]^{1.5})^2} \quad eq34$$

If the hydrogen pressure is high enough, the hydrogen order can varies from [-1, 2], for nitrite can varies from [-1, 1]. Which will cover all the range of the order we observed in our experiments.

4.3. Derivation of rate expressions, “N”-“N” bond coupling is the rate limiting

$H_2 + 2* \leftrightharpoons 2H^*$ (equilibrium reaction 1, K_1)

$NO_2^- + * \leftrightharpoons NO_2^{-*}$ (equilibrium reaction 2, K_2)

$NO_2^{-*} + H^* + H^+ \leftrightharpoons NO^* + H_2O + *$ (equilibrium reaction 3, K_3)

$NO^* + * \leftrightharpoons N^* + O^*$ (equilibrium reaction 4, K_4)

$O^* + 2H^* \leftrightharpoons 3* + H_2O$ (equilibrium reaction 5, K_5)

$N^* + H^* \leftrightharpoons NH^* + *$ (equilibrium reaction 6, K_6)

$NO^* + H^* \leftrightharpoons NOH^* + *$ (equilibrium reaction 7, K_7)

$"N^*" + "N^*" \rightarrow "N-N^*" + *$ (reaction 8, k_8) RDS

From reaction 1 to 7 is equilibrium reaction, then reaction 8 is the RDS which is N-N bond formation.

So based on the is equilibrium steps, we can get the surface coverage of all the “N” species, : $\theta_N, \theta_{NO_2^-}, \theta_{NO}, \theta_{NOH,} \theta_{NH}$

$\theta_{NO_2^-} = K_2[NO_2^-]\theta^*$

$\theta_{NO} = {K_1}^{0.5}K_2K_3[H^+][NO_2^-][H_2]^{0.5}\theta^*$

$\theta_N = {K_1}^{1.5}K_2K_3K_4K_5[H^+][NO_2^-][H_2]^{1.5}\theta^*$

$\theta_{NOH} = K_1K_2K_3K_7[H^+][NO_2^-][H_2]\theta^*$

$\theta_{NH} = {K_1}^{2.5} K_2 K_3 K_4 K_5 K_6 [H^+][NO_2^-][H_2]^2 \theta^*$

then we can have fourteen different combinations.

1, $N^* + N^* \rightarrow N_2 + 2*$

2, $N^* + NO^* \rightarrow N_2O^* + *$

3, $N^* + NOH^* \rightarrow N_2OH^* + *$

4, $N^* + NO_2^{-*} \rightarrow N_2O_2^{-*} + *$

5, $NO^* + NO^* \rightarrow N_2{O_2}^* + *$

6, $NO^* + NOH^* \rightarrow N_2O_2H^* + *$

7, $NO^* + NO_2^{-*} \rightarrow N_2O_3^{-*} + *$

8, $NOH^* + NOH^* \rightarrow N_2O_2{H_2}^* + *$

9, $NOH^* + NO_2^{-*} \rightarrow N_2O_3H^{-*} + *$

10, $NH^* + NH^* \rightarrow N_2{H_2}^* + *$

11, $NH^* + N^* \rightarrow N_2H^* + *$

12, $NH^* + NO^* \rightarrow N_2OH^* + *$

13, $NH^* + NO_2^{-*} \rightarrow N_2O_2H^{-*} + *$

14, $NH^* + NOH^* \rightarrow N_2O{H_2}^* + *$

The details are shown in Table A6. So in conclusion, the N-N bond formation is not the RDS in our situation.

Table A6. The nitrite order and hydrogen order based on different RDS.

RDS	Nitrite order	Hydrogen order
$N^* + N^*$	[0, 2]	[0, 3]
$N^* + NO^*$	[0, 2]	[-1, 2]
$N^* + NOH^*$	[0, 2]	[-0.5, 2.5]
$N^* + NO_2^{-*}$	[0, 2]	[-1.5, 1.5]
$NO^* + NO^*$	[0, 2]	[-2, 1]
$NO^* + NOH^*$	[0, 2]	[-1.5, 1.5]
$NO^* + NO_2^{-*}$	[0, 2]	[-2.5, 0.5]
$NOH^* + NOH^*$	[0, 2]	[-1, 2]
$NOH^* + NO_2^{-*}$	[0, 2]	[-2, 1]
$NH^* + NH^*$	[0, 2]	[1, 4]
$NH^* + N^*$	[0, 2]	[0.5, 3.5]
$NH^* + NO^*$	[0, 2]	[-0.5, 2.5]
$NH^* + NO_2^{-*}$	[0, 2]	[-1, 2]
$NH^* + NOH^*$	[0, 2]	[0, 3]

Reference

[1] D. Shuai, J. K. Choe, J. R. Shapley, C. J. Werth, *Environ. Sci. Technol.* **2012**, *46*, 2847–2855.

[2] R. Brunet Espinosa, D. Rafieian, R. G. H. Lammertink, L. Lefferts, *Catal. Today* **2016**, *273*, 50–61.

[3] T. Ye, D. P. Durkin, M. Hu, X. Wang, N. A. Banek, M. J. Wagner, D. Shuai, *ACS Appl. Mater. Interfaces* **2016**, *8*, 17739–17744.

[4] W. S. Lee, Z. Wang, W. Zheng, D. G. Vlachos, A. Bhan, *Catal. Sci. Technol.* **2014**, *4*, 2340–2352.

[5] D. E. Mears, *Ind. Eng. Chem. Process Des. Dev.* **1971**, *10*, 541–547.

Chapter 3

Enhanced transport in Gas-Liquid-Solid catalytic reaction by structured wetting properties: nitrite hydrogenation

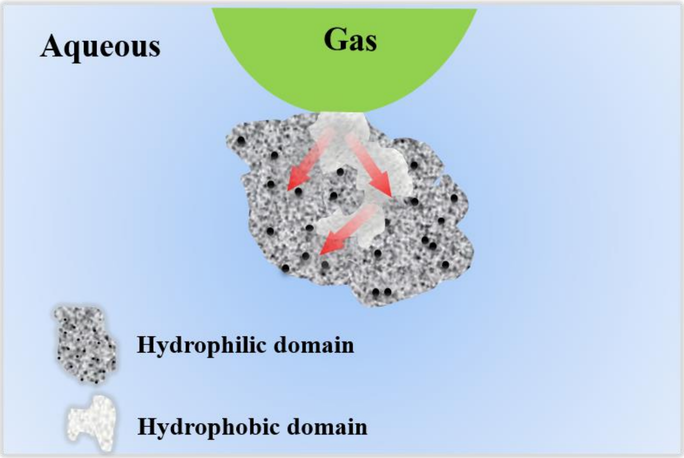

Published as: Structured catalyst enhancing transport in Gas-Liquid-Solid reaction: nitrite hydrogenation, Chemical Engineering & Processing: Process Intensification, Volume 148, February 2020, 107802

Abstract:

This chapter presents a new approach to improve mass transfer in and around catalyst particles in three-phase operation with micro-structured catalysts, containing hydrophilic and hydrophobic domains. Partially hydrophilic catalysts were prepared via physical mixing of hydrophobic perfluorinated octyltrichloro silane (FOTS)/γ-Al_2O_3 domains and hydrophilic Pd/γ-Al_2O_3 domains, resulting in manipulation of water wetting, both at the external surface and the pores inside the support particles. The modified catalysts were characterized with elemental analysis, XRF, N_2 physisorption and light microscopy after selective dyeing hydrophobic and hydrophilic domains. The catalysts are tested for hydrogenation of nitrite in water, which is an extremely fast reaction whereas the product distribution (N_2 versus NH_4^+) is also easily influenced by internal concentration gradients. Noticeably, the partially hydrophilic catalyst is more active and produces more ammonium compared to hydrophilic catalyst. This work demonstrates that this way of structuring the catalyst enables influencing the internal concentration gradients for aqueous systems. For the case of nitrite hydrogenation, we show that structured catalysts achieve the same rate per gram Pd at lower hydrogen pressure compared to classical hydrophilic catalysts. This results in formation of less ammonia, which is of practical importance for cleaning of drinking water.

1. Introduction

Nitrate contamination of groundwater, caused by landfills, livestock, over-fertilization and industry, is an emergent problem in the supply of safe drinking water [1–3]. Nitrate can be converted in the human body to more toxic nitrite, decreasing the oxygen transport capacity of blood especially in infants. Moreover, nitrite can react with amines and amides, resulting in carcinogenic N-nitroso compounds [4–8]. Therefore, the European Environment Agency has established its legal limits for nitrate and nitrite at 50 and 0.1 mg/L, respectively [9].

Nitrate and nitrite contaminants can be removed from water by several techniques, such as biological denitrification, ion exchange and catalytic hydrogenation. Biological denitrification is not applicable for drinking water, due to the low concentration of nutrients to sustain the growth of bacteria [5]. Ion exchange results in formation of a concentrated brine that cannot be easily discharged [5]. A promising strategy to convert these nitrates and nitrites is the catalytic reduction towards nitrogen with molecular hydrogen [1,10–24]. The reactions involved in nitrite hydrogenation are presented in equation 1 and 2. For practical applications, the selectivity to N_2 must be almost complete in order to prevent formation of ammonia as its permitted concentration (0.5 mg/L) in drinking water is even lower than that of nitrates (50 mg/L).

$$2NO_2^- + 3H_2 + 2H^+ \xrightarrow{Catalyst} N_2 + 4H_2O \qquad eq1$$

$$NO_2^- + 3H_2 + 2H^+ \xrightarrow{Catalyst} NH_4^+ + 2H_2O \qquad eq2$$

Transport of hydrogen to the catalyst in a slurry reactor is schematically shown in Figure 1, top of the figure. Hydrogen first dissolves in water at the gas-liquid interface and diffuses through the stagnant liquid film at the gas-liquid interface. The bulk of the water is well mixed and dissolved hydrogen diffuses through the stagnant liquid film at the outside of the catalyst support particles, followed by diffusion into the pores of the catalyst support, before reaching the active site. The catalyst is completely wetted with water and the pores are completely filled with water. In contrast, transport of nitrite and protons proceeds via diffusion from the bulk of the liquid, via the stagnant liquid film at the external catalyst surface, to the active sites inside the pores. The transport of hydrogen in water is generally more sluggish though, due to its low solubility. The consequence is that active sites in the catalyst support particles may be exposed to different nitrite, proton (pH) and hydrogen concentrations, resulting in lower reaction rates and changes in selectivity of the reaction [25]. It is generally accepted that the ammonium selectivity depends on the ratio of NO_2^-/H_2 at the active site, influencing the concentration of adsorbed species on the Pd surface [12]; formation of ammonia is minimal by minimizing the H_2 concentration. Unfortunately, too low H_2 concentration would also induce very low rates, because of kinetics and because of internal H_2 mass transfer limitation. Internal concentration gradients are undesired, causing variation in both selectivity to ammonia as well as activity on Pd particles, depending on the location in the catalyst support. The main challenge is to achieve a relatively low hydrogen concentration at all active sites, so that all active sites can operate at conditions close to the optimal NO_2^-/H_2 ratio with the optimal balance between activity and selectivity.

For this reason, usually slurry phase reactors are used [15,25,26] as internal mass transfer limitations can be partly suppressed by using small catalyst support particles. In contrast, trickle bed reactors may be more practical [27] but suffer more from internal diffusion limitations because of the larger support particle size. Recently, we demonstrated that a membrane contactor reactor [14,28] is favorable for this purpose, enabling operation at low hydrogen pressure without affecting the rate of reaction because of transport limitations.

An alternative approach to alleviate this problem is presented in Figure 1, bottom of the figure, in which the catalyst wettability is tailored to enhance transport of gaseous reactants towards the active sites, without sacrificing the accessibility of the reactants in aqueous phase. In this strategy, a fraction of the catalyst surface (external and internal) is selectively hydrophobized to enable direct contact with the gas bubbles, providing a rapid transport pathway for hydrogen. The remaining fraction of the catalyst is kept hydrophilic to facilitate transport of nitrite to the active sites. A key element in this approach is to restrict the spatial distribution of the metal clusters to the hydrophilic domains of the catalyst to ensure the accessibility of the active sites to the aqueous reactants. In this way, the gas-liquid interface is positioned inside the catalyst particles resulting in much shorter diffusion lengths of hydrogen dissolved in water.

Partially hydrophobic support materials have been explored previously [29–33]. “Janus” type of catalyst particles (The middle catalyst in Figure 1) have been developed to increase the external mass transfer in liquid-liquid phase systems [33–35], e.g. enhancing transport of 4-tert-butoxystyrene in water phase during hydrogenation. Note that in this case the catalyst particles are dense and only external surface is modified. Quintanilla et al. [31] reported that introducing hydrophobicity to a Pd/SiO_2 catalyst for hydrogenation of aromatic ketones, decreased the adsorption strength of alcohol on the surface of the support, thus suppressing consecutive hydrogenation to saturated alcohol. Thus, enhancing internal and external mass transfer via modification of both the internal and external surface of porous catalysts has not been reported before to the best of our knowledge, except for our previous work described below.

In our previous work, we reported on the influence of partial hydrophobization of $Pd/\gamma\text{-}Al_2O_3$ on the catalytic activity and selectivity of nitrite hydrogenation in a slurry reactor [25]. In that case, we compared the performance of fully hydrophilic $Pd/\gamma\text{-}Al_2O_3$ with two distinct types of partially hydrophobic catalysts. One type was prepared by physically mixing and pelletizing small particles of hydrophilic $Pd/\gamma\text{-}Al_2O_3$ and hydrophobic $\alpha\text{-}Al_2O_3$, resulting in catalysts containing well-defined hydrophilic and hydrophobic domains. The other type consisted of $Pd/\gamma\text{-}Al_2O_3$ functionalized with varying amounts of perfluorinated-octyltrichlorosilane. The catalytic experiments showed that the activity slightly increased when the catalyst was partially hydrophobized, regardless of the strategy employed to introduce hydrophobicity. Notably, the selectivity towards ammonia increased from 15 % in the case of hydrophilic $Pd/\gamma\text{-}Al_2O_3$ to 20 and 30 % for the catalyst made via physical mixing of hydrophilic and hydrophobic domains and for the $Pd/\gamma\text{-}Al_2O_3$ catalyst modified partially with FOTS, respectively. The system was not buffered, causing unfavorable high selectivity to ammonium due to pH gradients inside catalyst particles. The further increase in ammonia selectivity was rationalized in terms of local changes in the concentration of hydrogen relative to nitrite at the active sites inside the catalyst particles, due to enhanced transport of the hydrogen in the partially hydrophobic catalysts. However, further increase of the hydrophobicity of the catalysts lead to significant mass transport limitations of the nitrite ions dissolved in the aqueous phase, which negatively affected the activity. Although the change in selectivity is unfavorable in view of application, the results demonstrated that internal transport can be manipulated.

In this work, we report on the effect of hydrogen and nitrite concentration on the performance of catalysts containing hydrophobic and hydrophilic domains. The concept is explained in Figure 1, showing that gas bubbles will not only interact with the hydrophobic parts of the external surface, but will also fill the pores in the hydrophobic domains with gas. As a result, a gas-liquid interface exists inside the catalyst particles, resulting in extremely short diffusion pathways in wetted pores. We will test the hypothesis that a partially hydrophilic catalyst can operate at lower hydrogen pressure with the same activity and at the same time lower selectivity to ammonia, compared to a classical hydrophilic catalyst. In addition, the influence of the support particle size as well as the ratio between hydrophilic and hydrophobic domains will be discussed. All experiments are performed in the presence of CO_2 as a buffer, in order to achieve favorable low selectivity to ammonium.

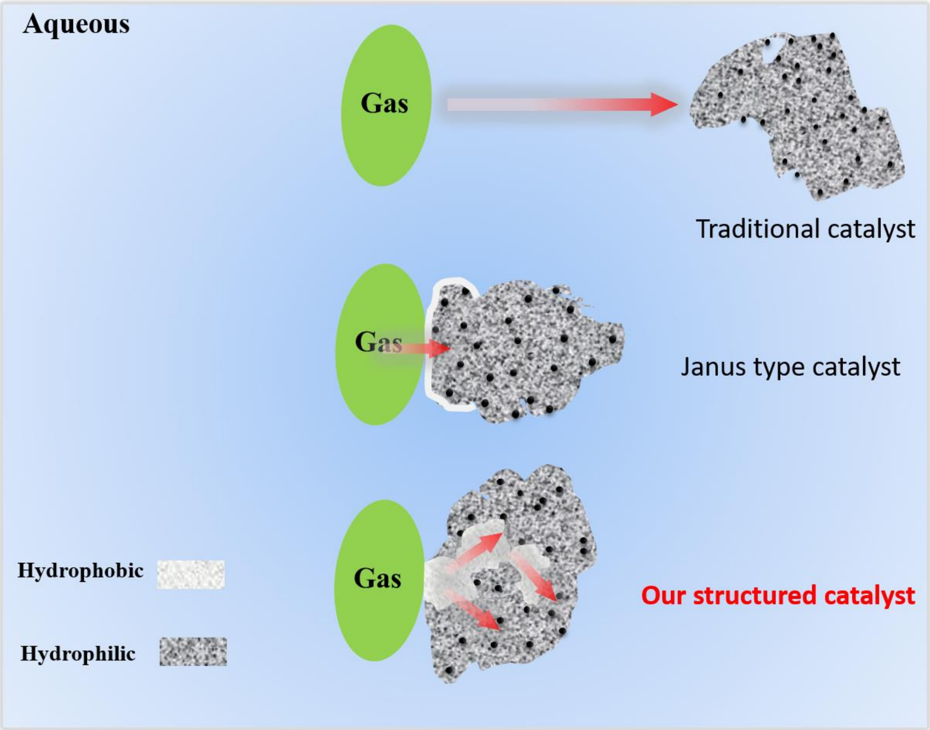

Figure 1. Schematic representation of the concept of the interaction of catalyst containing hydrophobic domains with gas bubbles in water (bottom), compared to a traditional hydrophilic catalyst (top) and a Janus particle with hydrophobicity exclusively at the external surface (middle).

2. Experimental section

2.1. Materials

Commercial γ-Al_2O_3 powder (surface area 198 m^2/g) was purchased from BASF. Palladium precursor tetraamminepalladium (II) nitrate solution (10 wt% in H_2O, 99.99 %), Trichloro(1H,1H,2H,2H-perfluorooctyl)silane ($CF_3(CF_2)_5CH_2CH_2SiCl_3$, FOTS, 97 %), n-hexane, sodium nitrite (99.99 %, used as source for nitrite ions (NO_2^-)), ammonium (50 % v/v water) were obtained from Sigma-Aldrich. Methylene blue hydrate ($C_{16}H_{20}ClN_3OS$, pure) was purchased from ACROS Organics. All the aqueous solutions were prepared using ultra purified water obtained with a water purification system (Millipore, Synergy).

2.2. Catalyst preparation

2.2.1. Parent catalyst hydrophilic Pd/γ-Al_2O_3 synthesis

The Pd/γ-Al_2O_3 (1 wt%) catalyst was prepared via wet impregnation. Typically 10 gram of the sieved alumina support (particle size less than 38 μm, mean particle size is 22 μm ± 0.1 as measured with dynamic light scattering method) was calcined at 600 °C for 4 hours to remove any organic contaminants. Then the support was suspended in 100 mL millQ water. The pH of the solution was adjusted around 9 by adding 2 mL ammonia solution, in order to ensure electrostatic interaction of $Pd(NH_3)_4^{2+}$ with the negatively charged alumina surface. Subsequently, 3 gram of the palladium precursor solution (10 wt%) was slowly added to the suspension. The final suspension was stirred at room temperature for at least 1 hour and then transferred to a rotary evaporator to remove the liquid at 70 °C under vacuum. Finally, the catalyst was calcined in air (flow rate 30 mL/min) at 400 °C for 3 hours (heating rate 5 °C/min), and subsequently reduced in 50 vol% H_2 diluted in N_2 (total flow rate 60 mL/min) at the same temperature for 3 hours.

2.2.2. Parent catalyst hydrophobic FOTS/γ-Al_2O_3 synthesis

γ-Al_2O_3 is hydrophobized by introducing FOTS according to a procedure described in detail elsewhere [25]. In short, 1.5 gram of γ-Al_2O_3 (after pretreatment as described above, particles smaller than 38 μm) was added to 40 mL solution of FOTS dissolved in hexane (25 mM) and the mixture was stirred for 10, 30, 60 or 120 min. The solvent was removed by filtration followed by drying in a vacuum oven at 100 °C for 1 hour, improving the bonding of FOTS to the support. The sample was rinsed with hexane to remove any physisorbed FOTS.

2.2.3. Partially hydrophilic catalyst synthesis

Partially hydrophilic catalysts were prepared by physical mixing of hydrophilic Pd/γ-Al_2O_3 and hydrophobic FOTS/γ-Al_2O_3, followed by pressing, breaking and sieving. A single batch of Pd/γ-Al_2O_3 was used as the parent hydrophilic catalyst. In addition, physical mixing avoids contact between FOTS and the Pd particles. Therefore, the dispersion of the Pd is constant in all experiments. The percentage of hydrophilic domains is expressed as weight percentage, which was varied between 20 % and 80 %. As an example, the 50 % hydrophilic catalyst was prepared by mixing 0.5 gram hydrophobized FOTS/γ-Al_2O_3 with 0.5 gram Pd/γ-Al_2O_3. The mixture was pressurized at 4000 bar for 2 min in a cold isostatic press. The pressurized pellet was broken and sieved to obtain samples with particle sizes in the windows 0 - 38, 45 – 100, 200 – 250, 250 – 300 and 300 – 425 μm.

2.3. Catalyst characterization

2.3.1. Parent catalyst hydrophilic Pd/γ-Al_2O_3

The BET surface area of the hydrophilic catalyst, degassed at 300 ^oC for 1 day, was determined with N_2-adsorption at 77 K (Micromeritics Tristar). The Pd loading on the alumina support was determined with X-ray fluorescence spectroscopy (XRF, Philips PW 1480). Pd particle size was determined using TEM (Tecnai F30), measuring at least 300 Pd particles at ten different spots in the catalyst. X-ray diffraction (XRD, Bruker D2 Phaser diffractometer), with Cu Kα radiation (λ= 0.1544 nm) was used to identify the phases present in the samples. The metal surface area that is accessible was determined with CO chemisorption at room temperature (Chemisorb 2750, Micromeritics). Typically, the sample was reduced at room temperature in hydrogen for 1 h and flushed with He at the same temperature for 0.5 h. Then, CO was introduced as pulses and the response was recorded using a TCD detector. Pd particle sizes are estimated assuming hemispherical metal particles and assuming that the stoichiometric ratio of adsorbed CO and Pd surface atoms is one. The mean catalyst support particle size was measured with dynamic light scattering (DLS) method using a Malvern Mastersizer 2000 with Hydro 2000S module.

2.3.2. Parent catalyst hydrophobic FOTS/γ-Al_2O_3

The thermal stability of FOTS on alumina was determined using thermo-gravimetrical analysis (TGA/SDTA851e, Mettler Toledo). Briefly, the sample was heated in 30 mL/min Ar flow to the target temperature varying between 100 °C and 300 °C, with a heating rate of 5 °C/min. The target temperature was maintained for 1h, followed by cooling down to room temperature. The BET surface area of the hydrophobic catalyst (after degassing at 135 °C for 1 day) was determined with N_2-adsorption 77 K (Micromeritics Tristar). The amount of FOTS on the surface was calculated based on elemental analysis (CHNS-O Analyzer, Interscience, Thermo Scientific) according equation 3:

$$SC\left(\frac{mol\ FOTS}{m^2}\right) = \%C * \frac{1}{100} * \frac{g\ C}{g\ total} * \frac{1\ mol\ C}{12\ g\ C} * \frac{1\ mol\ FOTS}{8\ mol\ C} * \frac{1\ g\ total}{BET\ m^2} \qquad eq3$$

Where SC is the surface coverage of FOTS, %C is the carbon weight concentration as obtained from the elemental analysis and BET is the surface area of the material according to N_2 physisorption; the factor 8 originates from the number of carbon atoms in FOTS.

2.3.3. Partially hydrophilic catalyst

To determine qualitatively the hydrophobicity of the materials, contact angle measurements were performed on a pellet of the sample. Even though surface roughness of the pellet will influence the contact angles, the method still indicates trends in hydrophobicity. The water contact angle was measured using an OCA 15 Dataphysics. Scanning Electron Microscopy (JEOL, JSM-6490) was used to study the catalyst surface morphology. Coverage with FOTS and Pd loading were determined via elemental analysis and XRF respectively, as described above. The catalyst support particle size of both fresh and spent catalyst was measured by dynamic light scattering (DLS) Malvern Mastersizer 2000 with Hydro 2000S module.

2.4. Catalytic tests

Activity and selectivity of the catalysts were measured in a 1 L batch reactor operated at 20 ^oC, atmospheric pressure and a pH value of 5.5, maintained by buffering continuously with CO_2 (0.1 bar). The glass reactor (DURAN® BAFFLED, WIDE MOUTH BOTTLE GLS 80®) has a diameter of 10.1 cm and height 22.2 cm (see **Chapter 2** Figure A1). The reactor has four connections on the reactor lid for gas-in, gas-out, sampling and a stirring shaft equipped with 4 stirring blades. Internal mass transfer limitation are examined on both experiments as well as calculations as described in details in the Appendix section mass transfer checking. External mass transfer calculation is shown in **Chapter 2** Appendix section 3.

Table 1. Operating conditions of the nitrite hydrogenation in slurry reactor.

Reaction temperature, ^oC	20
Reaction volume, L	0.3
pH of the solution	5.5
Stirring speed, rpm	625
Tested partially hydrophilic catalyst particle size, µm	100 - 250
Amount of catalyst, g	0.03
Initial nitrite concentration, mmol/L	1
Total gas flow rate, mL/min	100
Total operating pressure, bar	1
Carbon dioxide partial pressure, bar	0.1
Hydrogen partial pressure, bar	0.1 - 0.8
Helium partial pressure (balance), bar	0.1 - 0.8

Typically, 0.05 gram catalyst was suspended in 0.3 L millQ water and stirred at 625 rpm under 0.8 bar hydrogen (0.1 bar CO_2, 0.1 bar He) to remove oxygen and to reduce the catalyst for at least 1 hour. Reaction was started on introduction of 3 mL $NaNO_2$ solution (100 mmol/L). The hydrogen pressure was varied between 0.1 and 0.8 bar, and the nitrite concentration was varied between 0.3 and 1 mmol/L. Table 1 presents detailed reaction conditions.

Samples were taken at different reaction times using a 2.5 mL syringe (BD Plastipak) and filtered through a syringe filter (PTFE, 0.2 μm, Whatman) in order to remove the catalyst. Nitrite and ammonium concentrations were measured with ion-chromatography (DIONEX, ICS 3000) equipped with an UltiMate autosampler.

NO_2^- conversion and integral NH_4^+ selectivity were calculated according to equation 4 and equation 5, respectively. Since it is well known that ammonia and nitrogen are the only products formed during hydrogenation of nitrite [21,36–39] , nitrogen was calculated based on the mass balance. Since the formation rate of the N_2 is not practical to measure under our conditions, we calculated conversion and selectivity based on the nitrite and ammonium concentration in the liquid.

$$NO_2^-\ conversion = \frac{[NO_2^-]_{t0} - [NO_2^-]_{t1}}{[NO_2^-]_{t0}} * 100 \qquad eq\ 4$$

$$Integral\ NH_4^+\ selectivity = \frac{[NH_4^+]_{t1}}{[NO_2^-]_{t0} - [NO_2^-]_{t1}} * 100 \qquad eq\ 5$$

Where $[NO_2^-]_{t0}$ is the initial nitrite concentration, $[NO_2^-]_{t1}$ is the concentration of nitrite at t1, $[NH_4^+]_{t1}$ is the concentration of ammonium at t1.

Differential ammonium selectivity was calculated according to equation 6.

$$Differential\ NH_4^+\ selectivity = \frac{[formation\ rate\ NH_4^+]_{t1}}{[conversion\ rate\ NO_2^-\ ]_{t1}} * 100 \qquad eq\ 6$$

Where formation rate of NH_4^+ rate is calculated based on the polynomial fitting equation at t1, differential NO_2^- rate is also calculated according to the polynomial fitting equation at t1. Figure A1 shows a typical fitting example. It is noticeable that the polynomial fitting is used in all the experiments.

The apparent turn-over-frequency (TOF) was calculated based on differential NO_2^- rate at t1, according equation 7.

$$TOF = \frac{[conversion\ rate\ NO_2^-\ ]_{t1}\ mol * s^{-1}}{moles\ of\ available\ surface\ Pd\ mol} \qquad eq\ 7$$

Where the number of available Pd surface-atoms was obtained with CO-chemisorption.

3. Results and discussion

3.1. Catalyst preparation and characterization

3.1.1. Parent hydrophilic catalyst: Pd/γ-Al_2O_3

Table 2 shows the characterization results of the hydrophilic parent catalyst. The XRF results confirm that the Pd loading is close to the 1 wt% target. Also, deposition of Pd does not influence the BET surface area as well as the pore volume, indicating that the support structure remains unchanged.

Table 2. Characterization data of both parent catalysts, hydrophilic (Pd/γ-Al_2O_3), hydrophobic (FOTS/γ-Al_2O_3) and support material γ-Al_2O_3.

		Elemental analysis	N_2 physisorption		XRF	CO-chemisorption
Sample	Particle size (μm)	Carbon (wt%)	Specific surface area (m^2/g)	Pore volume (cm^3/g)	Pd loading (wt%)	Pd dispersion (%)
γ-Al_2O_3	0 - 38	n/a	198	0.67	n/a	n/a
Pd/γ-Al_2O_3	0 - 38	0.4	193	0.63	0.9	56
FOTS/γ-Al_2O_3	0 - 38	7.1	112	0.29	n/a	n/a

Furthermore, the crystal structure of pure alumina support and Pd-loaded support was measured with XRD. Figure A2 shows that the diffractogram remains unchanged during catalyst preparation and no palladium diffraction peaks were detected, suggesting that Pd is highly dispersed. Indeed, CO chemisorption (Table 1) confirms high Pd dispersion (56 %) in Pd/γ-Al_2O_3, which is equivalent to an averaged metal particle size of 2 nm. This is also in reasonable agreement with the HRTEM images, shown in Figure 2a as a typical example. The particle size distribution based on multiple micrographs is presented in Figure 2b, resulting in an averaged Pd particle size of 2.2 nm.

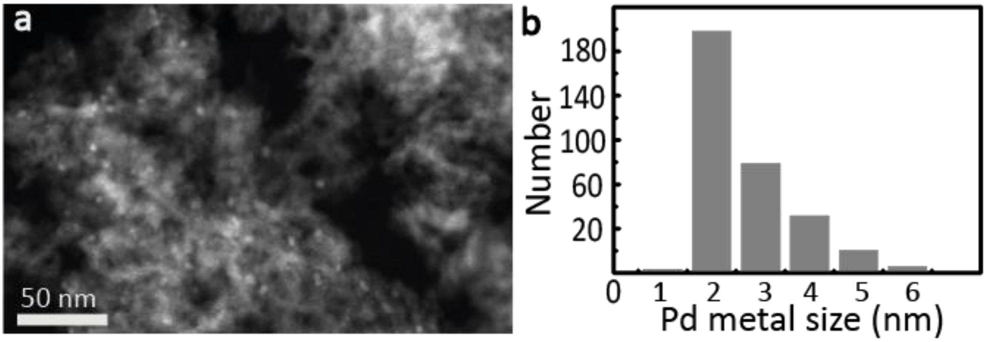

Figure 2. a) TEM image of the Pd/γ-Al_2O_3 catalyst particles, the bright spots are Pd metal particles, b) Pd metal size distribution based on 300 particle sizes.

3.1.2. Parent hydrophobic catalyst: FOTS/γ-Al_2O_3

The hydrophobic alumina particles were prepared via silane functionalization using FOTS. Figure 3a shows that 30 min of reaction of γ-Al_2O_3 with FOTS is already sufficient to saturate the carbon content at about 6.7 wt%. Surface density of FOTS is 3.5 μmol/m^2 as calculated based on equation 3. This is in good agreement with literature [40], indicating that γ-Al_2O_3 has been fully hydrophobized via reaction of FOTS with the hydroxyl groups on the surface of the alumina (see Figure A3).

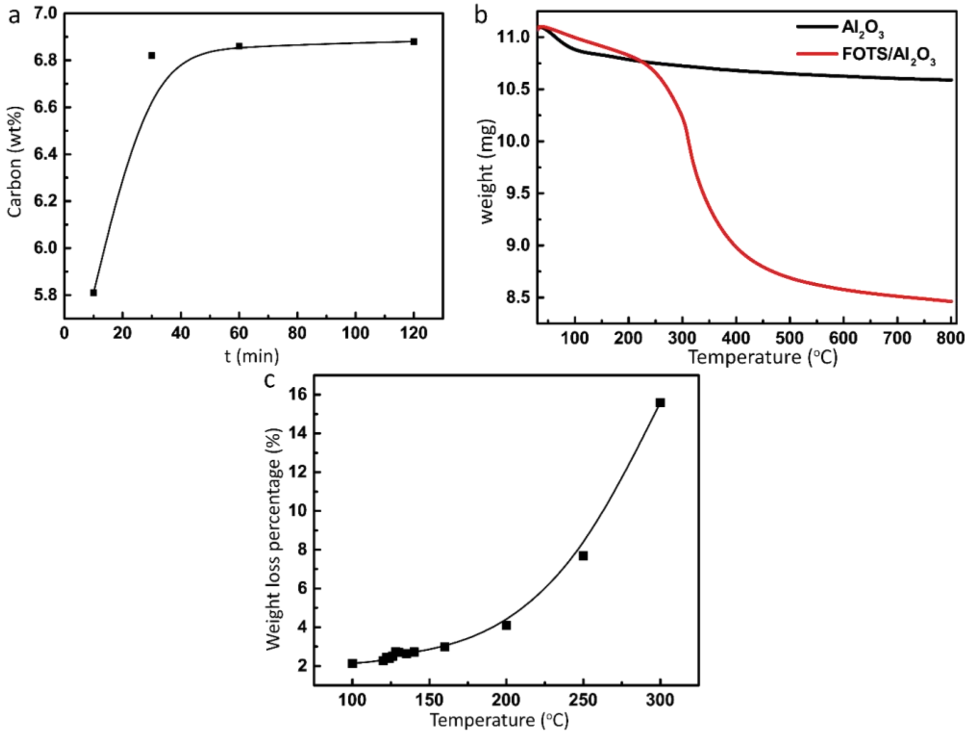

Figure 3. a) Influence of synthesis time on carbon concentration of FOTS/γ-Al_2O_3 measured by elemental analysis, b) TGA profile of FOTS/γ-Al_2O_3 in the temperature range of 25 to 800 ^{o}C (10 ^{o}C/min, 30 mL/min Ar), c) weight loss of FOTS/γ-Al_2O_3 as result of a TGA experiment with different final temperatures (30 mL/min Ar, 10 ^{o}C/min, 1h at final temperature).

The thermal stability of the FOTS was tested with TGA in Ar atmosphere up to 800 ^{o}C. Figure 3b shows the weight loss profile of FOTS/γ-Al_2O_3, showing significant weight loss centered at 300 ^{o}C in contrast with results on bare γ-Al_2O_3. In order to determine the temperature window in which the samples are not affected, TGA experiments were performed using different final temperatures. Figure 3c shows that the weight loss is below 3 % for temperatures below 150 ^{o}C, indicating that the FOTS is stable on the alumina surface at that temperature. Based on these results, the samples were degassed at 135 ^{o}C before N_2-physisorption measurements. The surface area presented in Table 2, obtained with the Brunauer–Emmett–Teller (BET) method, for the FOTS/γ-Al_2O_3 was 112 m^2/g, which is significantly smaller than the surface area of Pd/γ-Al_2O_3. The reduction in the surface area upon FOTS functionalization was also accompanied by a

50 % decrease in pore volume compared to Pd/γ-Al_2O_3 (Table 2), in agreement with the pore-size distribution presented in Figure A4, using the Barrett, Joyner, and Halenda method (BJH). Introduction of FOTS decreases the accessibility of the pores, which are typically smaller than 20 nm, probably due to due to partial pore filling as well as pore blockage [25].

3.1.3. Partially hydrophilic catalyst

The partially hydrophilic catalysts were prepared by mixing hydrophilic Pd/γ-Al_2O_3 and hydrophobic FOTS/γ-Al_2O_3 in different mass ratios (1:0, 4:1, 3:2, 1:1, 2:3 and 1:4; Pd/γ-Al_2O_3: FOTS/γ-Al_2O_3) followed by pelletizing at 4000 bar. The high pressure is intended to create strong mechanical binding between the hydrophilic and hydrophobic materials, minimizing catalyst attrition during reaction. Catalyst particle sizes distribution determined both before and after catalyst testing are presented in Figure A6, confirming that the level of attrition is not significantly influencing the catalytic results. The morphology of the partially hydrophilic catalysts was examined with SEM (Figure 4), showing no differences in morphology between Pd/γ-Al_2O_3 and FOTS/γ-Al_2O_3 particles in Figure 4a and b. In previous work in our group [25] two distinct surface topologies were observed by SEM after palletizing a mixture of Pd supported on γ-Al_2O_3 and FOTS-containing α-Al_2O_3, thanks to the different surface morphologies of the parent materials (e.g. γ- and α-Al_2O_3). Unfortunately, this is not possible for the samples in this study. Notably, inspection at higher magnification of the 20 % partially hydrophilic catalyst (Figure 4c and d) confirms the absence of any macro-porosity between parent particles with maximum size of 38 μm. Similar results were obtained for the 80 % and 50 % hydrophilic catalyst (see Figure A5). The distribution of hydrophilic domains in the catalyst is visualized with Methylene-blue (Figure A5c), wetting exclusively the hydrophilic domains. This confirms the presence of well-distributed hydrophilic domains at the surface of the catalyst particles. The size of the domains is similar to the size of the hydrophilic parent catalyst particles.

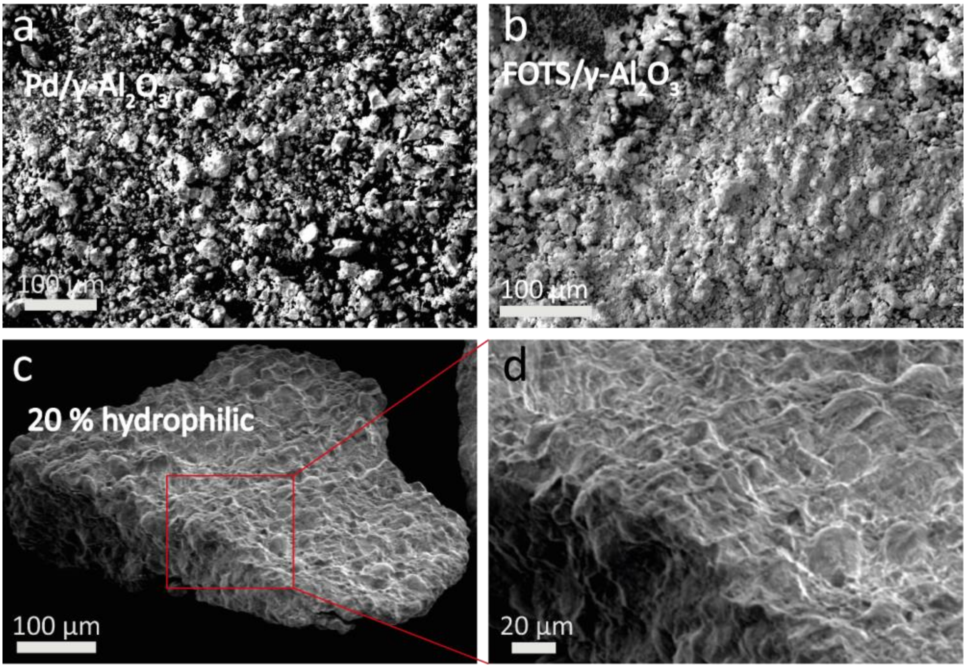

Figure 4. SEM image of a) Pd/γ-Al_2O_3 (0 – 38 µm), b) FOTS/γ-Al_2O_3 (0 – 38 µm), SEM image of a partially hydrophilic catalyst particle (300 – 425 µm) c) mixing 20 % Pd/γ-Al_2O_3 with 80 % FOTS/γ-Al_2O_3, d) the zoom-in of the particles shown in c.

Notably, increasing the content of hydrophobic FOTS/γ-Al_2O_3 leads to decreasing specific surface areas, pore volume and Pd loading and increasing carbon concentration. All these properties change linearly with the fraction of hydrophilic catalyst, as expected assuming the preparation procedure is well controlled and that the 100 - 250 µm fraction has the same composition as the initial mixture of hydrophilic and hydrophobic catalysts (Figure 5). Furthermore, the high-pressure treatment employed to create the partially hydrophilic catalysts did not change the surface area significantly (Table A1), indicating that the support structure was retained.

Figure 6 shows the same trend qualitatively for the contact angle of water droplets measured on the mechanically fabricated pellets of the partially hydrophilic catalysts. The contact angle increases significantly from 40° to 143° with increasing content of the hydrophobic parent domains, confirming that the hydrophobicity of the catalyst can be tuned by simply varying the ratio of Pd/γ-Al_2O_3 and FOTS/γ-Al_2O_3.

Table 3. Characterization of partially hydrophilic catalyst with different ratio and particle size between 100 and 250 μm: BET surface, pore volume, carbon concentration and Pd loading.

sample	BET surface area (m^2/g)	Pore volume (cm^3/g)	Carbon (wt%)	Pd loading (wt%)
100 % hydrophilic	184	0.41	0.4	1.1
80 % hydrophilic	167	0.35	1.4	0.7
50 % hydrophilic	152	0.29	3.4	0.5
20 % hydrophilic	131	0.23	5.5	0.2

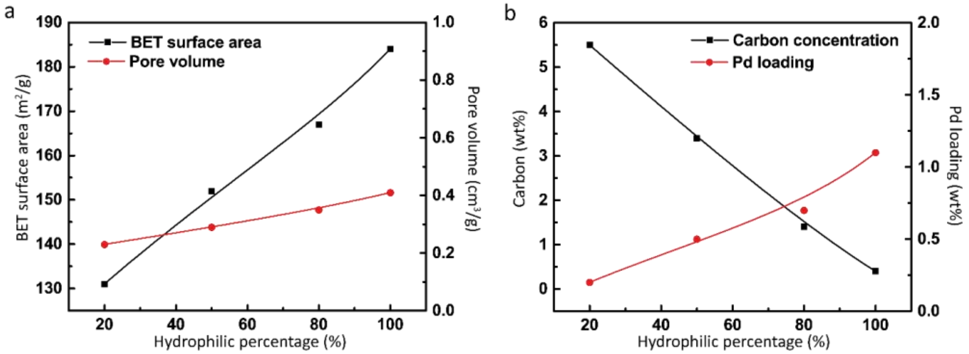

Figure 5. a) BET surface area, pore volume, b) carbon concentration and Pd loading as a function of the percentage of hydrophilicity.

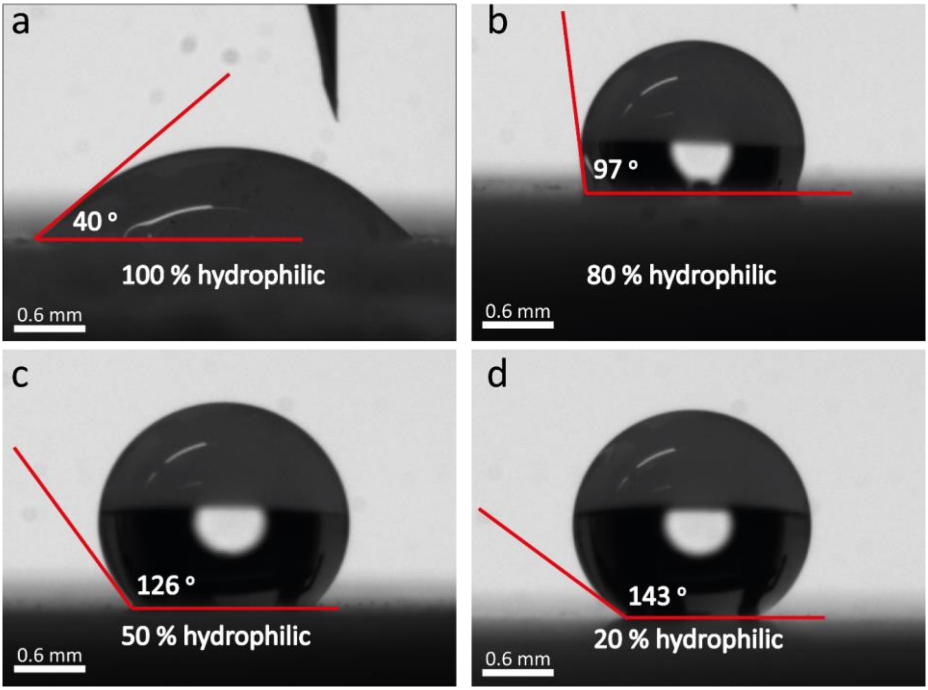

Figure 6. The contact angle pictures, a) fully hydrophilic, b) 80 % hydrophilic, c) 50 % hydrophilic, d) 20 % hydrophilic pelletized samples.

Table 4 shows the carbon concentrations measured on different particle sizes after crushing and sieving. Clearly, the composition of the catalyst does not vary with the particle size, when keeping the ratio of hydrophilic and hydrophobic parent catalyst constant. Thus, all fractions contained the same ratio of hydrophobic and hydrophilic domains, indicating that the particles of the two parent catalysts were homogeneously distributed in the pellet of the partially hydrophilic catalysts, before crushing. Also, the experimental values of the carbon concentration agree very well with the value expected based on the ratio of hydrophilic and hydrophobic parent catalyst.

Table 4. Variation in carbon concentration in partially hydrophilic catalyst with particle size and ratio of hydrophilic and hydrophobic parent catalyst.

Sample	Particle size (μm)			
	100 -250	250 - 300	300 - 425	Theoretical[a]
80 % hydrophilic	1.4	1.4	1.4	1.4
60 % hydrophilic	2.6	2.7	2.7	2.9
50 % hydrophilic	3.4	3.5	3.7	3.6
40 % hydrophilic	4.3	4.3	4.2	4.3
20 % hydrophilic	5.5	5.8	5.8	5.7

a, Theoretical value calculated based on the composition of mixture.

Similar results were obtained based on the Pd content as measured with XRF, as shown in Table 5 for the 80 % hydrophilic catalyst. Although the metal loading was slightly lower than the theoretical value, the variation with particle size is not significant. This confirms that hydrophilic and hydrophobic domains are homogeneously distributed over the fractions with different particles sizes.

Table 5. The distribution of Pd loading in different particles size in 80 % hydrophilic catalyst.

Sample	**Particle size (μm)**			
	100 - 250	250 - 300	300 - 425	Theoretical[a]
80 % hydrophilic	0.7 ± 0.1	0.6 ± 0.1	0.7 ± 0.1	0.88

a, Theoretical value were calculated based on the mixture of the parents ratio (80 %).

3.2. Catalytic performance

Figure 7 (black column) shows that the apparent initial TOF of the fully hydrophilic catalyst decreases with increasing catalyst particle size. Mass transfer limitation is dominating the rate of reaction when the particle size is larger than 100 μm. Calculation of the Weisz-Prater criteria (Table A2) confirms that catalyst particle larger than 100 μm results in severe mass transfer limitation for both hydrogen and nitrite. In contrast, the small catalyst particles are much more active and the Weisz-Prater criterion confirms that the rate is determined by kinetics only. The observed activity, 12 mol*s^{-1}*mol^{-1} Pd$_s$, is in good agreement with our previous work reporting on intrinsic kinetics [41]. The activity also agrees in order of magnitude with other studies, although it should be noted that precise comparison is not possible because of differences in experimental conditions [42,43].

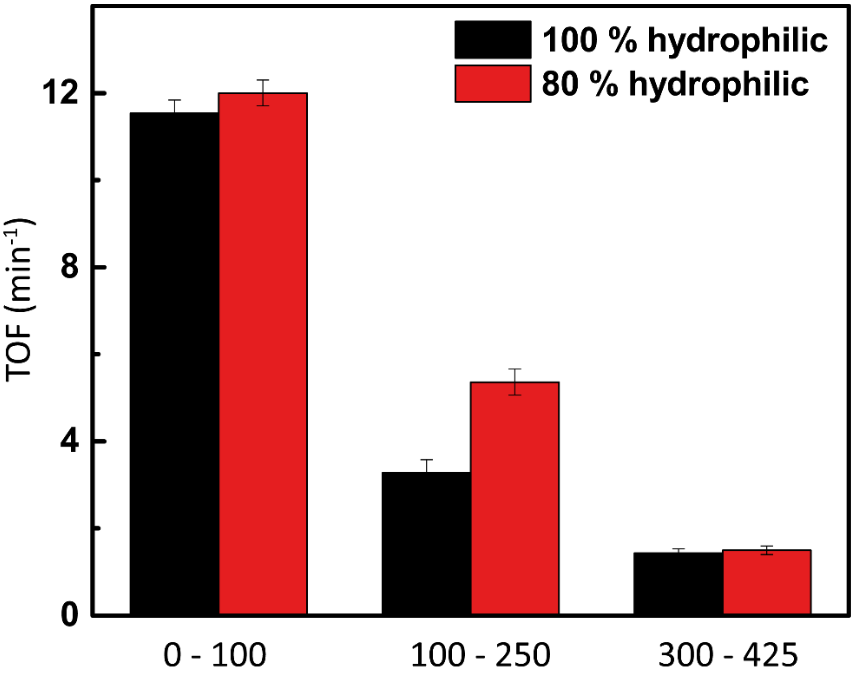

Figure 7. Initial apparent TOF measured on different catalyst particle size for 100 % hydrophilic catalyst and 80 % hydrophilic catalyst (30 mg catalyst, 0.3 mM NO_2^-, 0.8 bar H_2, 0.1 bar CO_2, 20 ^oC).

Figure 7 (red column) shows that the 80 % hydrophilic catalyst with particle size between 100 – 250 µm is significantly more active than the hydrophilic catalyst with the same particle size. No difference in activity is observed between the two types of catalysts with particles smaller than 100 µm, which is easily understood as internal diffusion limitation is not significant and therefore hydrophilic-hydrophobic structuring cannot enhance the reaction rate. This is in agreement with the results of

Franch et al. [25], reporting minor or no effect of similar hydrophilic-hydrophobic structuring on the reaction rate when using catalyst particle size between 40 and 100 µm.

Surprisingly, also the larger particles between 300 and 425 µm show similar activity for fully hydrophilic and partially hydrophobic catalyst. As shown in Figure A5c, the hydrophilic and hydrophobic domains are randomly distributed throughout the catalyst particles. Therefore, we propose that a significant fraction of the hydrophilic Pd/γ-Al_2O_3 domains are completely surrounded by FOTS/γ-Al_2O_3 domains, which cannot contribute to any activity as the active sites are not accessible for nitrite ions. The larger the catalyst particles, the more Pd/γ-Al_2O_3 domains are likely isolated. This adverse effect probably compensates the enhancement of mass transfer, increasing the activity. Therefore, catalysts with the particle size between 100 and 250 µm were selected for further catalytic testing.

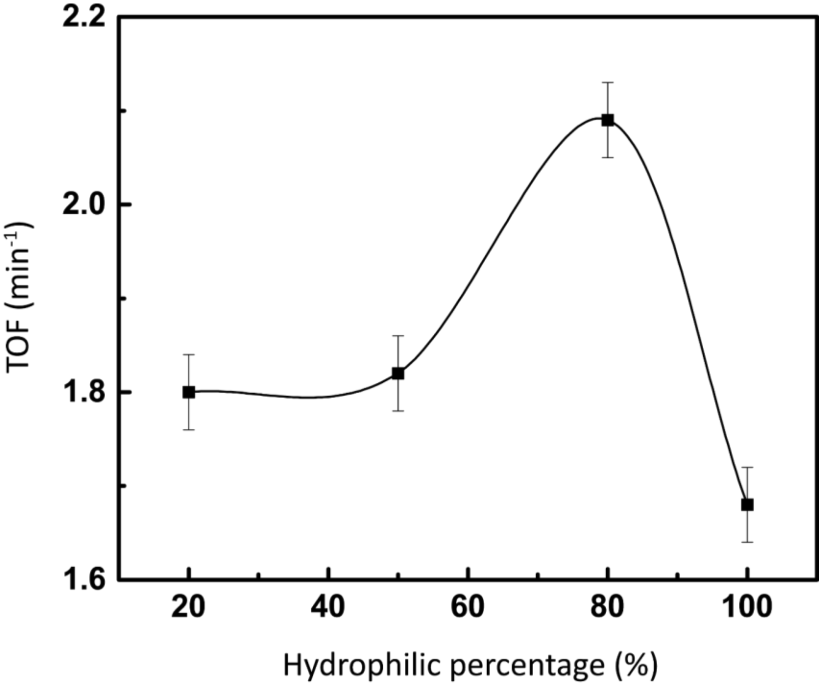

Figure 8. Influence of the percentage of hydrophilicity on the apparent TOF calculated based on initial rate of nitrite conversion for particles in the window 100-250 µm (30 mg catalyst, 1 mM NO_2^-, 0.8 bar H_2, 0.1 bar CO_2, 20 °C).

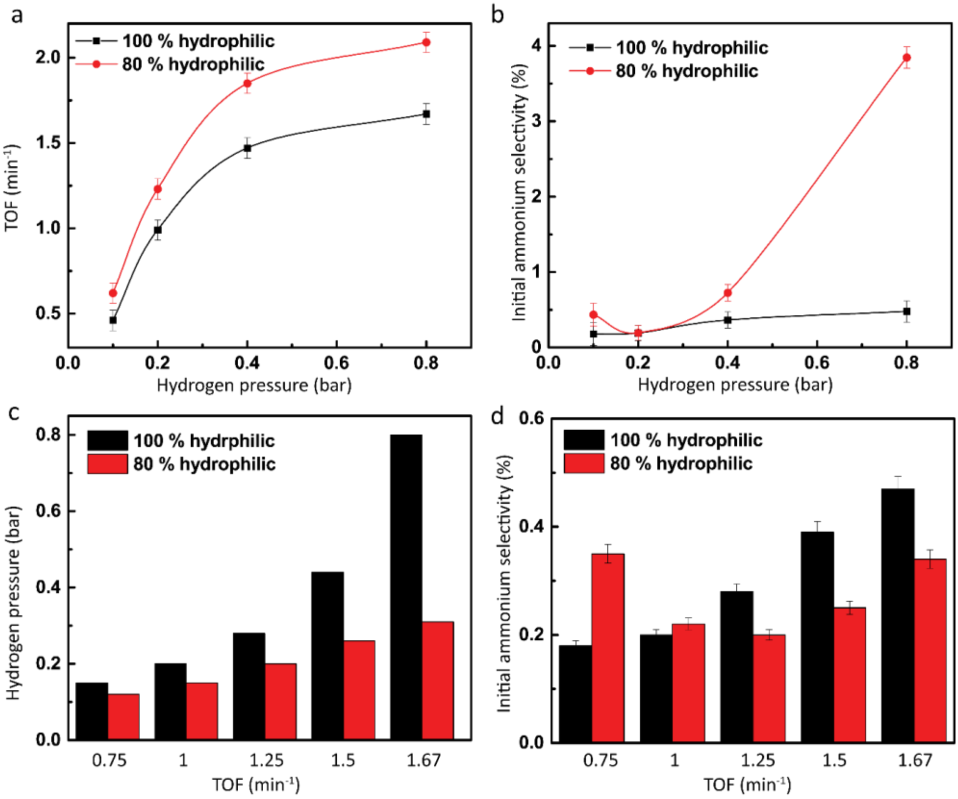

Figure 9. a) Influence of the hydrogen pressure on the initial apparent TOF for 100 % hydrophilic (black line) and 80 % hydrophilic (red line) catalyst, b) initial ammonium selectivity (differential ammonium selectivity) as function of hydrogen pressure for 100 % hydrophilic (black line) and 80 % hydrophilic (red line) catalyst (30 mg catalyst, 1 mM NO_2^-, 0.8 bar H_2, 0.1 bar CO_2, 20 °C), c) the required hydrogen pressures to achieve identical TOF levels on 100 % hydrophilic and 80 % hydrophilic catalyst, d) the resulting ammonium selectivity.

Figure 8 shows the effect of the hydrophilic/hydrophobic ratio on the initial catalytic activity (expressed as apparent TOF, mole nitrite per mole surface Pd), resulting in a volcano-like plot. The error margin is determined by multiple repetition of the experiment with 80 % hydrophilic catalyst. The 80 % hydrophilic catalyst is significantly more active than the fully hydrophilic catalyst. The activity decreases on further decreasing the hydrophilicity to 50 % and 20 %; note that a pure hydrophobic catalyst has no activity because it does not contain any Pd. Nevertheless, all partially hydrophilic catalyst are more active per mole surface-Pd and therefore utilize the active sites better then fully hydrophilic catalysts, which is attributed to enhancement of hydrogen transport to the active sites. The smaller effect on the 20 % and 50 % hydrophilic catalyst is probably caused by flotation during catalyst testing as observed visually. Mal-distribution of the catalyst in the reactor apparently compensates partly the favorable effect of hydrophilic-hydrophobic structuring.

Figure 9a, A8a and A9a show that the 80 % hydrophilic catalyst is noticeable more active than the 100 % hydrophilic catalyst independent of hydrogen pressure, in agreement with Figure 8. Figure 9a, A8a and A9a also show that activity increases with the hydrogen partial pressure for both catalysts, in general agreement with literature [11,21,36,39,44]. Both observations are valid for varying nitrite concentrations, as a result of varying nitrite conversion of 0 %, 20 % and 40 % in respectively Figures 9a, A8a and A9a.

Figure A7 shows experimental results on the formation of ammonium as function of nitrite conversion. The ammonium concentration increases with conversion for all the samples, due to the fact that ammonium cumulates in the batch experiment. Note that a small amount of ammonium is produced at the very beginning of the experiment. The absolute amount is constant, i.e. 0.88 µmol in all experiments. This effect is attributed to the presence of excess hydrogen on the Pd catalyst when starting the experiment by injecting the nitrite solution, as the catalyst is reduced in-situ before. Formation of the observed amount of ammonium requires 15.8 µmol atomic H, which is equivalent to 15 % of the ML capacity. Nevertheless, selectivity to ammonium is less than 5 % in all experiments, in agreement with others studies from our group [45] and by others [42,43], provided that the pH is buffered with CO_2. In contrast, selectivity to ammonium can be as high as 50 % when pH changes during reaction are not buffered [11–13,25,36,44].

In all cases, catalysts for nitrite hydrogenation are tested in slurry batch experiments, resulting in integral ammonium selectivity, i.e. based on the cumulative amount of ammonia formed according equation 5. Continuous operation is clearly favored for practical operation. The performance of a trickle-bed reactor in plug-flow regime is equivalent to a batch reactor, be it that variation in time in the batch reactor is equivalent to variation in residence time along the axis in a fixed bed reactor, under the condition that the hydrogen pressure is constant. In that case, the cumulative selectivity to ammonia is to be considered, after subtraction of the amount of ammonia formed immediately at the start as discussed above. Please note that the integral ammonium selectivity reported in Figure A8c, A8f, A9c and A9f for different nitrite concentration and conversion, have been corrected accordingly.

In case of a continuous stirred tank reactor (CSTR), the selectivity is determined by the conditions in the outlet of the reactor and the selectivity is determined by the ratio of the rates of formation of N_2 and ammonium at those conditions. We term this as differential ammonium selectivity (equation 6). Figure 9b, A8b and A9b present the differential ammonium selectivity as function of the hydrogen pressure at different nitrite conversion level, which is also a measure for the nitrite concentration, calculated according equation 6. Clearly, integral and differential selectivity to ammonia increase with hydrogen partial pressure (Figure 9b, A8b, A8c, A9b, and A9c). Figure A7 shows clearly that the selectivity to ammonia also increases with decreasing nitrite concentration, which can also be seen by comparing Figures 9b, A8b and A9b. These effects can be explained based on NO_2^-/H_2 ratio; higher ratios result in less ammonia formation [25].

Partially hydrophilic catalysts exhibit higher ammonium selectivity, both integral (Figure A8c and A9c) as well as differential (Figure 9b, A8b and A9b) in all cases, due to enhanced hydrogen mass transfer, thus increasing the hydrogen/nitrite ratio. The same trend was observed by Franch et al. [25], despite the smaller catalyst particles used (45 – 100 μm) and absence of any significant effect on activity.

Thus, partly hydrophobizing the catalyst enhances activity, at the expense of undesired increasing selectivity to ammonia. In other words, partly hydrophobic catalyst can achieve the same space-time-yield and equally efficient use of Pd as hydrophilic catalyst at lower hydrogen pressure. We will now discuss whether we can use this phenomenon to suppress ammonia formation in both plug flow reactors and CSTR reactors.

In the case of CSTR operation, considering differential ammonium selectivity, lower hydrogen pressure is sufficient for partially hydrophilic catalyst to achieve the same TOF as hydrophilic catalyst at higher hydrogen pressure (Figure 9c). This effect is the largest when operating at high TOF. Figure 9d presents the selectivity to ammonia for both catalysts when operating at the same TOF, at hydrogen pressures as discussed above. Remarkably, partially hydrophilic catalyst has lower selectivity to ammonium than hydrophilic catalyst when operating at high TOF, i.e. using the Pd catalyst most efficiently. The effect reverts when operating at unfavorable low TOF. Importantly, these effects are observed independent of nitrite conversion, i.e. nitrite concentration (Figure A8d, A8e, A9d and A9e).

A very similar result is obtained when considering operation in a plug flow trickle-bed reactor. Figure A8f and A9f present the integral ammonium selectivity for both catalysts operating at the same TOF, by selecting hydrogen pressures as discussed above. The trends for the integral and differential ammonium selectivity are similar. Thus, also in this case the partially hydrophilic catalyst produces less ammonium compared to hydrophilic catalyst, when operating at high TOF.

Qualitatively, this result can be understood by considering that internal concentration gradients are more dominant in hydrophilic supports. Operation at high apparent TOF then requires high hydrogen pressure, which causes high selectivity to ammonium, especially at the outer shell of the catalyst particles. In contrast, a partly hydrophilic catalyst develops less internal concentration gradients, lower hydrogen concentration is required to achieve the same activity and especially the outer shell of the catalyst operates at much lower hydrogen concentration. The result is a decreased selectivity to ammonium. This work demonstrates that it is possible to manipulate the performance of supported catalysts in three-phase operation in water, via structuring the catalysts in terms or wettability, both at the internal and external surface of the support. Additional work is required to use the same principle in combination with other solvents.

5. Conclusion

Catalysts containing hydrophilic and hydrophobic domains have been prepared with well controlled ratio of the amount of hydrophobic domains and hydrophilic domains, independent of the particle size. Noticeably, the partially hydrophilic catalyst is more active and produces more ammonium compared to hydrophilic catalyst. This demonstrates that internal concentration gradients are indeed influenced. For the case of nitrite hydrogenation, we conclude that structured catalysts achieve the same rate per gram Pd at lower hydrogen pressure compared to classical hydrophilic catalysts. This results in formation of less ammonia, which is of practical importance for cleaning of drinking water.

Reference

[1] A. J. Lecloux, *Catal. Today* **1999**, *53*, 23–34.

[2] V. Matějů, S. Čižinská, J. Krejčí, T. Janoch, *Enzyme Microb. Technol.* **1992**, *14*, 170–183.

[3] G. Gulis, M. Czompolyova, J. R. Cerhan, *Environ. Res.* **2002**, *88*, 182–187.

[4] S. Hôrold, T. Tacke, K. D. Vorlop, *Environ. Technol. (United Kingdom)* **1993**, *14*, 931–939.

[5] A. Kapoor, T. Viraraghavan, *J. Environ. Eng.* **1997**, *123*, 371–380.

[6] J. Martínez, A. Ortiz, I. Ortiz, *Appl. Catal. B Environ.* **2017**, *207*, 42–59.

[7] H. O. N. Tugaoen, S. Garcia-Segura, K. Hristovski, P. Westerhoff, *Sci. Total Environ.* **2017**, *599–600*, 1524–1551.

[8] S. Tyagi, D. Rawtani, N. Khatri, M. Tharmavaram, *J. Water Process Eng.* **2018**, *21*, 84–95.

[9] E. E. A. (EEA), **2002**.

[10] A. Bothner-By, L. Friedman, *J. Chem. Phys.* **1952**, *20*, 459–462.

[11] A. Pintar, G. Berčič, J. Levec, *AIChE J.* **1998**, *44*, 2280–2292.

[12] J. K. Chinthaginjala, L. Lefferts, *Appl. Catal. B Environ.* **2010**, *101*, 144–149.

[13] J. K. Chinthaginjala, J. H. Bitter, L. Lefferts, *Appl. Catal. A Gen.* **2010**, *383*, 24–32.

[14] H. C. Aran, J. K. Chinthaginjala, R. Groote, T. Roelofs, L. Lefferts, M. Wessling, R. G. H. H. Lammertink, *Chem. Eng. J.* **2011**, *169*, 239–246.

[15] Y. Zhao, J. A. Baeza, N. Koteswara Rao, L. Calvo, M. A. Gilarranz, Y. D. Li, L. Lefferts, *J. Catal.* **2014**, *318*, 162–169.

[16] R. Brunet Espinosa, L. Lefferts, *ACS Catal.* **2016**, *6*, 5432–5440.

[17] J. J. F. Scholten, in *Stud. Surf. Sci. Catal.*, **1979**, pp. 685–714.

[18] A. Obuchi, S. Naito, T. Onishi, K. Tamaru, *Surf. Sci.* **1982**, *122*, 235–255.

[19] S. B. Oblath, S. S. Markowitz, T. Novakov, S. G. Chang, *Inorg. Chem.* **1983**, *22*, 579–583.

[20] T.Tacke, *Tech. Univ. Carolo-Wilhelmina* **1991**, DOI http://dx.doi.org/10.1016/0039-6028(91)90317-L.

[21] J. Wärn, I. Turunen, T. Salmi, T. Maunula, *Chem. Eng. Sci.* **1994**, *49*, 5763–5773.

[22] E. E. A. (EEA), **2002**, DOI http://dx.doi.org/10.1016/0039-6028(91)90317-L.

[23] M. Vospernik, A. Pintar, G. Berčič, J. Levec, *J. Memb. Sci.* **2003**, *223*, 157–169.

[24] K. T. Ranjit, B. Viswanathan, *J. Photochem. Photobiol. A Chem.* **1997**, *108*, 73–78.

[25] C. Franch, R. G. H. Lammertink, L. Lefferts, *Appl. Catal. B Environ.* **2014**, *156–157*, 166–172.

[26] Y. Zhao, L. Jia, J. A. Medrano, J. R. H. Ross, L. Lefferts, *ACS Catal.* **2013**, *3*, 2341–2352.

[27] A. M. Bergquist, M. Bertoch, G. Gildert, T. J. Strathmann, C. J. Werth, *J. Am. Water Works Assoc.* **2017**, *109*, E129–E143.

[28] H. C. Aran, S. Pacheco Benito, M. W. J. Luiten-Olieman, S. Er, M. Wessling, L. Lefferts, N. E. Benes, R. G. H. Lammertink, *J. Memb. Sci.* **2011**, *381*, 244–250.

[29] V. Hessel, P. Angeli, A. Gavriilidis, H. Löwe, *Ind. Eng. Chem. Res.* **2005**, *44*, 9750–9769.

[30] M. J. Geerken, T. S. van Zanten, R. G. H. Lammertink, Z. Borneman, W. Nijdam, C. J. M. van Rijn, M. Wessling, *Adv. Eng. Mater.* **2004**, *6*, 749–754.

[31] A. Quintanilla, J. J. W. W. Bakker, M. T. Kreutzer, J. A. Moulijn, F. Kapteijn, *J. Catal.* **2008**, *257*, 55–63.

[32] C. Grote, M. Rosu, A. Schumpe, *Can. J. Chem. Eng.* **2010**, *88*, 633–637.

[33] H. Yang, X. Jiao, S. Li, *Chem. Commun.* **2012**, *48*, 11217–11219.

[34] A. Perro, F. Meunier, V. Schmitt, S. Ravaine, *Colloids Surfaces A Physicochem. Eng. Asp.* **2009**, *332*, 57–62.

[35] J. Faria, M. P. Ruiz, D. E. Resasco, *Adv. Synth. Catal.* **2010**, *352*, 2359–2364.

[36] R. Brunet Espinosa, D. Rafieian, R. S. Postma, R. G. H. Lammertink, L. Lefferts, *Appl. Catal. B Environ.* **2018**, *224*, 276–282.

[37] S. D. Ebbesen, B. L. Mojet, L. Lefferts, *J. Catal.* **2008**, *256*, 15–23.

[38] R. Zhang, D. Shuai, K. A. Guy, J. R. Shapley, T. J. Strathmann, C. J. Werth, *ChemCatChem* **2013**, *5*, 313–321.

[39] I. Mikami, Y. Sakamoto, Y. Yoshinaga, T. Okuhara, *Appl. Catal. B Environ.* **2003**, *44*, 79–86.

[40] U. Hanefeld, L. Lefferts, *Focus Catal.* **2017**, *2017*, 7.

[41] P. Xu, S. Agarwal, L. Lefferts, *J. Catal.* **2020**, *383*, 124–134.

[42] D. Shuai, J. K. Choe, J. R. Shapley, C. J. Werth, *Environ. Sci. Technol.* **2012**, *46*, 2847–2855.

[43] F. Deganello, L. F. Liotta, A. Macaluso, A. M. Venezia, G. Deganello, *Appl. Catal. B Environ.* **2000**, *24*, 265–273.

[44] R. S. Postma, R. Brunet Espinosa, L. Lefferts, *ChemCatChem* **2018**, *10*, 3770–3776.

[45] Y. Zhao, N. Koteswara Rao, L. Lefferts, *J. Catal.* **2016**, *337*, 102–110.

Appendix

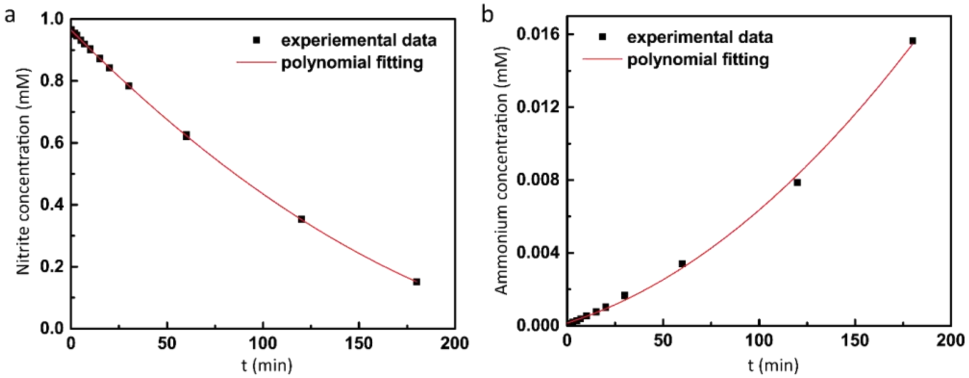

Figure A1. a) Nitrite concentration, b) ammonium concentration as a function of time obtained in slurry reactor with Pd/γ-Al_2O_3, initial nitrite concentration 1 mM and 0.8 bar hydrogen pressure; the red line represents polynomial fitting which is used to calculated the differential rate of nitrite and ammonium at different nitrite conversion level.

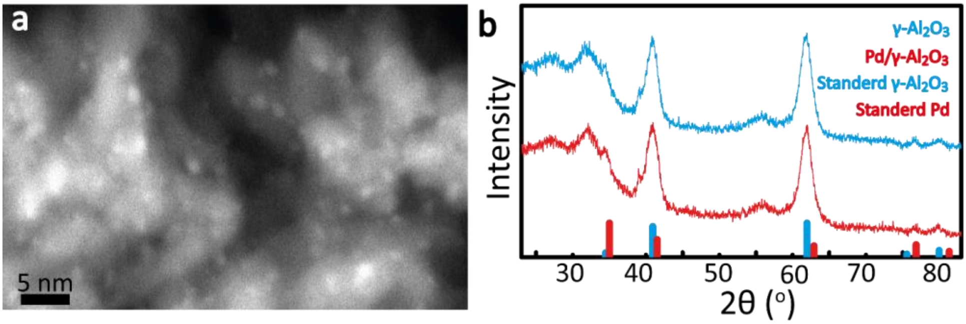

Figure A2. a) TEM image of the Pd/γ-Al_2O_3 catalyst particles, the white dots are Pd metal particles, b) XRD spectrum of pure γ-Al_2O_3 (blue line), and Pd/γ-Al_2O_3 (red line).

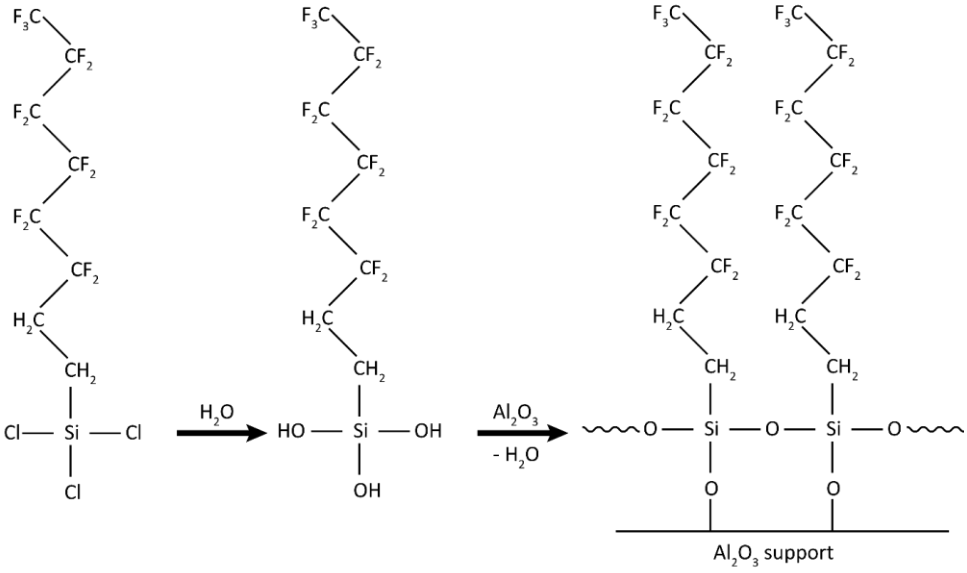

Figure A3. Surface mechanism of FOTS monolayer adsorption.

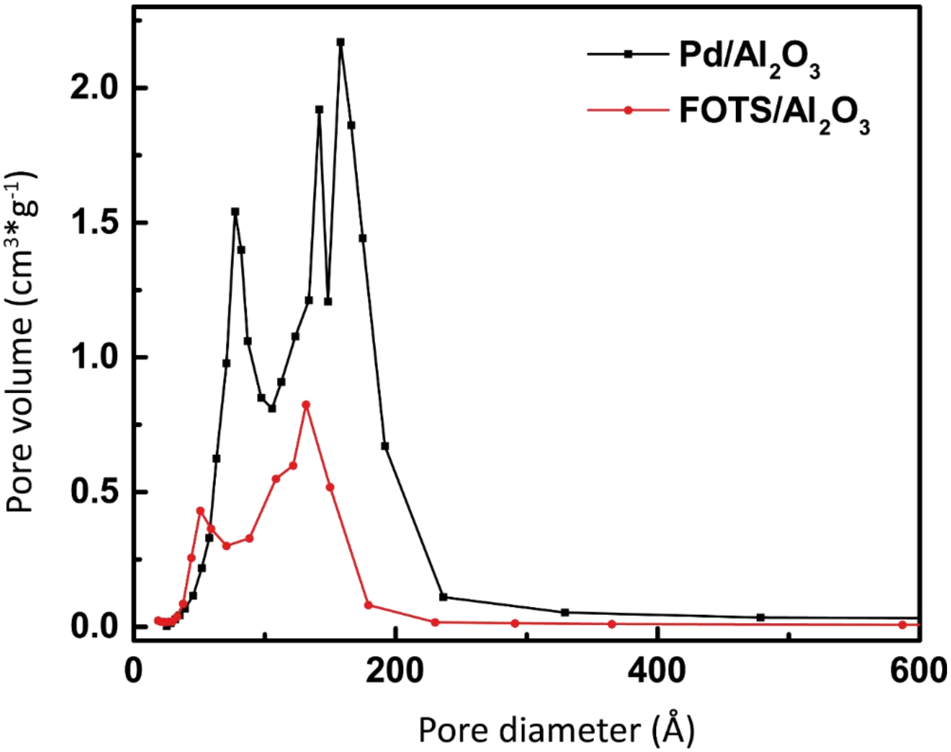

Figure A4. a) The plot of desorption information for FOTS/γ-Al_2O_3, b) the plot of desorption information for Pd/γ-Al_2O_3 obtained by BJH-method using desorption data.

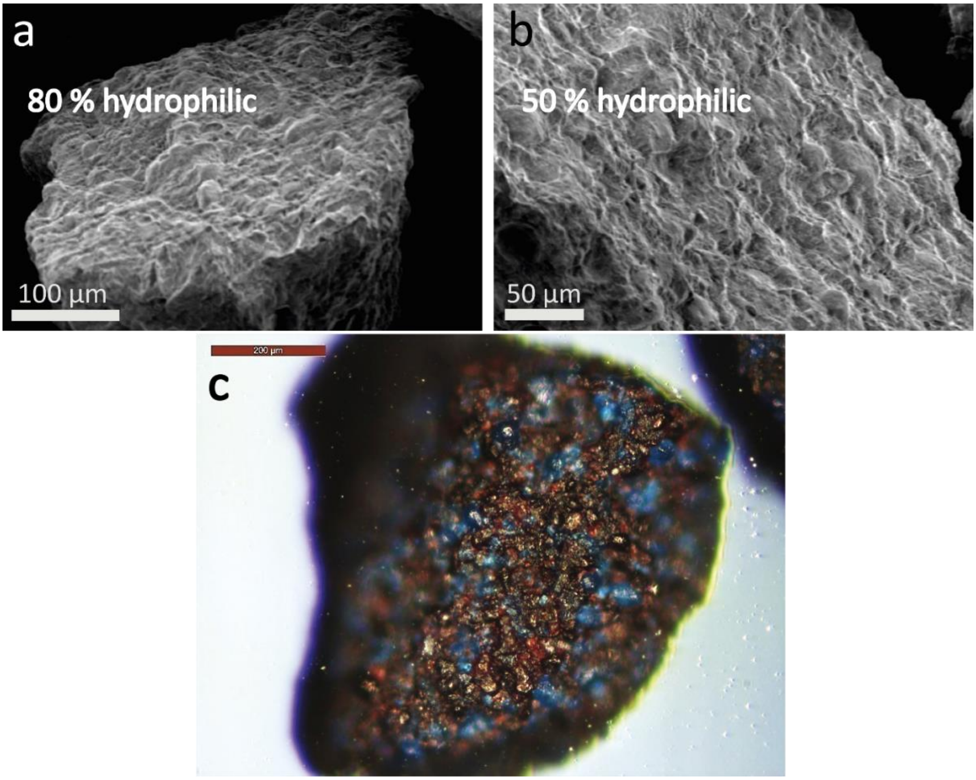

Figure A5. SEM image of a partially hydrophilic catalyst with particle size between 300 and 425 µm; a) mixing by 80 % Pd/γ-Al_2O_3 with 20 % FOTS/γ-Al_2O_3, b) mixing 50 % Pd/γ-Al_2O_3 with 50 % FOTS/γ-Al_2O_3, c) the picture is taken by the optical microscopy, one 50 % hydrophilic catalyst (300 – 425 µm) coloring with methylene blue.

Table A1. The surface area of the catalyst particles before and after pelletization, breaking and sieving.

Sample	Palletization, breaking and sieving	BET surface area (m^2/g)
Pd/γ-Al_2O_3_0-45 µm	before	193
Pd/γ-Al_2O_3 _0-45 µm	after	189

As shown in Table A1, the surface area of the catalysts are not influence by the high pressure press. So the structure of the support is maintain the same as before.

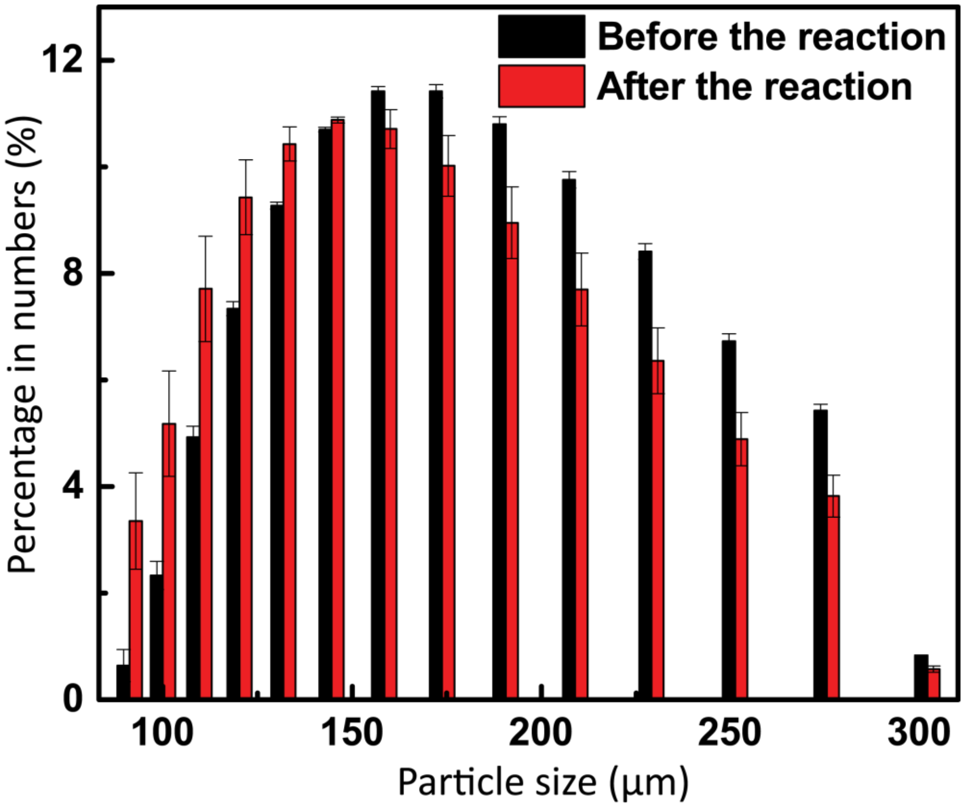

Figure A6. The catalyst particle size distribution before and after reaction for 100 – 250 μm range determined with DLS.

As shown in Figure A6, the particle size distribution are not much influenced by the reaction. So the structure of the catalyst is maintain the same structure as before.

Mass transfer checking

Weisz-Prater criterion

Weisz-Prater criterion is normally used as the criteria to estimate whether pore diffusion resistance can significantly influence the reaction rate [1].

$$C_{wp} = \frac{R_{obv} \times L^2 \times \rho_{Cat}}{C_s \times D_{eff}} \qquad eq\ 8$$

Where R_{obv} is the reaction rate per mass of catalyst (mol*s^{-1}*kg^{-1}), L is the catalyst particle radius (m), ρ_{Cat} is the density of the catalyst particles (kg*m^{-3}), C_s is the reactant concentration at the particle surface (mol*m^{-3}), and D_{eff} is the effective diffusivity (m^2*s^{-1}).

$$L = \frac{d_p}{3} \qquad eq\ 9$$

$$D_{eff} = \frac{D_{AB} \times \phi}{\tau} \qquad eq\ 10$$

In which d_p is radius of the catalyst particles, D_{AB} is the bulk diffusion coefficient of species, ϕ is the particle porosity, normally between 0.2 and 0.7, based on the BET measurement, here we get 0.7, and τ is the tortuosity, normally varies between 1 and 10, here we choose 3.

If there is no obvious diffusion limitations: $C_{wp} < 1$

However, if there is severe diffusion limitations: $C_{wp} > 1$

In Table A2, shown the calculation of the Weize-Prater criterion for different catalyst particles size.

Table A2. The calculation of Weisz-Prater criterion on different size of hydrophilic catalyst.

Particle size (µm)	Weisz-Prater (nitrite)	Weisz-Prater (hydrogen)
0 - 38	0.8	0.2
38 - 45	3.5	0.9
45 - 100	7.3	1.9
100 - 250	12.1	3.2
250 - 300	20.4	5.5
300 - 425	22.7	6.1

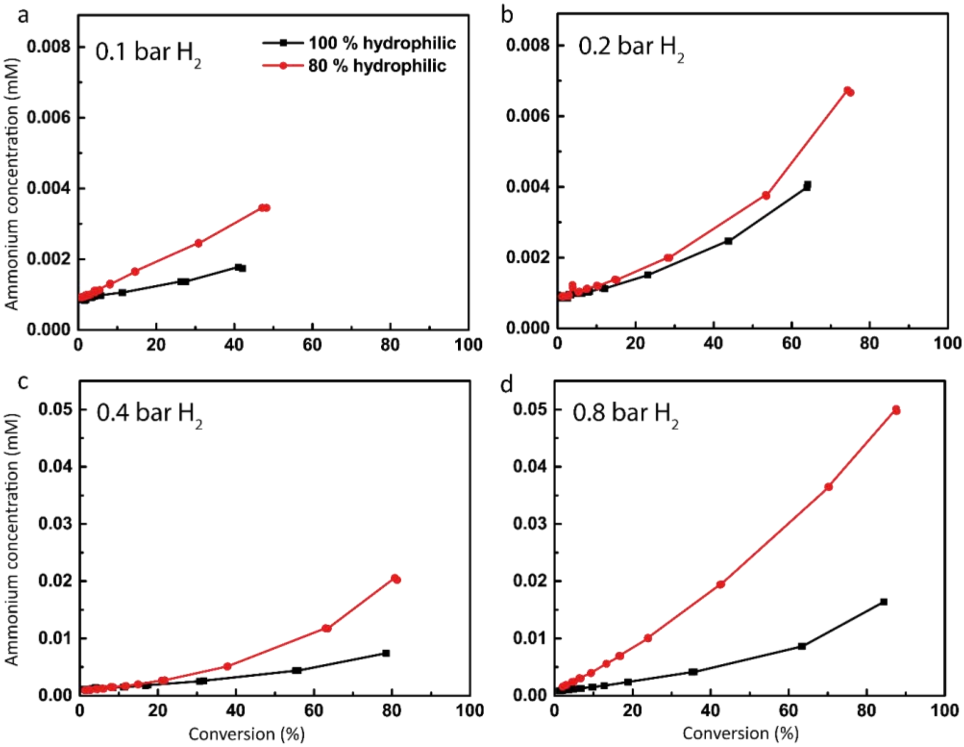

Figure A7. a-d) Ammonium selectivity as a function of nitrite conversion at varying hydrogen pressure for 100 % hydrophilic (black line) and 80 % hydrophilic (red line) catalyst (30 mg catalyst, 1 mM NO_2^-, 0.8 bar H_2, 0.1 bar CO_2, 20 °C).

Table A3. Checking the initial ammonium formation.

Initial ammonium formation (mM)	0.00088
Required amount of H atom to form initial ammonium (mol)	1.58E-05
Amount of catalyst used per experiment (mg)	30
Pd loading (wt%)	0.9
Pd dispersion (%)	56
Available Pd (mol)	1.14E-04
Available H atom (mol)	1.14E-04

According to the calculation, the amount of the hydrogen atom formed due to the in-situ pretreatment is enough to form the amount of initial ammonium. So it is logical to believe that the initial ammonium formation is caused by the in-situ reduction which is not the results of the steady experiment, so it is necessary to subtract the initial amount of ammonium.

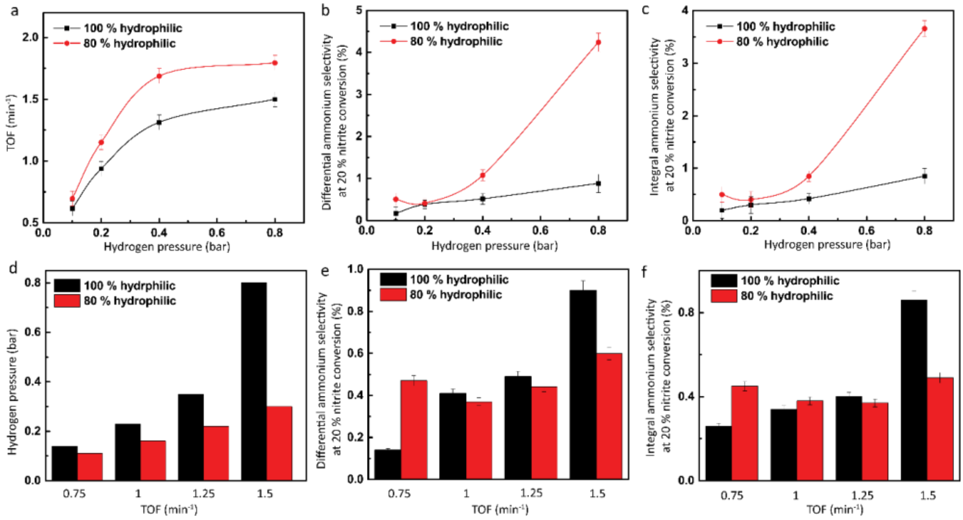

Figure A8. a) Influence of the hydrogen pressure on the apparent TOF at 20 % nitrite conversion (0.8 mM nitrite) for 100 % hydrophilic (black line) and 80 % hydrophilic (red line) catalyst, b) differential ammonium selectivity and c) integral ammonium selectivity at 20 % nitrite conversion as function of hydrogen pressure for 100 % hydrophilic (black line) and 80 % hydrophilic (red line) catalyst (30 mg catalyst, 1 mM NO_2^-, 0.8 bar H_2, 0.1 bar CO_2, 20 °C), d) the required hydrogen pressures to achieve identical TOF levels on 100 % hydrophilic and 80 % hydrophilic catalyst, e) the resulting differential ammonium selectivity and f) integral ammonium selectivity. Note that integral selectivity data were corrected for initial formation of ammonium.

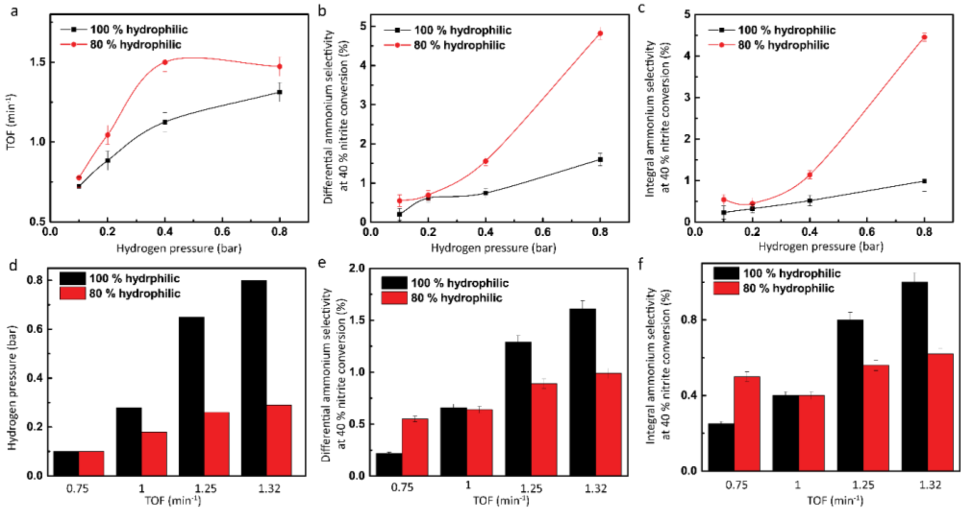

Figure A9. a) Influence of the hydrogen pressure on the apparent TOF at 40 % nitrite conversion (0.6 mM nitrite) for 100 % hydrophilic (black line) and 80 % hydrophilic (red line) catalyst, b) differential ammonium selectivity and c) integral ammonium selectivity at 40 % nitrite conversion as function of hydrogen pressure for 100 % hydrophilic (black line) and 80 % hydrophilic (red line) catalyst (30 mg catalyst, 1 mM NO_2^-, 0.8 bar H_2, 0.1 bar CO_2, 20 °C), d) the required hydrogen pressures to achieve identical TOF levels on 100 % hydrophilic and 80 % hydrophilic catalyst, e) the resulting differential ammonium selectivity and f) integral ammonium selectivity. Note that integral selectivity data were corrected for initial formation of ammonium.

Reference

[1] D. Shuai, J. K. Choe, J. R. Shapley, C. J. Werth, *Environ. Sci. Technol.* **2012**, *46*, 2847–2855.

Chapter 4

Effect of oxygen on formic acid decomposition over Pd catalyst

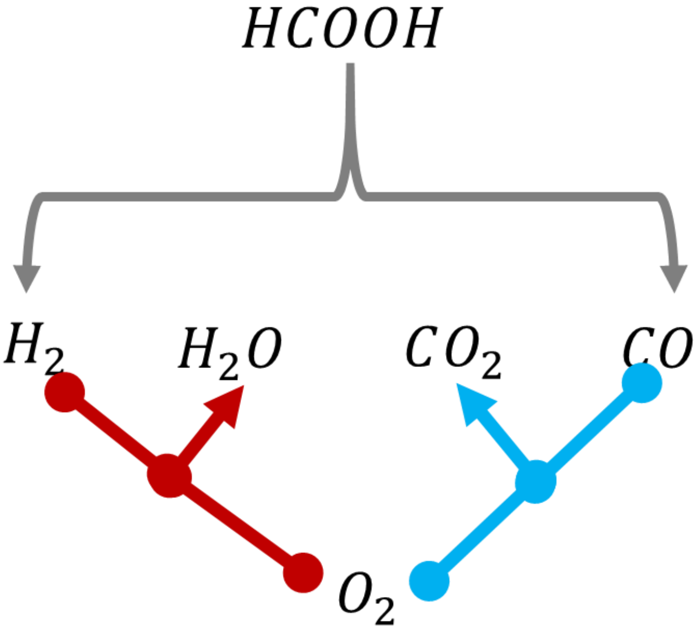

Abstract:

It is well known that Pd based catalyst deactivate during formic-acid decomposition in aqueous phase at mild temperatures, which is explained by CO poisoning. This study shows that deactivation of Pd/γ-Al_2O_3 catalysts can be suppressed by adding traces of oxygen, assigned to removal of CO by oxidation to CO_2. The activity of the catalyst during operation is maintained, promoting the H_2 production compared to operation is absence of any oxygen. Clearly, oxygen mainly oxidizes CO instead of H_2 under the condition that the oxygen concentration is kept below 0.1 vol%, under the conditions in this study. Further increasing the oxygen concentration up to 2 vol% still increases conversion rate of formic-acid but also decreases the hydrogen yield significantly because formic-acid oxidation becomes dominating. The results of this study are important because the effect of traces of oxygen form ambient has not been considered in the majority of the reports in literature.

1. Introduction

In times of fossil fuel resources shortage, the search for alternative and sustainable energy sources has become more pressing than ever. Hydrogen has attracted an increasing level of attention as an important energy vector and may play a very significant role in power distribution in the future. However, due to the extremely low critical point and very low density of hydrogen gas, it is particularly difficult to store efficiently, especially on long term. Many molecules have been proposed as hydrogen carriers, e.g. ammonia [1], methanol [2], methane [3] as well as higher hydrocarbons [4]. Another option is formic-acid which can be produced from CO_2 and green hydrogen [5–7], resulting in a carbon-neutral process. Hydrogenation of CO_2 to formic-acid requires either high pressure or operation in aqueous solution, preferably at basic conditions, because of thermodynamic limitations [6]. Formic-acid is a low-toxic chemical that can be easily stored, transported and handled. In addition, formic-acid is a significant by-product from biomass conversion. This work focusses on using liquid-phase formic-acid as a hydrogen storage material.

Obviously, in order to make the stored hydrogen available, formic-acid needs to be decomposed to CO_2 and H_2 according equation 1. Homogeneous catalysts for formic-acid decomposition have been intensively studied [5,8,9]. Unfortunately, separation of the dissolved catalyst and the use of organic solvents, ligands and additives complicate the design of suitable devices [10]. Therefore, application of heterogeneous catalysts is preferred. Previous studies on heterogeneous catalysis have been performed in gas phase, requiring elevated temperatures [11–13] and operation in aqueous phase at mild temperatures might be advantageous. Various Pd based mono- [14], bi- [15] and tri-metallic [16] catalysts have been identified as most active at low temperature and also resulting in high H_2 selectivity. The main drawback of these Pd-based catalyst operated at mild temperature is poisoning by CO, which is formed via the dehydration reaction [17–20], according equation 2.

$$HCOOH\ (l) \rightarrow CO_2(g) + H_2\ (g)\ \Delta G = -48.4\ kJ/mol\ ,\ \Delta H = 31.21\ kJ/mol \qquad eq1$$

$$HCOOH\ (l) \rightarrow CO(g) + H_2O\ (l)\ \ \Delta G = -28.5\ kJ/mol\ ,\ \Delta H\ = 28.40\ kJ/mol \qquad eq2$$

So far, all heterogeneous catalysts studies suffer from deactivation to some extent. However, the deactivation mechanism is still under debate. Ruthven et al. [21] proposed that deactivation is due to formation of palladium hydride, supposedly β-Pd hydride, which is not active. Hu et al. [22] suggested that catalyst deactivation is caused by occupation of active sites by protons, CO_2, H_2O and HCOO intermediate species. However, CO poisoning [17,19,20,23] is proposed most frequently to cause catalyst deactivation. CO adsorbs much more strongly on Pd than H_2 and CO_2, considering adsorption enthalpies of 150 kJ/mol for CO [24] at low coverage, versus 100 kJ/mol [25] and 80 kJ/mol [26] for H_2 and CO_2, respectively. Jiang et al. [18] confirmed presence of chemisorbed CO during formic-acid decomposition, using ATR-IR spectroscopy.

CO adsorbed on Pd reacts easily with oxygen at room temperature forming CO_2 in aqueous phase as e.g. observed with ATR-IR [27]. Therefore it may be expected presence even traces of oxygen would influence the formic-acid decomposition reaction. It is remarkable that in several studies on formic-acid decomposition in aqueous phase, the gas composition in the reactor is not clearly defined [18,20,28–33], while other studies were performed in a reactor open to ambient [14,34–38]. Only in a few studies oxygen was rigorously removed [21,39,40], but the influence of the oxygen concentration on formic-acid decomposition has not been reported yet. This study reports on the influence of oxygen on rate, selectivity and deactivation in formic-acid decomposition over Pd catalysts.

2. Experimental section

2.1. Materials

Commercial γ-Al_2O_3 powder purchased from BASF, characterized by a surface area of 195 m^2/g, was used as catalyst supports in this study. Tetraamminepalladium (II) nitrate solution (10 wt. % in H_2O, 99.99 %) was purchased in Sigma-Aldrich was used as catalyst precursor solution. Ammonium (50 % v/v water) was obtained from Sigma-Aldrich. Formic-acid (≥ 98 %) and sodium hydroxide was purchased from Sigma-Aldrich. Pre-mixed O_2 in Ar (0.1 vol%) was purchased from Linde. All the aqueous solutions were prepared using ultra purified water obtained with a water purification system (Millipore, Synergy).

2.2. Catalyst preparation

The Pd/γ-Al_2O_3 catalyst containing 1 wt% of palladium, was prepared by wet impregnating method. The method was described in elsewhere [41,42]. In brief, 10 g of the sieved support (size less than 20 μm) was calcined at 600 °C in air for 4 hours to remove any organic pollutions. Then the support was suspended in 100 mL millQ water, the pH of the solution was adjusted by adding 2 mL ammonia solution to maintain the pH around 9, checked with a pH meter in order to ensure electrostatic interaction of $Pd(NH_3)_4^{2+}$ with the negatively charged alumina surface. Then 3 g of the original palladium precursor solution ($Pd(NO_3)_2 \cdot 4NH_3$) was added in the suspension slowly and stirred at room temperature for at least 1 hour. Further, the solution was transferred to the rotary evaporator to remove the liquid during 2 h at 70 °C. Then the catalyst was calcined in air at 400 °C for 3 h (5 K/min), switched to N_2 gas for 20 min, followed by reduction in 50 vol% hydrogen diluted in nitrogen (total flow rate 60 mL/min) at the same temperature for 3 h.

2.3. Catalyst characterization

The BET surface area of the catalyst, degassed at 300 °C for 1 day, was determined with N_2-adsorption at 77 K (Micromeritics Tristar). The Pd loading on the alumina support was determined with X-ray fluorescence spectroscopy (XRF, Philips PW 1480). The metal surface area that is accessible was determined with CO chemisorption at room temperature (Chemisorb 2750, Micromeritics). Typically, the sample was reduced at room temperature in hydrogen for 1 h and flushed with He at the same temperature for 0.5 h. Then, CO was introduced as pulses and the response was recorded using a TCD detector. Pd particle sizes are estimated assuming hemispherical metal particles and assuming that the stoichiometric ratio of adsorbed CO and Pd surface atoms is one. X-ray photoelectron spectroscopy (XPS) was conducted by an Omicron Nanotechnology GmbH (Oxford Instruments) surface analysis system with a photon energy of 1486.7 eV (Al Kα X-ray source) with a scanning step size of 0.1 eV and a pass energy of 20 eV. Due to the poor electrical conductivity of sample surface, it is necessary to neutralize charge on the sample with an electron spray. The spectra were corrected using the binding energy of C 1s peak as a reference.

2.4. Catalytic tests

Activity and selectivity of the catalysts were measured in a 1 L batch reactor operated at 20 ^{o}C at atmospheric pressure. The glass reactor (DURAN® BAFFLED, WIDE MOUTH BOTTLE GLS 80®) has a diameter of 10.1 cm and height 22.2 cm (see **Chapter 2** Figure A1). The reactor has four connections on the reactor lid for gas-in, gas-out, sampling and a stirring shaft equipped with 4 stirring blades (**Chapter 2**, Figure A1).

Typically, 0.1 gram catalyst was suspended in 0.3 L milli-Q water and stirred at 625 rpm while flushing with a mixture gas of Ar and oxygen (between 0 and 2 vol% oxygen) with a flow rate of 50 mL/min for at least one hour to remove any gasses dissolved in the water and gas in the 700 ml gas cap. The reaction was started by introducing 60 μL pure formic-acid solution. The initial pH was varied between 2 and 10 by adding the appropriate amount of sodium hydroxide (1 M solution) to the formic-acid solution. The stability experiments were performed by injecting additional 15 μL pure formic-acid, one hour after the first injection. This procedure was repeated three times.

The procedure described above includes experiments in Ar, in absence of any oxygen and this experiment is termed as inert-experiment. In addition, a semi-inert-experiment was conducted while flowing pure Ar (50 mL/min), like in the inert experiment, with the difference that the gas pipe was positioned above the liquid level so that dissolved oxygen as well as gasses produced during the experiment are very slowly removed from the water phase.

Samples were taken at different reaction times using a 2.5 mL syringe (BD Plastipak) and filtered through a syringe filter (PTFE, 0.2 µm, Whatman) in order to remove the catalyst. Formic-acid concentrations were measured with ion-chromatography (DIONEX, ICS 3000) equipped with an Ultimate autosampler. The gas products were measured with an online micro-GC, sampling every 5 minutes, measuring the concentrations of H_2, CO_2 and CO. The amounts of H_2, CO_2 and CO was calculated in moles based on the H_2, CO_2 and CO concentration profile as obtained with GC, the Ar gas-flow-rate and integrated over time.

Formic-acid conversion and H_2, CO_2, CO yield were calculated according to equation 3, 4, 5 and 6, respectively.

$$HCOOH\ conversion = \frac{n_{HCOOH,t0} - n_{HCOOH,t1}}{n_{HCOOH,t0}} * 100 \qquad eq\ 3$$

$$H_2\ yield = \frac{n_{H_2,t1}}{n_{HCOOH,t0}} * 100 \qquad eq\ 4$$

$$CO_2\ yield = \frac{n_{CO_2,t1}}{n_{HCOOH,t0}} * 100 \qquad eq\ 5$$

$$CO\ yield = \frac{n_{CO,t1}}{n_{HCOOH,t0}} * 100 \qquad eq\ 6$$

$n_{HCOOH,t0}$ and $n_{HCOOH,t1}$ are the initial amount of formic-acid in moles and at t1, respectively. Likewise, $n_{H_2,t1}$, $n_{CO_2,t1}$and $n_{CO,t1}$are the integral amounts of H_2, CO_2 and CO formed at t1 in moles, respectively.

The apparent turn-over-frequency (TOF) was calculated according equation 7, based on conversion at t1 lower than 20 %.

$$TOF = \frac{[conversion\ rate\ HCOOH\ ]_{t1}\ mol * s^{-1}}{moles\ of\ available\ surface\ Pd\ mol} \qquad eq\ 7$$

The number of available Pd surface-atoms was obtained with CO-chemisorption.

Table 1. Operating conditions of the nitrite hydrogenation in slurry reactor.

Reaction temperature, °C	20
Reaction volume, L	0.3
pH of the solution	2 - 10
Stirring speed, rpm	625
Tested partially hydrophilic catalyst particle size, µm	0 - 20
Amount of catalyst, g	0.1
Initial formic-acid concentration, mmol/L	1.5 - 10
Total gas flow rate, mL/min	50
Total operating pressure, bar	1
Oxygen partial pressure, bar	0 – 0.02
Ar partial pressure (balance), bar	0.98 - 1

2.5. ATR-IR

The preparation of catalyst layer on the ATR crystal is described elsewhere [27,43–46] and **Chapter 5**. Briefly, a suspension containing 0.1 g 1 wt% Pd/γ-Al_2O_3 dispersed in 20 mL 2-propanol was prepared. In order to prevent cracking of the catalyst layer, the suspension was sonicated with an ultrasonic processor (Fisher Scientific-705) for 1 hour. Subsequently, the suspension was spray-coated on a trapezoidal ZnSe crystal (52.5 mm * 20 mm* 2 mm, facet angle 45 °, Anadis instruments BV), which was placed on a hot plate at 150 °C, resulting in about 5 mg catalyst on the crystal. Then, the coated crystal was calcined at 300 °C (1 °C/min) for 1h in N_2 atmosphere (20 mL/min). It was mounted in a home-build in-situ Attenuated Total Reflection Infrared Spectroscopy (ATR-IR) cell which has been described in detail elsewhere [43,44]. The cell was mounted in the sample compartment of an infrared spectrometer (Tensor 27, Bruker) equipped with a liquid nitrogen cooled MCT detector. All the liquid flows were pumped by a peristaltic pump (Verderflex) downstream of the ATR-IR cell, which is important to prevent formation of gas bubbles in the cell (See in **Chapter 5** Scheme 1).

Once the cell was assembled in the IR spectrometer, it was flushed with Ar/H_2O with a flow rate of 0.5 mL/min until a stable water spectrum was obtained. Once the water spectrum was stable, the background spectrum was collected. Subsequently, the cell with the catalyst layer was flushed with formic-acid solution (10 mM) at pH 5 or 3, degassed with Ar before the experiment for at least 3 h. The catalysts in the ATR cell was exposed to the liquid flow during 10 minutes, where after the liquid flow was stopped, mimicking a batch reactor. ATR-IR spectra were recorded at room temperature ($20 \pm 1\ ^{o}C$) in an air-conditioned room. Each spectrum was acquired by averaging of 128 scans taken with a resolution of 4 cm^{-1}. The collected spectra were averaged over 60 s. The catalyst layers were re-used a few time and comparable results were obtained, indicating that the catalyst layer is stable during the experiments.

3. Results

3.1. Catalyst characterization

Table 2 reports the properties of the $Pd/\gamma\text{-}Al_2O_3$ catalyst. The high surface area $\gamma\text{-}Al_2O_3$ support assisted to achieve high metal dispersion, as determined with CO-chemisorption. XPS measurements showed that the sample stored in ambient conditions contains 30 % of the Pd in oxidized state (shown in Figure A1), in reasonable agreement with literature [19,37].

Table 2. Catalyst characterization

Catalyst	$Pd/\gamma\text{-}Al_2O_3$
Catalyst specific surface area, m^2/g	195
Metal loading, wt%	0.9
Metal dispersion, %	38
Mean metal particle size, nm	2.8
Pd^0/Pd^{2+}	2.3

3.2. Formic-acid decomposition in inert

Figure 1 shows a typical result of a formic-acid decomposition experiment, showing the decreasing concentration of formic-acid as well as the concentrations of H_2 and CO_2 in the gas-stream during the experiment. CO was never detected in any experiment in this study. Note that the differences in the shape of the profiles are caused by the fact that the liquid phase can be considered as a batch reactor, the formic-acid concentration is converted with a decreasing rate in time. In contrast, the gas phase products are measured in the gas stream passing through the reactor and the low concentrations observed in the first half hour are due to the fact that the concentrations of H_2 and CO_2 in the gas cap have to build up first. Consequently, information on gas-phase products is delayed. Nevertheless, the amount of H_2 and CO_2 produced and removed from the reactor at a certain time can be calculated based on the concentration profile and Ar gas-flow-rate, integrated over time, as shown in Figure 2a.

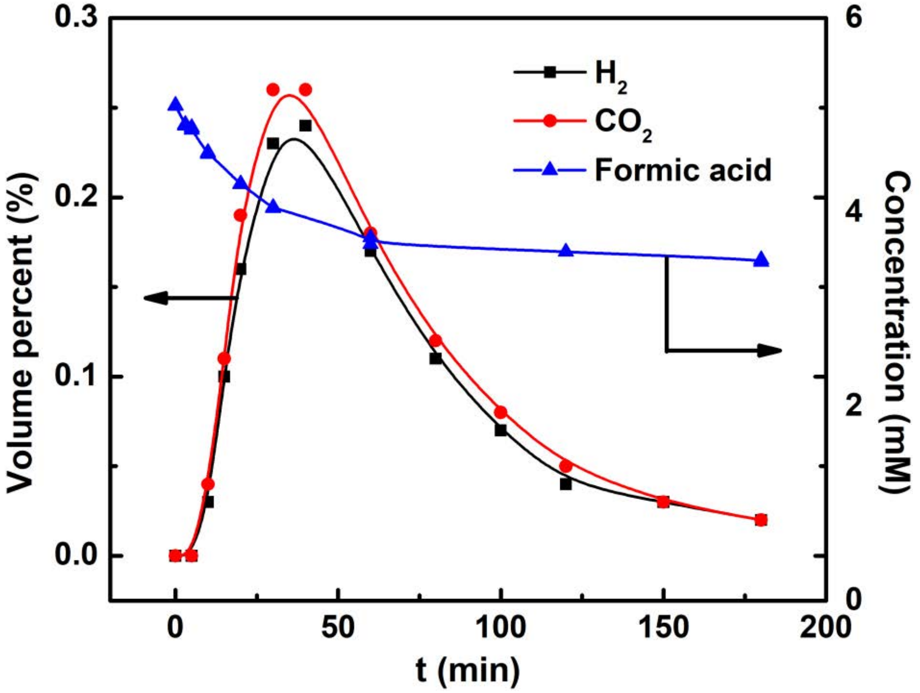

Figure 1. H_2 and CO_2 volume percent in the composition gas analyzed by a micro-GC sampling every 5 min and formic-acid concentration profile (5 mM formic-acid, 50 mL/min Ar flow through, 100 mg catalyst).

Figure 2a shows the amount of formic-acid converted (based on the formic-acid concentration in Figure 1) and the amounts of H_2 and CO_2 produced (calculated as explained above). Figure 2b shows in more detail the same for the initial phase of the experiment. The results clearly show that the reaction rate is constant during the first half our, whereas the amounts of gas-phase products show a clear delay, as discussed above. Therefore, the initial turn over frequencies (TOF) are calculated based on conversion of formic-acid at low conversion. Furthermore, the reaction becomes extremely slow after typically one hour, as can be seen (Figure 2a) according both the amount of formic-acid remaining as well as according the almost constant cumulative amount of gas-phase products. Furthermore, H_2 and CO_2 are produced in equal amount, in agreement with the stoichiometry of the decomposition reaction. Also, the number of moles formic-acid (0.5 mmol) converted after 3 hours agree well with the amount of H_2 and CO_2 formed.

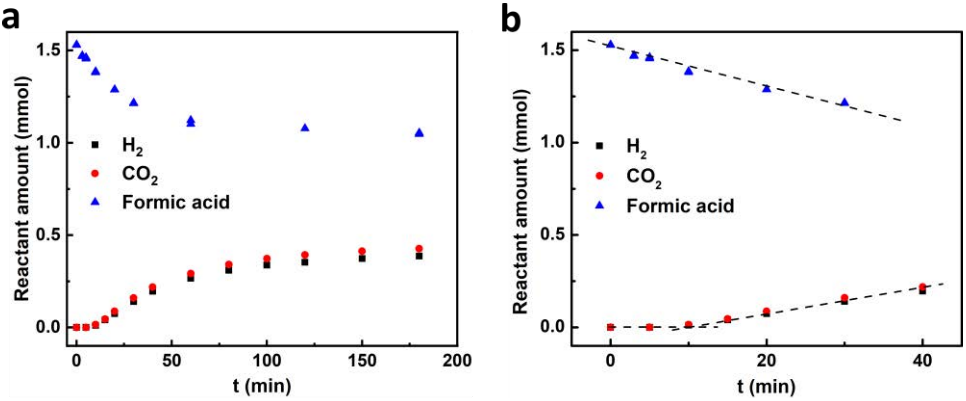

Figure 2. a) Formic-acid, H_2 and CO_2 content profile during the reaction, b) the zoom-in Figure 2a the initial 20 % conversion of formic-acid data (5 mM formic-acid, 50 mL/min Ar flow through, 100 mg catalyst).

The results are not influenced by internal mass transfer according to calculation the Weisz Prater number as shown in the Appendix section 1, as the estimated value is much lower than 1. However, we cannot rule out any effects of formation of bubbles in the catalyst pores, which might both slow down as enhance internal transport, the latter by causing chaotic movement of the liquid in the catalyst pore according to the "oscillation theory" [47–49]. Also, any influence of external mass transfer can be ruled out based on calculations shown in Appendix section 2.

3.3. Effect of oxygen

Figure A2 in Appendix shows the conversion of formic-acid in time for experiments with oxygen concentrations between 0 and 2 vol%. Clearly, the presence of oxygen enhances conversion. Figure 3a shows more clearly the effect of oxygen at low concentrations, i.e. below 0.1%. Figure 3b shows that the initial apparent TOF increases with oxygen concentration between 0 to 2 vol% with almost a factor 3. However, the initial TOF is constant within experimental error at O_2 concentration below 0.1 vol%, in agreement with the fact that conversion seems independent of oxygen concentration during the first 30 minutes in Figure 3a.

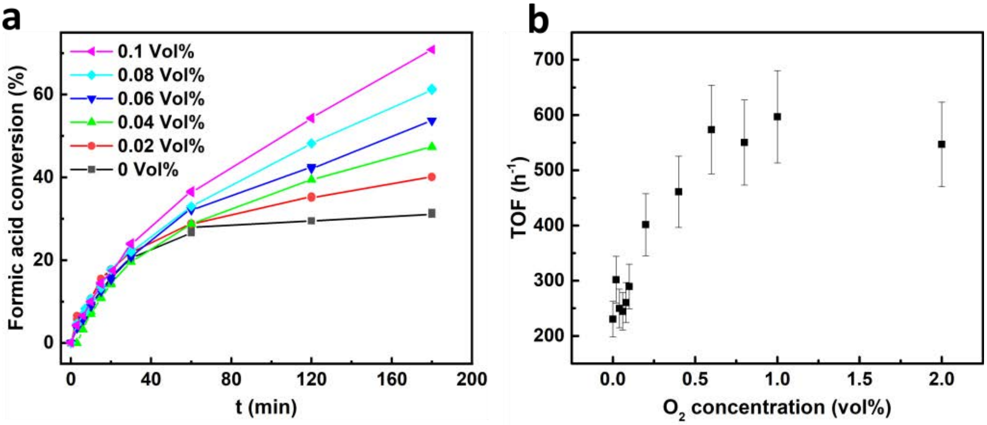

Figure 3. a) Formic-acid conversion profile at extreme low O_2 concentration (0 – 0.1 vol%), b) the initial apparent TOF plot with the O_2 concentration (0 – 2 vol%) applied (5mM formic-acid, 50 mL/min Ar/O_2 flow through, 100 mg catalyst).

Figure 4a shows formic-acid conversion, and H_2 and CO_2 yields after three hours of reaction, calculated by integrating the H_2 and CO_2 concentrations in gas-phase as explained in section 3.2 and based on the final conversions shown in Figures 3 and A2. Figure 4a shows that the hydrogen yield is maximal at 0.1 vol%. In contrast, the CO_2 yield increases with oxygen concentration until formic-acid is completely converted within 3 hours. A similar trend in H_2 and CO_2 yield is also observed after 30 minutes reaction time as shown in Figure A3. Figure 4a also shows that the CO_2 yield is always higher than the H_2 yield; the difference clearly increases with increasing oxygen concentration as shown in Figure 4b.

The mass balance in Figure 4a is not completely closed and about 10 % of the C seems lost, caused by the delay in the gas phase analysis data as discussed in section 3.2. This is illustrated by Figure A4, showing that when formic-acid is completely decomposed, i.e. no further H_2 and CO_2 are produced, detection of H_2 and especially CO_2 in the gas phase continues for more than two hours. This is caused by slowly flushing out the gasses and the effect is much stronger for CO_2 because of the relatively high solubility of CO_2 in water. The accuracy of the C-mass balance is probably most affected by CO_2 remaining in the water in the reactor.

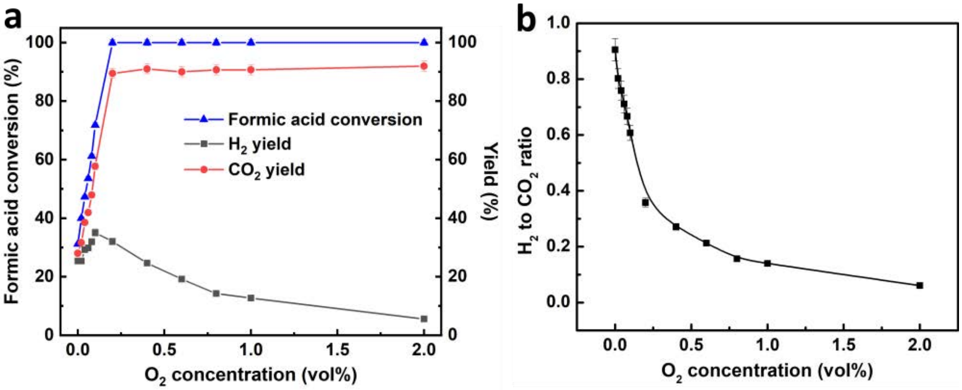

Figure 4. a) Formic-acid conversion, H_2 yield and CO_2 yield under different oxygen concentration at 3 hours reaction, b) H_2 to CO_2 ratio plot with the O_2 concentration applied (5 mM formic-acid, 50 mL/min Ar/O_2 flow through, 100 mg catalyst).

Figure 5 shows the formic-acid conversion profiles of an experiment in inert with an experiment under semi-inert conditions, i.e. by flushing only the gas-cap with inert without bubbling through the liquid. The black square shows 17 % conversion in three hours under inert-experiment condition. In contrast, much higher conversion (68 %) is obtained under semi-inert conditions. The difference is caused by oxygen dissolved in the water as it is not removed with Ar under semi-inert conditions.

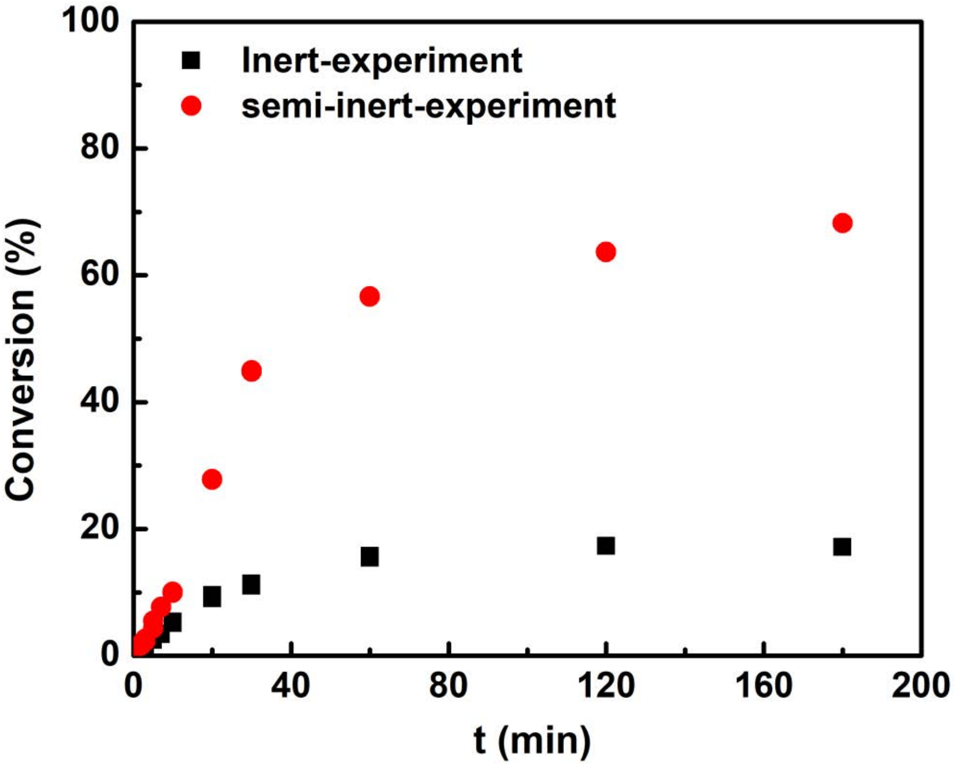

Figure 5. The conversion of 5 mM formic-acid with 50 mg 1 wt% Pd/γ-Al_2O_3 in presence of different amounts of traces of oxygen in the reaction system at the start of the batch experiment (5 mM formic-acid, 50 mg catalyst, inert-experiment: Ar gas flow through liquid 50 mL/min, semi-inert-experiment: Ar gas flow above liquid 50 mL/min).

3.4. Effect of formic-acid concentration

Figure 6 shows that the initial apparent TOF, in presence of 0.1 vol% oxygen, remains almost constant on changing the formic-acid concentration. Note that varying the initial formic-acid concentration between 2 to 10 mM also changed the initial solution pH between 3.2 to 2.9 [50]. As shown in Figure A5, the rate of reaction decreases with increasing pH, but the change within the pH window between 2.9 and 3.2 appears smaller than experimental accuracy. Therefore, it can be concluded that the apparent order in formic-acid is zero under our experimental condition. Different reaction orders in formic-acid are reported in literature [20,29,51] but unfortunately the oxygen concentration was not well controlled in these studies. The importance of oxygen will be discussed later on.

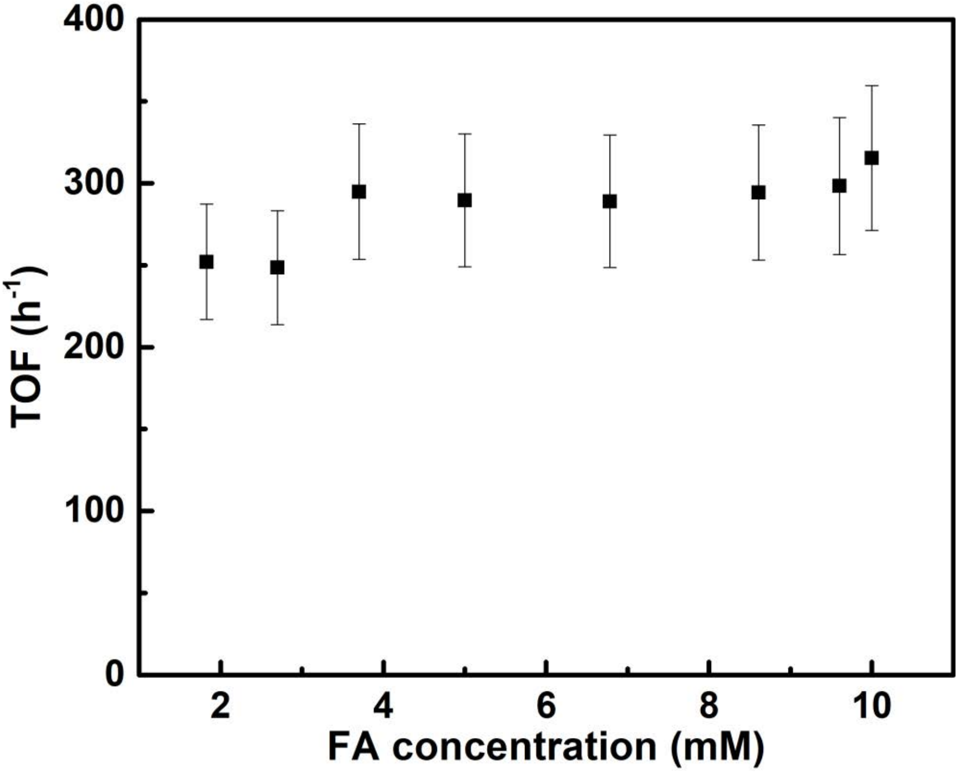

Figure 6. The initial apparent TOF plots with different formic-acid concentration (2 – 10 mM) under 0.1 vol% oxygen concentration (50 mL/min Ar/O_2 flow through, 100 mg catalyst).

3.5. Catalyst stability

Catalyst stability was tested in both inert (Ar) as well as in presence of 0.1 vol% O_2. A single batch of the catalyst was tested during four hours by adding the same amount of the formic-acid every 60 min to the batch reactor. Figure 7a shows the results under inert atmosphere. Clearly, formic-acid is almost fully converted in the first hour. The activity decreased significantly in the second hour after dosing additional formic-acid solution, and even more so after dosing for the third and fourth time. The catalyst clearly deactivates under inert condition. On the contrary, in the same experiments performed in 0.1 vol% oxygen, as shown in Figure 7b, the catalyst maintained its activity in three runs, only showing mild deactivation in the fourth run.

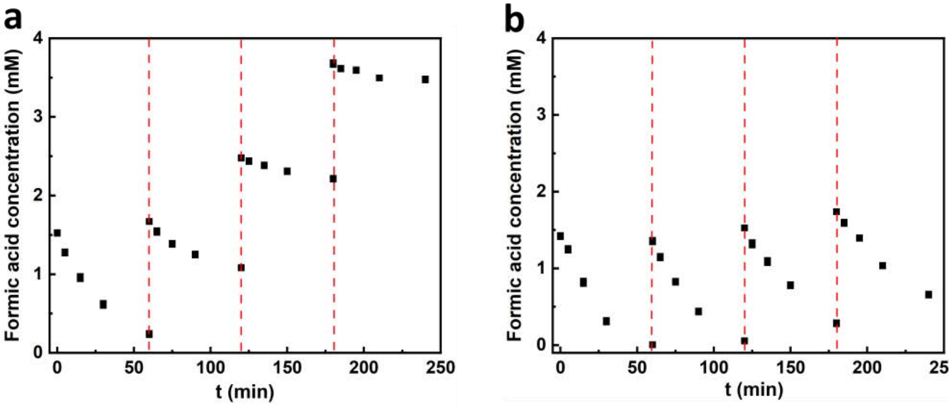

Figure 7. Pd catalyst stability for formic-acid decomposition under a) inert gas; b) 0.1 vol% O_2;15 µL pure formic-acid solution was added to the batch reactor every 60 min.

3.6. ATR experiments on formic-acid decomposition

Figure 8 presents the ATR-IR spectra obtained with bare ZnSe, a bare alumina layer and a catalyst layer, exposed to formic-acid solutions for at least 10 minutes at pH 3 and 5. The dark yellow line shows the spectrum on bare ZnSe at pH 5, showing three peaks at respectively 1581, 1380 and 1350 cm^{-1}. These three peaks are also observed in the experiments with the Al_2O_3 layer and the Pd/Al_2O_3 layer at different pH condition and are assigned to free formate in the bulk solution, in agreement with literature [18]. Note that the absolute intensities in Figure 4 cannot be compared because the optical properties of the layers are different. The red line shows the spectrum obtained with Pd/Al_2O_3 at pH 5, showing an additional peak at 2350 cm^{-1} which is assigned to CO_2 [19,52–55], confirming the formation of CO_2 via Pd-catalyzed formic-acid decomposition. The black spectrum presents the result of the same experiment at pH 3, revealing both a larger CO_2 peak at 2350 cm^{-1} as well as a clear shoulder peak around 1610 cm^{-1}, which however cannot be assigned at this time.

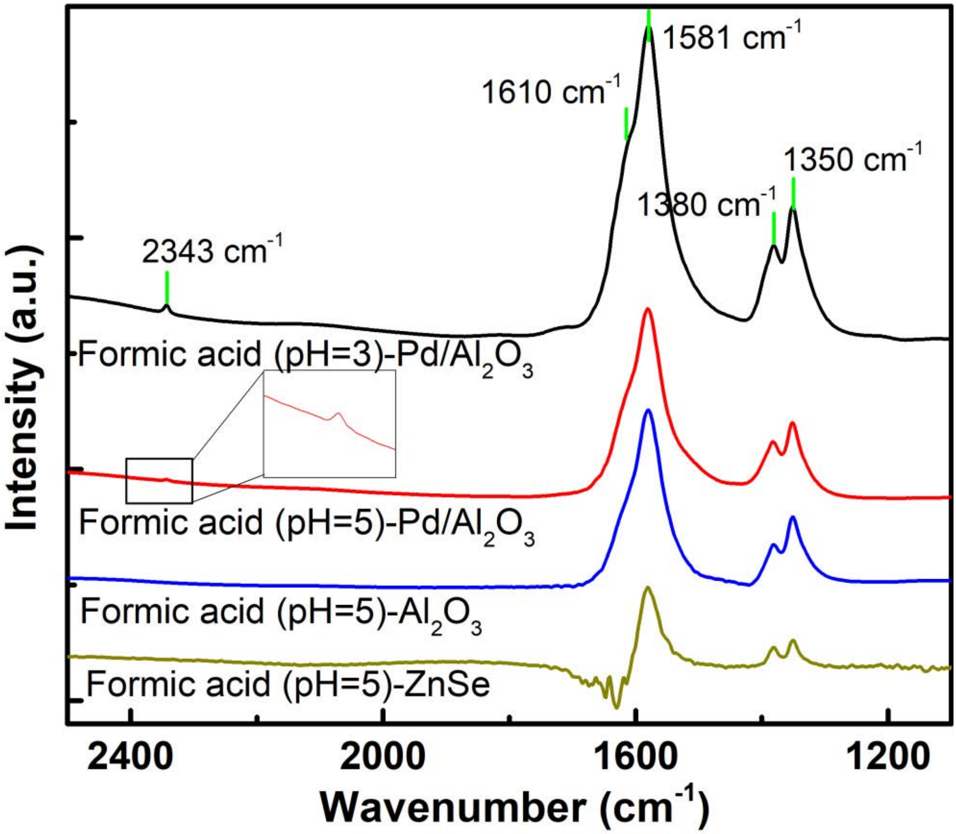

Figure 8. ATR-IR spectra after exposure to formic-acid solutions: Dark yellow represents formic-acid at pH 5 spectrum on bare ZnSe (the intensity was multiplied by five), blue line represents formic-acid at pH 5 spectrum on Al_2O_3 layer, red line and black line represent formic-acid spectrum on Pd/Al_2O_3 layer at pH 5 and pH 3, respectively (5 mg catalyst, 3 wt% Pd/Al_2O_3, 10 mM formic-acid, 0.5 mL/min flow rate).

Figure 9a shows how the peaks in ATR-IR spectra develop during exposure to formic-acid (pH = 3) for 5 minutes, finally resulting in the spectrum shown in Figure 8. Figure 9b shows a zoom-in of the window between 1700 and 2200 cm^{-1}, revealing two peaks at 2110 cm^{-1} and 1830 cm^{-1}, assigned to linear bonded and bridged bonded CO on the Pd surface [27], demonstrating the formation of adsorbed CO. The same experiment at pH 5 (Figure A6a) does not result in detection of CO during exposure to formic-acid, although minor peaks can be observed when the flow is stopped, mimicking a batch experiment (Figure A6c).

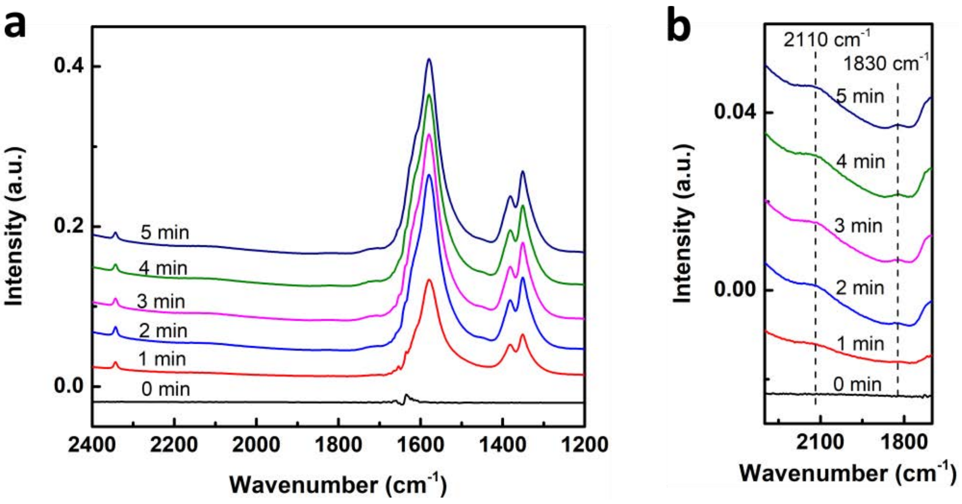

Figure 9. a) ATR-IR spectra of formic-acid decomposition at pH = 3 flowing for 5 min, b) zoom-in a) in the window of 1700 and 2300 cm-1 (5 mg 1 wt% catalyst on ZnSe, 10 mM formic-acid solution)

4. Discussion

4.1. Catalyst characterization

Pd catalyst was obtained with good dispersion and mean metal particles size of 2.8 nm. The small Pd particles oxidized easily in air as observed with XPS in Table 2. The catalysts were used as prepared without any further pretreatment before the reaction, thus Pd and PdO co-exist initially. It is well known Pd^{2+} can be reduced to Pd^0 metal state by formic-acid [14,33,56,57]. According to recent studies [22,38], in-situ reduction with H_2 does not influence catalyst activity. In any case, any formic-acid consumption due to PdO reduction in our experiments can maximally convert 0.2 % of the initial amount of formic-acid. So, this would not influence the catalyst activity.

4.2. Activity in inert atmosphere

As shown in Figure 1, the catalyst deactivated during the reaction when oxygen is absent, as only a small fraction of formic-acid is converted and the reaction rate is very small after two hours. The same is also observed in the experiment with repeatedly dosing of formic-acid in Figure 7a. Deactivation is attributed to poisoning with CO as also suggested in literature [18,20–22,29,32,36,58]. However, CO was not detected with GC, as CO absorbs very strongly on Pd and cannot desorb at room temperature. The amount of CO required to completely cover the Pd surface is a small as $3.2*10^{-3}$ mmol CO, which can be produced by dehydration (equation 2) of only 0.2 % of the initial amount of formic-acid.

Formation of adsorbed CO during formic-acid decomposition is confirmed by ATR-IR experiments in Figure 9b. This agrees well with Jiang et al. [18], reporting similar results with ATR-IR. The peaks are slightly blue-shifted compared to our previous study [27], possibly caused by differences in pH, the surface coverage of CO or interaction with formate ions. Clearly, in-situ detection is required as CO could not be detected on spent catalyst as reported by Hu et al. [22], probably caused by oxidation of CO in air.

In previous studies, TOFs were calculated based on the production rate of H_2 [14,28,29,51,59] or total gas production rate (H_2 and CO_2) [22,34,35], resulting in TOFs typically between 100 and 1000 h^{-1}. Unfortunately, the level of conversion is not reported, making direct comparison impossible. On top of that, the presence of oxygen was not clearly reported, which is important as will be discussed below.

Table 3 summarizes the results of studies performed in well controlled inert atmosphere. Clearly, the initial apparent TOF in our work is in the same order of magnitude or somewhat larger as reported in literature [40,60–62], despite differences in precise conditions and uncertainty about any undesired effect of mass transfer, except for our data. The fact that high TOF is observed at low formic-acid concentration is in line with the order zero in formic-acid (Figure 6), also confirming that formic-acid mass transfer cannot be limiting in our experiments.

Table 3. Literature data on rate of formic-acid decomposition over supported Pd catalysts in inert atmosphere.

catalyst	Temperature	Formic-acid concentration	pH	Pd metal size	Support size	TOF
Pd/C [40]	20 – 25 °C	1000 mM	1.9	1.9 - 3.2 nm	N.A.	60 – 100 h^{-1}
Pd/H-BETA(0.5) [60]	50 °C	1000 mM	1.9	3.4 nm	N.A.	59.2 h^{-1}
Pd/SiO_2 [61]	30 °C	1000 mM	1.9	3.5 nm	N.A.	23.4 h^{-1}
Pd/g-C_3N_4 [62]	30 °C	1000 mM	1.9	4.6 nm	N.A.	35 h^{-1}
This work	20 °C	5 mM	3	2.8 nm	≤ 20 μm	230 h^{-1}

4.3. Influence of pH

The activity of the Pd catalyst decreases with increasing pH, independent of the oxygen concentration as shown Figure A5 in presence of 0.1 vol% O_2 and under inert conditions. This agrees well with the observations in ATR-IR experiments that both CO_2 and adsorbed CO form faster at pH 3 (Figure 9) than at pH 5 (Figure A6). The results suggest that un-dissociated formic-acid rather than formate ions react, but this observation can also be interpret in terms of the electrochemical potential of the Pd particles, which decreases with increasing pH.

Many reports in literature [20,34,37] report on the influence of the ratio of formic-acid and sodium-formate in the reaction mixture, without considering that the actual concentration of formate-ions is determined by the acid-base equilibrium of the dissociation of formic-acid (equation 8) as also argued for the first time in [51].

$$HCOOH \leftrightarrow HCOO^{-} + H^{+} \qquad eq\ 8$$

The consequence is that the reactant concentration, i.e. the sum of formate and formic-acid, is not constant so that a clear observation on the effect of pH on the reaction rate is not obtained. Nevertheless, the qualitative observation that basic solutions result is very low reaction rates, is in agreement with observations in literature [30,37,51,63].

4.4. Activity in presence of oxygen

Figure 3b shows that the apparent initial TOF increases with increasing oxygen concentration, although the effect is insignificant when varying the oxygen concentration in a narrow window between 0 and 0.1 vol%. Figure 3a shows that the catalyst activity remains higher during the experiment on increasing the oxygen concentration, achieving much higher conversion. In other words, catalyst deactivation is suppressed by oxygen, even if the oxygen concentration is very low, i.e. below 0.1 vol%. The result in Figure 7b confirms that catalyst stability is significantly improved by introducing trace amount of oxygen. However, it is also clear that deactivation occurs in the fourth run, suggesting that a second deactivation mechanism is in operation. In any case, low oxygen concentration improves stability of Pd catalysts for formic-acid decomposition.

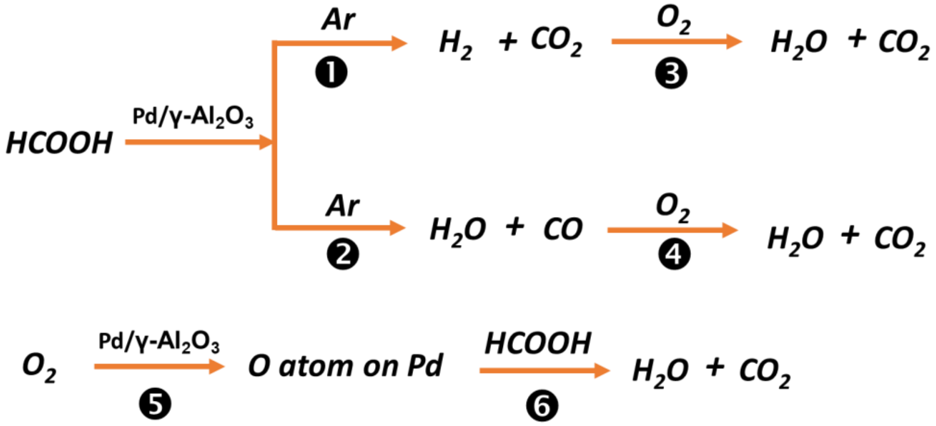

Scheme 1. Formic-acid decomposition reactions under oxygen condition.

Oxygen may be involved in three reactions as presented in Scheme 1. Firstly, oxygen may react with CO to form CO_2 (step 4), termed as CO oxidation. Secondly oxygen may oxidize H_2 to H_2O (step 3), termed as H_2 oxidation, which are both consecutive reactions. Thirdly, formic-acid may react directly (step 6) with oxygen dissociated on the Pd surface (step 5), termed as formic-acid oxidation.

The effect of small concentrations of oxygen on catalyst performance is attributed to step 4, decreasing the CO coverage of the Pd surface and suppressing or even preventing deactivation.

In principle, the conversion rate of formic-acid could also be boosted via the reaction in step 5 and 6, i.e. direct deep oxidation of formic-acid. There are three arguments against this proposition. Firstly, if steps 5 and 6 would take over completely after one hour in the experiment with 0.1 vol% O_2 (see Figure 3a), i.e. forming CO_2 and H_2O exclusively during the second and third hour, the H_2/CO_2 ratio would decrease from 0.73 (Figure A7) after 1 hour to 0.32 after 3 hours. However, the observed H_2/CO_2 ratio after 3 hours is 0.58 (Figure A7), implying that H_2 formation via reaction 1 continued during the whole experiment. Be noted that the H_2/CO_2 ratio is calculated based on the integral amounts of the H_2 and CO_2 produced. Secondly, the H_2 yield increases under 0.1 vol% oxygen concentration as can be seen in Figure 4a and A3b, implying that H_2 formation rate increases over the whole experiment. Thirdly, the presence of a very small amount of O_2 in the reactor, i.e. by removing oxygen only in the gas cap before the experiment and leaving dissolved oxygen in water behind (Figure 5), increases the conversion after 3 hours from 17 % (in inert conditions) to 68 %. Stoichiometric reaction of O_2 dissolved in water in equilibrium with air could account for an increase in conversion of maximal 11 %. The real contribution is even smaller because the oxygen concentration in water will decrease somewhat during flushing the gas cap with inert. These three observations demonstrate that preventing deactivation via CO oxidation is the dominant mechanism, explaining the increase in conversion when adding low oxygen concentrations ($\leq$ 0.1 vol%), instead of direct oxidation of formic-acid.

On the other hand, the situation is quite different at higher O_2 concentrations, where step 3 and 6 clearly dominate, decreasing the H_2 yield, as shown in Figure 4a. It is clear that oxygen not only suppresses deactivation, but also influences the rate of conversion of formic-acid by opening an additional reaction pathway, influencing also the product distribution.

There are three types of experiments used in literature for studying formic-acid decomposition. First, in many studies the experiments were conducted in air, implying that oxygen is present in both the gas above the solution as well as in the solution [16,18,20,22,28,30–35,37,38,58,59,64–68,]. Second, in some studies the air above the solution was removed by flushing with inert before the reaction was initiated, implying that oxygen dissolved in the liquid might still be present [19,51,69–71]. This is the same, somewhat poorly defined, situation as we applied in Figure 5, demonstrating a strong influence on the reaction rate. Third, in a few studies air was completely removed from the reactor including the solution, which is the standard method in this study [21,39,40,60–62,72,73]. The results confirm that Pd catalysts deactivate [21,39,62,72], in agreement with our results in inert. Our study shows not only that presence of oxygen at low concentration, i.e. 0.1%, suppresses catalyst deactivation, but also that the observed reaction rates are strongly influenced by the presence of oxygen in the concentrations window between 0.2 and 2%. Therefore, the effect of oxygen, even on the level of traces, should be rigorously considered in future research on efficient catalysts for formic-acid decomposition.

5. Conclusion

The kinetics of formic-acid decomposition over Pd catalyst supported on alumina is strongly influenced by deactivation during the batch experiment, dominantly caused by CO poisoning. Deactivation can be suppressed by dosing trace amounts of oxygen. However, oxygen reacts not only with CO, preventing deactivation, but also with H_2 simultaneously. Operation at oxygen concentrations below 0.1 vol% enhances the production of hydrogen, as efficient prolonging catalyst activity dominates over consecutive oxidation of hydrogen. Furthermore, oxygen concentrations between 0.1

vol% and 2 vol% cause significant increase in the rate of conversion of formic-acid and influences also the product distribution, i.e. decreasing the hydrogen yield, which in many cases is not accounted for in reported batch experiments on Pd catalyzed decomposition of formic-acid in literature.

Reference

[1] W. Wang, J. M. Herreros, A. Tsolakis, A. P. E. York, *Int. J. Hydrogen Energy* **2013**, *38*, 9907–9917.

[2] M. Bertau, H. Offermanns, L. Plass, F. Schmidt, H. J. Wernicke, *Methanol: The Basic Chemical and Energy Feedstock of the Future: Asinger's Vision Today*, **2014**.

[3] E. Rivard, M. Trudeau, K. Zaghib, *Materials (Basel).* **2019**, *12*, DOI 10.3390/ma12121973.

[4] U. Bossel, B. Eliasson, *Eur. Fuel Cell Forum, Lucerne* **2002**, 36.

[5] R. van Putten, T. Wissink, T. Swinkels, E. A. Pidko, *Int. J. Hydrogen Energy* **2019**, DOI 10.1016/j.ijhydene.2019.01.153.

[6] K. Grubel, H. Jeong, C. W. Yoon, T. Autrey, *J. Energy Chem.* **2020**, *41*, 216–224.

[7] D. A. Bulushev, J. R. H. Ross, *Catal. Rev. - Sci. Eng.* **2018**, *60*, 566–593.

[8] M. Grasemann, G. Laurenczy, *Energy Environ. Sci.* **2012**, *5*, 8171–8181.

[9] M. Yadav, Q. Xu, *Energy Environ. Sci.* **2012**, *5*, 9698–9725.

[10] A. Boddien, H. Junge, *Nat. Nanotechnol.* **2011**, *6*, 265–266.

[11] D. A. Bulushev, M. Zacharska, Y. Guo, S. Beloshapkin, A. Simakov, *Catal. Commun.* **2017**, *92*, 86–89.

[12] M. Sridhar, D. Ferri, M. Elsener, J. A. Van Bokhoven, O. Kröcher, *ACS Catal.* **2015**, *5*, 4772–4782.

[13] F. Sánchez, D. Motta, N. Dimitratos, *Appl. Petrochemical Res.* **2016**, *6*, 269–277.

[14] Z. L. Wang, J. M. Yan, H. L. Wang, Y. Ping, Q. Jiang, *Sci. Rep.* **2012**, *2*, 598.

[15] W. Y. Yu, G. M. Mullen, D. W. Flaherty, C. B. Mullins, *J. Am. Chem. Soc.* **2014**, *136*, 11070–11078.

[16] Z. Dong, F. Li, Q. He, X. Xiao, M. Chen, C. Wang, X. Fan, L. Chen, *Int. J. Hydrogen Energy* **2019**, *44*, 11675–11683.

[17] Y. Wang, Y. Qi, D. Zhang, C. Liu, *J. Phys. Chem. C* **2014**, *118*, 2067–2076.

[18] K. Jiang, K. Xu, S. Zou, W. Bin Cai, *J. Am. Chem. Soc.* **2014**, *136*, 4861–4864.

[19] Q. Lv, Q. Meng, W. Liu, N. Sun, K. Jiang, L. Ma, Z. Peng, W. Cai, C. Liu, J. Ge, L. Liu, W. Xing, *J. Phys. Chem. C* **2018**, *122*, 2081–2088.

[20] M. Yurderi, A. Bulut, M. Zahmakiran, M. Kaya, *Appl. Catal. B Environ.* **2014**, *160–161*, 514–524.

[21] D. M. Ruthven, R. S. Upadhye, *J. Catal.* **1971**, *21*, 39–47.

[22] C. Hu, J. K. Pulleri, S. W. Ting, K. Y. Chan, *Int. J. Hydrogen Energy* **2014**, *39*, 381–390.

[23] M. Navlani-García, D. Salinas-Torres, D. Cazorla-Amorós, *Energies* **2019**, *12*, DOI

10.3390/en12214027.

[24] M. Peter, S. Adamovsky, J. M. Flores Camacho, S. Schauermann, *Faraday Discuss.* **2013**, *162*, 341–354.

[25] M. Lischka, A. Groß, *Res. Signpost* **2003**, *661*, 111–132.

[26] F. Solymosi, A. Berkó, *J. Catal.* **1986**, *101*, 458–472.

[27] S. D. Ebbesen, B. L. Mojet, L. Lefferts, *Phys. Chem. Chem. Phys.* **2009**, *11*, 641–649.

[28] X. Zhou, Y. Huang, C. Liu, J. Liao, T. Lu, W. Xing, *ChemSusChem* **2010**, *3*, 1379–1382.

[29] K. Tedsree, T. Li, S. Jones, C. W. A. Chan, K. M. K. Yu, P. A. J. Bagot, E. A. Marquis, G. D. W. Smith, S. C. E. Tsang, *Nat. Nanotechnol.* **2011**, *6*, 302–307.

[30] L. Yang, X. Hua, J. Su, W. Luo, S. Chen, G. Cheng, *Appl. Catal. B Environ.* **2015**, *168–169*, 423–428.

[31] J. Liu, L. Lan, R. Li, X. Liu, C. Wu, *Int. J. Hydrogen Energy* **2016**, *41*, 951–958.

[32] F. Sanchez, M. H. Alotaibi, D. Motta, C. E. Chan-Thaw, A. Rakotomahevitra, T. Tabanelli, A. Roldan, C. Hammond, Q. He, T. Davies, A. Villa, N. Dimitratos, *Sustain. Energy Fuels* **2018**, DOI 10.1039/C8SE00338F.

[33] S. Zhang, B. Jiang, K. Jiang, W. Bin Cai, *ACS Appl. Mater. Interfaces* **2017**, *9*, 24678–24687.

[34] Q. Zhu, N. Tsumori, Q. Xu, *J. Am. Chem. Soc.* **2015**, *137*, 11743–11748.

[35] S. J. Li, Y. Ping, J. M. Yan, H. L. Wang, M. Wu, Q. Jiang, *J. Mater. Chem. A* **2015**, *3*, 14535–14538.

[36] Q. Y. Bi, J. D. Lin, Y. M. Liu, H. Y. He, F. Q. Huang, Y. Cao, *Angew. Chemie - Int. Ed.* **2016**, *55*, 11849–11853.

[37] J. Li, W. Chen, H. Zhao, X. Zheng, L. Wu, H. Pan, J. Zhu, Y. Chen, J. Lu, *J. Catal.* **2017**, *352*, 371–381.

[38] Y. Kim, D. H. Kim, *Appl. Catal. B Environ.* **2019**, *244*, 684–693.

[39] K. Mandal, D. Bhattacharjee, S. Dasgupta, *Int. J. Hydrogen Energy* **2015**, *40*, 4786–4793.

[40] M. Navlani-García, K. Mori, A. Nozaki, Y. Kuwahara, H. Yamashita, *ChemistrySelect* **2016**, *1*, 1879–1886.

[41] P. Xu, S. Agarwal, L. Lefferts, *J. Catal.* **2020**, *383*, 124–134.

[42] P. Xu, S. Agarwal, J. F. Albanese, L. Lefferts, *Chem. Eng. Process. - Process Intensif.* **2020**, *148*, DOI 10.1016/j.cep.2020.107802.

[43] S. D. Ebbesen, B. L. Mojet, L. Lefferts, *Langmuir* **2008**, *24*, 869–879.

[44] S. D. Ebbesen, B. L. Mojet, L. Lefferts, *J. Catal.* **2008**, *256*, 15–23.

[45] S. D. Ebbesen, B. L. Mojet, L. Lefferts, *J. Phys. Chem. C* **2009**, *113*, 2503–2511.

[46] Y. Zhao, N. Koteswara Rao, L. Lefferts, *J. Catal.* **2016**, *337*, 102–110.

[47] L. B. Datsevich, *Appl. Catal. A Gen.* **2003**, *247*, 101–111.

[48] L. B. Datsevich, *Catal. Today* **2003**, *79–80*, 341–348.

[49] L. B. Datsevich, *Appl. Catal. A Gen.* **2003**, *250*, 125–141.

[50] Zumdahl, *Lab Man. Zumdahl/Zumdahl's Chem.* **2003**, 656.

[51] S. Akbayrak, Y. Tonbul, S. Özkar, *Appl. Catal. B Environ.* **2017**, *206*, 384–392.

[52] H. A. Bullen, S. A. Oehrle, A. F. Bennett, N. M. Taylor, H. A. Barton, *Appl. Environ. Microbiol.* **2008**, *74*, 4553–4559.

[53] J. Y. Wang, H. X. Zhang, K. Jiang, W. Bin Cai, *J. Am. Chem. Soc.* **2011**, *133*, 14876–14879.

[54] M. F. Baruch, J. E. Pander, J. L. White, A. B. Bocarsly, *ACS Catal.* **2015**, *5*, 3148–3156.

[55] J. E. Pander, M. F. Baruch, A. B. Bocarsly, *ACS Catal.* **2016**, *6*, 7824–7833.

[56] Q. Wang, Y. Wang, P. Guo, Q. Li, R. Ding, B. Wang, H. Li, J. Liu, X. S. Zhao, *Langmuir* **2014**, *30*, 440–446.

[57] W. J. Lee, Y. J. Hwang, J. Kim, H. Jeong, C. W. Yoon, *ChemPhysChem* **2019**, *20*, 1382–1391.

[58] M. Caiti, D. Padovan, C. Hammond, *ACS Catal.* **2019**, *9*, 9188–9198.

[59] Q. Y. Bi, J. D. Lin, Y. M. Liu, F. Q. Huang, Y. Cao, *Int. J. Hydrogen Energy* **2016**, *41*, 21193–21202.

[60] M. Navlani-García, M. Martis, D. Lozano-Castelló, D. Cazorla-Amorós, K. Mori, H. Yamashita, *Catal. Sci. Technol.* **2015**, *5*, 364–371.

[61] J. García-Aguilar, M. Navlani-García, Á. Berenguer-Murcia, K. Mori, Y. Kuwahara, H. Yamashita, D. Cazorla-Amorós, *Langmuir* **2016**, *32*, 12110–12118.

[62] Y. Wu, M. Wen, M. Navlani-García, Y. Kuwahara, K. Mori, H. Yamashita, *Chem. - An Asian J.* **2017**, *12*, 860–867.

[63] Q. F. Deng, Z. F. Zhang, F. J. Cui, L. H. Jia, *Int. J. Hydrogen Energy* **2017**, *42*, 14865–14871.

[64] K. Tedsree, T. Li, S. Jones, C. W. A. Chan, K. M. K. Yu, P. A. J. Bagot, E. A. Marquis, G. D. W. Smith, S. C. E. Tsang, *Nat. Nanotechnol.* **2011**, *6*, 302–307.

[65] M. Hattori, D. Shimamoto, H. Ago, M. Tsuji, *J. Mater. Chem. A* **2015**, *3*, 10666–10670.

[66] Y. Kim, J. Kim, D. H. Kim, *RSC Adv.* **2018**, *8*, 2441–2448.

[67] T. Y. Ding, Z. G. Zhao, M. F. Ran, Y. Y. Yang, *J. Colloid Interface Sci.* **2019**, *538*, 474–480.

[68] J. Sun, H. Qiu, W. Cao, H. Fu, H. Wan, Z. Xu, S. Zheng, *ACS Sustain. Chem. Eng.* **2019**, *7*, 1963–1972.

[69] M. H. Jin, D. Oh, J. H. Park, C. B. Lee, S. W. Lee, J. S. Park, K. Y. Lee, D. W. Lee, *Sci. Rep.* **2016**, *6*, 33502.

[70] Y. Yu, X. Wang, C. Liu, F. Vladimir, J. Ge, W. Xing, *J. Energy Chem.* **2020**, *40*, 212–216.

[71] M. Navlani-García, D. Salinas-Torres, K. Mori, A. F. Léonard, Y. Kuwahara, N. Job, H.

Yamashita, *Catal. Today* **2019**, *324*, 90–96.

[72] M. Navlani-García, K. Mori, A. Nozaki, Y. Kuwahara, H. Yamashita, *Ind. Eng. Chem. Res.* **2016**, *55*, 7612–7620.

[73] M. Wen, K. Mori, Y. Futamura, Y. Kuwahara, M. Navlani-García, T. An, H. Yamashita, *Sci. Rep.* **2019**, *9*, 1–10.

Appendix

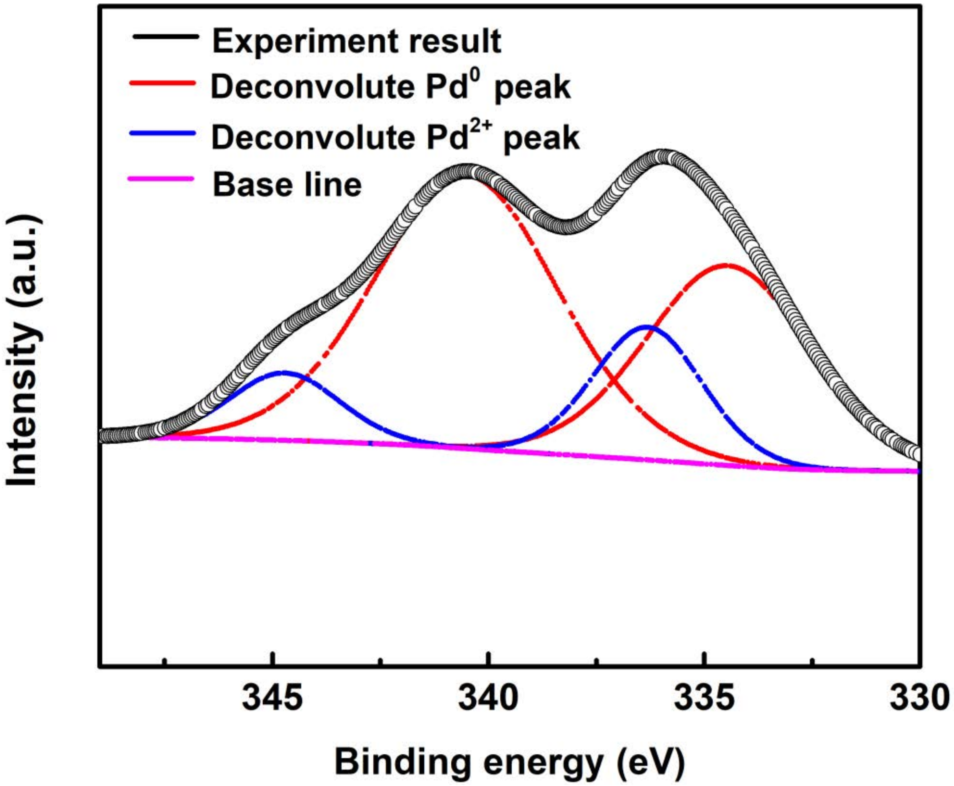

Figure A1. XPS spectra of fresh Pd/γ-Al_2O_3 catalyst kept under ambient atmosphere.

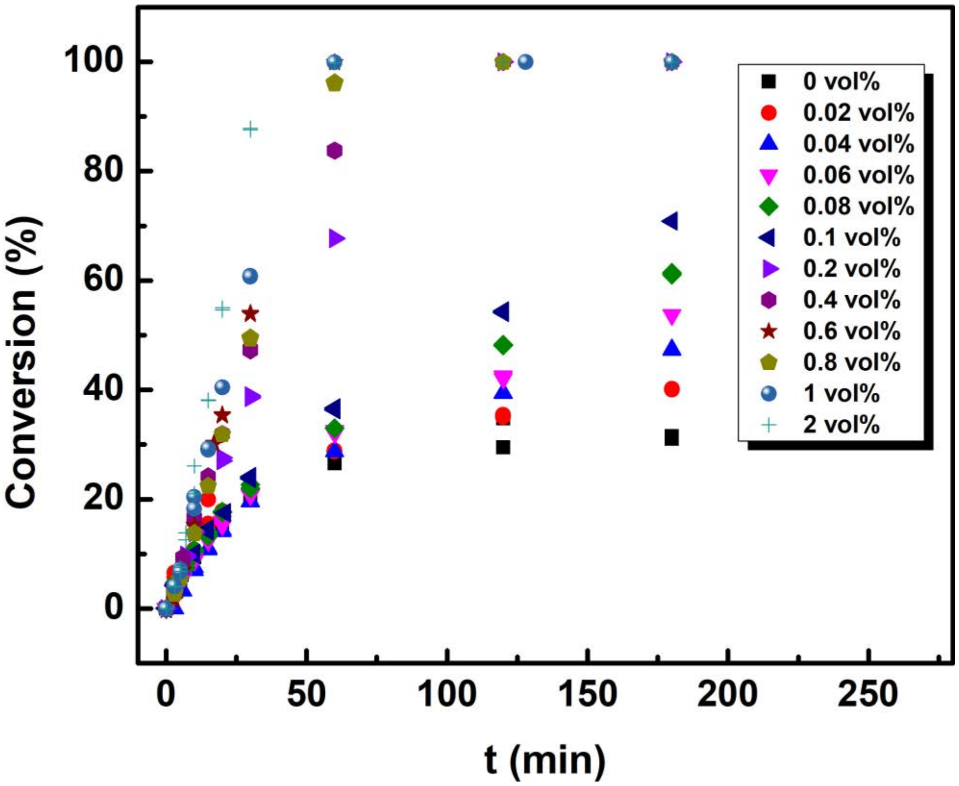

Figure A2. Formic-acid conversion plot under different oxygen concentration varies from 0 to 2 vol% (5 mM formic-acid, 100 mg catalyst, 50 mL/min Ar/O_2 flow through).

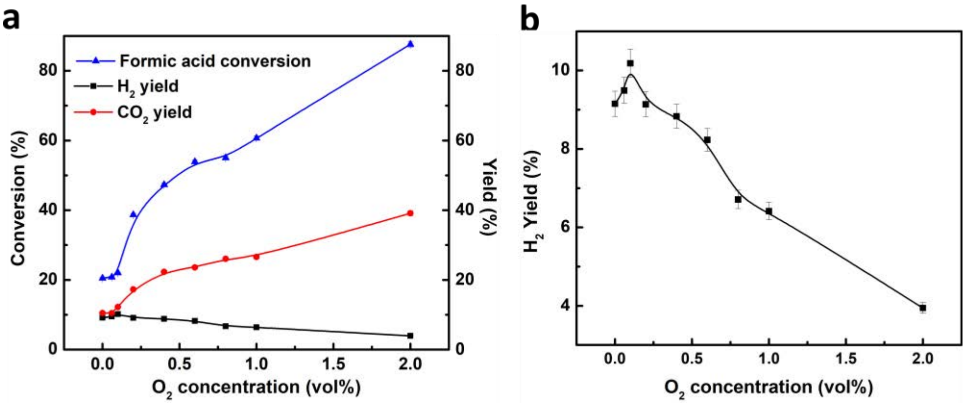

Figure A3. a) Formic-acid conversion, H_2 yield and CO_2 yield under different oxygen concentration at 30 min reaction time, b) the zoom-in H_2 yield profile shown in a (5 mM formic-acid, 50 mL/min Ar/O_2 flow through, 100 mg catalyst).

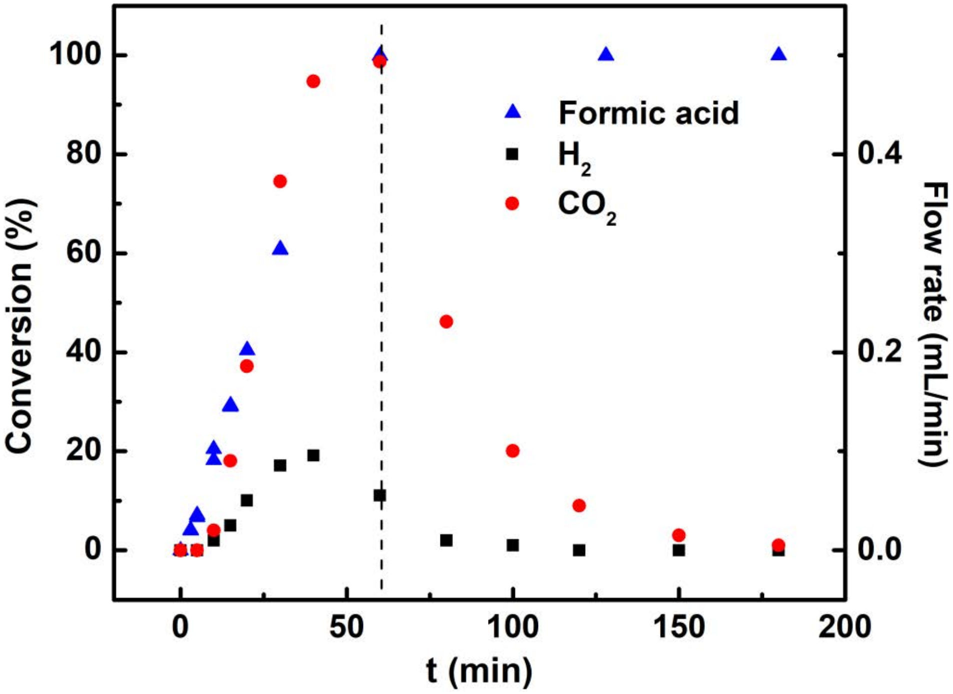

Figure A4. Formic-acid conversion, H_2 and CO_2 production rate plot with reaction time (100 mg catalyst, 5 mM formic-acid, 1 vol% oxygen, 50 mL/min Ar/O_2 flow through).

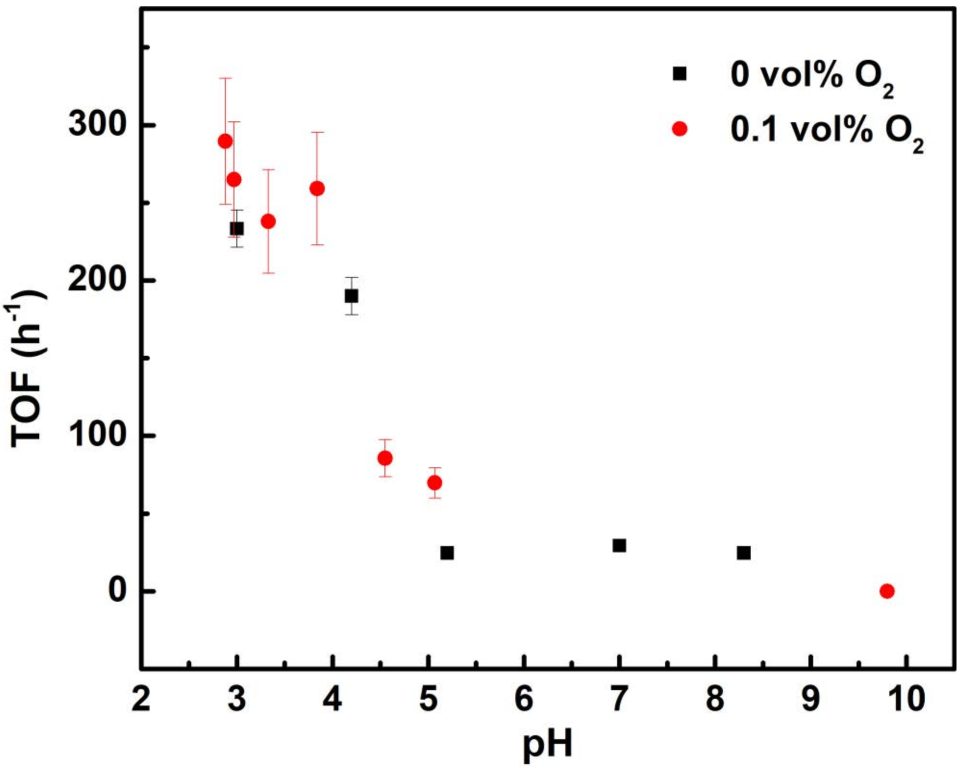

Figure A5. Apparent initial TOF plots with different pH of the solution and oxygen concentration (5 mM formic-acid, 50 mL/min Ar flow through or 50 mL/min Ar/O_2 (0.1 vol%) flow through, 100 mg catalyst) (The reaction rate at pH above 5 is at the detection limit of the measurement under inert condition).

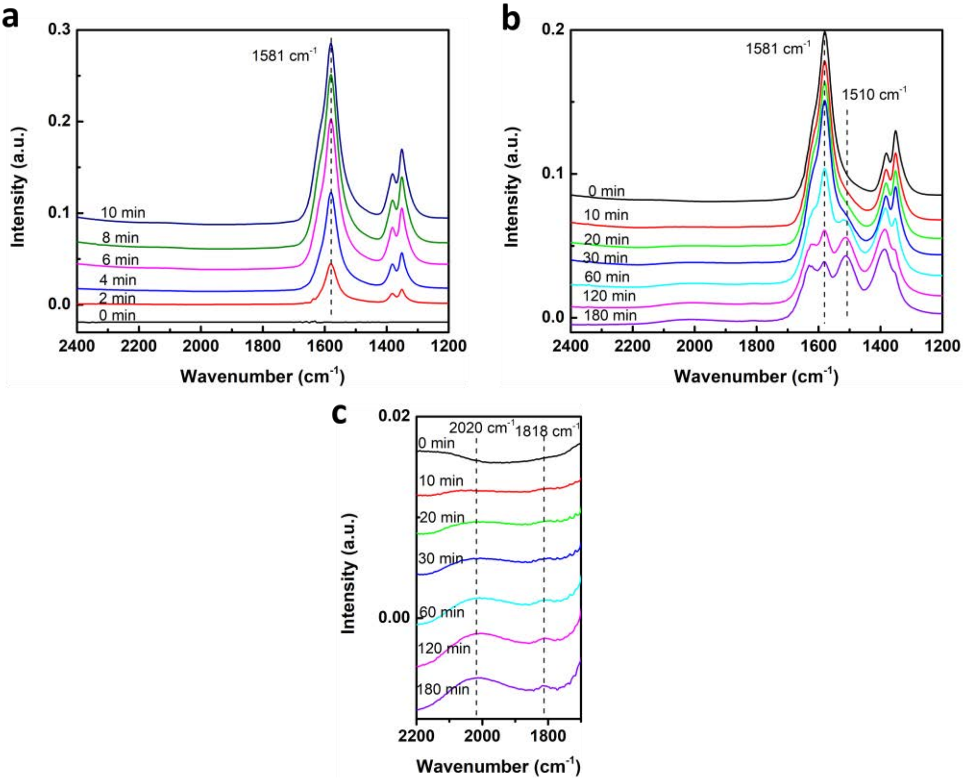

Figure A6. a) ATR-IR spectra of formate decomposition at pH = 5 for 10 min, b) after stopping the flow, mimicking a batch reaction during another 180 min, c) the same figure of b with a zoom-in the range of 1700 and 2200 cm^{-1} (5 mg 1 wt% catalyst on ZnSe, 10 mM formic-acid solution, 0.5 mL/min flow rate).

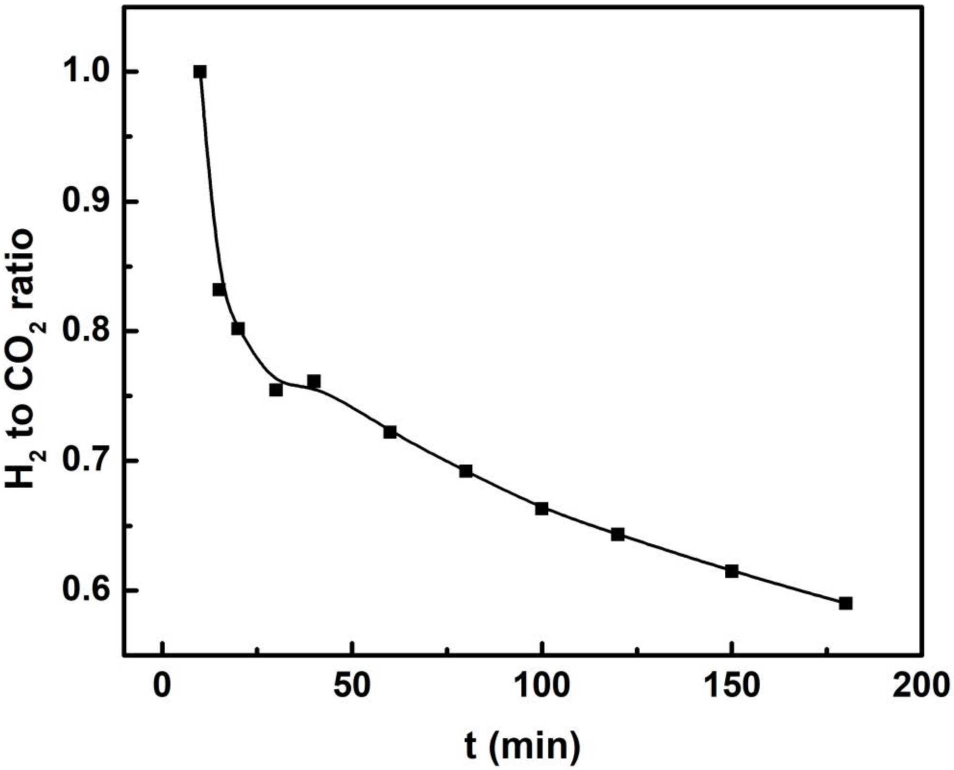

Figure A7. H_2 to CO_2 ratio plots with time under 0.1 vol% O_2 condition (5 mM formic-acid, 50 mL/min Ar/O_2 flow through, 100 mg catalyst).

1. Internal mass transfer

Weisz-Prater criterion is normally used as the criteria to estimate whether pore diffusion resistance can significantly influence the reaction rate [1,2].

$$C_{wp} = \frac{R_{obv} \times L^2 \times \rho_{Cat}}{C_s \times D_{eff}} \qquad eq11$$

Where R_{obv} is the reaction rate per mass of catalyst (mol*s^{-1}*kg^{-1}), L is the characteristic length (m), ρ_{Cat} is the density of the catalyst particles (1059 kg*m^{-3}), C_s is the reactant concentration at the particle surface (5 mol*m^{-3}), and D_{eff} is the effective diffusivity (m^2*s^{-1}).

$$L = \frac{d_p}{3} \qquad eq12$$

$$D_{eff} = \frac{D_{AB} \times \phi}{\tau} \qquad eq13$$

In which d_p is radius of the catalyst particles ($5*10^{-6}$ m), D_{AB} is the bulk diffusion coefficient of formic-acid (1.5×10^{-9} m^2*s^{-1}) [3], ϕ is the particle porosity, normally between 0.2 and 0.7, based on the BET measurement, here we use 0.7, and τ is the tortuosity, normally varies between 1 and 10, here we choose 3.

Table A1 shows oxygen the Weisz-Prater criterion concentration varies calculated as calculated for experimental data obtained at different oxygen concentrations. All values are well smaller than 1, meaning that internal mass transfer limitation has negligible influence on the reaction rate.

Table A1. At different reaction conditions, calculate the formic-acid Weisz-Prater criterion.

Formic-acid concentration (mM)	Oxygen concentration (vol%)	Formic-acid Weisz-Prater
5	0	0.003
5	0.1	0.004
5	2	0.008

2. External mass transfer

The external mass transfer limitation can validated by comparing between reaction rate and liquid-solid mass transfer rate. No liquid-solid mass transfer limitation are expected if liquid-solid mass transfer rate is much larger than the observed reaction rate [4]:

$$rate_{l-s} \gg rate_{obv} \qquad eq14$$

Where $rate_{l-s}$the estimated liquid-solid is mass transfer rate, and $rate_{obv}$ is observed reaction rate. The mass transfer is first order. So the maximum mass transfer rate at concentration C_s in the bulk of the liquid, can be calculated by the following equation:

$$rate_{l-s} = k_{ls} * a_s * C_s \quad eq15$$

Where k_{ls} is liquid-solid mass transfer coefficient, a_s geometric surface area of the catalyst per volume of solution.

The L-S mass transfer coefficient for formic acid is calculated according to the following expression:

$$k_{ls} = \frac{D_{AB} * Sh}{d_h} \quad eq16$$

in which D_{AB} is the formic acid diffusion coefficient in pure water (1.5×10^{-9} m^2*s^{-1}), d_h is the hydrodynamic size of the catalysts ($1.5*10^{-5}$ m). In a typical slurry tank reactor, as the small particles essentially move with the liquid, with limited shear at the surface of the particles, this indicated the value of Sh is rather similar to the value for a particle in stagnant liquid (Sh = 2).

$$k_{ls} = \frac{1.5 * 10^{-9} * 2}{1.5 * 10^{-5}}\ m * s^{-1} = 2 * 10^{-4}\ m * s^{-1}$$

The geometric surface area of the catalyst per volume of solution is:

$$a_s = \frac{A_p * m}{\rho_c * V_p * V_R} \qquad eq17$$

Where A_p is the geometric surface area of one catalyst particle (m^2), m is the mass of the catalyst in the experiments ($10*10^{-5}$ kg), V_p is the volume of one catalyst particle (m^3), and V_R is the volume of reaction solution ($3*10^{-4}$ m^{-3}).

$$a_s = \frac{4\pi * (1.5 * 10^{-5}\ m)^2 * 10 * 10^{-5}\ kg}{1059\ kg * m^{-3} * \frac{4\pi}{3} * (1.5 * 10^{-5}\ m)^3 * 3 * 10^{-4}\ m^3} = 62.95\ m^{-1}$$

The mass transfer rate constant was then calculated by multiplying the mass transfer coefficient by the geometric surface area of the catalyst per volume of solution:

$$k_{ls} * a_s = 2 * 10^{-4} * 62.95\ s^{-1} = 1.26 * 10^{-2}\ s^{-1}$$

For an example, at formic acid concentration is 5 mM, the mass transfer rate is 3.78 mM*min^{-1}, which is significantly larger than even the highest reaction rate (0.1 mM*min$_{-1}$) at same formic acid concentration. Therefore, L-S mass transfer is not limiting.

Reference

[1] P. B. Weisz, C. D. Prater, in *Adv. Catal.*, **1954**, pp. 143–196.

[2] J. C. Vedrine, in *NATO ASI Ser. Ser. B Phys.*, Springer US, Boston, MA, **1983**, pp. 505–536.

[3] L. Dunn, R. Stokes, *Aust. J. Chem.* **1965**, *18*, 285.

[4] A. J. Frierdich, J. R. Shapley, T. J. Strathmann, *Environ. Sci. Technol.* **2008**, *42*, 262–269.

Chapter 5

Formic acid generating *in-situ* H_2 and CO_2 for nitrite reduction in aqueous phase

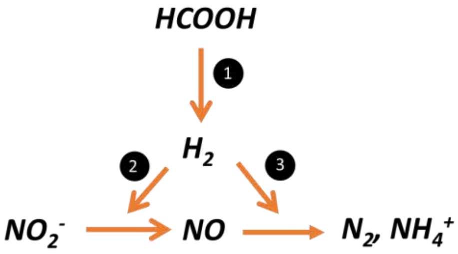

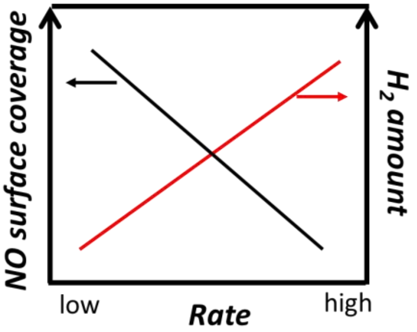

Abstract:

The aim of this work is to use formic-acid as the in-situ hydrogen supplier and pH buffer to reduce nitrite. The catalytic performance of Pd/γ-Al_2O_3 were evaluated. Formic-acid can reduce nitrite in the pH range between 4.5 and 8, producing negligible amounts of ammonium. By investigating the effect of pH, traces of oxygen and formic-acid concentration on the rates, it is proved that the rate of conversion on nitrite with formic-acid as well as the rate of formic-acid decomposition are controlled by competitive adsorption on Pd of nitrite, forming NO, and formic-acid, forming adsorbed hydrogen and CO_2. The adsorbed species are studied with ATR-IR technique. Formic-acid decomposition required an ensemble of empty sites indicating low surface coverage with NO. The NO surface coverage decreases with adsorbed hydrogen surface coverage increasing, which in turn depends on the rate of formic-acid decomposition. This causes order 1.4 in formic-acid for formic-acid decomposition. When the pH of the solution is below 4.5, homogeneous disproportionation reaction of nitric acid occurs, resulting in catalyst poisoning with NO generated by the homogeneous disproportionation reaction. The catalyst shows no activity at pH above 8 due to the fact that formate ions are not reactive under our condition.

1. Introduction

Nitrate and nitrite pollution in water is becoming a severe problem globally, caused by emissions from agriculture and industry [1], threatening human health, including blue-baby-syndrome, high blood pressure, diabetes, liver damage, and various types of cancers [2–5]. Therefore, the World Health Organization (WHO) maximized acceptable concentrations in drinking water, i.e. 50 mg/L for nitrate, 3 mg/L for nitrite, and 1.5 mg/L for ammonia, respectively [6].

Nitrate and nitrite ions can be removed from water by several techniques, including biological denitrification, ion exchange and catalytic reduction. Biological denitrification is not applicable for drinking water, due to lack of nutrients to sustain the growth of bacteria [7]. Ion exchange results in formation of a concentrated brine after the treatment [7]. Among these techniques, catalytic reduction of nitrate by reducing agents had been considered as one of the most promising methods because it could convert nitrate to harmless nitrogen gas with a high efficiency [8–23]. For practical applications, further improvement of the selectivity to N_2 is necessary for purification of drinking water, preventing any formation of ammonia.

Since the first paper on catalytic reduction of nitrate by Vorlop and Tacke [3], numerous studies [7,24–32] have been reported, mostly using hydrogen as the reducing agent. It is well known that reduction of nitrate proceeds in two steps requiring bimetallic catalyst [33–38]. First, nitrate is reduced to nitrite, requiring a non-noble promotor such as e.g. Cu, which is generally rate determining. Furthermore, conversion of nitrite is much faster and determines the selectivity to ammonium and nitrogen. The reactions are shown below. Therefore, in this paper nitrite reduction is studied as a model reaction.

$$NO_3^- + H_2 \xrightarrow{Pd-Cu/\gamma-Al_2O_3} NO_2^- + H_2O \qquad eq\ 1$$

$$2NO_2^- + 3H_2 + 2H^+ \xrightarrow{Pd/\gamma-Al_2O_3} N_2 + 4H_2O \qquad eq\ 2$$

$$NO_2^- + 3H_2 + 2H^+ \xrightarrow{Pd/\gamma-Al_2O_3} NH_4^+ + 2H_2O \qquad eq\ 3$$

Using hydrogen as reducing agent has the disadvantages in terms of hydrogen transportation and storage at high pressure. In addition, it is well known that the nitrogen selectivity can be improved by decreasing the pH [39–42], e.g by adding co-feeding CO_2 in many lab studies. For practical application, this method is less suitable. Note that the reaction consumes protons and the pH will increase during reaction. Formic-acid, however, can be used as an alternative reductant, decomposing not only H_2 but also CO_2, buffering the solution pH during the reaction. A few studies report on catalytic reduction of nitrate with formic-acid as the reducing agent [35,43–45], reporting low selectivity to ammonium.

IR spectroscopy used with an Attenuated Total Reflection in-situ cell (ATR-IR), depositing a thin catalyst layer on the internal reflection crystal, is an ideal technique for studying adsorbed species at the solid–liquid interface. In our group, ATR-IR spectroscopy has been used for CO oxidation and nitrite reduction with H_2 both in aqueous phase [46–50]. NO adsorbed on Pd was observed as an important intermediate species during nitrite reduction, which readily converts to N_2.

The goal of this work is to study the performance of Pd catalyst in reduction of nitrite with formic-acid under well controlled conditions, including pH, the presence of oxygen traces and the formic-acid concentration. ATR-IR technique is used to understand the intermediate species during the reaction. The interplay between formic-acid decomposition and nitrite reduction is discussed.

2. Experimental section

2.1. Materials

Commercial γ-Al_2O_3 powder purchased from BASF with a surface area of 195 m^2/g, was used as catalyst support in this study. Tetra-ammine-palladium (II) nitrate solution (10 wt% in H_2O, 99.99 %), purchased in Sigma-Aldrich, was used as catalyst precursor. Sodium nitrite (99.99 %) which is purchased from Sigma–Aldrich is used to prepare nitrite (NO_2^-) solutions. Aqueous ammonium solution (50 % v/v water, Sigma-Aldrich) is used to adjust the pH for the catalyst preparation. Formic acid (≥ 98 %), sodium formate and sodium hydroxide were purchased from Sigma-Aldrich. All aqueous solutions were prepared using ultra purified water obtained from a water purification system (Millipore, Synergy).

2.2. Catalyst preparation

The preparation method is described in detail elsewhere [51]. In brief, Pd/γ-Al_2O_3 catalyst containing 1 wt% of palladium, was prepared by wet impregnation. Typically 10 gram of the sieved support (particles smaller than 38 μm, mean particles size 22 μm) was calcined at 600 ^oC for 4 hours to remove any organic contamination. Then the support was suspended in 100 mL milliQ water and the pH of the solution was adjusted to 9 by adding 2 mL ammonia solution, as checked with a pH meter (Hanna instruments, pH 209). Then, 3 gram of the palladium precursor solution ($Pd(NO_3)_2{\cdot}4NH_3$) was slowly added to the suspension. The suspension was stirred at room temperature for at least 1 hour. The solution was transferred to a rotary evaporator to remove the liquid during 2 hours. Finally, the catalyst was calcined in air at 400 ^oC for 3 hours (heating rate 5 K/min), followed by reduction in hydrogen (30 mL/min) diluted with nitrogen (total 60 mL/min) at the same temperature for 3 hours. Catalyst with 3 wt% Pd loading was prepared following the same procedure, except for adding more Pd precursor.

2.3. Catalyst characterization

The surface area of the prepared catalyst was determined based on the BET N_2-adsorption isotherms obtained at 77 K (Micromeritics Tristar). The Pd loading was determined with X-ray fluorescence spectroscopy, XRF (Philips PW 1480). CO chemisorption at room temperature was used to determine the accessible metal surface area (Chemisorb 2750, Micromeritics). Typically, the sample was reduced at room temperature in hydrogen for 1 hour and then flushed with He at the same temperature for 0.5 hour. Then CO was introduced as pulses and the responses were recorded using a TCD detector. We assumed that the stoichiometric ratio of number of adsorbed CO molecules and number of accessible Pd surface atoms is one.

2.4. Catalytic tests and analysis

Activity and selectivity of the catalysts were measured in a 1 L batch reactor at 20 °C and atmospheric pressure. The glass reactor with 10 cm inner diameter and 12.7 cm height, has four connections on the reactor lid for gas-in, gas-out, sampling and stirring shaft, respectively (**Chapter 2**, Figure A1). The possible reactions involved in formic-acid decomposition and nitrite reduction are given in the following equations:

$$2NO_2^- + 3H_2 + 2H^+ \xrightarrow{Pd/\gamma-Al_2O_3} N_2 + 4H_2O \qquad eq\ 2$$

$$NO_2^- + 3H_2 + 2H^+ \xrightarrow{Pd/\gamma-Al_2O_3} NH_4^+ + 2H_2O \qquad eq\ 3$$

$$HCOOH \xrightarrow{Pd/\gamma-Al_2O_3} CO_2 + H_2 \qquad eq\ 4$$

$$HCOOH \xrightarrow{Pd/\gamma-Al_2O_3} CO + H_2O \qquad eq\ 5$$

Typically for a standard experiment, 0.10 g catalyst was suspended in 0.3 L milliQ water and stirred at 625 rpm under 1 bar helium for at least 1 h, removing dissolved oxygen. Reaction is initialized by introducing of 3 mL $NaNO_2$ solution (100 mmol/L) and 3 mL formic-acid (1 M) at the same time in the glass reactor. The pH of the solution was varied between 2.8 and 9 by adding appropriate amounts of the sodium hydroxide solution (1 M) to formic-acid solution (1 M). The initial pH of the solution was measured after injecting the concentrated formic-acid and sodium hydroxide solution to the bulk solution. The formic-acid concentration was varied between 5 mM and 40 mM. The formic-acid concentration is defined as the sum of the concentrations of formic-acid and formate ions termed as formic-acid throughout the paper. During the experiment, the reactor is flushed with 50 mL/min He. This is termed as "inert-flow-through", in contrast to "ambient-batch" meaning that the reactor is not flushed with inert gas both before and during the reaction, implying batch operation regarding the gas phase.

Table 1. Range of operating conditions of the reduction of nitrite with formic-acid in a slurry reactor

Reaction temperature, °C	20
Reaction volume, L	0.3
Stirring speed, rpm	625
Average catalyst partials size, µm	22
Total operating pressure, bar	1
Amount of the catalyst, g	0.05 - 0.1
Initial nitrite concentration, mmol/L	1
Initial formic-acid concentration, mmol/L	5 - 40
pH of the solution	2.5 – 9
Mole of oxygen at ambient atmosphere without degassing (dissolved in liquid and above the liquid), mol [52]	0.0066

Samples were taken using a 2.5 mL syringe (BD Plastipak), in which the samples were filtered through a syringe filter (PTFE, 0.2 µm, Whatman), removing the catalyst particles. Formic-acid, nitrite, nitrate and ammonium concentrations in the reactants and products were measured with ion-chromatography (DIONEX, ICS 3000) equipped with an UltiMate autosampler. Since it is well known that ammonia and nitrogen are the only products formed during reduction of nitrite [20,40,46,53,54] including nitrite reduction with formic-acid [45], nitrogen was calculated based on the mass balance. All experiments on reduction of nitrite with formic-acid were performed while flowing He through the reactor as described, resulting in concentrations of gas products below the detection limit of the GC.

The formic-acid conversion, nitrite conversion, ammonium yield, nitrate yield and nitrogen yield are calculated by the following equations:

$$HCOO^{-}\ conversion = \frac{[HCOO^{-}]_{t0} - [HCOO^{-}]_{t1}}{[HCOO^{-}]_{t0}} * 100 \qquad eq\ 6$$

$$NO_2^{-}\ conversion = \frac{[NO_2^{-}]_{t0} - [NO_2^{-}]_{t1}}{[NO_2^{-}]_{t0}} * 100 \qquad eq\ 7$$

$$NH_4^{+}\ yield = \frac{[NH_4^{+}]_{t1}}{[NO_2^{-}]_{t0}} * 100 \qquad eq\ 8$$

$$NO_3^{-}\ yield = \frac{[NO_3^{-}]_{t1}}{[NO_2^{-}]_{t0}} * 100 \qquad eq\ 9$$

$$N_2\ yield = \frac{1}{2} \times (NO_2^{-}\ conversion - NH_4^{+}\ yield) \qquad eq\ 10$$

Where $[HCOO^{-}]_{t0}$ is the initial concentration of formic-acid, $[NO_2^{-}]_{t0}$ is the initial nitrite concentration, $[HCOO^{-}]_{t1}$, $[NO_2^{-}]_{t1}$, $[NH_4^{+}]_{t1}$ and $[NO_3^{-}]_{t1}$ are the each compound concentration at t1.

2.5. ATR-IR

The preparation of catalyst layer on the ATR crystal is described elsewhere [42,46–48,55]. Briefly, a suspension containing 0.1 g 3 wt% Pd/γ-Al_2O_3 or γ-Al_2O_3 dispersed in 20 mL 2-propanol was prepared. In order to prevent cracking of the catalyst layer, the suspension was sonicated with an ultrasonic processor (Fisher Scientific-705) for 1 hour. Subsequently, the suspension was spray-coated on a trapezoidal ZnSe crystal (52.5 mm * 20 mm* 2 mm, facet angle 45 °, Anadis instruments BV), which was placed on a hot plate at 150 °C, resulting in about 5 mg catalyst on the crystal. Then, the coated crystal was calcined at 300 °C (1 °C/min) for 1h in N_2 atmosphere (20 mL/min). It was mounted in a home-build in-situ Attenuated Total Reflection Infrared Spectroscopy (ATR-IR) cell which has been described in detail elsewhere [46,55]. Figure 1a shows a SEM micrograph of the catalyst layer in top view, showing a reasonable homogeneous layer coated on the surface. Figure 1b shows that the thickness of the layer is about 5 µm and uniform. The experimental setup is shown in below Scheme 1. The cell was mounted in the sample compartment of an infrared spectrometer (Tensor 27, Bruker) equipped with a liquid nitrogen cooled MCT detector. All the liquid flows were pumped by a peristaltic pump (Verderflex) downstream of the ATR-IR cell, which is important to prevent formation of gas bubbles in the cell (Scheme 1).

Once the cell was assembled in the IR spectrometer, it was flushed with Ar/H_2O with a flow rate of 0.5 mL/min until a stable water spectrum was obtained. Subsequently, the cell with the catalyst layer was flushed with different solutions, including nitrite (10 mM) both at pH 4 and 7 or mixture of formic-acid (10 mM) and nitrite solutions (10 mM), again at both pH 3 and pH 5. All solutions were degassed with Ar before the experiment for at least 3 h. ATR-IR spectra were recorded at room temperature (20 ± 1 °C) in an air-conditioned room. Each spectrum was acquired by averaging of 128 scans taken with a resolution of 4 cm^{-1}. The interval between the start of two subsequent spectra was 120 s. Once the water spectrum was stable, the background spectrum was collected. The catalyst layers were re-used a few time and comparable results were obtained, indicating that the catalyst layer is stable during the experiments.

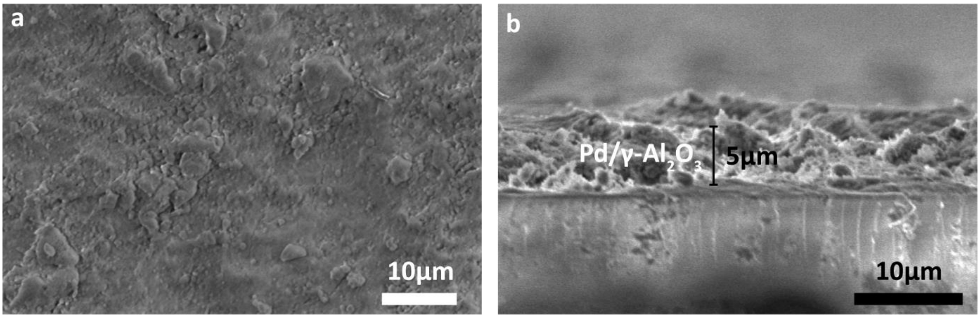

Figure 1. SEM micrographs of (a) top view and (b) cross section view of Pd/γ-Al_2O_3 on a glass plate with identical dimensions as the ZnSe crystal.

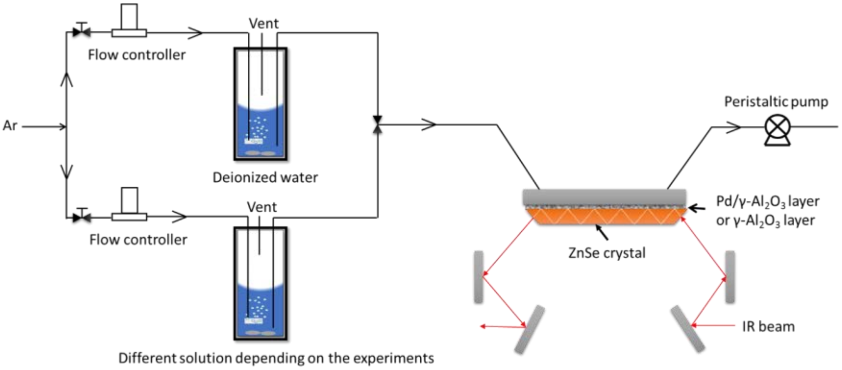

Scheme 1. Scheme of the ATR-IR setup.

3. Results

3.1. Characterization

Table 2 reports the Pd loading of the prepared catalysts, both close to the targeted values of 1 wt% and 3 wt%, respectively. The 1 wt% catalyst was used in the kinetic batch experiments, whereas 3 wt% catalyst was used for the ATR-IR experiments, increasing the intensity of IR adsorption bands of species adsorbed on the Pd surface. The specific surface area of the support and 1 wt% Pd/γ-Al$_2$O$_3$ catalyst are similar, indicating that the structure and porosity of the support remained unchanged. In contrast, 3 wt% Pd/γ-Al$_2$O$_3$ shows a minor decrease in surface area, indicating that some pores might be blocked. The metal dispersion for 3 wt% loading is lower than for 1 wt% metal loading, as expected.

Table 2. Characterization of two catalysts.

Catalyst materials	Pd loading (%)	Specific surface area (m^2*g)	Dispersion (%)
γ-Al$_2$O$_3$	N.A.	198	N.A.
1 wt% Pd/γ-Al$_2$O$_3$	0.9	195	56
3 wt% Pd/γ-Al$_2$O$_3$	3.1	180	35

3.2. Nitrite reduction with formic-acid; effect of pH

Figure 2 presents the results of two typical nitrite reduction experiments with formic-acid, at pH 2.8 and pH 4.8 respectively. We conducted the same experiment at different pH values in the window between 2.8 to 9. Figure 2a shows insignificant conversion of formic-acid at pH 2.8 over three hours reaction time. In contrast, nitrite converts significantly while formation of nitrate was observed. Since the Pd catalyst was exposed to ambient and was not reduced before the reaction, oxidation of nitrite by PdO might contribute. Based on the dispersion of Pd and assuming monolayer coverage with O, this can contribute maximal 3 % of the amount of nitrate detected in Figure 2a. Therefore, nitrate is mainly formed via another reaction, to be discussed later. Ammonium, the common side product of nitrite reduction, was not detected under pH 2.8 condition.

Figure 2b shows that formic-acid does react with nitrite at pH 4.8. The difference with pH 2.8 is that both formic-acid and nitrite are converted significantly, although conversion of nitrite is relatively slow. Furthermore, no nitrate is formed at pH 4.8. Formation of ammonium as side product is not detected in both experiments and remains below the detection limit in all experiments in this study, implying that the yield of ammonium is less than 0.1 %. Thus, nitrogen is the only significant product of reduction of nitrite with formic-acid, according to the overall redox reaction [45] :

$$3HCOO^- + 3H^+ + 2NO_2^- \rightarrow 3CO_2 + N_2 + 2H_2O + \ 2OH^- \quad eq11$$

This remarkable selectivity is ascribed to relatively slow decomposition of formic-acid, keeping the effective concentration of H_2 low, which is favorable for preventing ammonia formation [3,56]. In addition, CO_2 is also produced acting as a local pH buffer, keeping the pH low which is also known to suppress formation of ammonium [57,58].

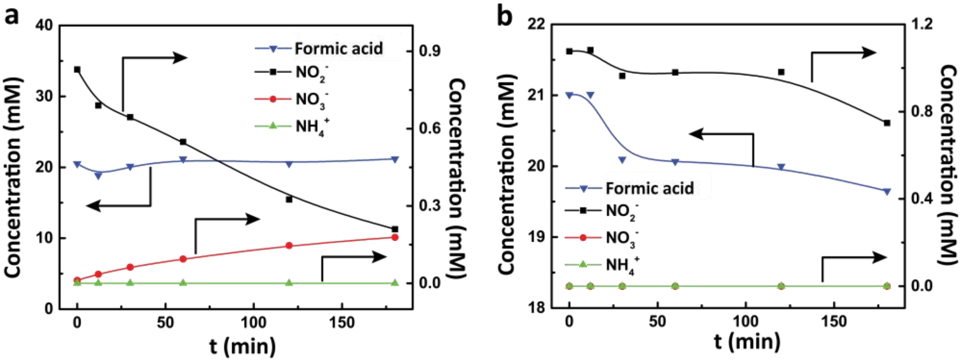

Figure 2. Concentration profile of formic-acid, nitrite, nitrate and ammonium at a) pH 2.8 and b) pH 4.8, respectively (100 mg 0.9 wt% catalyst, 20 mM formic-acid solution, and 1 mM nitrite, inert-flow-through, 50 mL/min He).

Figure 3 presents the influence of pH on formic-acid conversion, nitrite conversion and product distribution after 3 hours reaction time, including the final observations in Figure 2. Consistent with the data in Figure 2, no significant conversion of formic-acid is detected when the pH of the solution is below 4, whereas formation of nitrate is observed. In contrast, formic-acid is consumed and nitrite is hydrogenated to N_2 at pH 4.8 or higher, without any formation of NO_3^-. The catalyst showed maximal nitrite conversion without formation of nitrate at pH 4.8 and the activity dropped with further increasing pH. No conversion whatsoever of formic-acid and nitrite is observed at pH 9.

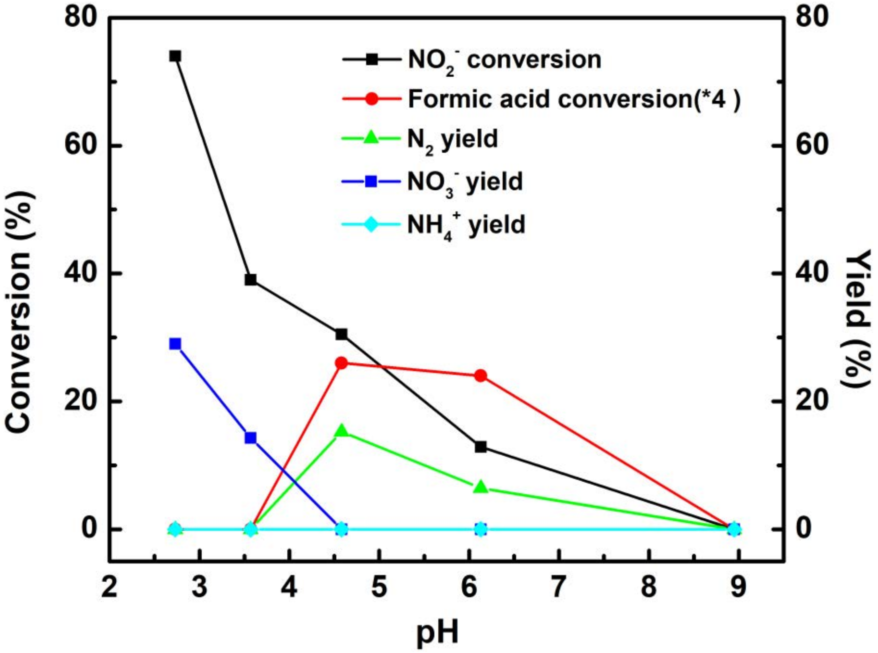

Figure 3. Nitrite conversion, formic-acid conversion and nitrate concentration under different pH and inert-flow-through mode after 3 hours (100 mg 0.9 wt% catalyst, 20 mM formic-acid, 1 mM nitrite, 50 mL/min He), formic-acid conversion is multiplied with a factor of four.

3.3. ATR-IR

3.3.1. Nitrite adsorption

Figure 4 presents the spectra obtained on the same samples exposed to nitrite solution for at least 10 minutes. Only one peak is observed at 1235 cm^{-1} on both ZnSe and Al_2O_3 layer (dark yellow line and blue line), which is assigned to free nitrite, in good agreement with previous studies by Ebbesen et al. [48,50,55] and Zhao et al. [42]. The red line displays the spectrum of Pd/Al_2O_3 exposed to nitrite at pH 7. In addition to the peak at 1235 cm^{-1}, also observed on bare ZnSe and Al_2O_3, two additional peaks are found at 1330 and 1425 cm^{-1}, assigned to adsorbed NO_x^- (x=2, 3) species [55]. Note that the catalyst was stored in ambient and was not reduced before the experiment, so that adsorbed oxygen on Pd might oxidize nitrite to nitrate. The noise between 1600 and 1680 cm^{-1} is an artifact caused by the subtraction of the water signal [59,60]. The black line represents the spectrum on Pd/Al_2O_3 exposed to nitrite at pH 4. Three peaks at 1235, 1330 and 1425 cm^{-1} are identical with the experiment at pH 7. However, an extra peak is observed at 1723 cm^{-1}, assigned to NO adsorbed on Pd, based on our previous ATR-IR studies on nitrite reduction [42,46,48,50,55]. Apparently, adsorbed NO (NO_{ads}) is formed at pH 4 and not at pH 7.

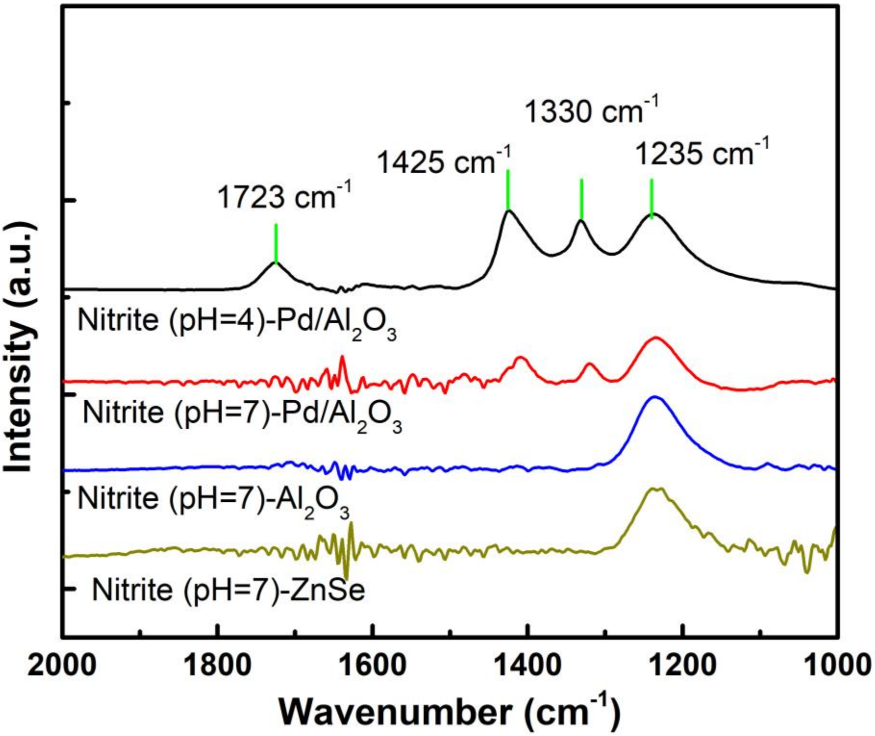

Figure 4. ATR-IR spectra obtained after exposure to nitrite solutions: dark yellow line represents the nitrite spectrum on ZnSe at pH 7, blue line represents nitrite spectrum on Al_2O_3 layer under pH 7, red line and black represents nitrite spectrum on Pd/Al_2O_3 layer under pH 7 and 4, respectively (5 mg catalyst, 3 wt% Pd/Al_2O_3, 10 mM nitrite, 0.5 mL/min flow rate).

3.3.2. Reaction of formic-acid and nitrite

Figure 5a shows ATR-IR spectra during flowing a solution containing both formic-acid and nitrite at pH 3 over the catalyst layer for 38 minutes. The intensities of the peaks increase with time. Several peaks observed can be assigned based on the results in the previous sections. The strong peak at 1581 cm^{-1} is assigned to free formic-acid (**Chapter**

4, Figure 8) and the peak at 1235 cm^{-1} is assigned to free nitrite. The peak at 1716 cm^{-1} is assigned to NO adsorbed on Pd as discussed above as well [42,46,48,50,55] and the small redshift is likely due to differences in the surface coverage, influencing the extent of dipole-dipole coupling. The complex overlapping peaks between 1300 and 1500 cm^{-1} are tentatively assigned to free formic-acid in water (**Chapter 4**, Figure 8, 1380 and 1350 cm^{-1}) and NO$_x^-$ (x = 2, 3) species (Figure 4, 1425 and 1330 cm^{-1}).

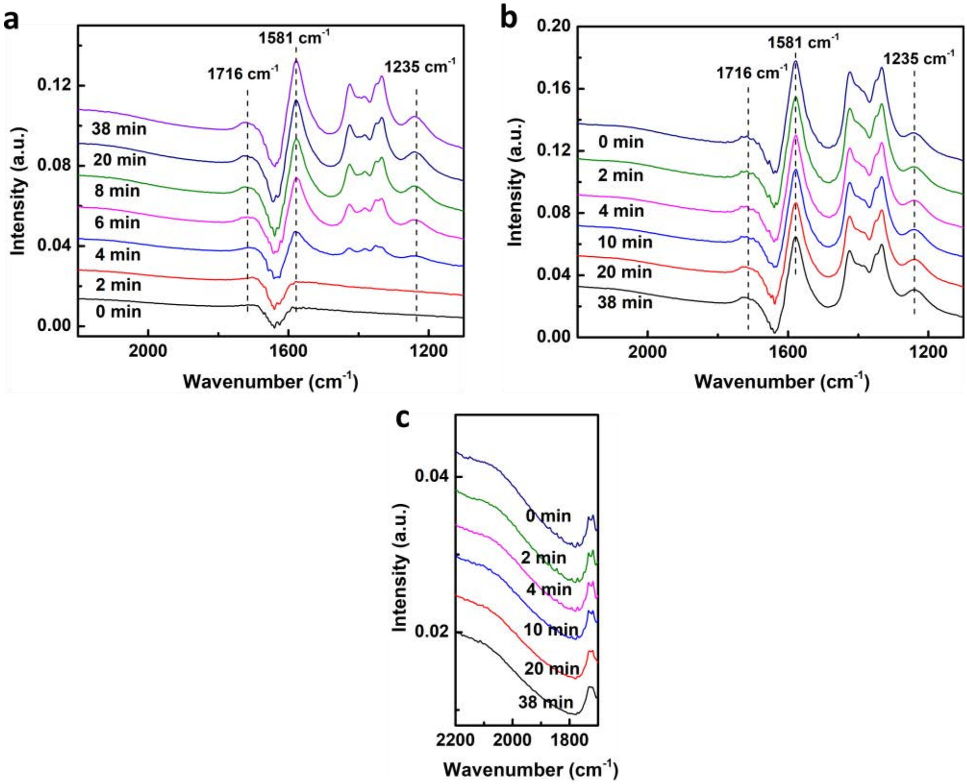

Figure 5. a) Reduction of nitrite with formic-acid at pH 3 for 38 min, b) after stopping the flow to mimic the batch reaction for another 38 min, c) zoom in the range between 1700 and 2200 cm^{-1} in Figure b (5 mg 3 wt% catalyst on ZnSe, 10 mM formic-acid, 10 mM nitrite, 0.5 mL/min flow rate).

After 38 min, the liquid flow was stopped, leaving the solution in the reactor in contact with the catalyst layer, mimicking a batch reaction experiment. The important observation in Figure 5b is that the spectrum does not change at all with time, indicating there is no detectable reaction of formic-acid with nitrite, in good agreement with observations in batch experiments at low pH, as described above. Figure 5c shows a zoom-in of Figure 5b in the range between 1700 and 2200 cm^{-1} in order to see the C-O vibration peaks. It is clear that no peaks assigned to adsorbed CO are observed.

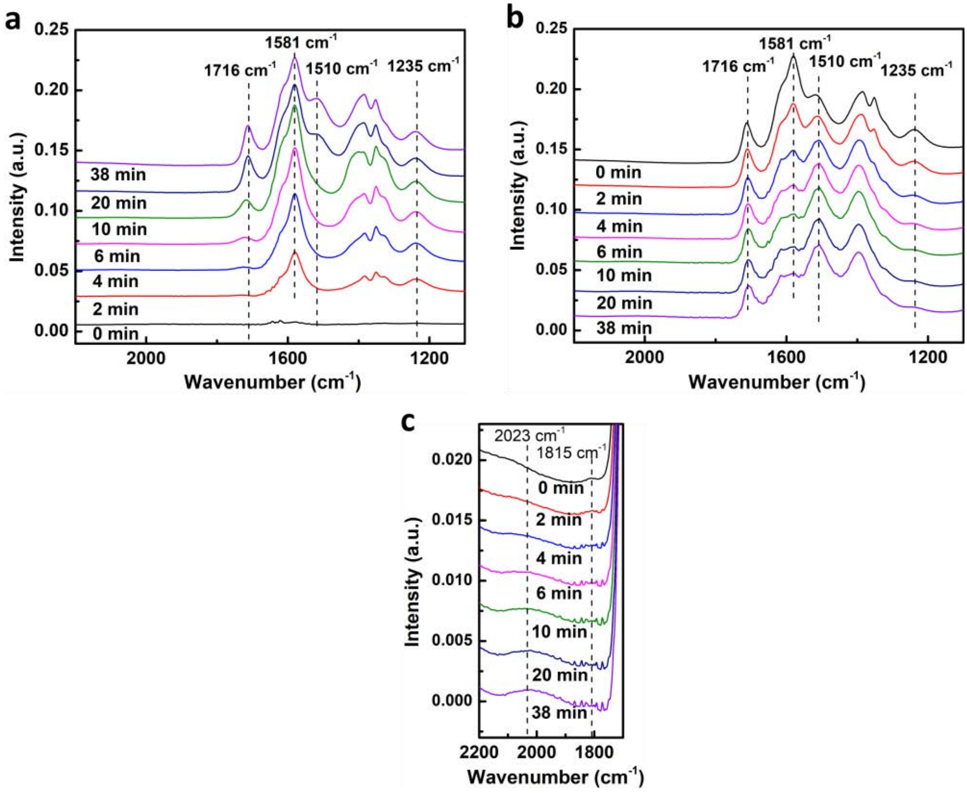

Figure 6. a) ATR-IR spectra of reduction of nitrite with formic-acid at pH 5 for 38 min, b) after stopping the flow, mimicking a batch reaction during another 38 min, c) zoom in Figure b in the range of 1700 and 2200 cm^{-1} (5 mg 3 wt% catalyst on ZnSe, 10 mM formic-acid solution, 10 mM nitrite, 0.5 mL/min flow rate).

Figure 6a shows time-evolved ATR-IR spectra during exposure to formic-acid and nitrite solution at higher pH, i.e. pH 5. Clearly, the intensities of all peaks increase again with time. It is noticeable that a new shoulder peak is observed at 1510 cm^{-1} with increasing intensity in time. Based on our previous study on nitrite hydrogenation with ATR-IR, the peak at 1510 cm^{-1} was assigned to $NH_{2,ads}$ on the Pd surface (1510 cm^{-1}) by

Ebbesen et al. [46] as intermediate species during nitrite reduction. It should be noted though that a peak at the same wavelength (1510 cm^{-1}) is also observed during decomposition of formic-acid shown in **Chapter 4,** Figure A6b. The other peaks observed in the window between 1300 and 1500 cm^{-1} are assigned to free formic-acid and adsorbed NO_x^- (x=2, 3). Possibly carbonate, generated during the reaction, also contributes to the complex set of IR peaks [61,62]. Summarizing, the IR peaks in the window between 1300 and 1500 cm^{-1} are not well understood.

After flowing during 38 min, the flow was again stopped to mimic a batch experiment. Figure 6b shows that peak intensities change significantly with reaction time, in contrast to Figure 5b. Both peaks assigned to formic-acid (1581 cm^{-1}) and bulk nitrite (1235 cm^{-1}) gradually disappeared, indicating conversion of formic-acid via reaction with nitrite. The peaks assigned to adsorbed NO (1716 cm^{-1}) and intermediate species (1510 cm^{-1}) appear stable during the experiment. Figure 6c shows the zoom-in Figure 6b in the range of typical vibration in CO_{ads}. Peaks assigned to chemisorb CO are appear slowly during 38 minutes batch experiment.

3.4. Effect of oxygen on nitrite reduction

Table 3 reports the nitrite conversion and formic-acid conversion achieved after 2 hours reaction with air present in the reactor, as described as ambient-batch mode and inert-flow-through mode. The reaction rate was much faster under inert-flow-through condition in absence of any oxygen. The nitrite conversion under inert-flow-through condition is three times higher than in presence of oxygen, whereas the effect on formic-acid conversion is weaker.

The efficiency of formic-acid to reduce nitrite is defined as below:

$$Formic - acid\ efficiency = \frac{amount\ of\ formic{-}acid\ used\ for\ nitrite\ reducion}{total\ amount\ of\ converted\ formic{-}acid} \times 100 \qquad eq12$$

The presence of traces of oxygen clearly decreases the efficiency and a larger fraction of formic-acid apparently decomposes instead of reacting with nitrite.

Table 3. Formic-acid (pH = 5) reduces nitrite, influences of the oxygen content (100 mg 0.9 wt% catalyst, 1 mM nitrite, 20 mM formic-acid)

Atmosp-here	Initial nitrite (mM)	Initial formic-acid (mM)	Formic-acid conversion at 2 h (%)	Nitrite conversion at 2 h (%)	Formic-acid efficiency (%)
Inert-flow-through	1	20	5.1 ± 0.3	33.3 ± 1	48.4 ± 4
Ambient-batch	1	20	3.1 ± 0.1	8.9 ± 0.1	21.7 ± 1

3.5. Effect of formic-acid concentration

The influence of the concentration of formic-acid on the rate of nitrite reduction was measured between 5 and 40 mM under inert-flow-through at pH 5. Figure A1, A2, A3 and A4 present the concentration profiles and Table 4 summarizes the results, reporting the conversion of formic-acid and nitrite after 2 hours reaction. Nitrite conversion increases with increasing formic-acid concentration as expected. Surprisingly, also the formic-acid conversion increases with increasing initial concentration.

Table 4. Formic-acid and nitrite conversion with different formic-acid concentration at pH 5 and inert-flow-through condition (100 mg 0.9 wt% catalyst, 1 mM nitrite)

Initial formic-acid (mM)	Initial nitrite (mM)	Formic-acid conversion at 2 h (%)	Nitrite conversion at 2 h (%)	Formic-acid efficiency (%)
40	1	12.4 ± 0.1	66.1 ± 0.1	20 ± 1
20	1	5.1 ± 0.3	33.3 ± 1	48.4 ± 4
10	1	4.6 ± 1	13 ± 3	42.8 ± 19
5	1	2.4 ± 0.1	0.94 ± 0.05	100 ± 10

3.6. Effect of H_2 on nitrite reduction with formic-acid

Figure 7 presents concentration profiles of formic-acid, nitrite, ammonium and nitrate during reduction of nitrite with formic-acid at pH 3. Pure H_2 gas was introduced to the reactor after two hours, resulting in fast conversion of nitrite without producing any detectable ammonium, i.e. the concentration remained below the detection limit of 1 μM.

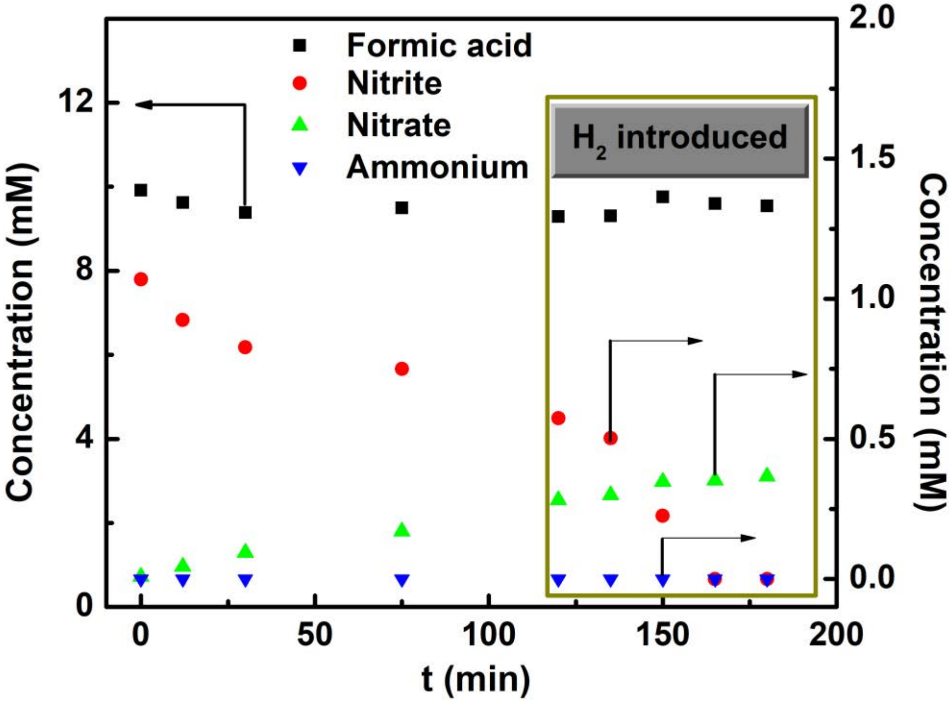

Figure 7. Nitrite reduction with formic-acid (pH = 3) performed under ambient-batch mode (100 mg 0.9 wt% catalyst, 10 mM formic-acid, 1 mM nitrite), hydrogen is introduced (1bar, 100 mL/min flow rate) in the solution after 2 h of reaction.

4. Discussion

The results obtained at low pH will be discussed first, followed by a detailed discussion for the case of intermediate pH values resulting in reaction of nitrite and formic-acid. Finally, the absence of any activity at high pH will be discussed.

4.1. Nitrite reduction with formic-acid at low pH

As shown in Figure 2a and 3, formic-acid is not converted at low pH. Nitrite was consumed, and nitrate was formed at the same time. Garron et al. [45] reported a similar phenomenon, i.e. formation of nitrate at low pH, but also claiming that at the same time nitrite was reduced by formic-acid, which is not in agreement with our results. The catalysts are different, as Garron et al. used a 5 wt% Pd/SiO_2 catalyst, a much higher loading compared to the catalyst used in this study, i.e. 0.9 wt% Pd/Al_2O_3. The ATR data in Figure 5b, mimicking a batch experiment, confirm that nitrite and formic-acid are not converted under low pH condition, throughout the experiment.

Note that the reactant concentration and catalyst amount are quite different in the ATR-IR experiment compared to a normal batch experiment. The molar ratio of formic-acid/nitrite/Pd-surface equals to 719:36:1 in a batch experiment, in contrast to the ATR experiment with molar ratios of formic-acid/nitrite/Pd-surface of 2069:2069:1. However, the reaction rates, estimated according to the rate of disappearance of nitrite in Figure 6b and the rate in batch experiments, normalized on the number of Pd atoms in the surface of the catalyst, are very similar, as shown in a detailed calculation in Appendix section 1.

Nitrate formation was suggested to proceed as a homogeneous disproportionation reaction of nitrous-acid forming NO and nitric-acid (eq 14) exclusively at sufficiently low pH, shifting the equilibrium in equation 13 to the right [45,63]. The reaction in equation 15 closes the catalytic cycle with acid, in this case formic-acid, acting as the catalyst [63].

$$HCOOH + NO_2^- \leftrightarrow HNO_2 + HCOO^- \quad eq\ 13$$

$$3HNO_2 \rightarrow 2NO + HNO_3 + H_2O \quad eq\ 14$$

$$HNO_3 + HCOO^- \rightarrow NO_3^- + HCOOH \quad eq\ 15$$

As shown in Figure 4, adsorbed NO is observed with ATR-IR at pH 3 based on the peak at 1723 cm^{-1}, confirming that the homogeneous disproportionation reaction is significant at low pH. In contrast, adsorbed NO is not detected at pH 7, in agreement with the fact that the disproportionation reaction (eq 14) proceeds exclusively at low pH.

Any contribution to the formation of nitrate via oxidation of nitrite ions by oxygen adsorbed on the Pd surface [55] is smaller than 5 % of the total conversion of the nitrite, assuming a fully O-covered Pd surface. Figure 4 shows that NO_x^- (x=2, 3) was observed on Pd catalyst, supporting the hypothesis that nitrite oxidizes to nitrate. Furthermore, the dominance of the homogeneous disproportionation reaction is confirmed with two control experiment in absence of any catalyst and in ambient in Figure A5. Nitrate is formed in absence of catalyst in a nitrite solution acidified to pH 3 with formic-acid as well as hydrochloric-acid. Note that the reaction time, typically a few hours, is not well defined in these experiments as the homogeneous reaction cannot be stopped in a controlled manor.

4.2. No formic-acid conversion at low pH

Figures 2a, 3 and 5b all show absence of any conversion of formic-acid at low pH. In **Chapter 4**, we found that Pd based catalyst suffers severe CO poisoning during formic-acid decomposition. Figure 5c shows the ATR-IR spectra in the range of CO_{ads} peaks during the batch reaction. It clearly shows no peaks that can be assigned to adsorbed CO, implying that CO_{ads} poisoning is not the reason that formic-acid is not converted.

One might speculate that the catalyst is deactivated for formic-acid conversion by nitrate. However, this can also be ruled out based on the observation that addition of nitrate in a formic-acid decomposition experiment has no effect on the rate of decomposition of formic-acid (Figure A6). Nitrate is not converted in this experiment because nitrate reduction requires a bimetallic catalyst, for instance Cu-Pd catalyst [28,35,43–45], instead of a monometallic Pd catalyst.

Therefore we suggest that the deactivation for formic-acid decomposition is caused by NO_{ads}. Noticeably, adsorbed NO is detected in ATR-IR (Figure 5) according the peak at 1716 cm^{-1}, preserving constant intensity during the experiment mimicking a batch experiment (Figure 5b). Figure 7 shows introduction of hydrogen induced rapid conversion of nitrite, without forming any nitrate. This proofs that the specie adsorbed on Pd, responsible for deactivation for formic-acid decomposition, is not deactivating the catalyst for nitrite hydrogenation. This agrees very well with the proposition that adsorbed NO is responsible, as previous ATR-IR studies showed that adsorbed NO is a key reaction surface-intermediate in reduction of nitrite with H_2 over Pd catalysts. Adsorbed NO on Pd converts readily with H_2 to N_2 [46]. In short, adsorbed NO is the reason for poisoning the catalyst for formic-acid decomposition.

4.3. Nitrite reduction with formic-acid at intermediate pH

Catalytic reaction of nitrite and formic-acid at pH above 4.5 results in simultaneous conversion of formic-acid and nitrite (Figure 2b and 3). This is in good agreement with the observations in Figure 6b, showing that nitrite (1235 cm^{-1}) and formic-acid (1581 cm^{-1}) peaks gradually disappeared in batch operation under pH 5 condition. Nitrate was not formed, implying that the homogeneous disproportionation reaction forming NO was prevented and catalyst remained active for formic-acid decomposition.

Interestingly, adsorbed NO is observed both at pH 3 (Figure 5b) and pH 5 (Figure 6b) but the origin is completely different. The NO_{ads} peak at pH 3 in Figure 5b is due to the homogeneous disproportionation reaction, as it is also observed in absence of any formic-acid (Figure 4), i.e. in absence of reductant. The amount of NO_{ads} is accumulating with the reaction time, preventing dissociation of formic-acid to form H_2 or chemisorbed H. Therefore, NO_{ads} cannot convert, resulting in poisoning the Pd catalyst as discussed above.

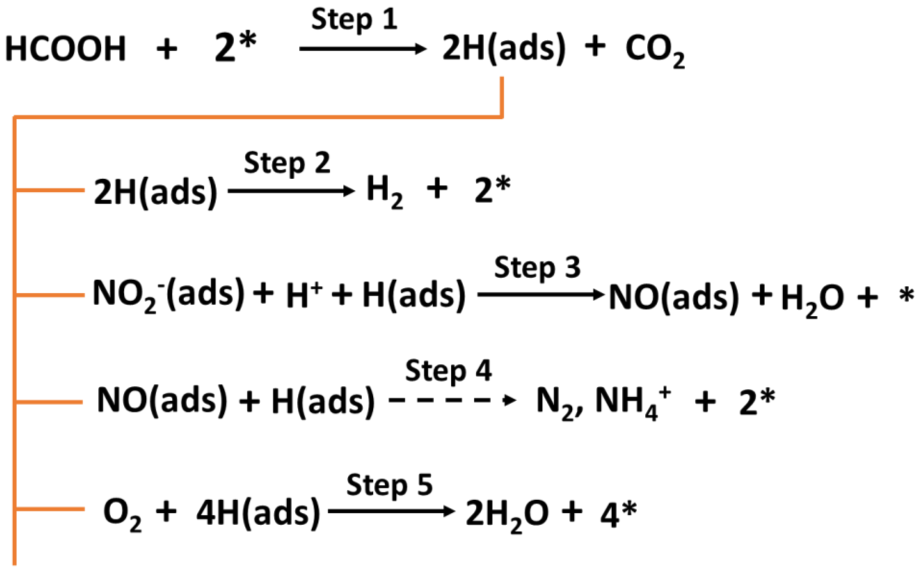

Scheme 2. Reaction scheme of nitrite reduction with formic-acid.

In contrast, adsorbed NO formed in presence of formic-acid and nitrite at pH 5 in Figure 6b is a reaction intermediate of nitrite reduction. Scheme 2 presents a reaction scheme with the most important steps, occurring during nitrite reduction with formic-acid. Note that in most of these steps multiple elementary reactions are lumped. In step 1, formic-acid decomposes to adsorbed H_{ads} and CO_2, requiring at least two active sites. It is likely that this steps would require even more Pd sites to allow formic acid to decompose, as Navlani-García et al. [64] reported that formic-acid decomposition is structure sensitive. Small Pd particles are less active, indicating that formic-acid decomposition requires an ensemble of Pd sites. Once H_{ads} is produced via step 1, H_{ads} can be consumed via steps 2, 3, 4 and 5. In step 2, two H_{ads} atoms desorb associatively to H_2 leaving the Pd surface. Step 3 and step 4 are in agreement with the nitrite reduction mechanism discussed from **Chapter 2**, although in step 4 the elementary steps are discussed in **Chapter 2** are lumped, accounting for the conversion of NO_{ads} to the products N_2 and ammonium. For the detailed discussion on nitrite reduction mechanism, please refer to **Chapter 2**. Summarizing, formation of NH_{ads} via dissociative hydrogenation of $HNOH_{ads}$ is the rate determining elementary reaction (RDS) within step 4. The RDS is after the formation of NO_{ads}, whereas the equilibria of elementary steps forming $HNOH_{ads}$ are on the side of NO_{ads}, so that adsorbed NO is visible with ATR-IR (Figure 6).

When oxygen is present, step 5 influences the performance. Table 3 shows that nitrite conversion was much higher under inert-flow-through condition than ambient-batch condition and the formic-acid efficiency is much lower under ambient-batch condition. This can be understood easily, as oxygen reacts readily with H_{ads}, competing with steps 3 and 4 and resulting in decreased nitrite conversion and decreased formic-acid efficiency under ambient-batch condition. As discussed in **Chapter 4**, oxygen can also react with CO_{ads} but this seems to be a limited effect as adsorbed CO is hard to detect with ATR-IR under these conditions (Figure 6c).

It is surprising that the presence of traces of oxygen decreases formic-acid conversion (Table 3), opposite to the observation in **Chapter 4** Figure 5, showing that formic-acid decomposition is greatly enhanced by the presence of small amounts of oxygen, preventing poisoning of the catalyst with CO_{ads}. As discussed above, oxygen reacts with H_{ads} (step 5,) decreasing the H_{ads} surface coverage. Therefore the rate of step 4 decreases, increasing the surface coverage of NO_{ads}, in agreement with the observations of Ebbesen that adsorbed NO forms on Pd exposed to nitrite at low H_{ads} surface coverage [46]. Consequently, less empty active sites are available for formic-acid decomposition, lowering the formic-acid conversion under ambient-batch condition. In short, formic-acid and NO_{ads} compete for Pd sites, whereas adsorbed NO can only form if formic-acid is also activated.

Table 4 shows that the conversion rate of nitrite increases with increasing concentration of formic-acid at pH 5, as expected as more reductant is available. Note that any change in pH during the experiment is buffered by the solution of formic-acid and sodium formate. Surprisingly, also the formic-acid conversion increases which indicates the reaction order in formic-acid is above 1 (Figure A7). Two factors contribute to this observation. Firstly, step 1 in Scheme 2 is enhanced by increasing the formic aid concentration, increasing the decomposition rate directly. Secondly, for the same reason the H_{ads} coverage increases, enhancing step 4 and decreasing the coverage of NO_{ads} and increasing the fraction of empty sites. So, step 1 is enhanced by both increasing formic-acid concentration and increasing availability of sufficient Pd ensembles required for the reaction. Finally, associative desorption to H_2 (step 2) is second order in the H_{ads} coverage, explaining that H_2 formation is more enhanced that nitrite reduction, decreasing the efficiency with increasing formic-acid concentration as observed in Table 4.

From a practical point of view, high formic-acid efficiency is preferred, achieved best at low formic-acid concentration (Table 4), at the expense of a very low reaction rate. At these conditions, all H atoms generated react with nitrite and no H_2 is flushed out of the reactor. Higher nitrite conversion rates can be achieved at higher formic-acid concentration, however also resulting in significant loss of H_2 flushed out of the reactor. Therefore, reaction in the batch mode without gas flowing through the reactor during the reaction is preferred, preventing H_2 gas escapes from the reactor. Flushing oxygen out of the reactor before the reaction is initiated would be preferred though, improving both rate and efficiency (Table 3). Formation of ammonium is negligible because formic-acid releases adsorbed H very slowly via decomposition compared with H_2 gas flowing continuously through the reactor (**Chapter 2** and **3**).

4.4 Nitrite reduction with formic-acid at high pH

At very high pH no reaction because formate ions cannot decompose to provide H_2 under our condition (**Chapter 4**, Figure A5) which is also in good agreement with literatures [65–67]. Therefore, no conversion for formic-acid and nitrite are expected.

5. Conclusions

This work demonstrates that formic-acid can reduce nitrite in the pH range between 4.5 and 8, producing negligible amounts of ammonium. The effect of pH, traces of oxygen and formic-acid concentration on the rates were determined and surface intermediates were observed with ATR-IR spectroscopy. The rate of conversion on nitrite with formic acid as well as the rate of decomposition of formic acid are controlled by competitive adsorption on Pd of nitrite, forming NO_{ads}, and formic-acid, forming adsorbed hydrogen and CO_2. Dissociative adsorption of formic acid required an ensemble of empty Pd atoms and therefore low coverage with NO. The coverage with NO is low if sufficient adsorbed H is available to convert NO rapidly to N_2, which in turn depends on the rate of dissociative adsorption of formic acid. This causes that formic-acid decomposition is 1.4 order in formic-acid. Homogeneous disproportionation reaction of nitric acid proceeds when the pH is below 4.5, resulting in catalyst poisoning with NO generated by the homogeneous disproportionation reaction independent of the catalyst. The catalyst shows no activity at pH above 8 due to the fact that formate ions are not reactive under our conditions.

Reference

[1] G. Gulis, M. Czompolyova, J. R. Cerhan, *Environ. Res.* **2002**, *88*, 182–187.

[2] C. S. Bruning-Fann, J. B. Kaneene, *Vet. Hum. Toxicol.* **1993**, *35*, 521–538.

[3] S. Hörold, K.-D. Vorlop, T. Tacke, M. Sell, *Catal. Today* **1993**, *17*, 21–30.

[4] V. Matějů, S. Čižinská, J. Krejčí, T. Janoch, *Enzyme Microb. Technol.* **1992**, *14*, 170–183.

[5] J. Schullehner, B. Hansen, M. Thygesen, C. B. Pedersen, T. Sigsgaard, *Int. J. Cancer* **2018**, *143*, 73–79.

[6] W. H. Organization, "Guidelines for Drinking-water Quality FOURTH EDITION," **n.d.**

[7] A. Kapoor, T. Viraraghavan, *J. Environ. Eng.* **1997**, *123*, 371–380.

[8] A. J. Lecloux, *Catal. Today* **1999**, *53*, 23–34.

[9] A. Bothner-By, L. Friedman, *J. Chem. Phys.* **1952**, *20*, 459–462.

[10] A. Pintar, G. Berčič, J. Levec, *AIChE J.* **1998**, *44*, 2280–2292.

[11] J. K. Chinthaginjala, L. Lefferts, *Appl. Catal. B Environ.* **2010**, *101*, 144–149.

[12] J. K. Chinthaginjala, J. H. Bitter, L. Lefferts, *Appl. Catal. A Gen.* **2010**, *383*, 24–32.

[13] H. C. Aran, J. K. Chinthaginjala, R. Groote, T. Roelofs, L. Lefferts, M. Wessling, R. G. H. H. Lammertink, *Chem. Eng. J.* **2011**, *169*, 239–246.

[14] Y. Zhao, J. A. Baeza, N. Koteswara Rao, L. Calvo, M. A. Gilarranz, Y. D. Li, L. Lefferts, *J. Catal.* **2014**, *318*, 162–169.

[15] R. Brunet Espinosa, L. Lefferts, *ACS Catal.* **2016**, *6*, 5432–5440.

[16] J. J. F. Scholten, in *Stud. Surf. Sci. Catal.*, **1979**, pp. 685–714.

[17] A. Obuchi, S. Naito, T. Onishi, K. Tamaru, *Surf. Sci.* **1982**, *122*, 235–255.

[18] S. B. Oblath, S. S. Markowitz, T. Novakov, S. G. Chang, *Inorg. Chem.* **1983**, *22*, 579–583.

[19] T.Tacke, *Tech. Univ. Carolo-Wilhelmina* **1991**, DOI http://dx.doi.org/10.1016/0039-6028(91)90317-L.

[20] J. Wärn, I. Turunen, T. Salmi, T. Maunula, *Chem. Eng. Sci.* **1994**, *49*, 5763–5773.

[21] E. E. A. (EEA), **2002**, DOI http://dx.doi.org/10.1016/0039-6028(91)90317-L.

[22] M. Vospernik, A. Pintar, G. Berčič, J. Levec, *J. Memb. Sci.* **2003**, *223*, 157–169.

[23] K. T. Ranjit, B. Viswanathan, *J. Photochem. Photobiol. A Chem.* **1997**, *108*, 73–78.

[24] G. Strukul, R. Gavagnin, F. Pinna, E. Modaferri, S. Perathoner, G. Centi, M. Marella, M. Tomaselli, *Catal. Today* **2000**, *55*, 139–149.

[25] O. M. Ilinitch, L. V. Nosova, V. V. Gorodetskii, V. P. Ivanov, S. N. Trukhan, E. N. Gribov, S. V. Bogdanov, F. P. Cuperus, *J. Mol. Catal. A Chem.* **2000**, *158*, 237–249.

[26] Y. Sakamoto, K. Nakamura, R. Kushibiki, Y. Kamiya, T. Okuhara, *Chem. Lett.* **2005**, *34*, 1510–1511.

[27] D. Gašparovičová, M. Králik, M. Hronec, Z. Vallušová, H. Vinek, B. Corain, *J. Mol. Catal. A Chem.* **2007**, *264*, 93–102.

[28] U. Prüsse, M. Hähnlein, J. Daum, K. D. Vorlop, *Catal. Today* **2000**, *55*, 79–90.

[29] A. Pintar, J. Batista, J. Levec, T. Kajiuchi, *Appl. Catal. B Environ.* **1996**, *11*, 81–98.

[30] J. Sá, J. Montero, E. Duncan, J. A. Anderson, *Appl. Catal. B Environ.* **2007**, *73*, 98–105.

[31] H. O. N. Tugaoen, S. Garcia-Segura, K. Hristovski, P. Westerhoff, *Sci. Total Environ.* **2017**, *599–600*, 1524–1551.

[32] S. Tyagi, D. Rawtani, N. Khatri, M. Tharmavaram, *J. Water Process Eng.* **2018**, *21*, 84–95.

[33] G. Mendow, N. S. Veizaga, C. A. Querini, B. S. Sánchez, *J. Environ. Chem. Eng.* **2019**, *7*, 102808.

[34] S. Guo, K. Heck, S. Kasiraju, H. Qian, Z. Zhao, L. C. Grabow, J. T. Miller, M. S. Wong, *ACS Catal.* **2018**, *8*, 503–515.

[35] Y. Ding, W. Sun, W. Yang, Q. Li, *Appl. Catal. B Environ.* **2017**, *203*, 372–380.

[36] O. S. G. P. Soares, M. F. R. Pereira, J. J. M. Órfão, J. L. Faria, C. G. Silva, *Chem. Eng. J.* **2014**, *251*, 123–130.

[37] S. Hamid, S. Bae, W. Lee, M. T. Amin, A. A. Alazba, *Ind. Eng. Chem. Res.* **2015**, *54*, 6247–6257.

[38] S. Jung, S. Bae, W. Lee, *Environ. Sci. Technol.* **2014**, *48*, 9651–9658.

[39] K. N. Heck, S. Garcia-Segura, P. Westerhoff, M. S. Wong, *Acc. Chem. Res.* **2019**, *52*, 906–915.

[40] R. Brunet Espinosa, D. Rafieian, R. S. Postma, R. G. H. Lammertink, L. Lefferts, *Appl. Catal. B Environ.* **2018**, *224*, 276–282.

[41] Y. Zhao, W. Liang, Y. Li, L. Lefferts, *Catal. Today* **2017**, *297*, 308–315.

[42] Y. Zhao, N. Koteswara Rao, L. Lefferts, *J. Catal.* **2016**, *337*, 102–110.

[43] E. kyoung Choi, K. hyun Park, H. bin Lee, M. Cho, S. Ahn, *J. Environ. Sci. (China)* **2013**, *25*, 1696–1702.

[44] Y. Wu, Y. Hu, J. Cheng, Y. Guo, *2010 4th Int. Conf. Bioinforma. Biomed. Eng. iCBBE 2010* **2010**, 2–5.

[45] A. Garron, F. Epron, *Water Res.* **2005**, *39*, 3073–3081.

[46] S. D. Ebbesen, B. L. Mojet, L. Lefferts, *J. Catal.* **2008**, *256*, 15–23.

[47] S. D. Ebbesen, B. L. Mojet, L. Lefferts, *Phys. Chem. Chem. Phys.* **2009**, *11*, 641–649.

[48] S. D. Ebbesen, B. L. Mojet, L. Lefferts, *J. Phys. Chem. C* **2009**, *113*, 2503–2511.

[49] B. L. Mojet, S. D. Ebbesen, L. Lefferts, *Chem. Soc. Rev.* **2010**, *39*, 4643–4655.

[50] S. D. Ebbesen, B. L. Mojet, L. Lefferts, *J. Phys. Chem. C* **2011**, *115*, 1186–1194.

[51] P. Xu, S. Agarwal, L. Lefferts, *J. Catal.* **2020**, *383*, 124–134.

[52] Fondriest Environmental Inc., "Fundamentals of Environmental Measurements: Dissolved Oxygen," can be found under https://www.fondriest.com/environmental-measurements/parameters/water-quality/dissolved-oxygen/, **2016**.

[53] R. Zhang, D. Shuai, K. A. Guy, J. R. Shapley, T. J. Strathmann, C. J. Werth, *ChemCatChem* **2013**, *5*, 313–321.

[54] I. Mikami, Y. Sakamoto, Y. Yoshinaga, T. Okuhara, *Appl. Catal. B Environ.* **2003**, *44*, 79–86.

[55] S. D. Ebbesen, B. L. Mojet, L. Lefferts, *Langmuir* **2008**, *24*, 869–879.

[56] R. S. Postma, R. Brunet Espinosa, L. Lefferts, *ChemCatChem* **2018**, *10*, 3770–3776.

[57] C. Franch, R. G. H. Lammertink, L. Lefferts, *Appl. Catal. B Environ.* **2014**, *156–157*, 166–172.

[58] F. Deganello, L. F. Liotta, A. Macaluso, A. M. Venezia, G. Deganello, *Appl. Catal. B Environ.* **2000**, *24*, 265–273.

[59] M. J. Weaver, S. Zou, C. Tang, *J. Chem. Phys.* **1999**, *111*, 368–381.

[60] R. Gómez, A. Rodes, J. M. Orts, J. M. Feliu, J. M. Pérez, *Surf. Sci.* **1995**, *342*, DOI 10.1016/0039-6028(95)00890-X.

[61] J. E. Pander, M. F. Baruch, A. B. Bocarsly, *ACS Catal.* **2016**, *6*, 7824–7833.

[62] M. F. Baruch, J. E. Pander, J. L. White, A. B. Bocarsly, *ACS Catal.* **2015**, *5*, 3148–3156.

[63] R. B. King, N. K. Bhattacharyya, K. D. Wiemers, *Environ. Sci. Technol.* **1996**, *30*, 1292–1299.

[64] M. Navlani-García, K. Mori, A. Nozaki, Y. Kuwahara, H. Yamashita, *ChemistrySelect* **2016**, *1*, 1879–1886.

[65] L. Yang, X. Hua, J. Su, W. Luo, S. Chen, G. Cheng, *Appl. Catal. B Environ.* **2015**, *168–169*, 423–428.

[66] J. Li, W. Chen, H. Zhao, X. Zheng, L. Wu, H. Pan, J. Zhu, Y. Chen, J. Lu, *J. Catal.* **2017**, *352*, 371–381.

[67] Q. F. Deng, Z. F. Zhang, F. J. Cui, L. H. Jia, *Int. J. Hydrogen Energy* **2017**, *42*, 14865–14871.

Appendix

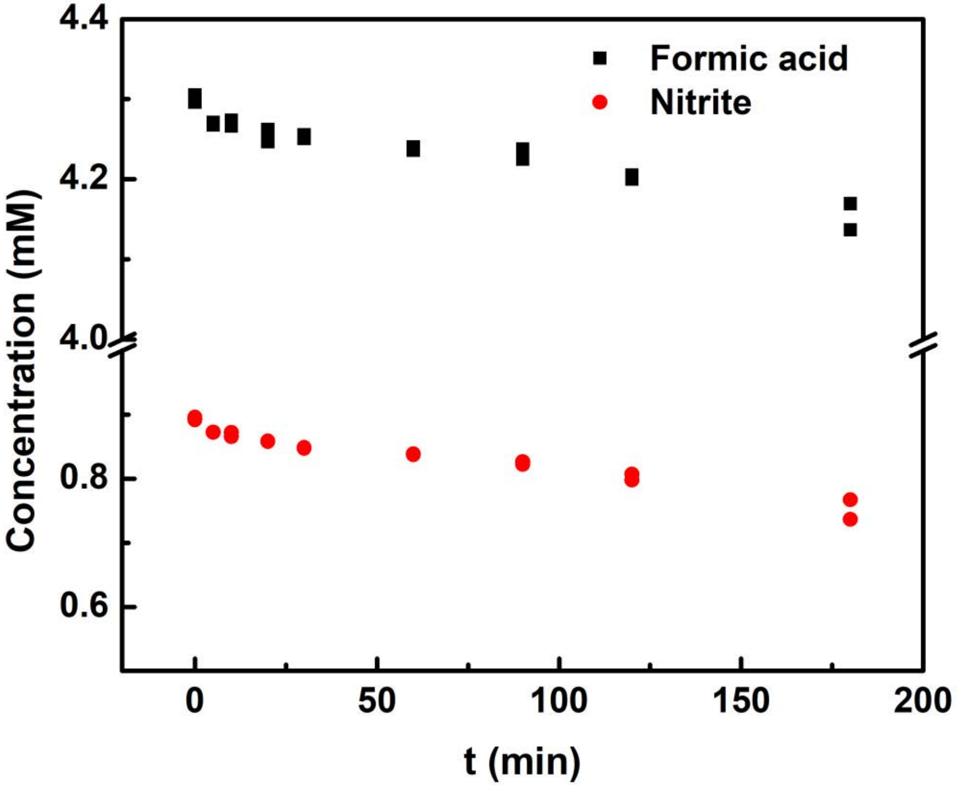

Figure A1. Concentration profile of formic-acid, nitrite under inert-flow-through mode at pH 5 condition 100 mg 0.9 wt% catalyst, 5 mM formic-acid solution, 1 mM nitrite).

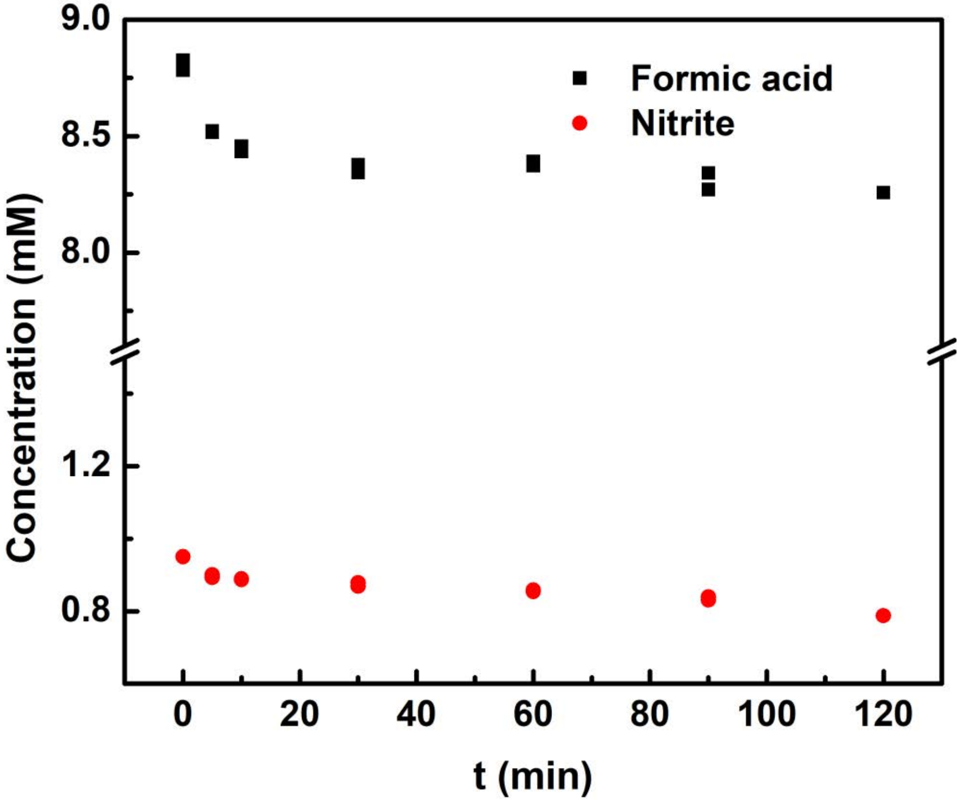

Figure A2. Concentration profile of formic-acid, nitrite under inert-flow-through mode at pH 5 condition 100 mg 0.9 wt% catalyst, 10 mM formic-acid solution, 1 mM nitrite).

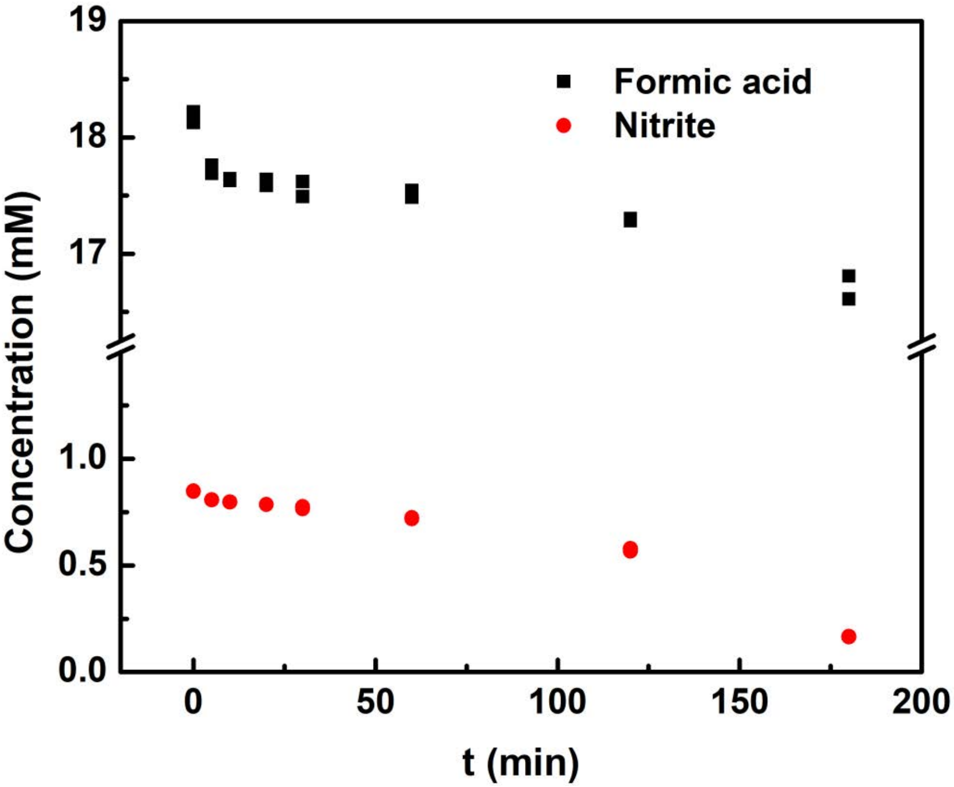

Figure A3. Concentration profile of formic-acid, nitrite under inert-flow-through mode at pH 5 condition 100 mg 0.9 wt% catalyst, 20 mM formic-acid solution, 1 mM nitrite).

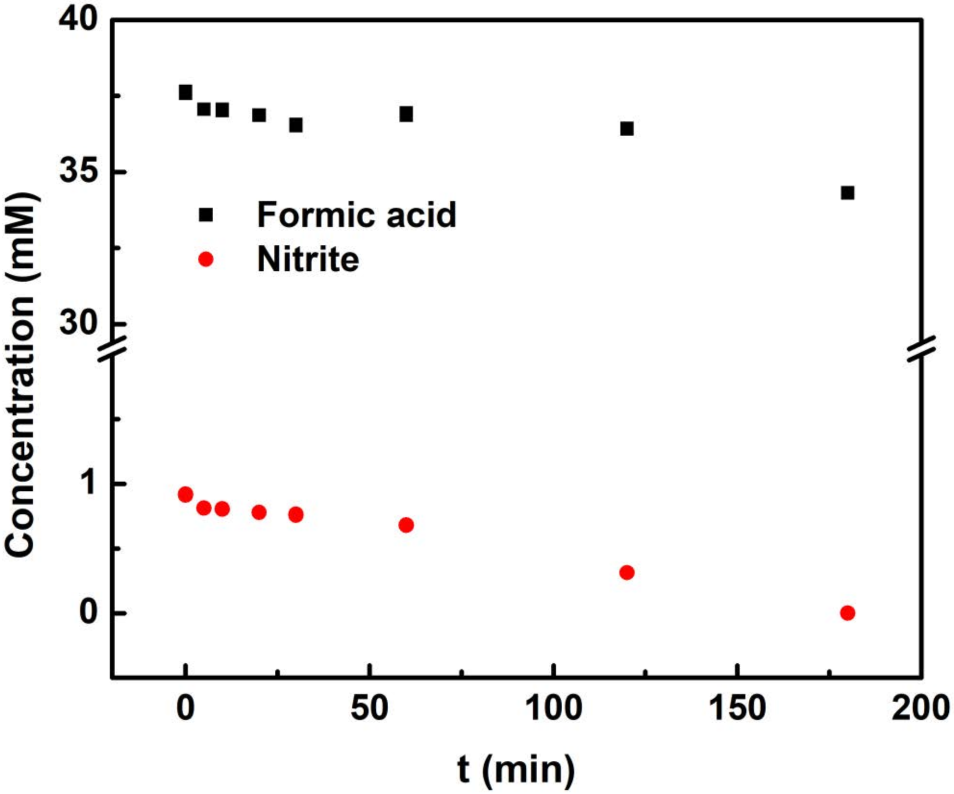

Figure A4. Concentration profile of formic-acid, nitrite under inert-flow-through mode at pH 5 condition 100 mg 0.9 wt% catalyst, 40 mM formic-acid solution, 1 mM nitrite).

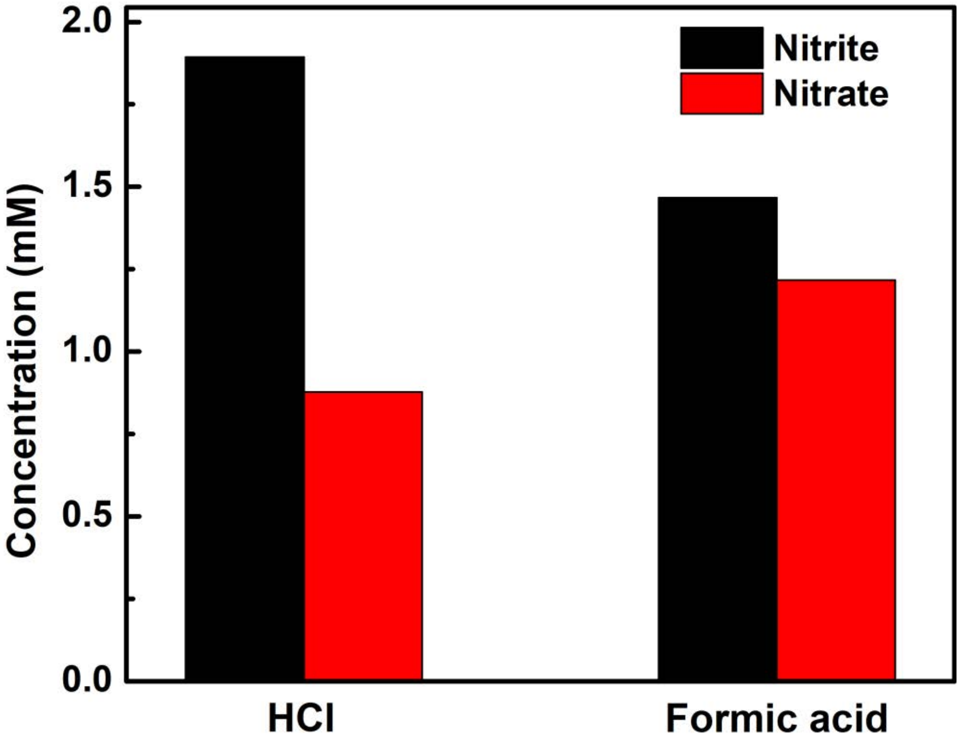

Figure A5. HCl (left bar), formic-acid (pH=3) (right bar) reacts with nitrite under ambient-batch mode, respectively (10 mM formic-acid, 10 mM HCl, 3 mM nitrite).

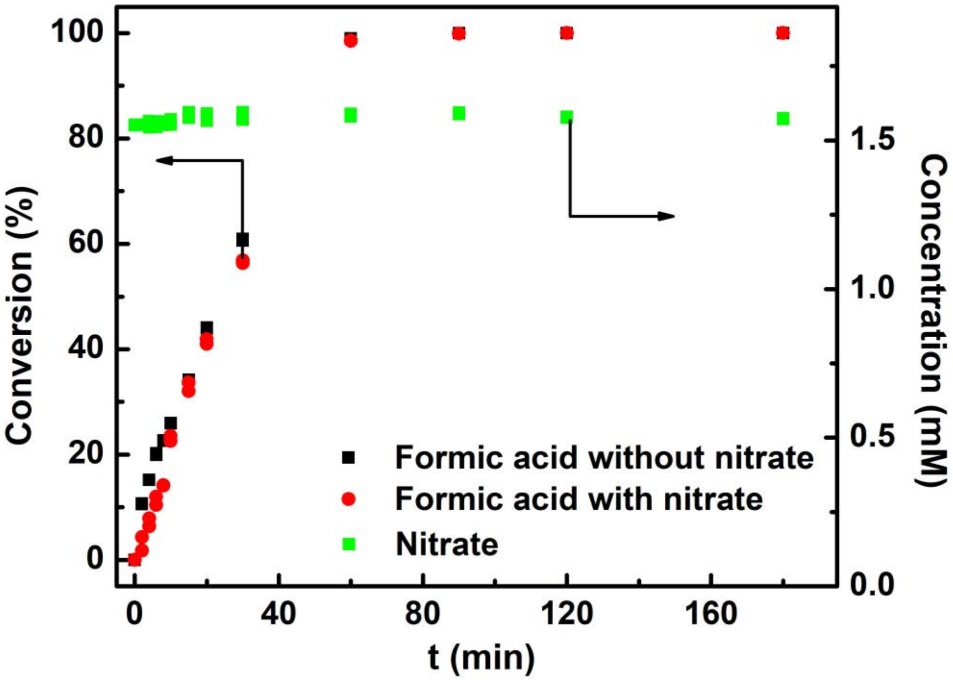

Figure A6. Formic-acid decomposition (pH = 3) experiments was performed under ambient-batch mode in presence of 0 mM and 1.5 mM nitrate, respectively.

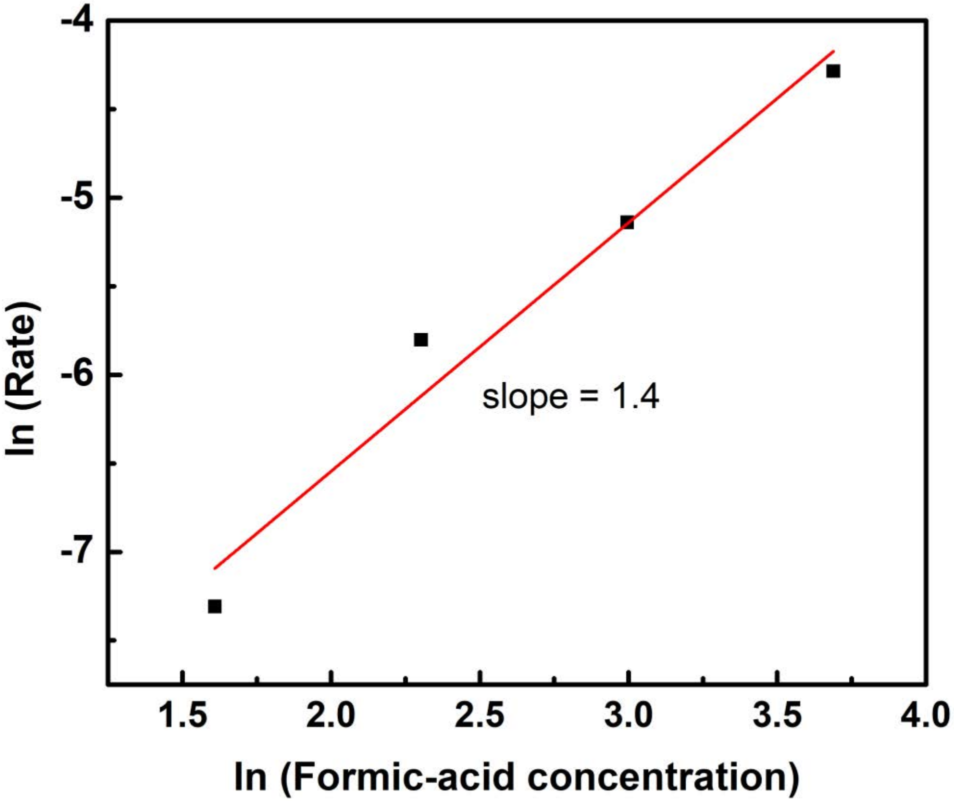

Figure A7. Effect of the initial formic-acid concentration on the formic-acid decomposition rate.

1. Calculation the nitrite reduction rate in batch and ATR experiments

1.1. Batch experiment

The reaction rate was estimated based on a the batch experiment at pH 5 (1 mM nitrite, 20 mM formic-acid, 100 mg catalyst, 50 ml/min He flow through). As shown in Table 4, nitrite conversion after 2 hours is 33 %, resulting in an averaged rate:

$$average\ rate = \frac{converted\ nitrite}{reaction\ time} = \frac{1\ mM * 0.33 * 0.3\ L}{120\ min} = 8.25 * 10^{-7}\ mol/min$$

Amount of surface Pd (mol) is calculated based on the dispersion by:

$$n_{Pd} = \frac{mass\ of\ catalyst * loading\ of\ Pd * dispersion\ of\ Pd}{molecular\ weight\ of\ Pd}$$

$$= \frac{100\ mg * 0.009 * 0.56}{106.42\ g/mol} = 4.7 * 10^{-6}\ mol$$

Apparent TOF is calculated by:

$$apparent\ TOF = \frac{average\ rate}{n_{Pd}} = \frac{8.25 * 10^{-7} mol/min}{4.7 * 10^{-6}\ mol} = 0.18\ min^{-1}$$

1.2. ATR experiment

The ATR reaction rate is estimated based on the results shown Figure 6b, observing disappearance of the free nitrite peak within 38 min. The reaction volume is the volume of the ATR cell, estimated as 0.4 mL based on the dimension of the cell. The average reaction rate is estimated according:

$$average\ rate = \frac{nitrite\ concentration\ in\ the\ ATR\ cell}{reaction\ time} = \frac{10\ mM * 0.4\ mL}{38\ min}$$

$$= 1 * 10^{-7}\ mol/min$$

Amount of the surface Pd (mol) based on the dispersion of Pd is calculated by:

$$n_{Pd} = \frac{mass\ of\ catalyst * loading\ of\ Pd * dispersion\ of\ Pd}{molecular\ weight\ of\ Pd} = \frac{5\ mg * 0.031 * 0.35}{106.42\ g/mol}$$

$$= 5.1 * 10^{-7}\ mol$$

Apparent TOF is calculated by:

$$apparent\ TOF = \frac{average\ rate}{n_{Pd}} = \frac{1 * 10^{-7} mol/min}{5.1 * 10^{-7} mol} = 0.19\ min^{-1}$$

Therefore the rate observed in both experiments are remarkably similar.

Chapter 6

Conclusions and outlook

1. Nitrite hydrogenation and mass transfer

Catalytic conversion of nitrite is considered as a promising method for drinking water purification. Pd based catalyst is proved as the most active catalyst for nitrite hydrogenation. However, to design the reactor and process, the reaction orders and reaction mechanism are desired. In **Chapter 2** we performed an intrinsic kinetic study on Pd/Al_2O_3 catalyst. The reaction was performed in a wide window of nitrite and hydrogen concentrations, resulting in significant variation in reaction orders. Reaction order 2 in hydrogen and negative order, i.e -0.9, in nitrite are observed at low hydrogen concentration combined with high nitrite concentration. The reaction order 2 in hydrogen at low hydrogen concentration indicates that adsorbed H (H_{ads}) is not only involved in the rate determining step (RDS), but also be involved in three pre-equilibria elementary steps, determining the concentration of other surface intermediates in the RDS. Based on this rule, different reaction pathways and RDSs have been discussed. It turns out that formation of NH_{ads} via dissociative hydrogenation of $HNOH_{ads}$ is the RDS, whereas N-N bond formation is not rate determining. Product N_2 forms via reaction of NH_{ads} with either NO_{ads}, NOH_{ads} or $HNOH_{ads}$. However, the elementary steps for N_2 and ammonium formation are still not clear. NO_{ads} is an important intermediate specie [1]. The kinetic study revealed that the possible reaction pathways to N_2 and ammonium separate after NO_{ads} formation (Scheme 1). However the reaction pathways to N_2 and ammonium are not clear yet. Therefore, it is advised to perform additional ATR-IR transient experiments only on NO hydrogenation over Pd catalyst in order to understand the intermediates during the NO hydrogenation. For the transient experiments on NO hydrogenation, the catalyst is first reduced with H_2 resulting in Pd hydride. Then NO saturated solution flows through the ATR-IR cell, and the reaction intermediates are observed which will help understand the reaction mechanism after NO formation in the nitrite hydrogenation.

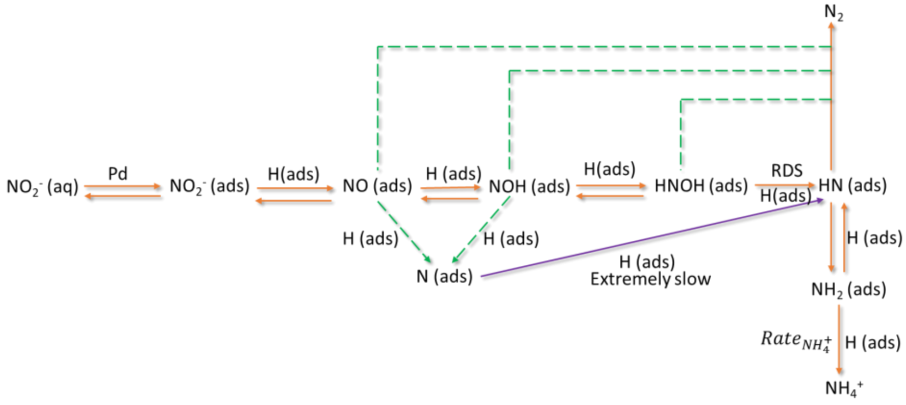

Scheme 1. Proposed mechanism of nitrite hydrogenation over Pd catalyst, dashed line indicate three possible reaction steps contributing to formation of N_2, as well as two possible steps to N_{ads} (**Chapter 2**)

In **Chapter 3**, we successfully synthesized partially hydrophilic catalyst and investigated the performance for nitrite hydrogenation. The partially hydrophilic catalyst is synthesized by physical mixing hydrophilic domains and hydrophobic domains, both smaller than 38 μm, followed by pelletization, breaking and sieving to obtain ideal particle size. The hydrophobic domains are modified with FOTS (Trichloro(1H,1H,2H,2H-perfluorooctyl)silane) without containing any Pd active sites, whereas hydrophilic domains contains the Pd metal. The ratio of hydrophilic domain and hydrophobic domain in the partially hydrophilic catalyst is well controlled, and the ratio is independent of the particle size of the final catalyst. Via this method to obtain the partially hydrophilic catalyst is intend to modify the catalyst particles not only the outer surface of the catalyst but also the inner surface (**Chapter 3**). We show that partially hydrophilic catalysts achieve the same rate per gram Pd at lower hydrogen pressure compared to fully hydrophilic catalysts. It is found that partially hydrophilic catalyst, sized between 100 and 250 μm, shows the best performance. However, when the size of partially hydrophilic catalyst is larger than 250 μm, the activity decreases. This is ascribed to the physical mixing method, likely leading to isolated domains, i.e. hydrophilic domains surrounded completely by hydrophobic domains so that these are inaccessible for reactants in water. Therefore, isolated domains decrease the number of active sites contributing to the reaction. Therefore, it is important to manipulate the distribution of hydrophilic and hydrophobic domains in the whole catalyst particles, preventing this isolation phenomenon.

In order to prove the hypothesis that isolated zones exist when partially hydrophilic catalyst particles are larger than 250 µm, we currently collaborate with Forschungszentrum Jülich GmbH using Time-of-Flight Secondary Ion Mass Spectrometry (ToF-SIMS) equipment to analysis our partially hydrophilic catalyst, focusing on the distribution of the hydrophobic domains in the partially hydrophilic catalyst. We use 30keV Bi beam generating the secondary ions for the mass spectroscopy to analysis our sample in the area of 131.25 * 131.25 µm. In order to obtain the inner side of the catalyst particle information, we use 1keV O_2 beam for sputtering the sample in the area of 400 * 400 µm and gaining depth. Therefore, the catalyst are removed layer by layer, and we obtained 36 images from top to the depth of 20 to 40 µm in total, and nine images are equally chosen according to the position of the layer shown in Figure 1. Be noted the initial hydrophilic and hydrophobic domain size are below 38 µm, and mean particle size is around 26 µm. It is clear that the black areas (hydrophobic domains) or white areas (hydrophilic domains) are all interconnected to each other, and no isolated area is observed. This is in good agreement with our hypothesis in **Chapter 3** to explain the activity enhanced in the partially hydrophilic catalyst (100 - 250 µm). In order to prove that there are isolated domains in the big catalyst particles (300 – 425 µm) resulting in losing active sites, our future step is to characterize our big partially hydrophilic catalyst (300 – 425 µm). However the drawback of this characterization method is that the catalyst are destroyed with high energy. In order to overcome this drawbacks, hyperspectral X-ray computed tomography method are worth to try which allows the internal elemental chemistry of an object to be reconstructed and visualized in three dimensions [2].

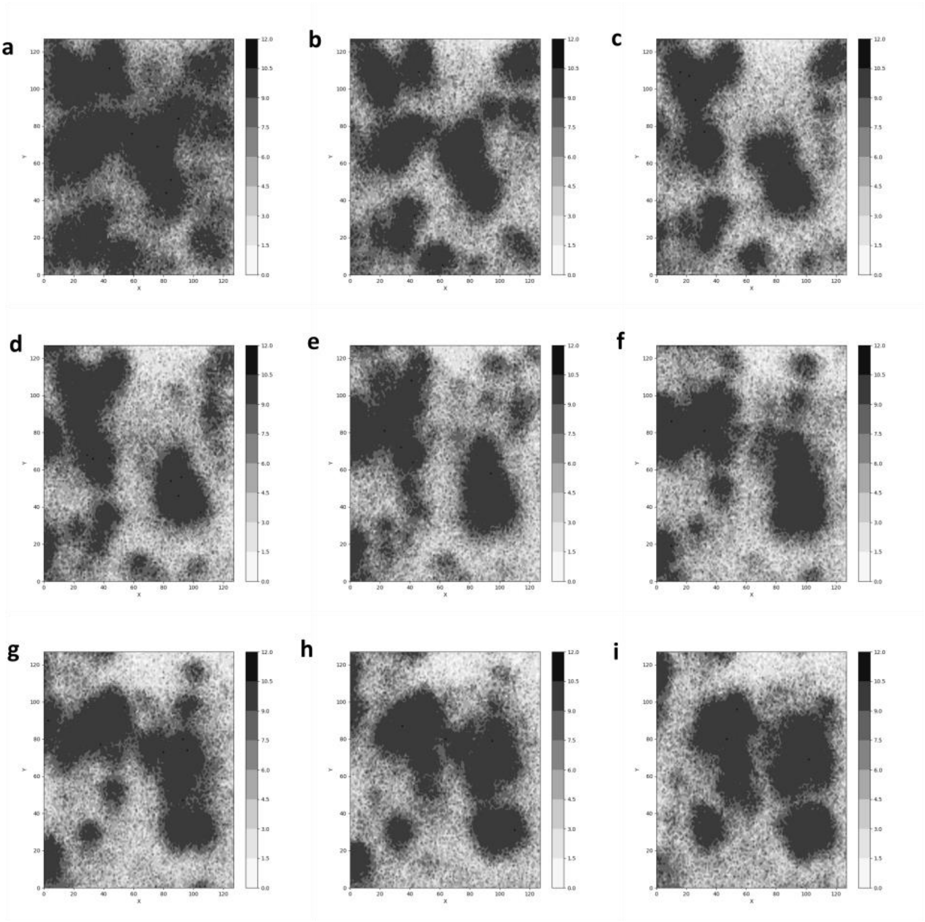

Figure 1. ToF- SIMS analysis different layers from top to the depth of 20 – 40 μm (a-i) of a 50 % hydrophilic catalyst (100 – 250 μm) (**Chapter 3**) in the area of 131.25 *131.25 μm, and the black area indicates the rich fluor area meaning hydrophobic domains (analysis beam 30keV Bi generating the secondary ions for the mass spectroscopy, sputter beam 1keV O_2 for effective sputtering the sample and gaining depth in a reasonable time).

Alternative method to avoid the isolated domains is to use additive manufacturing, also known as 3D printing. So far there are quite few attempts using 3D printing technique to fabricate Pd and Cu catalyst [3,4], with the advantage of 3D printing, the structure of the catalysts are well controlled. Generally, support like SiO_2 and Al_2O_3 are used to fabricate the catalyst. However the high temperature treatment (more than 1000 °C) is required to improve the structure strength. In order to prevent the high temperature treatment, the thermoplastics are considered. Hydrophobic domain material can be used as ABS, Teflon and polypropylene. PET and nylon can be used as hydrophilic domain material [5]. The active metal precursor solution is added to hydrophilic or hydrophobic domain printing material when printing materials is melting before printing. However the challenge is that the metal ions buried in the solution cannot be reduced afterwards implying the low efficiency of the metal impregnation. Another challenge is the catalyst particle size which depends on the 3D printing accuracy. The printing accuracy largely depends on the printing machine, printing materials, the design of the structure and the printing method such as fused deposition modeling (FDM), stereolithography (SLA), and selective laser sintering (SLS), material jetting and metal printing (specifically DMLS and SLM) [5]. Here we propose few different patterns as the inspiration for the hydrophilic/phobic catalyst shown in Figure 2.

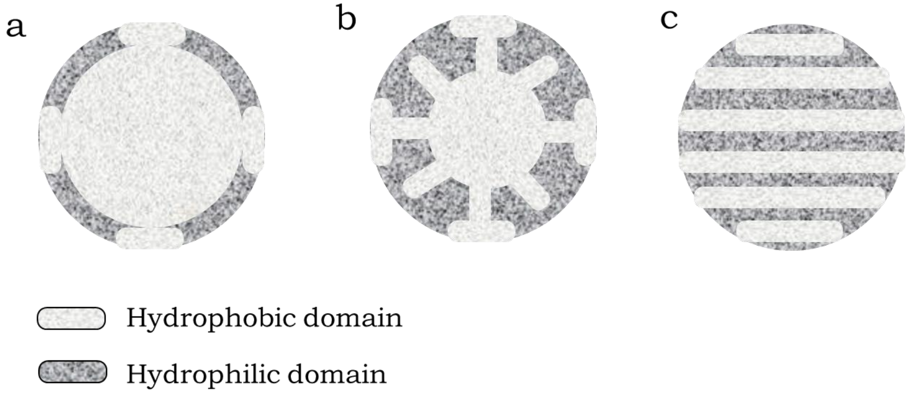

Figure 2. Listed few proposed hydrophilic/phobic catalyst structure, the pattern is the cross section of the catalyst.

2. Formic acid decomposition and mass transfer

Formic acid has been extensively studied as a liquid hydrogen carrier [6–8]. However it is known that supported Pd catalysts suffer from serious deactivation, mostly assigned to CO poisoning [9,10]. In **Chapter 4**, we present the influence of trace amounts of oxygen on the rate of formic acid decomposition. It is found that by introducing trace amounts of oxygen, the catalyst activity, stability and hydrogen yield can be improved. The hydrogen yield is maximal at using a gas mixture containing 0.1 vol% oxygen, under our conditions. However, increasing the oxygen concentration from 0.1 to 2 vol%, decreases the hydrogen production significantly and the formic acid oxidation reaction gradually dominates the reaction.

It is clear, according to our experimental results, that oxygen could suppress the catalyst deactivation but cannot completely prevent catalyst deactivation, which implies that deactivation is not only caused by CO poisoning. We summaries there are three possible ways which could lead to the deactivation. Firstly, the catalyst is slowly poisoned by the intermediates or products such as CO_2, formate and H_2. Secondly, catalyst losing activity is caused by the active metal or active sites losing. Thirdly, the impurity of the formic acid causes the activity decreasing.

For the first hypothesis, I suggest to determine any influence on catalyst performance of pre-treatments with CO_2, formate and H_2. That means before adding the formic acid to initiate the reaction, first pre-treat the reaction solution and catalyst with selected chemicals. Then formic acid solution is added to the solution to initiate the reaction. As we noticed that few previous studies [11,12] reporting deactivation mechanism do not take oxygen into account. Therefore, oxygen is needed to be rigorously removed in further experiments, since we know that oxygen affects the catalyst performance significantly (**Chapter 4**). For the active metal or sites losing, I propose to conduct the characterization on spent catalyst. To check the metal loading, XRF is an ideal opinion. For the active sites, we can use TEM to check the metal particle size after the experiments comparing with fresh catalyst. CO-chemisorption can also be used for checking the metal dispersion after the experiments. For the impurity of the formic acid, since most impurity is coming from acetic acid [13], the effect of the acetic acid can be tested by adding extra amount of acetic acid to the formic acid solution.

The possible influence of mass transfer is barely discussed in literature on formic acid decomposition. However, it is known that significant amounts of gas products are generated in the formic acid decomposition reaction, which could cause chaotic movement of the liquid in the catalyst pore according to the “oscillation theory” [14–16]. The effects of bubbles formation in the catalyst pores might slow down or enhance internal mass transport. Jin et al. [17] demonstrated that 3D interconnected pore structure of mesoporous silica supports is more favorable for mass transfer than 2D cylindrical mesoporous structure, and the better mass transfer provides higher catalytic activity in formic acid decomposition. Therefore, it is important to investigate the influence of pore size and porosity. I suggest to conduct experiments on different catalyst supports with different pore size, such as γ-Al_2O_3, α-Al_2O_3 and entangled carbon nanofiber to compare the catalyst performance.

As we known that gas bubble is more affinity to a hydrophobic surface, in order to improve the gas transportation in the pores, we suggest to introduce hydrophobic domains next to the hydrophilic domains similar structure as we discussed in **Chapter 3**. With the help of the hydrophobic domains, we expect that the chance of gas bubbles trapped in the hydrophilic domains which contains the active metal exclusively is minimized. However the structure of the hydrophobic domains is also important for transporting the gas products to the outside of the catalyst. Therefore, the support with big pores and 3D interconnected channel is preferred such as hydrophbized α-Al_2O_3 and entangled carbon nanofibers. Alternative method is 3D printing as we discussed in the previous section, we propose to use 3D printing to fabricate the catalyst to manipulate the hydrophilic and hydrophobic domains distribution (Figure 2).

Hydrogen gas is mostly used as the reactant for nitrite hydrogenation, with the disadvantage that hydrogen may not be available locally and requiring strict measures to ensure safe operation. Formic acid is an alternative reductant for nitrite, studied in **Chapter 5**. It is found that formic acid successfully reduces nitrite in the pH range between 4.5 and 8, forming negligible amounts of ammonium. By investigating the effect of the oxygen and initial formic acid concentration on the rates, order 1.4 in formic acid for formic acid decomposition is observed and the rate of conversion on nitrite with formic acid as well as the rate of formic acid decomposition are controlled by competitive adsorption on Pd of nitrite, forming NO_{ads}, and formic-acid, forming H_{ads} and CO_2. Formic acid dissociative adsorption requires an ensemble of empty Pd atoms and therefore low coverage with NO_{ads}. The coverage with NO_{ads} is low requiring sufficient adsorbed H to convert NO_{ads} rapidly to N_2, which in turn depends on the rate of formic acid dissociative adsorption. When pH of the solution is higher than 8, there is no nitrite conversion observed, due to formate ions do not show activity over Pd catalyst to provide H_2 (**Chapter 4**). The nitrite disproportionation reaction takes place homogeneously when pH is below 4.5, and the formation of NO results in catalyst poisoning (Equation 1).

$$3HNO_2 \rightarrow 2NO + HNO_3 + H_2O \qquad eq1$$

Due to the involvement of protons in the reaction, conductivity of the support could be play a role during the reaction. As electron moves much faster than the molecules diffusing in the liquid phase to the active site on catalyst, the mass transfer rate can be improved with using electrons instead of using H_2 to reduce nitrite (Figure 3). In turn, it will also diminish the competition between different species such as nitrite, NO_{ads}, formic acid and H_{ads}. In addition, based on our group previous work on nitrite hydrogenation, it is proved that using carbon nanofibers as the support achieved much higher activity than the non-conductive support γ-Al_2O_3 [18]. Therefore, we suggest to test conductive support like carbon comparing with γ-Al_2O_3 support.

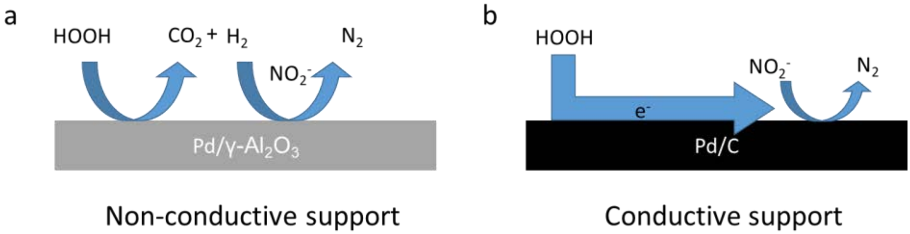

Figure 3. a) Formic acid decomposition and nitrite reduction on the non-conductive support γ-Al_2O_3, b) formic acid decomposition and nitrite reduction on the conductive support carbon.

In order to diminish the surface competition between formic acid, H_{ads}, nitrite and NO_{ads}, we suggest to introduce second active metal. Bi- and tri-metal catalysts have been investigated for formic acid decomposition [19–21], showing significantly promotion the catalyst activity and stability. Pd/Ag [20] is the most common metal combination selected for formic acid decomposition. We suggest to conduct nitrite reduction with formic acid over this catalyst.

Reference

[1] S. D. Ebbesen, B. L. Mojet, L. Lefferts, *J. Catal.* **2008**, *256*, 15–23.

[2] C. K. Egan, S. D. M. Jacques, M. D. Wilson, M. C. Veale, P. Seller, A. M. Beale, R. A. D. Pattrick, P. J. Withers, R. J. Cernik, *Sci. Rep.* **2015**, *5*, 15979.

[3] A. S. Díaz-Marta, C. R. Tubío, C. Carbajales, C. Fernández, L. Escalante, E. Sotelo, F. Guitián, V. L. Barrio, A. Gil, A. Coelho, *ACS Catal.* **2018**, *8*, 392–404.

[4] C. R. Tubío, J. Azuaje, L. Escalante, A. Coelho, F. Guitián, E. Sotelo, A. Gil, *J. Catal.* **2016**, *334*, 110–115.

[5] B. Redwood, "Dimensional accuracy of 3D printed parts | 3D Hubs," can be found under https://www.3dhubs.com/knowledge-base/dimensional-accuracy-3d-printed-parts/, **2020**.

[6] K. Grubel, H. Jeong, C. W. Yoon, T. Autrey, *J. Energy Chem.* **2020**, *41*, 216–224.

[7] R. van Putten, T. Wissink, T. Swinkels, E. A. Pidko, *Int. J. Hydrogen Energy* **2019**, DOI 10.1016/j.ijhydene.2019.01.153.

[8] L. Zhang, W. Wu, Z. Jiang, T. Fang, *Chem. Pap.* **2018**, *72*, 2121–2135.

[9] S. Il Choi, J. A. Herron, J. Scaranto, H. Huang, Y. Wang, X. Xia, T. Lv, J. Park, H. C. Peng, M. Mavrikakis, Y. Xia, *ChemCatChem* **2015**, *7*, 2077–2084.

[10] M. Navlani-García, D. Salinas-Torres, D. Cazorla-Amorós, *Energies* **2019**, *12*, DOI 10.3390/en12214027.

[11] M. Caiti, D. Padovan, C. Hammond, *ACS Catal.* **2019**, *9*, 9188–9198.

[12] C. Hu, J. K. Pulleri, S. W. Ting, K. Y. Chan, *Int. J. Hydrogen Energy* **2014**, *39*, 381–390.

[13] W. J. Arthur, G. W. Stkuthers, *Anal. Chem.* **1949**, *21*, 1209–1210.

[14] L. B. Datsevich, *Appl. Catal. A Gen.* **2003**, *247*, 101–111.

[15] L. B. Datsevich, *Catal. Today* **2003**, *79–80*, 341–348.

[16] L. B. Datsevich, *Appl. Catal. A Gen.* **2003**, *250*, 125–141.

[17] M. H. Jin, D. Oh, J. H. Park, C. B. Lee, S. W. Lee, J. S. Park, K. Y. Lee, D. W. Lee, *Sci. Rep.* **2016**, *6*, 33502.

[18] J. K. Chinthaginjala, L. Lefferts, *Appl. Catal. B Environ.* **2010**, *101*, 144–149.

[19] H. Alamgholiloo, S. Zhang, A. Ahadi, S. Rostamnia, R. Banaei, Z. Li, X. Liu, M. Shokouhimehr, *Mol. Catal.* **2019**, *467*, 30–37.

[20] S. Akbayrak, *J. Colloid Interface Sci.* **2019**, *538*, 682–688.

[21] Z. Dong, F. Li, Q. He, X. Xiao, M. Chen, C. Wang, X. Fan, L. Chen, *Int. J. Hydrogen Energy* **2019**, *44*, 11675–11683.

Scientific contributions

List of publications

1. **Pengyu Xu**, Shilpa Agarwal, Leon Lefferts, Mechanism of nitrite hydrogenation over Pd/γ-Al_2O_3 according a rigorous kinetic study, **Journal of Catalysis**, Volume 383, March 2020, Pages 124-134

2. **Pengyu Xu**, Shilpa Agarwal, Jimmy Faria Albanese, Leon Lefferts, Structured catalyst enhancing transport in Gas-Liquid-Solid reaction: nitrite hydrogenation, **Chemical Engineering & Processing: Process Intensification**, Volume 148, February 2020, 107802

3. **Pengyu Xu**, Shilpa Agarwal, Leon Lefferts, Formate as the in-situ H_2 and CO_2 supplier for nitrite hydrogenation in aqueous phase, **in preparation**

4. **Pengyu Xu**, Fernando D. Bernal-Juan and Leon Lefferts, Oxygen effect on supported palladium catalyst for formic acid dehydrogenation, **submitted to Journal of Catalysis**

Oral presentations

1. Effect of oxygen for formic acid decomposition on Pd catalyst --- The 11th International Conference on Environmental Catalysis (***ICEC**, 6th - 9th September 2020, Manchester, UK*)

2. Trace of oxygen stabilizes support palladium catalyst for formic acid dehydrogenation --- The Netherlands' Catalysis and Chemistry Conference (***NCCC XXI**, 2nd – 4th March 2020, Noordwijkerhout, NL*)

3. Structured catalyst with enhanced gas transfer in Gas-Liquid-Solid reaction system --- North American Catalysis Society Meeting (***NAM 26,*** *23th – 28th June 2019, Chicago, USA*)

4. Structured catalyst enhancing transport in Gas-Liquid-Solid reaction: nitrite hydrogenation --- The 6th International Conference on Structured Catalysts and Reactors (***ICOSCAR 6,*** *11th – 13th September 2019, Bad Herrenalb, DE*)

Poster presentations

1. Trace of oxygen stabilizes support palladium catalyst for formic acid dehydrogenation --- 17th International Congress On Catalysis (***ICC 2020,*** *14th – 19th June 2020, San Diego, USA*)

2. Mechanism of nitrite hydrogenation over Pd/γ-Al_2O_3 according a rigorous kinetic study --- 14th European Congress on Catalysis *(**EuropaCat,** 18th – 23th August 2019, Aachen, DE)*

3. Nitrite hydrogenation kinetics over Pd/γ-Al_2O_3 catalyst in slurry reactor ---- The Netherlands' Catalysis and Chemistry Conference *(**NCCC XX,** 4th - 6th March 2019, Noordwijkerhout, NL)*

4. Nitrite reduction kinetics over supported Pd catalyst in aqueous phase ---- The Netherlands' Catalysis and Chemistry Conference *(**NCCC XIX,** 5th - 7th March 2018, Noordwijkerhout, NL)*

Acknowledgements

Now it comes to end of my PhD, this four years are the exciting and fruitful journey for me. I am very grateful that I made a choice to come abroad for the PhD. Every moment of this beautiful experience will be perfectly kept in my mind. I got a long list to thank, however sometime you feel it is difficult to express the feeling which are you really want to say. When I was told by my dear supervisor at the beginning of my PhD, "I think you need to take some English course", this is how I started my PhD.

Yes, the first person I want to thank is my supervisor and promotor Leon, who is a wise, respectable and precisian, but also he is an amiable and cheerfully and always opening the door for discussion. I still remember the first skype interview which turned out really bad. I am really appreciate that you gave me second chance to speak with you, even the second time I would not say it was good, but I thought it was good enough. With a long process and waiting, finally my personal first time flight, first time oversea, first time to speak English everyday was coming. It was exciting but also difficult for me, but with your warm welcome, I finally adjusted to the new environment. At the beginning one and half years, I was trying to catch up with the project and trying to do my best to understand the project, and more and more I can give more input and we can have more discussion. I really enjoy the discussion between us, maybe sometime we cannot get something solid but at least we knew that we were moving forward. With the pure pleasure of discovery the mystery, it is the charm of science. Your attitude to the precise of the details will come along with me for the rest of my life. The last I have to mention is the last year issue which I was facing, you helped me out. Thank you Leon, thanks for all this four years walking through my PhD.

Shilpa, you are my daily supervisor, but I believe our relationship is beyond just as the colleague. You are savior for me, and every time after we have the meeting with Leon, I was always full of questions. At the beginning my knowledge and also my poor English gave a lot troubles, but you always help me with the knowledge and also English. The most important thing I valued is that your selfless encourage which really helps me a

lot. I slowly learn how to think, how to speak and how to make questions. You are there when I need help no matter how busy you are. We were not only talking about work also life, you are my friend. Now you are far away in UK with James, I knew you like your new job and I am really glad for you. Hope you are doing all great together with James. I am really appreciate what you did for me for the last year of my PhD, you know what I mean, and I own you.

Bert, you are an extremely helpful person, however it is tough at the beginning. After few beers, things will be solved I am sure. You always try your best to solve people problems in the lab, I have no doubt that you are the master in the lab and the king of Friday afternoon. It has been a good time working with you, even we still argue with something, but I am appreciate that. Tom are the rock star, I still remember one time in the bar hearing your band playing music. It is a special time for me and I still hold one of your album. You also help me a lot about the equipment, thanks to that. Now you start your new career in another lab, I wish you all the best with your future. Karin, you are like a big mom in the lab, you control most things in the lab, and try to keep thing more organized and clean. I always used a lot filters, but every time you give me a big bottle, I am really appreciate.

Dorothy, thank you very much for making me feel comfortable at the group at the beginning of my PhD. You always try to convince me to join the coffee break or other activity, and I felt really luck at that time. Now you are moving to another group to seek your new career, and I hope you are doing better and better. Anne, our new secretary, you are a nice person, always willing to help with other people, special during the lock down time. You helped me a lot with my insurance. But finally we got it done. Thank you, and wish you have a good time in the group and good luck with your guitar lesson. Jimmy, you are an enthusiastic person, and you always have some ideas. I have a good time with you when I worked with Shahab, it was a nice experience, even though we all have been through a lot during that time. However the outcome is sparkling for me at least. I wish you all the best for your career at UT.

The first year I came abroad alone and came to a group without Chinese people, which is quite an experience for me, but now I look it back that I really appreciate that time, because it helped me to grow fast and more independent. However there are few people

I must mention, they are my mentors. Reza, you are my first office mate at my beginning PhD. I was really nervous at the beginning, one part is because my English is horrible, and I barely can speak a long sentence; second part is I am a person who need time to warm up to get used to the new environment. But you are like big brother for me, and you walked me through most important palaces in UT, and I still remember you treat me for the first meal at UT which I will never forget. Thank you. However later on you moved to another group, I am regret I cannot do more to help you. I wish you all the best in your future life. Kamila, a girl from Kazakhstan, to be honest I am always trying to speak Chinese with you, actually you can speak a little bit. But I want to thank you that you always encourage me to speak English even though I cannot speak well. Gabriele, thanks for helping with me to practice my English, and we used to talk a lot in the lab. It was a nice time for me. Also thank you for helping with the moving, since I cannot drive the car here. That was a big help. Really thanks. Yinnan, thank you very much at the beginning of my PhD to help me with the experiments even though you are in Finland.

Rolf, we are more or less the same time start PhD, you are a nice person, helpful with discipline, and you help me a lot with the lab work special with the ion chromatography. Every time you use your magic hand to save the machine. I remember after one year of using manual injecting ion chromatography, one day you told me the auto sampler is working. I really thank you for that. You are also the big fun of Friday borrel, at the beginning I did not join too much. But every time you insist me to join the drink, and at last I joined the drink, but the beginning memory become blurry you know what I mean. Thank you for helping me to get to know the group much faster. You are a good friend. Tushar, I heard how wild you were before, but I never saw, and now you got your small family. You are the person never say no, and I always get help from you. Thank you very much and wish the best luck for the future. Guido, I heard you were a party animal, and I actually saw you are a party animal. But now you changed quite a lot from my view, thanks for Michela and Alessandro. You have learnt quite a lot Chinese from me, maybe it is time to teach me some Italian. Now you start your new stage of your life, and I wish you and your family all the best and good luck in the future work at CPM. Pengcheng, as you are new to CPM. You are a helpful person and now I get someone can speak Chinese

in the group finally. I really appreciate that. You are a typical Chinese, and you work hard. I wish all the best for your PhD research in CPM. Fernando, you just joined CPM family, and I thank you for helping me with some remaining experiments and I wish you the best for the coming PhD study.

Maria, you were doing the master assignment at CPM group and later on you decided to accept the challenge offered by Jimmy. I am happy you can stay for the PhD. Since we share quite some common knowledge for the research filed, we have a lot of discussion on science, but not limit to science and I am happy to work and talk with you. You are a person always helping others, sometimes I even think you are helping too much. I am very sorry to leave you a bad impress on your first borrel, since I am not really an alcoholic, but I do really appreciate the outcome of that borrel, and I wish you and Rolf will be happy forever.

Nuria, you are my office mate and friend. I still remember you complaint that at the beginning I did not ask you to take lunch together, and I am quite sorry about that, but we later become really good friends. You are a person who is always full of energy and we have spent so much time to discuss all kind of the things, and I am really like it and I will memorize forever. I also have a lot of memory about our CPM karaoke. Now you are far in France to pursue your career and I really wish you can find your career in Spain with your Ruben.

Koen, you are my first student. I am happy you chosen my topic, and you did a good job. Thanks for being my first student. I wish you all the best in your future life. Hilbert, you are a huge Dutch boy. You did well on research and you were very integrated with group social part. Thank you for the help on research. Now you are doing the master in UT, I wish all the best for your study. Youssef, you are a very practical person and you have some brilliant idea in the lab. I am sorry the last month of your assignment, I cannot be at UT. But you did a good job. I thank you for the effort you put on the research. I am sure you will do well in your job. Shahab, my first master student. First I want to thank you chosen my topic and stay with me to finish the project. We together have been through quite a lot. I am really appreciate the time we worked together. At beginning you are quite introvert with the group, but later on you have been an important part of the group. It is pity you cannot find the position at CPM. But now you are start your PhD

career at SPT, and I am sure you will be a doctor someday, and I wish you all the best my friend. Erwin, my last student, your work is also finished, and I am glad you achieved quite good results. We are looking forward to publish it and I wish all the best for your coming study.

There are many more people helped me during my PhD period and I may not mention your name but it does not mean you are not important, and I thank you all for helping me during my time here, and I wish you all best in your future. The last but not the least, I want to thank my family and my girlfriend Youzi. 感谢爸妈对我一直以来的理解支持与鼓励，希望你们的儿子没让你们失望。

2020.09.02, Enschede

Pengyu Xu (徐鹏宇) was born in Xiangyang, Hubei, China, in 1990. He received his bachelor degree in Chemical Engineering and Technology from Hubei University, China in June 2013. After his bachelor degree, he received his master degree in Analytical Chemistry from Shanghai University in June 2016. In September 2016, he started his Ph.D. degree in University of Twente, The Netherlands in the Catalytic processes and Materials group (CPM). The current thesis presents the outcome of his Ph.D. research.

9 789036 550475